ABSTRACT

Title of Thesis: CHARACTERIZATION AND MODELING OF BRUSHLESS DC MOTORS AND ELECTRONIC SPEED CONTROLLERS WITH A DYNAMOMETER

Robert H. Brown
Masters of Science, 2019

Thesis directed by: Professor Inderjit Chopra
Professor Anubhav Datta
Department of Aerospace Engineering

The global drone market is expected to grow from $4.9 billion to $14.3 billion within the next decade, indicating a heavy demand for high performance electric aircraft. Modern drones are propelled with brushless DC (BLDC) motors and electronic speed controllers (ESCs). However, a current lack of information concerning the performance and efficiency of BLDC motors and ESCs prevents their use in rigorous aircraft design. Low cost hobby ESCs and BLDCs are typically used in research aircraft, but few technical details are released by their manufacturers.

To better understand these devices, a custom dynamometer was constructed to study the performance of ESCs and BLDC motors. By properly recording the DC, AC, and mechanical power, information on peak efficiency and performance for the ESCs and BLDC motors are determined experimentally. Motors between 920 KV to 2500 KV were tested with 18 A, 30 A, and 40 A ESCs. A combination of these tests were carried out at 7.2 V, 11.1 V, and 14.8 V DC to explore trade

offs in the design process. While typically neglected in formal analysis, this work seeks to better understand the power loss mechanisms in ESCs, as it was found that ESCs could have efficiencies as low as 65%, reducing the overall efficiency of the system considerably. This custom dynamometer features a load varying device, power analyzers, and a unique two DAQ setup to properly capture the high frequency electrical signals of BLDC motors.

From the sets of experimentally recorded motor and ESC tests, a novel analytical model is developed to predict the performance of ESCs and BLDC motors. At the heart of this modeling effort is describing the 3 phase AC circuit as a single equivalent circuit, which encapsulating the motor's performance. This work is critical in the design process, as properly sizing ESCs, motors, and rotors for an electric aircraft can improve aircraft endurance and range. Performance metrics are extracted from experimental results and are fit into the analytical model. Predictions for the system's mechanical power, AC power, and DC power agree well with experimental results, demonstrating applicability of the robust model.

CHARACTERIZATION AND MODELING OF BRUSHLESS DC MOTORS AND ELECTRONIC SPEED CONTROLLERS WITH A DYNAMOMETER

by

Robert H. Brown

Thesis submitted to the Faculty of the Graduate School of the
University of Maryland, College Park in partial fulfillment
of the requirements for the degree of
Master of Science
2019

Advisory Committee:
Professor Inderjit Chopra, Co-Chair
Professor Anubhav Datta, Co-Chair
Professor Christopher Cadou

Preface

No motors, ESCs, or electric components were shorted in the making of this thesis.

Dedication

To my Mother and Father

I am forever grateful for the help you gave me during this journey.

Acknowledgments

Words cannot express the gratitude I have to the many people who have helped me over the years.

First and foremost is Dr. Chopra, as my advisor he has always managed to bring out the best problem solving skills in me. You have taught me something that you will not find in any textbook: *to never stop thinking about the problem.* For someone so important and on so many committees, I have always been amazed at how every time I come by your office you were able to meet with me and answer my questions. I will never forget the day when I sat in your office and you invited me to join the Rotorcraft Center, at first I did not believe it because it was too good to be true! It is an honor to be your student, and I look forward to working together in the future.

Dr. Datta, I am lucky to have you as my co-advisor. Your ability to ask the hard, direct questions has instilled a mentality in me to always be improving and refining my work. Due to your key insights into motor theory, I was able to progress my modeling work considerably. Your feedback allowed me to craft a physics based motor theory. Without your help this thesis would have been 100 pages shorter.

Dr. Cadou, thank you for lending me the critical pieces of equipment needed to make this dynamometer possible. I greatly appreciate the assistance you have given me over the past year to get this work started. Thank you for your help and for being on my committee.

Dr. VT, thank you for helping me relate my work back to the world of rotors.

You were able to ask fundamental questions, which allowed me to think critically about how my work fits into the grand scheme. Through our conversations you were able to help me get a glimpse of the bigger picture, and for that I am thankful.

Dr. Maqbool, you are the mentor that has known me the longest. The experience I gained working for you has always helped me stand out, and it never would have been possible if our paths did not cross. I still have the quadcopter we built sitting next to me on my desk, as it is a constant reminder of the fond memories. You were the first one who convinced me to go to graduate school and I am grateful for following your advice. Thank you for your encouragement and friendship.

Brent Mills, thank you for your help in getting me up to speed with motor theory. When I was first getting started the world of motors seemed like a jungle, but you were able to guide me to the most important points. I would often show you my data and analysis first because I valued your opinion and you weren't afraid to tell me some hard truths. It was difficult to find someone to talk about the finer points of my model, but you were always available to meet and ask meaningful questions that lead me to new discoveries.

Thank you to the various friends I have made here at the Rotorcraft Center: Ilya, Ehis, Vikram, and Brandyn. I appreciate your feedback on my work and keeping me sane through the hard times. Finally, I would like to thank my family members for their support, especially my fiancé Leah who has always been my biggest supporter.

Table of Contents

Commonly Used Definitions

A	Rotor Area, πR^2
C_0	ESC transformation offset
C_1	ESC transformation slope
C_P	Rotor shaft power coefficient, $\frac{P_R}{\rho A(\Omega R)^3}$
C_Q	Rotor torque coefficient, $\frac{Q_R}{\rho A(\Omega R)^2 R}$
C_T	Rotor thrust coefficient, $\frac{T_R}{\rho A(\Omega R)^2}$
η_{ESC}	ESC efficiency, $\frac{P_{AC}}{P_{DC}}$
η_m	Motor efficiency, $\frac{P_m}{P_{AC}}$
η_{sys}	Overall system efficiency, $\frac{P_m}{P_{DC}}$
f_{sw}	MOSFET switching frequency
GR	Gear ratio
$i(t)$	Instantaneous current
$v(t)$	Instantaneous voltage
I_{DC}	DC Current
I_o	Current required to overcome static motor friction
I_{pk}	Peak current
I_{rms}	Root mean square value of current, $rms\{i(t)\}$
K_E	Motor back voltage constant, $V_E = K_E\omega$
K_T	Motor torque constant, $Q = K_T I$
KV	Manufacturer specified RPM/V_{DC} for a BLDC motor, includes ESC
N	DC Ground
N^*	Neutral point of AC system
N_p	Number of pole pairs, $(\#\ of\ magnets)/2$
ω	Motor RPM
ω_e	Electrical driving frequency, $N_p\omega$
Ω	Rotor RPM
ω_{NL}	Motor no-load speed
P_{AC}	Active AC Power, $\frac{1}{T}\int_0^T v(t)i(t)dt$
P_{cond}	Conduction power loss, I^2R
P_{DC}	DC Power, $V_{DC}I_{DC}$
P_{ESC}	ESC Power, $P_{DC} - P_{AC}$
pf	Power factor, $\frac{P_{AC}}{S}$
p_{inst}	Instantaneous power, $v(t)i(t)$
P_m	Motor output power, $Q\omega$
P_{sw}	Switching power loss
Q	Mechanical torque
Q_{1-6}	MOSFET numbering
Q_{stall}	Motor torque at 0 RPM
R	Rotor radius

R_{ESC}	ESC equivalent resistance
R_m	Motor resistance
S	Apparent power in AC system, $V_{rms}I_{rms}$
T_R	Throttle input to ESC, normalized between $0 \leq T_R \leq 1$
θ	Motor shaft angle
θ_e	Electrical angle, $N_p\theta$
$v_{AN}(t)$	Instantaneous voltage of line A wrt DC Ground
$v_{AN^*}(t)$	Instantaneous voltage of phase A wrt motor neutral point
V_{DC}	DC Voltage
$V_{LL,rms}$	Line-to-line rms voltage, ex. V_{AC}, V_{BC}, etc.
$V_{ph,rms}$	Phase rms voltage, ex. V_{AN^*}, V_{BN^*}, etc.
V_{pk}	Peak value of phase voltage
I_{pk}	Peak value of line current

2S, 3S, 4S	Battery cell count (nominally 7.4 V, 11.1 V, and 14.8 V, respectively)
AC	Alternating current
BLDC Motor	Brushless DC motor
DC	Direct current
ESC	Electronic Speed Controller
Line-to-line	Voltage of one line measured wrt another line
MOSFET	Metal Oxide Field Effect Transistor
Phase	Voltage of one line measured wrt common point, typically N^*
rms	Root mean square
RPM	Revolutions per minute

Chapter 1: Introduction

1.1 Electric Aviation Demands

The world of Aerospace is changing fast. Electrification of aircraft has allowed for flying to become an everyday occurrence, with millions of worldwide drone users taking to the skies. Emergence of light weight composite structures, high density lithium polymer batteries, and reliable low-cost sensors have allowed for an increased interest into electric aviation. One of the largest advancements in recent decades are high power to weight ratio brushless DC (BLDC) motors. Increased efficiency and peak power allow for small, unmanned autonomous aircraft to complete useful tasks such as surveillance, infrastructure inspections, and package delivery. The promise of a new electric aircraft market has excited investors, as the global drone market is expected to grow from $4.9 billion in 2019 to $14.3 billion by 2028 [1].

Inexpensive drones have opened the door to a transportation revolution - urban air mobility. Recent interest in urban air mobility has placed a great deal of importance on electric aircraft. Prominent companies such as Uber have taken interests in air taxis, and promise to deliver full scale 4,000 lbs autonomous electric aircraft by 2023 [2, 3]. Numerous startups have emerged recently to provide low cost mobility and shipping solutions to Uber and other customers. Most of these

companies aim for "on demand aviation", where users are able to summon aircraft directly to their location and carry them a short 20 minutes to their destination.

Demand for electric motors comes from efficiency, economic, and reliability standpoints. An hour's flight time in a single engine airplane costs $3 in electricity and $40 in gasoline [4]. This difference can be associated with increased electric motor efficiency and increased aircraft performance associated with reduced system mass. Additionally, electric motors can be sized to directly drive propellers, eliminating heavy and expensive gearboxes and further reduces costs.

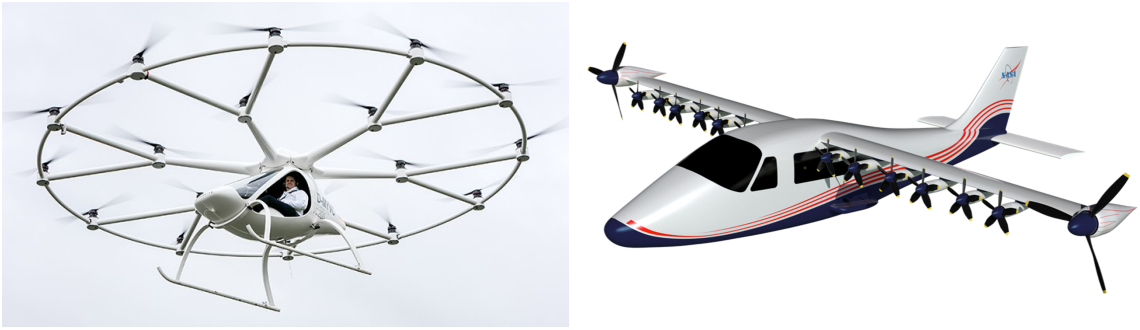

Figure 1.1: Left: E-volo's VoloCopter. Right: NASA's X-57.

The first manned e-VTOL personal air vehicle, E-volo's VoloCopter, flew on March 30th, 2016 [5]. Following this, many companies have begun testing radical designs, featuring distrusted electric propulsion systems, with the goal of carrying passengers. Introduction of manned electric aircraft is first expected in niche markets, such as electrifying 3 hour flight time trainer aircraft [4]. Within the last couple of years, the Vertical Flight Society's eVTOL Aircraft Directory has expanded to include over 200 electric aircraft, with designs ranging from vectored thrust configurations to personal hover bikes [6].

NASA's X-57 Maxwell is an experimental aircraft right on the front lines of electric aviation. An Italian Tecnam P2006T gas driven airplane has been retrofitted to become an all electric aircraft with the intent of increasing cruise performance by 2.5 times the base model [7]. A disturbed electric power and propulsion system allows for the X-57 to replace it's 74.5 kW, 275 kg gas motors and propeller with a 60 kW, 125 kg electric motor and rotor. The reduction in mass shows a 76.6% increase in propulsor specific power density, 0.27 kW/kg for a gas propulsors, and 0.48 kW/kg for electric propulsors [8].

For small unmanned autonomous air vehicles ($>$ 10 lbs), physically small sized motors are required. For a 160 W power requirement, a small gas powered engine such as the AP Yellowjacket was found to have a specific power density of 1.1 kW/kg [9]. For comparison at 160 W peak power, brushless DC electric motors tested in this thesis contain a specific power density up to 4.9 kW/kg, whereas commercially available electric brushed DC motors have specific power densities up to 1.0 kW/kg. Electric motors scale well with size, making them excellent candidates for powering unmanned air vehicles.

Modern electric motors use advanced electromagnetic, thermal, and structural design practices to improve performance. Both the Maxwell's engines and future NASA designs are using finite element modeling approaches to accurate represent the electromagnetic interactions between the motor's rotor and stator. In an effort to increase performance and eliminate weight, designs seek to optimize air gap length, minimize rotor temperature, and reduce the number of heavy iron components. The most ambitious of these programs targets >13 kW/kg with 95% efficient electric

motors for use in hybrid-electric propulsion schemes, outlined in [10, 11]. Thermal management and a system's focus effort seeks to properly incorporate electric motors into future aircraft designs [7,11]. Design of the motor is dependent upon the mission requirements.

To better understand the motor and rotor interaction, consider the following example of a typical propulsion design. High fidelity aerodynamic models exist to allow for blade design and optimization. Typically, the aerodynamic design determines a required rotor torque and RPM such that propulsion and lift requirements are satisfied. In this example suppose the rotor has a 2500 RPM requirement and that two brushless motors are under consideration, with masses of 30 grams and 50 grams respectively. Ideally, the least massive motor should be selected. However, the efficiencies curves of the motors must be considered, and are overlaid with the rotor's requirement in figure 1.2.

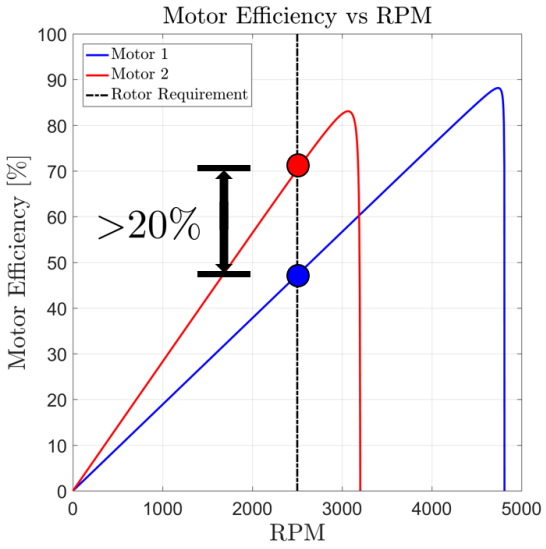

Figure 1.2: Components considered for equivalent circuit modeling.

Once the motor's performance is factored into the design, it is clear that motor 2 should be selected, as this design requires less power to operate. A design tradeoff exists between motor efficiency and motor mass, as more efficient motors are heavier but require less power to operate. Exchanging mass and power can change the aircraft's performance, endurance, payload capability, and range. An unaddressed question in research is considering which motor controller to use, as again heavier controllers tend to be more efficient. This example demonstrates a key point, that performance parameters of commercial off the shelf components must be available for use in detailed electric aircraft design.

1.2 Commercial Off the Shelf Components

Improving range and endurance for electric aircraft relies on knowing key performance parameters related to their propulsion system. An accurate knowledge of motor performance, design trade offs, and power losses are needed for comprehensive aircraft design. Knowing how the motor's efficiency changes with RPM and torque allows gearing to be designed such that both the rotor and the motor operate at peak performance. More efficient propulsor designs require less power, translating into longer flight times, increased range, and a more flexible mission profile.

Unfortunately, many BLDC motor suppliers do not provide detailed information on their motor's performance. A typical brochure on BLDC motor performance is shown in figure 1.3, and shows the motor's DC current draw at various DC voltages, with different rotors attached to the motor. While this information is useful

to hobbyist, it becomes largely irrelevant when considering designing an electric aircraft. The reason is that it does not infer how the motor performance will change when a different load is applied, or when a different motor controller is used. For example, using a more efficient motor controller may deliver more power to the motor, thereby changing its performance for the same amount of input power.

MOTOR VERSION	VOLTAGE LiHV [V]	PROPELLER SIZE	THROTTLE RANGE	AMPERAGE [A] (LOWER IS BETTER)	POWER INPUT [W] (LOWER IS BETTER)	POWER INPUT [hp] (LOWER IS BETTER)	THRUST OUTPUT [g] (HIGHER IS BETTER)	THRUST OUTPUT [N] (HIGHER IS BETTER)	THRUST OUTPUT [lb] (HIGHER IS BETTER)	RPM [rev/min] (HIGHER IS BETTER)	EFFICIENCY [g/W] (HIGHER IS BETTER)	EFFICIENCY [lb/hp] (HIGHER IS BETTER)
KDE2814XF-775 (775Kv) KDEXF-UAS35 S.R. ENABLED	11.6V (3S) 13.1V MAX	12.5" x 4.3 DUAL-EDN (KDE)	25.0%	0.8	10	0.01	130	1.27	0.29	2700	13.00	21.37
			37.5%	1.7	22	0.03	240	2.35	0.53	3680	10.91	17.93
			50.0%	3.1	40	0.05	410	4.02	0.90	4680	10.25	16.85
			62.5%	5.0	65	0.09	600	5.88	1.32	5640	9.23	15.18
			75.0%	7.6	99	0.13	810	7.94	1.79	6600	8.18	13.45
			87.5%	11.0	144	0.19	1060	10.40	2.34	7500	7.36	12.10
			100.0%	14.6	191	0.26	1340	13.14	2.95	8400	7.02	11.53
		12.5" x 4.3 TRIPLE-EDN (KDE)	25.0%	1.0	13	0.02	160	1.57	0.35	2580	12.31	20.23
			37.5%	2.1	27	0.04	290	2.84	0.64	3520	10.74	17.66
			50.0%	3.9	51	0.07	480	4.71	1.06	4480	9.41	15.47
			62.5%	6.5	85	0.11	700	6.86	1.54	5440	8.24	13.54
			75.0%	9.9	129	0.17	950	9.32	2.09	6320	7.36	12.11
			87.5%	14.8	193	0.26	1240	12.16	2.73	7200	6.42	10.56
			100.0%	18.8	246	0.33	1530	15.00	3.37	7880	6.22	10.22
		15.5" x 5.3 DUAL-EDN (KDE)	25.0%	1.5	19	0.03	300	2.94	0.66	2280	15.79	25.96
			37.5%	3.6	47	0.06	570	5.59	1.26	3120	12.13	19.94
			50.0%	6.9	90	0.12	860	8.43	1.90	3900	9.56	15.71
			62.5%	11.7	153	0.21	1230	12.06	2.71	4580	8.04	13.22
			75.0%	17.4	227	0.30	1590	15.59	3.51	5180	7.00	11.52
			87.5%	24.3	318	0.43	1900	18.63	4.19	5640	5.97	9.82
			100.0%	30.3	396	0.53	2240	21.97	4.94	6080	5.66	9.30
	15.4V (4S) 17.4V MAX	12.5" x 4.3 DUAL-EDN (KDE)	25.0%	1.2	20	0.03	230	2.26	0.51	3540	11.50	18.91
			37.5%	2.4	41	0.05	410	4.02	0.90	4740	10.00	16.44
			50.0%	4.6	80	0.11	670	6.57	1.48	6000	8.38	13.77
			62.5%	7.7	133	0.18	970	9.51	2.14	7280	7.29	11.99
			75.0%	11.6	201	0.27	1300	12.75	2.87	8340	6.47	10.63
			87.5%	16.9	294	0.39	1690	16.57	3.73	9480	5.75	9.45
			100.0%	22.3	388	0.52	2110	20.69	4.65	10440	5.44	8.94
		12.5" x 4.3 TRIPLE-EDN (KDE)	25.0%	1.5	26	0.03	280	2.75	0.62	3320	10.77	17.70
			37.5%	3.1	53	0.07	490	4.81	1.08	4580	9.25	15.20
			50.0%	5.6	97	0.13	790	7.75	1.74	5720	8.14	13.39
			62.5%	9.5	165	0.22	1120	10.98	2.47	6880	6.79	11.16
			75.0%	14.9	259	0.35	1490	14.61	3.28	7920	5.75	9.46
			87.5%	21.0	365	0.49	1870	18.34	4.12	8840	5.12	8.42
			100.0%	27.5	478	0.64	2320	22.75	5.11	9640	4.85	7.98

***Note** : performance chart provided under the test conditions listed below. Measurements taken under alternate conditions will affect the final results.*
***Location** : KDE Direct HQ Dynamometer V2 (Bend, Oregon)*
***Altitude** : 3730 ft (1137 m)*
***Pressure** : 30.3 inHg (1026 hPa)*
***Temperature** : 72 °F (22°C)*
***Humidity** : 35% (Relative)*

Figure 1.3: Information typically given for BLDC performance.

Given the lack of information from manufacturers, several design and engineering questions remain unaddressed:

1. What operating conditions produce the maximum efficiency for the motor and the ESC?

2. How does motor performance change when different rotors are used?

3. How does the change in throttle setting impact the output torque and speed of the motor?

4. What is the peak power output of the motor? Max continuous?

5. How does changing motor controller effect the motor's performance?

Due to the coupled nature of the controller and the motor, these are quite involved questions to answer. Additionally, from manufacturer specified details, designers are unaware where the power loss in the system is occurring, either in the motor controller, the wiring, or the motor itself.

When designing electric aircraft, it is critical to the designer to know which motor and motor controller to use. To do this, key performance information about the motor is required, however mostly not provided by the manufacturer. Even less understood are the Electronic Speed Controllers (ESCs), which are responsible for open loop control of the motor. Exact knowledge of the maximum efficiency points of an ESCs and BLDC motors allow designers to evaluate tradeoffs between selecting different motors with specific ESCs. This problem is unexplored in research, as only moderate attempts have been made to better understand power loss for BLDC motors and ESCs. A clear need is established - to develop an apparatus for testing commercial off the shelf components to determine their performance criteria.

1.3 The Need for a Dynamometer

A dynamometer was created to study BLDC motor and ESC characteristics. A dynamometer is a device that is used to vary the load on a motor, while simultaneously record the electrical and mechanical power. With this information, an analytical model was developed to help understand propulsion system performance. A key point in this work is to study both the ESC and BLDC motor performance, with ESCs being a special focus of this work. It was found that ESC peak efficiency points are different than BLDC motors, which is critical knowledge to designers.

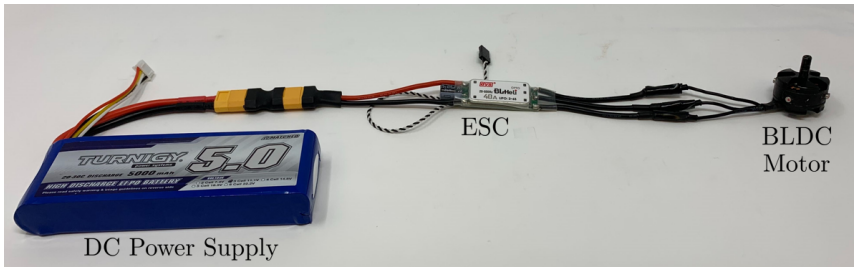

Figure 1.4: Components considered for equivalent circuit modeling.

A typical propulsion system used in a University research setting is shown in figure 1.4. It contains a DC power supply, the ESC, and a BLDC motor. There are three types of power in this setup: the DC power, the AC power, and mechanical power. The DC power supply emits a steady voltage and current to the ESC, the ESC modulates this power into the AC voltage and current signals for the motor, and the motor converts this electrical power into mechanical power. To isolate the performance of the ESC and BLDC motor separately, both a DC and AC power analyzer are used. As a result, there are three different efficiencies one may discuss

for this system: the ESC efficiency η_{ESC}, the motor efficiency η_m, and the overall system efficiency η_{sys}. These definitions can be expanded below:

$$\eta_{ESC} = \frac{P_{AC}}{P_{DC}} = \frac{P_{AC}}{V_{DC} I_{DC}} \tag{1.1}$$

$$\eta_m = \frac{P_m}{P_{AC}} = \frac{Q\omega}{P_{AC}} \tag{1.2}$$

$$\eta_{sys} = \eta_{ESC}\eta_m = \frac{P_{AC}}{P_{DC}} \frac{P_m}{P_{AC}} = \frac{Q\omega}{V_{DC} I_{DC}} \tag{1.3}$$

where P_{DC}, P_{AC}, and P_m are the DC, AC, and mechanical powers, η_{ESC}, η_m, and η_{sys} are the ESC, motor, and system efficiencies, and V_{DC}, I_{DC}, Q, and ω are the DC voltage, DC current, motor output torque, and motor rotational speed, respectively. A diagram relating the different powers and efficiencies can be found below:

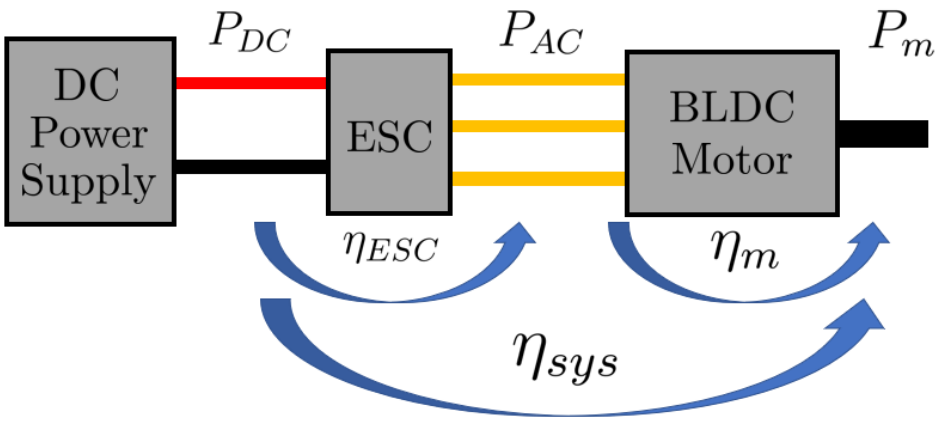

Figure 1.5: Propulsion system power and efficency breakdown for an ESC and BLDC motor.

Each efficiency relates to a particular transformation of power in the propulsion system. ESCs transform DC power into AC power to run the motor, whereas the motors transform AC power into mechanical power. Increasing the ESC effi-

ciency allows for more power to be available to the motor, meaning that a different performance is expected for the same amount of input power. Typically researchers discuss equation 1.3 when discussing propulsion system performance, only relating the DC input power to the mechanical output power. This is a high-level view, as it does not distinguish between motor and controller inefficiencies during the power conversion process. By properly recording the AC power of the system, researchers can use this information to search for high efficiency ESCs and BLDC motors.

As a result, testing motors is coupled with testing ESCs. Without the motor, the ESC does not output any AC signals and without the ESC, the motor cannot spin. It is not possible to test one without the other. The work in this thesis focuses on developing an experimental apparatus to study motor performance. This information is then used to develop an analytical, first principles based model for both the ESC and the BLDC motor.

1.4 Outline of This Thesis

Each Chapter in this thesis is self contained and independent. However, subsequent chapters build off the foundations of previous Chapters, which is critical for the modeling attempt. The organization of this thesis is as follows:

Chapter 2: Introduction to motor performance and component breakdown. Before modeling attempts can be made, it is essential to understand the critical components in DC motors and ESCs. Key concepts such as the brushed motor model are covered to give additional context into motor operation.

Chapter 3: A detailed explanation of dynamometer components, sensors, and power analyzers is provided. Here the DC, AC, and mechanical power analyzers are explained, with special attention is given to measure the 3 phase AC power. The final 2 DAQ configuration is described in detail.

Chapter 4: An analytical model is derived for both the BLDC motor and ESC. The goal of this section is to identify parameters that do not change with different operating conditions. Both the BLDC motor and the ESC are modeled using equivalent circuit diagrams.

Chapter 5: Experimental results for 7 BLDC motors and 3 ESCs are given at DC voltages of 7.2 V, 11.1 V, and 14.8 V. A description of extracting performance variables from experimental data is given. Additional topics, such as motor variation testing and rotor/motor/ESC pairing are addressed at the end of the chapter.

Chapter 6: Conclusions about this work and areas for future work are described. Future work includes enlarging the dynamometer to handle larger motors, as well as closed loop control of a motor, ESC, and rotor.

Chapter 2: DC Motors

2.1 Basic Motor Performance - the Brushed Motor Model

Motors convert electrical power into mechanical power. Before describing the different types of motors, a brief discussion on motor performance is required. An equivalent circuit can be drawn, which encapsulates both the electrical and mechanical properties of the system.

A motor is a series of coils and magnets, which operate under the principles of electromagnetic induction. The core concept of any electric motor is that passing current through a wire creates a magnetic field around the wire and this is used to spin the rotor. If a separate magnetic field is created and is brought close to the wire, the interaction of these magnetic fields causes an electromagnetic force to develop on the coil according to Flemin's left hand rule [12]:

$$F_B = BlI \tag{2.1}$$

Now consider if the wire is bent into a loop like figure 2.1.

The current on the left side of the centerline passing through the magnetic field B causes a force to be generated at a distance r on segment l. The result is a

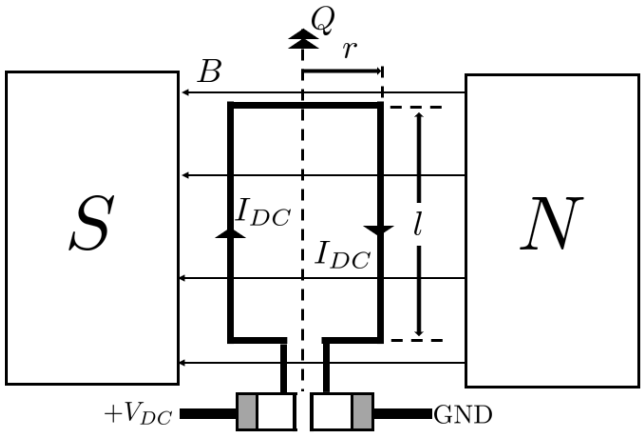

Figure 2.1: Generation of a magnetic torque for a current.

magnetic force which is generated out of the page. However, since that wire is bent in a loop, the same current must now pass through the right hand side of the wire l, meaning the result of this interaction is a magnetic force into the page. This results in a torque Q to be generated and is equal to:

$$Q = 2rF_B = 2rBlI \tag{2.2}$$

This forms the very basic relation that the output torque of the motor is proportional to the current, by some constant K_T:

$$Q = K_T I \tag{2.3}$$

Now consider a stationary magnetic field and the wire is moving perpendicular to the field with some speed v, shown in figure 2.2. Farraday's law of electromagnetic induction dictates that a voltage differential must be created to oppose the change

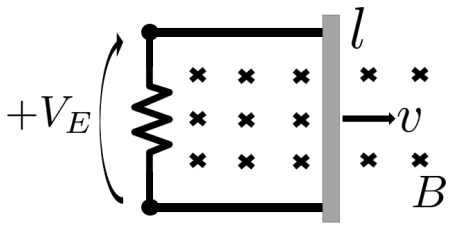

Figure 2.2: Generation of back-EMF in a moving wire.

in magnetic flux:

$$V_E = vBl \tag{2.4}$$

This shows that a voltage is generated across the wire and is proportional to the speed of the moving wire. If the wire was moving around in a rotor, the speed would be proportional to the RPM of the motor:

$$\omega = \frac{v}{r}$$

Thus, for a motor, the back electromagnetic force, or back EMF, generated in the coil windings can be written as:

$$V_E = K_E \omega$$

Where K_E is some proportaionality constant, relating voltage induced in the coil to RPM.

Both K_T and K_E are fundamental constants in motor theory. They are functions of the magnetic field strength, material design of the motor, number of turns in the inductors, and overall electrical design of the motor. A commonly employed

tool for steady-state analysis is to simplify the motor into an equivalent electrical model. To demonstrate the key concepts of motor performance, a sufficient motor model [12–14] is shown in figure 2.3.

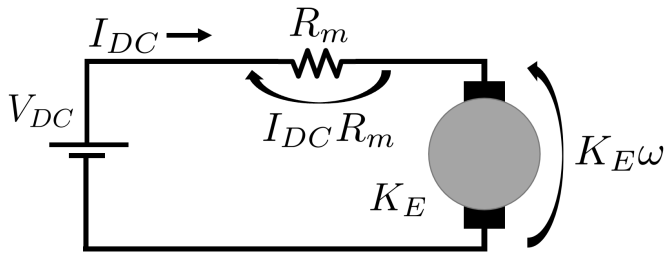

Figure 2.3: Simplified motor electrical circuit, the arrows indicate component voltage drop.

An equivalent circuit is developed, that contains a motor resistance R_m and an induced back voltage $K_E\omega$ from the rotating magnets. Based on figure 2.3, the sum of voltages around the loop is equal to 0:

$$V_{DC} = V_{R_m} + V_E$$

Substituting terms yields the following:

$$V_{DC} = I_{DC}R_m + K_E\omega \tag{2.5}$$

Output torque is related to the DC current, from equation 2.3, but must be augmented with an additional torque to overcome the static friction of the motor:

$$Q = Q_{EM} - Q_{static}$$

$$Q = K_T(I_{DC} - I_o) \tag{2.6}$$

Where the term $K_T I_o$ is the torque required to overcome the internal friction of the motor. Equations 2.5 and 2.6 are considered to be the fundamental equations of an electric motor. These two equations can be combined together to determine the linear relationship between RPM and torque:

$$Q = \frac{K_T}{R_m}[V_{DC} - I_o R_m] - \frac{K_T K_E}{R_m}\omega \tag{2.7}$$

which is plotted in figure 2.4. Equation 2.7 states that the Q vs RPM relationship is linear in nature, with a slope related to the parameters of the motor and a y-intercept related to the DC supply voltage V_{DC}.

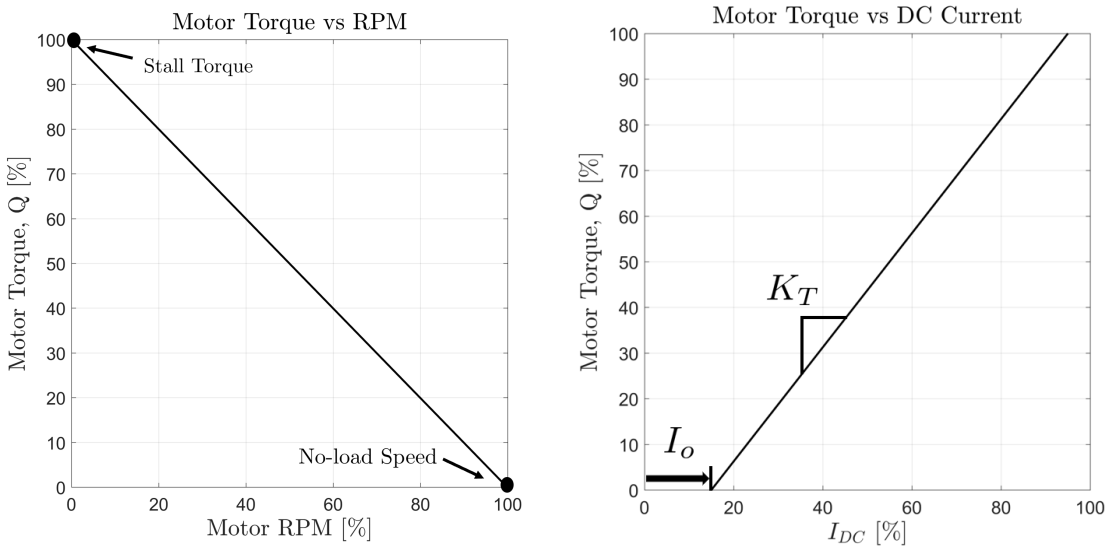

Figure 2.4: Left: Torque vs RPM relation. Right: Torque vs current relation.

There are two key points along the Q vs RPM line: the stall torque and the no-load speed. Stall torque is defined as the torque generated from the motor when

the shaft is no longer rotating, and is the maximum torque the motor can produce. Such a torque is useful to hold positions of shafts at a constant angle, for example in a robot arm. The other point is the no-load speed, which is the RPM that the motor shaft spins when no load is applied to the motor. This is the maximum RPM that the motor shaft spins.

The no load speed can be found by setting torque equal to 0 in equation 2.7:

$$\omega_{NL} = \frac{V_{DC} - I_o R_m}{K_E} \tag{2.8}$$

Similarly, the stall torque can be found by setting RPM to 0 in equation 2.7:

$$Q_{stall} = \frac{K_T}{R_m}[V_{DC} - I_o R_m] \tag{2.9}$$

Both of these are significant as they relate to the maximum performance of the motor: either maximum rotational speed or maximum load. The torque-RPM line can be separated into three regions, which relates to the load on the motor and is depicted in figure 2.5.

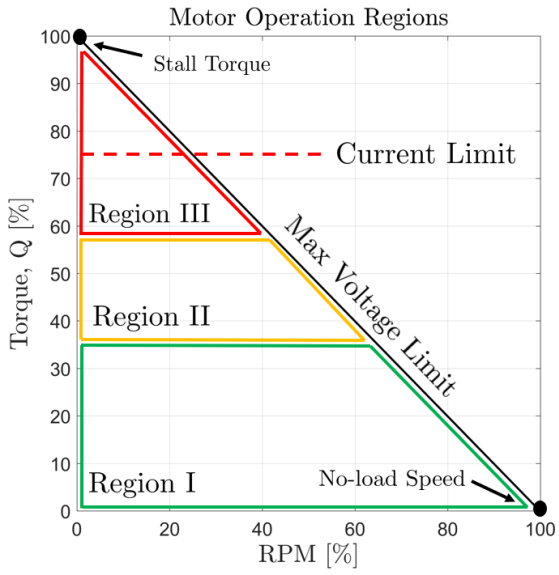

Figure 2.5: Motor operation regions.

Region 1: Region of continuous use. High RPM and low torque. This region contains the location of the maximum efficiency of the motor. Rotors should be sized to operate in this region during trim.

Region 2: Intermittent use region. Region contains the location of maximum power output for the motor. Motor operation should only enter this region during maneuvers.

Region 3: Limited use region. High torque and and low RPM. Region contains the current limit for either the motor or the controlling electronics. Motor operation should only enter this region during protracted maneuvers. Extended time in this region could cause thermal effects to degrade the motor's performance, both electrically and/or physically.

A properly sized motor operation should be contained in region I, with only short

term use in the other regions during take-off, landing, or maneuvers. Here the load on the motor is lowest, and the motor operates close to its maximum efficiency point.

Power output from the motor is the product of the mechanical output torque with the mechanical RPM:

$$P_m = Q\omega \tag{2.10}$$

and can be reformulated as:

$$P_m = (\frac{K_T}{R_m}[V_{DC} - I_o R_m] - \frac{K_T K_E}{R_m}\omega)\omega$$

$$P_m = \frac{K_T}{R_m}[V_{DC} - I_o R_m]\omega - \frac{K_T K_E}{R_m}\omega^2 \tag{2.11}$$

The maximum power rotational speed $\omega_{max\ P}$ can be found by differentiating equation 2.11 with respect to RPM:

$$\frac{dP_m}{d\omega} = \frac{K_T}{R_m}[V_{DC} - I_o R_m] - 2\frac{K_T K_E}{R_m}\omega_{max\ P} = 0$$

$$\omega_{max\ P} = \frac{1}{2}(\frac{V_{DC} - I_o R_m}{K_E}) = \frac{\omega_{NL}}{2} \tag{2.12}$$

Maximum power lies at half of the no-load speed ω_{NL}. Maximum power occurs when the distrubition between torque and RPM is balanced at half of no load speed and half of stall torque. Equation 2.11 can be plotted and is shown below:

Note that at ω_{NL} and Q_s the mechanical output power is 0. Again, this corresponds to the limits of the motor, at maximum RPM there is no load and

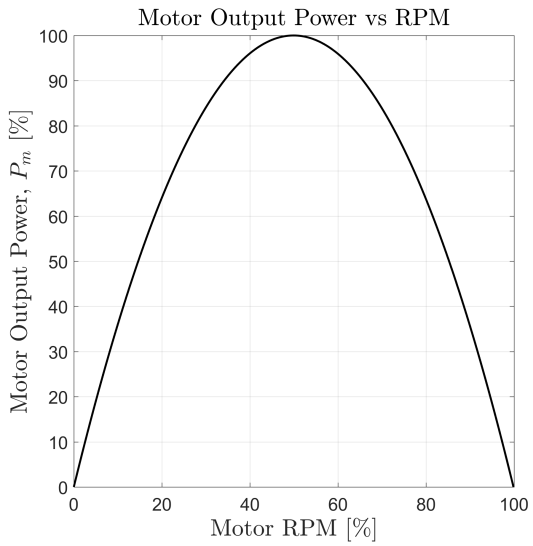

Figure 2.6: Motor output power vs RPM.

thus no output power. Since the input and output powers have been identified, the overall efficiency can be evaluated.

The ratio of mechanical output power to DC input power is the system efficiency:

$$\eta_{sys} = \frac{P_m}{P_{DC}} = \frac{Q\omega}{V_{DC} I_{DC}}$$

$$\eta_{sys} = \frac{K_T(\frac{V_{DC} - K_E\omega}{R_m} - I_o)}{V_{DC}(\frac{V_{DC} - K_E\omega}{R_m})} \tag{2.13}$$

Maximum efficiency of the system occurs at ω_{opt}, and can be found by differentiating equation 2.13 with respect to the RPM, to find:

$$\frac{d\eta_{sys}}{d\omega} = \frac{K_T(K_E^2\omega^2 - 2K_E V_{DC}\omega + (V_{DC}^2 - I_o R_m V_{DC})}{V_{DC}(V_{DC} - R_m\omega)} = 0$$

$$\omega_{opt} = \frac{V_{DC} - \sqrt{I_o R_m V_{DC}}}{K_E} \tag{2.14}$$

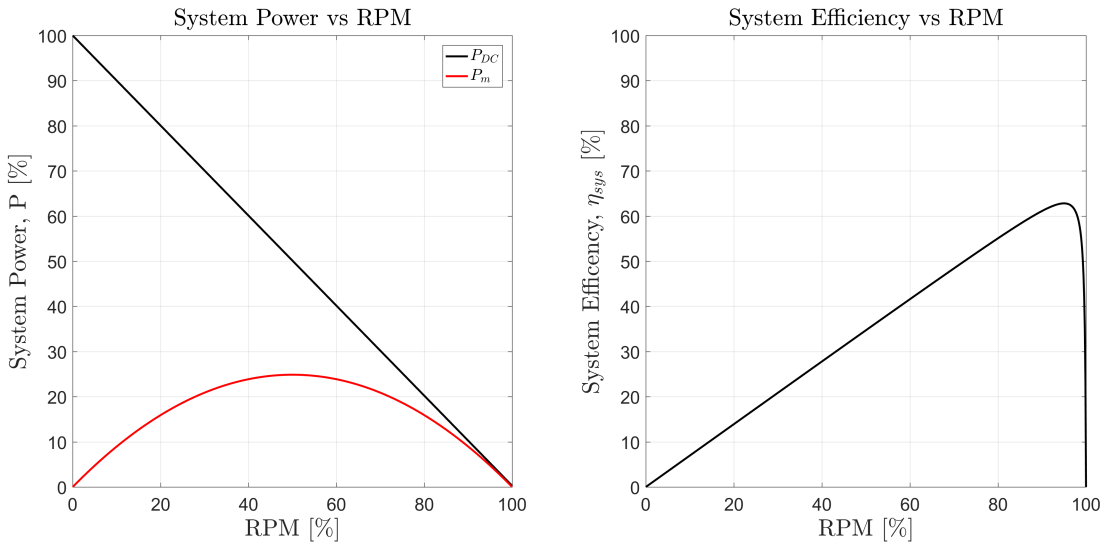

Figure 2.7: System powers and efficiency vs RPM.

The optimal RPM for system performance is typically between 75% to 95% of the motor's no-load speed, and can have a maximum efficiency of 95% for brushless motors and 75% for brushed motors. A typical plot of a motor's efficiency curve is shown in figure 2.7. Motor performance is augmented by changing the voltage of the motor, which is done using user throttle.

2.1.1 User Input Throttle

The motor equations shown so far assumed that the motor was operating at the full supply voltage V_{DC}. A more realistic model for motor operation is shown in figure 2.8. User throttle T_R is a value between 0-1, and has been normalized appropriately. The throttle is analogous to the gas pedal on a car, depending on how far down the gas pedal is pressed, more or less fuel enters the engine. With more fuel, the engine produces more power, and the car responds appropriately.

A voltage regulator is a device that has an output voltage proportional to

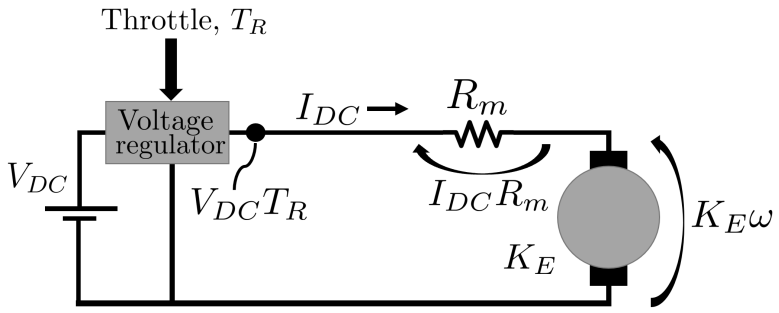

Figure 2.8: Motor efficiency vs RPM.

some input signal, called the throttle T_R. This means that the output voltage of the regulator, which is the voltage acting across the simplified motor circuit, is $V_{DC}T_R$. Meaning that at 60% throttle, the motor has $0.6V_{DC}$ acting across the circuit. The regulation and modulation schemes employed for brushed and brushless motors are discussed in section 2.3.

Changing the voltage seen by the motor is accomplished by changing the throttle T_R into the voltage regulator. This changes the voltage acting across the motor, and thereby changes the performance of the motor. Applying Kirchhoff's voltage law to the right side of figure 2.8 yields:

$$V_{DC}T_R = I_{DC}R_m + K_E\omega \tag{2.15}$$

the torque-current relation, equation 2.6, remains unchanged for a given V_{DC}. However, the user throttle T_R appears when evaluating the motor's performance:

$$Q = \frac{K_T}{R_m}[V_{DC}T_R - I_oR_m] - \frac{K_TK_E}{R_m}\omega \tag{2.16}$$

$$P_m = \frac{K_T}{R_m}[V_{DC}T_R - I_o R_m]\omega - \frac{K_T K_E}{R_m}\omega^2 \tag{2.17}$$

$$\eta_{sys} = \frac{K_T(\frac{V_{DC}T_R - K_E\omega}{R_m} - I_o)}{V_{DC}(\frac{V_{DC}T_R - K_E\omega}{R_m})} \tag{2.18}$$

changing the input throttle to the motor shifts the plots in a predictable manner. The change in performance for different throttles is shown in figures 2.9 and 2.10.

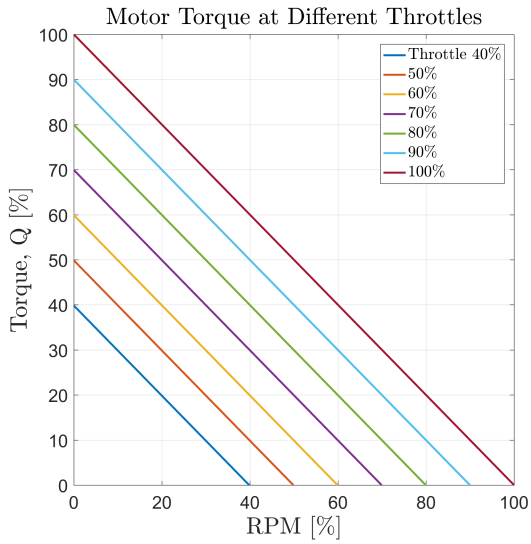

Figure 2.9: Torque-RPM curves at different throttles.

A reduction in throttle changes the no-load speed and stall torque of the motor by:

$$\omega_{NL}(T_R) = \frac{V_{DC}T_R - I_o R_m}{K_E}$$

$$Q_{stall}(T_R) = \frac{K_T}{R_m}[V_{DC}T_R - I_o R_m]$$

Throttle has a linear relationship with the torque-RPM curves, and can be though of as shifting the plots left or right. Increasing throttle allows for a higher no-load speed and higher value of stall torque to be achieved, which consequently

shifts the maximum power point higher up the power axis and to the right in RPM. This is because the maximum power point is still half of the no-load speed, and since no-load speed increases, so must the maximum power point.

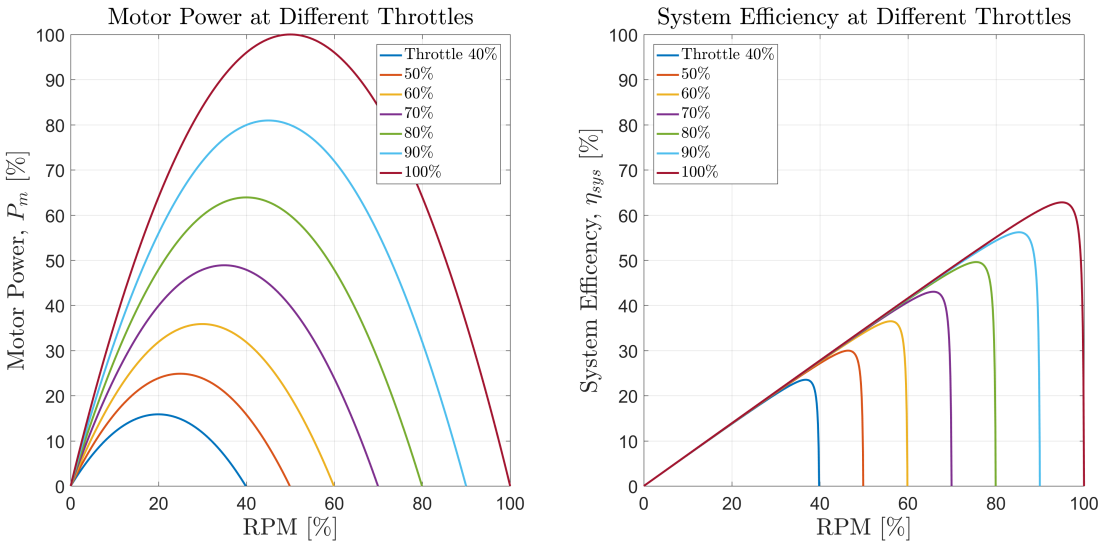

Figure 2.10: System performance at different throttles.

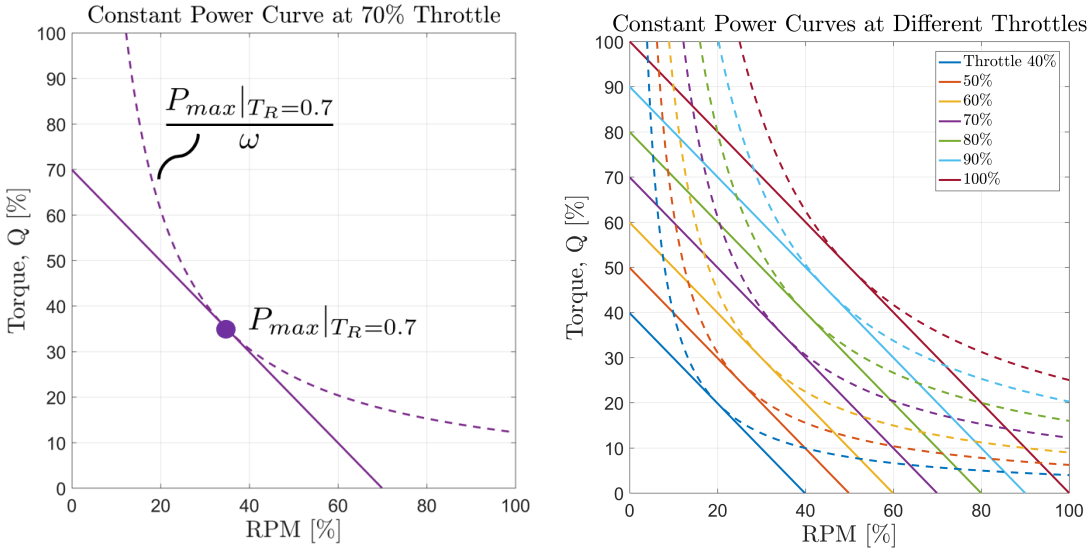

Figure 2.11: Constant power curves, solid lines indicate torque-RPM relationship whereas dotted lines indicate constant power curves.

The user or closed loop controller, changes the throttle value to the voltage regulator. This regulator acts like a value, and changes the voltage available for the

motor. Changing the motor voltage allows more or less power to be delivered to the motor, and has 2 effects: faster RPM for the same load, or more current (and thus more torque) for the same RPM.

Certain motor applications require constant power, and so it is important to know how these power curves affect throttle, RPM, and torque requirements. For a given power P, the torque required to produce a constant power is $Q = P/\omega$. An example is shown in figure 2.11, with the left plot showing the required torque to generate peak power at 70% throttle $P_{max}|_{T_R=0.7}$. For 70% throttle clearly only one torque and RPM value satisfies this power requirement. However the figure on the right shows how the peak powers curves of a given throttle setting only intersect the torque-RPM lines for throttle settings above the original setting. Although the peak power is only reached once for a given throttle, it is reached an infinite number of times for the throttle settings above it. However, as the peak power increases, fewer throttle settings are available to meet the requested torque and RPM requirements.

Now that the basics have been discussed, key terms for motor performance must be identified.

2.1.2 K_T, K_E, and KV

Precise definitions of K_T, K_E, and KV are required for discussing brushless motors. These quantities are often misquoted, so it is important to remember the context that are provided. Incorrectly using one quantity for another can lead one to arrive at incorrect conclusions. These quantities are defined as:

1. K_T [Nm/A] - the amount of torque produced for each amp of current

2. K_E [Vs/rad] - the amount of back EMF (voltage) produced for each rad/s of mechanical rotation

3. KV [RPM/V] - Manufacturer specified ω_{NL} per volt of DC voltage applied to the ESC (ω_{NL} =KV V_{DC}). This quantity is not motor specific as it includes the ESC.

Typically manufactures provide only the KV rating for a BLDC motor, but this is not useful for engineering applications. Use of KV only tells the motors no-load speed at full throttle, but does not describe how the torque-RPM evolves. For this, K_T and K_E, as well as additional motor parameters, are required. Due to a lack of manufacturer specified modeling values, only general statements can be made. Typically, a lower KV motor translates to a motor with a higher torque constant K_T. For example, if choosing between a 935 KV and 2500 KV BLDC motor, the 935 KV motor would be selected for operation with larger/slower rotors.

However, even this simplification may not always be adequate, as manufacturers typically do not specify which ESC was used. During testing for this work, it was found that a 920 KV motor has $K_T = 13.20$ mNm/A, whereas a 935 KV motor had a $K_T = 13.85$ mNm/A when tested at $V_{DC} = 7.2V$ with a MultiStar 30A ESC. The reason for this dependency between KV and K_T or K_E is that KV involves the motor and the ESC performance, whereas K_T and K_E are only related to the motor performance. In terms of practical engineering application, KV value does not accurately describe the motor's performance.

There are multiple ways of defining K_T and K_E. References [12,13,15] include definitions of BLDC motors that rely on the peak voltage V_{pk} and peak current I_{pk}. The reason for this is that BLDC motors operate on AC waveforms, meaning there are multiple ways to define K_T and K_E. These values of K_T and K_E are given in the context of a model, and so usually are easy to interpret. The ideal ratio of K_T/K_E is of importance when discussing BLDC motors. Based on the waveform properties and the motor type, the following chart can be obtained and is taken from [13]:

Table 2.1: Ideal K_T and K_E based on motor type.

	DC	Squarewave 3 Phase	Sinewave 3 Phase
K_T [Nm/A]	Q/I_{DC}	Q/I_{pk}	Q/I_{pk}
K_E [Vs/rad]	V_E/ω	$V_{pk,LL}/\omega$	$V_{pk,LL}/\omega$
K_T/K_E	1	1	$\sqrt{3}/2$

For this work, the ratios of voltage and torque are related using the rms value of voltage and current, as this is easy to calculate during a test. Additionally, determining the peak voltage and current usually is difficult due to the presence of electrical noise. Further information on the model used in this work can be found in Chapter 4. It is up to the reader to infer the proper use of the quoted values in any manual or data sheet. For now, a detailed component breakdown of brushed motors, brushless motors, and ESCs are given.

2.2 Motor Component Theory

Brushed and brushless DC motors operate with a fixed DC supply voltage, hence the name DC. There are two major differences between brushed and brushless

motors:

1. Commutation of a brushed motor is built into the device, whereas in a brushless motor it is contained in the ESC

2. Commutation methods for a brushed motor are mechanical, whereas brushless motors are commutated with electronic methods

Next sections describe the construction and operation of the brushed motors, brushless motors, and ESCs.

2.2.1 Brushed DC Motors

Brushed motors are the simplest types of motors. They are cheap, easy to use, and available in all ratings. The disadvantages of these motors is that they have a low power-to-weight ratio and they are not suited to long term operation [16].

Every motor contains fundamentally two parts: the rotor and the stator. The rotor is the component that rotates and transmits the mechanical torque to the load, whereas the stator remains stationary and houses the internal components of the motor. Commutation is the process of reversing the direction of current into the motor to keep it spinning, and can be accomplished either mechanically (brushed) or electronically (brushless).

Use of a mechanical commutator means that physical contact with the rotor must be made to continue reversing the direction of current within a motor. A commutator is a device which ensures an electrical contact from the voltage supply V_{DC} and the rotating coil of wire is kept constant.

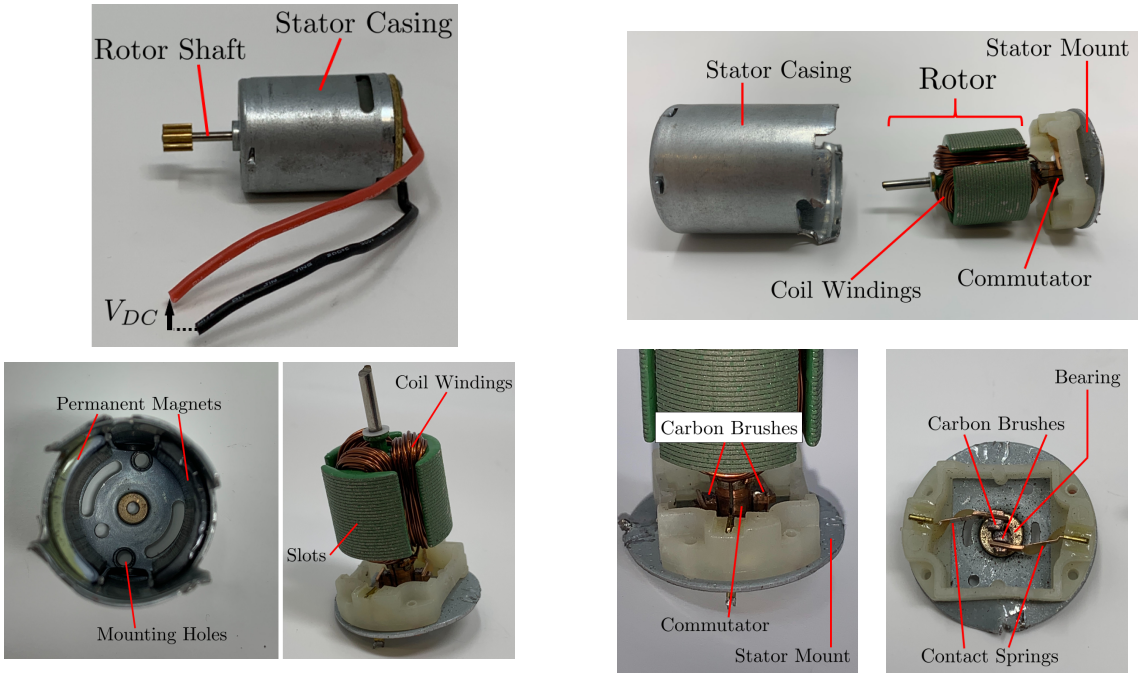

Figure 2.12: Components in a brushed motor.

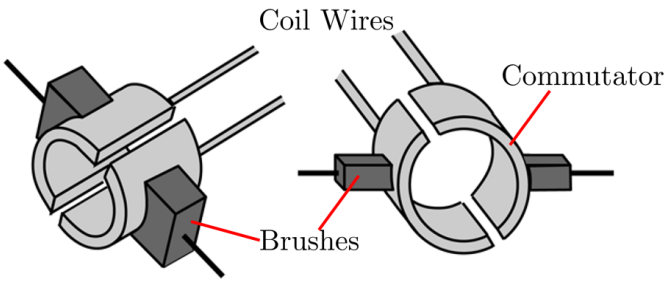

Figure 2.13: Commutator and brushes for a brushed motor.

Coil wires are connected to the commutator so the commutator rotates with the rotor. Carbon brushes connect the rotating wire to the non-rotating stator, and are used to electrically complete the circuit. Construction of a brushed motor is relatively simple, as shown in figure 2.12.

These brushes are a key distinction in a brushed motor, hence the name. The brushes ensure consistent current flow through the motor. To better illustrate how

a brushed motor is commutated, consider figure 2.14. Here a wire is wrapped to form a loop within a permanent magnetic field, similar to figure 2.1. The flow of current generates a torque as a result of equation 2.3. If there was no way to reverse

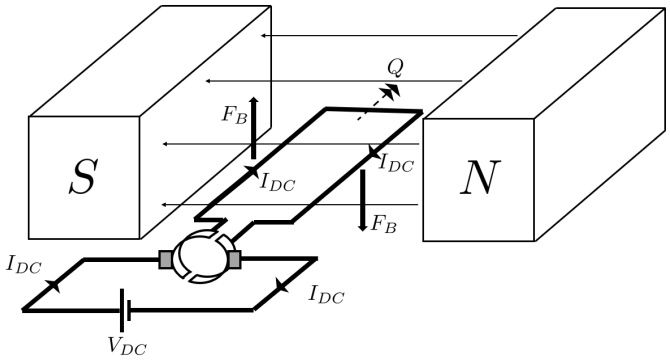

Figure 2.14: Generation of a magnetic torque for a current.

the direction of current, then the area of the coil becomes perpendicular to the field at the top of the rotation. At this point, no torque will be generated because the moment arm is 0, however the rotor has some angular velocity and so it continues to spin. If the direction of current does not change, then the resulting magnetic force generated after the midpoint will start to slow down, and eventually reverse the rotation of the rotor. To prevent this, the direction of current must be reversed with a commutator, depicted in figures 2.15 and 2.16.

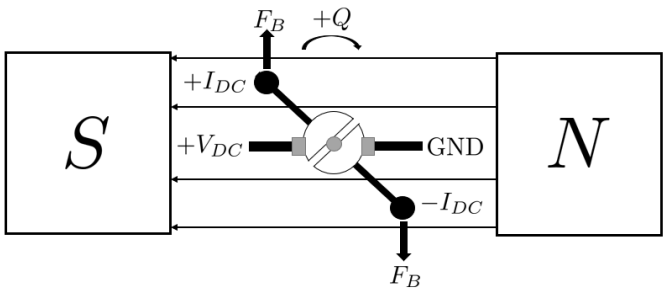

Figure 2.15: Before midpoint.

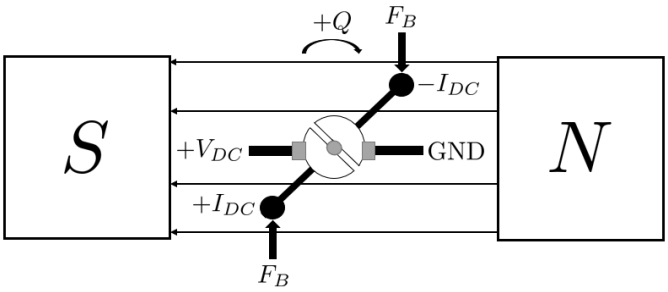

Figure 2.16: After midpoint.

By constantly changing the direction of current in the coil, it ensures continuous rotation of the rotor. Additional coils of wires are used to ensure the torque output remains constant. Use of springs, brushes, and rotating components means that considerable wear and tear takes place during motor operation. Sparking can also occur during a commutation event, resulting in a loss of power.

Control and simplicity for a brushed motor is not to be overstated. The model outlined in section 2.1.1 is exceptionally well suited to describe a brushed motor. To control the speed of a brushed motor, a modulated signal called an analog duty cycle signal is used.

A voltage modulation board is placed between the DC power supply and the brushed motor. The microcontroller communicates with this board and passes the user throttle T_R to the voltage modulation board. The modulation board typically consists of MOSFETs, which can either be in an on or off state. By changing the amount of time the MOSFET is open, or allowing current to flow, the effective output voltage can be controlled. The throttle T_R commands how much voltage the motor sees by controlling the duty cycle of the motor. The effective output voltage

is a function of the throttle command T_R:

$$V_{DC,eff} = V_{DC} T_R = V_{DC} \frac{t_{on}}{t_{on} + t_{off}} \tag{2.19}$$

In this context, the user throttle is the same as the analog duty cycle ratio. Reversing the direction of motor rotation can be achieved by reversing the polarity of the motor. By flipping the hot and ground terminals, current will flow in the opposite direction as before and thus, the motor spins in the opposite direction. Typically the control of motor speed and direction is accomplished within a single device, called an H-bridge, shown in figure 2.17.

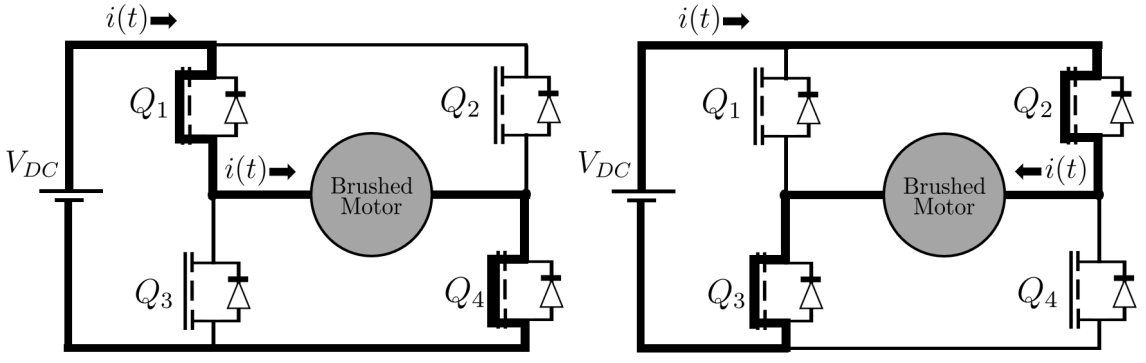

Figure 2.17: Left: Positive brushed motor rotation. Right: Reverse brushed motor rotation.

H-bridges consists of 4 MOSFETS, arranged in a 2 per pair fashion, which allows current to enter the motor in either a positive or negative direction. By determining which pair of MOSFETs are conducting or nonconducting, the direction of motor current entering the motor can be controlled. Regulating the length of time that the MOSFETs are conducting controls the current entering the motor. When the positive direction signal is sent, MOSFETs Q_1 and Q_4 are activated, allowing

current to flow in the positive direction and results in the motor spinning in the positive direction. When the reverse direction signal is sent, MOSFETS Q_2 and Q_3 are active and the direction of current is reversed, resulting in a reversed RPM. A short will occur if Q_1 and Q_3 or Q_2 and Q_4 are opened at the same time. The basic components to build and control a brushed motor are used in brushless motor operation.

2.2.2 Brushless DC Motors

Brushless motors operate on the same principles as brushed motors, but are augmented to allow for electronic commutation. Allowing for electronic commutation greatly enhances the life of a DC motor, as the physical brushes in a brushed motors degrade over time. The construction of a brushless motor is almost identical to that of a brushed motor, with two major differences:

1. No mechanical carbon brushes

2. Additional motor phases to allow for electronic commutation

Electronic commutation of a BLDC motor will be explained in section 2.3. Construction of the BLDC motor is shown in figure 2.18. Just like a brushed motor, BLDC motors consist of a rotor and a stator. The stator has three phases of wires wrapped around a central core to enhance the magnetic field of the motor.

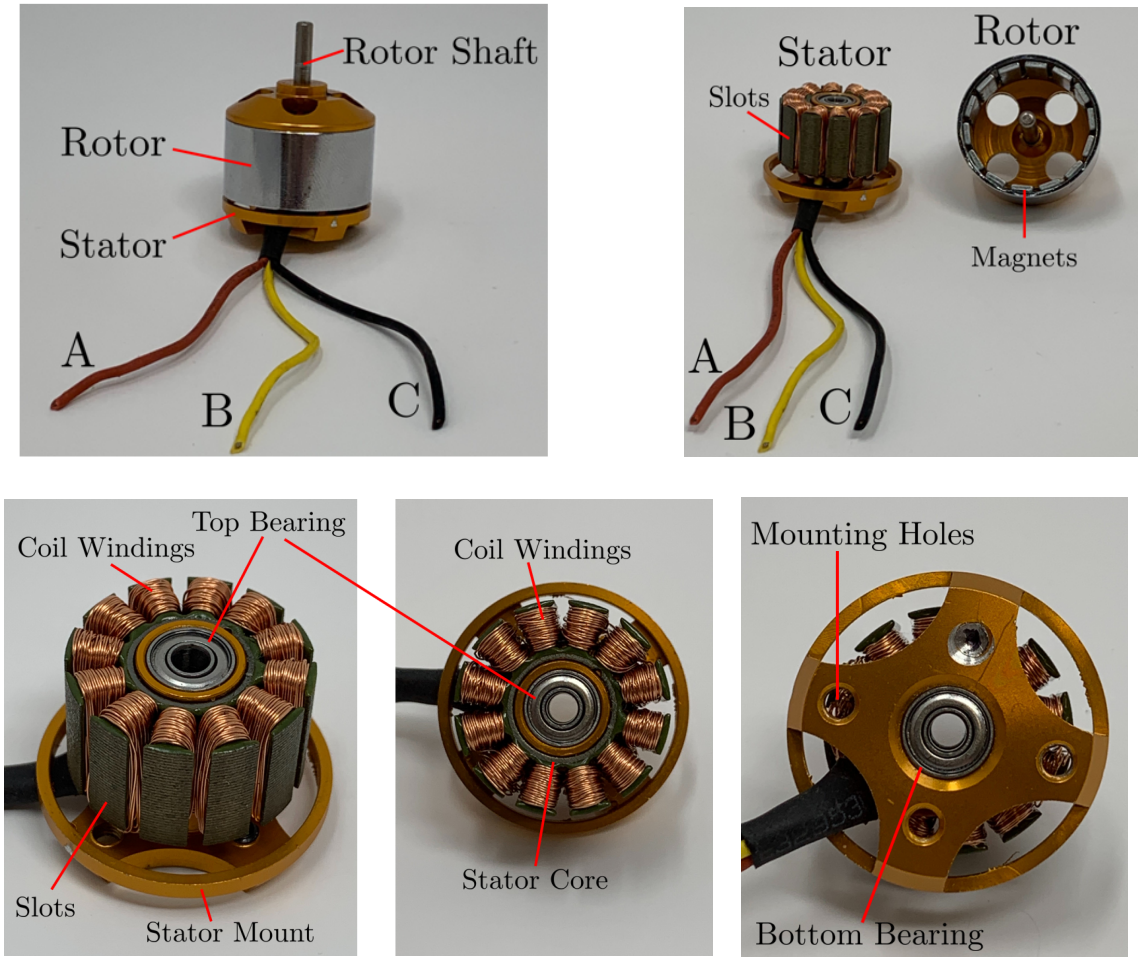

Figure 2.18: Components in a brushless motor.

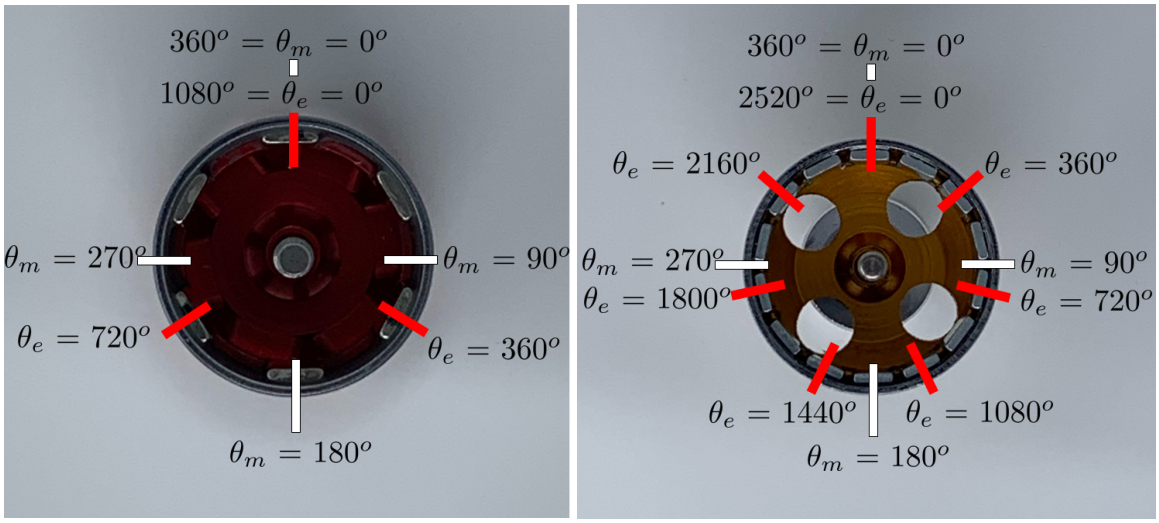

Figure 2.19: Left: 3 pole pair motor. Right: 7 pole pair motor.

These phases can be combined into either a wye (Y) or delta (Δ) configuration, and are discussed in more detail in section 3.5.2. The stator has mounting holes on the bottom to allow for bolts to attach the motor to the aircraft's structure. Conducting wire is wrapped in a loop to form an inductor, and then placed around the core's ferromagnetic material to enhance the magnetic properties of the electromagnets. These loops are referred to as slots, and are part of the stator.

The rotor consists of magnets with alternating polarity facing towards the center of the motor. An important concept with BLDC motors is the concept of pole pairs. Each north and south pole facing the center of the rotor makes a single pole pair, meaning that:

$$N_p = number\ of\ pole\ pairs = \frac{number\ of\ magnets}{2} \tag{2.20}$$

The electrical and magnetic frequencies are related to one another by this ratio N_p. If there were only 2 magnets, then for every 1 mechanical revolution, the induced back-EMF would experience 1 electrical cycle. If the number of magnets are doubled to 4, then for half a mechanical revolution, the back-EMF experiences 1 electrical cycle. The electrical angle θ_e is necessary for electronic commutation, and is related to the mechanical angle θ by [15]:

$$\omega_e = N_p \omega \tag{2.21}$$

$$\theta_e = N_p \theta$$

where N_p is the number of pole pairs of the motor, and ω is the mechanical RPM. This relationship for a 3 pole pair and 7 pole pair motor is shown in 2.19. The takeaway is that for a given electrical frequency ω_e, doubling the mechanical rotation speed ω has the effect as doubling the number of poles N_p (or quadruplicating the number of magnets). All motors used in this study are 7 pole pair motors, as this arrangement is most common for commercially avialble motors.

As mentioned previously, the stator houses the slots for the motor, which are the inductors inside a brushless motor. The ratio of poles to slots considered the gearing for the motor, and can augment the motor's K_T and K_E value. A high number of pole pairs is indicative of a motor that has a higher K_T, whereas fewer pole pairs means that the motor has a lower K_T and thus a higher RPM. Pole pairs are related to the electrical frequency of the signals for a brushless motor, and are interpreted by the ESC.

2.3 Electronic Speed Controllers

ESCs commutate, or spin, the BLDC motor by electronically regulating the direction of current into the motor by alternating which phases of the motor are energized. By changing the direction and strength of the magnetic field, a push-pull mechanism is developed that causes the rotor to chase the magnetic field. Metal Oxide Silicon Field Effect Transistors (MOSFETs) are used to regulate the direction of current into the BLDC, by changing which MOSFETs are conducting at a time. A typical ESC and MOSFET configuration is shown in figure 2.20.

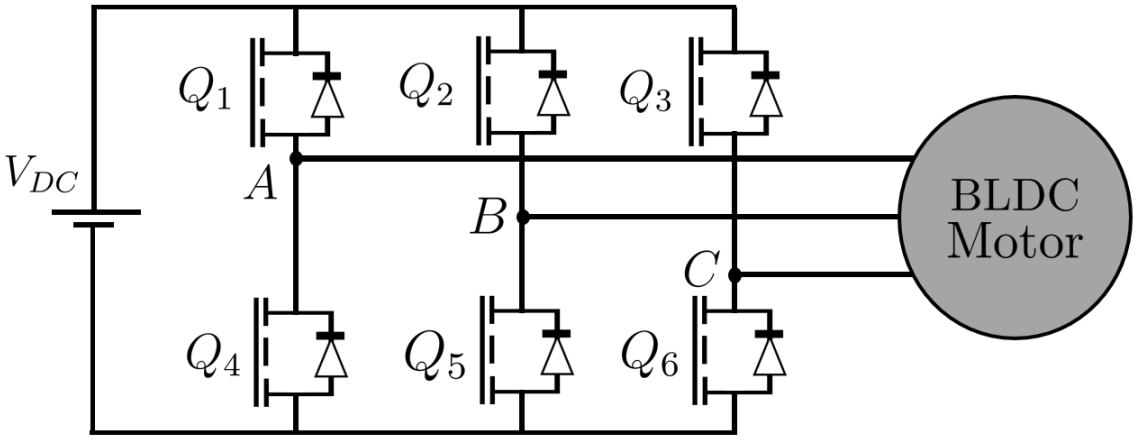

Figure 2.20: 6 MOSFET configuration for an ESC.

Six MOSFETs are used to commutate a BLDC motor, with 2 conducting at any time. If Q_1 and Q_5 are conducting, then current forms the DC supply, through Q_1, into the motor by line A, and then out of the motor from line B, through Q_5, and then returns to the DC supply. During this time, $i_A > 0$ and $i_B < 0$, which changes the orientation of the magnetic field inside the motor. One half of the coils are energized with positive current, which pulls on the rotor via magnetic forces. The second half of the coils are energized with negative current, resulting in a magnetic repulsion which pushes the rotor.

Most low cost commercial ESCs and BLDC motors use 120^o, 6-step commutation methods. The 120^o refers to the conduction interval of the MOSFET, meaning each MOSFET is on for $1/3^{rd}$ of an electrical revolution, with 2 on at any one time. Coils are connected together, in an either a Y or a Δ configuration, to allow the same current to pass through the both positively and negatively charged coils. Six step refers to six commutation intervals, required for one electrical revolution, $\theta_e = 0^o$ to

360^o.

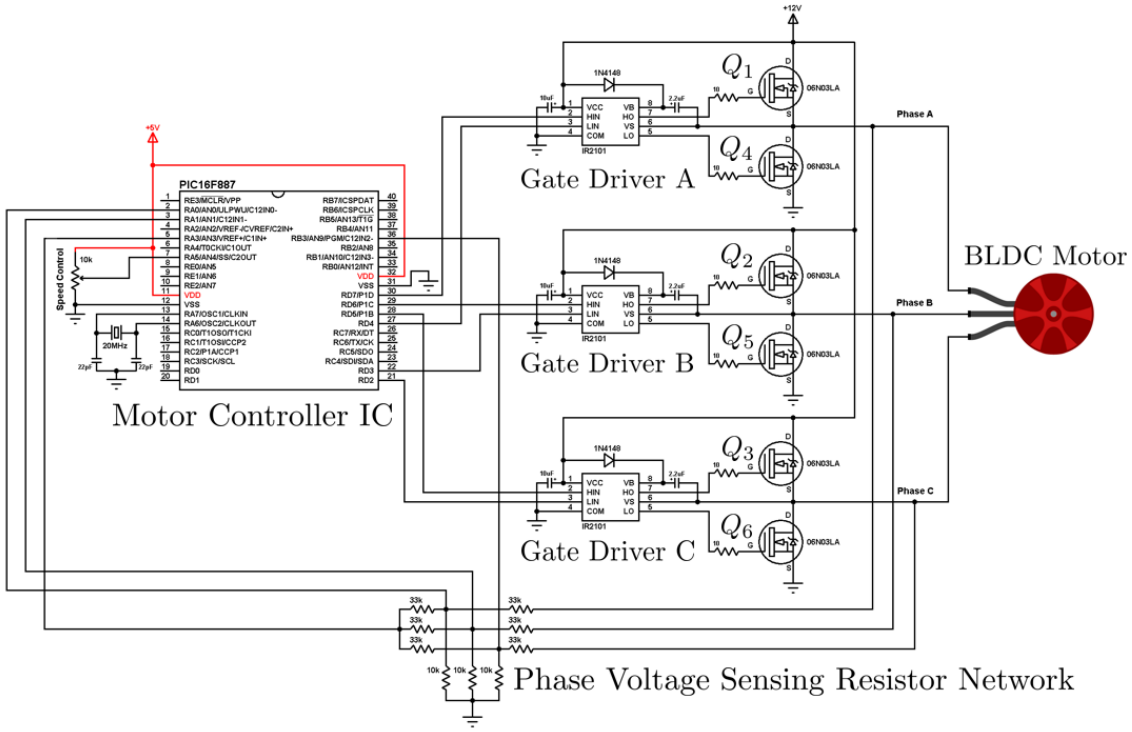

Figure 2.21: Detailed electrical schematic of a sensorless ESC.

The primary component in an ESC are the 6 MOSFETS, which are responsible for commutating the BLDC motor. Each MOSFET is controlled by a gate driver, which in turn is controlled by the motor controller IC. The motor controller chip is responsible for sensing the voltage of the motor phases and comparing this to its own commutating logic. The commutating logic is the set of instructions that dictates which MOSFETs, and therefore which phases, are active at one time. Commutating logic timing is heavily dependent on the location of the rotor. Chaning the active MOSFETs changes which lines are pushing and pulling the rotor's magnets, and hence mistiming commutation intervals results in a loss in performance and at worst an electrical short.

To detect the rotor's position, two different methods are used: sensored and sensorless ESCs. A sensored ESC uses hall effect sensors to detect the rotor's position. As the alternating magnetic fields of the motor pass by the hall effect sensor, a series of digital 1s and 0s are read into the ESC's microcontroller. The exact sequence of 1s and 0s from the three hall effect sensors are used to determine the rotor's exact location [17, 18]. The other type of ESC is a sensorless ESC.

Sensorless refers to an ESC which detects the rotor's position by the use of back-EMF. The motor's voltage and current waveform are well defined, and thus by tracking the back-EMF voltage, the electrical angle θ_e can be deduced. To sense the voltage of each phase, a resistor network is employed to reduce the voltage of the phase to within the range of the microcontroller's analog-to-digital converter. As the rotor spins, it induces an EMF in the coil wingdings of the phases of the motor. Sensorless ESCs are referred to as sensorless in that they do not have hall effect sensors to measure the rotor's location. Instead they sense the voltage waveforms of the motor to infer the rotor's location. The use of sensorless or sensored ESC depends upon the application.

Sensorless ESCs are the more popular choice for today's electric aircraft, whereas sensored ESCs are used more in land based applications. Sensorless ESCs operate best when the rotor is spinning at high RPMs, since the back-EMF is proportional to the RPM of the rotor. When at low RPM, the maximum value of the back-EMF ($V_E = K_E\omega$) is not large enough for accurate detection by the microcontroller, and thus the ESC can not properly commutate a BLDC motor. This is not a problem for high RPM rotors for electric aircraft, but is a problem for accurate

small angle control or low RPM. Since the sensored ESC can accurately detect the rotor's location for all RPMs, they work well at low speeds. Typical applications involve ground vehicles or devices which use high torque, low RPM operation.

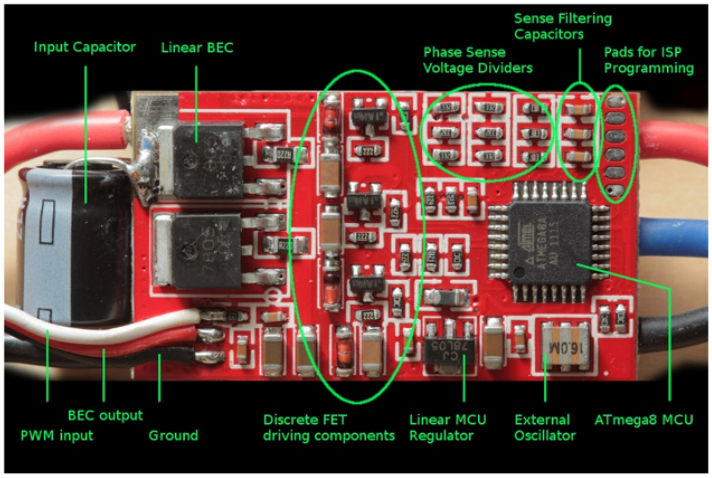

Figure 2.22: Detailed electrical schematic of an ESC.

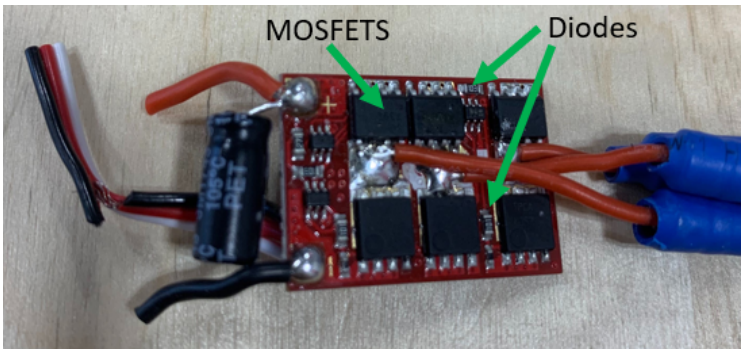

Figure 2.23: Component identification of a sensorless ESC.

A detailed component breakdown of a sensorless ESC is given in figures 2.23 and 2.22. Controlling the MOSFETs is accomplished with a gate driver, which is an electrical component that interprets the microcontrollers signal and augments it to drive the gate terminal of the MOSFET. A series of additional components, like

diodes, capacitors, and resistors are used to increase the performance of an ESC. From the aforementioned list, the most important components are resistors, as they are essential in determining the phase voltages and thus commutating the BLDC motor.

2.3.1 Commutation Logic

With the ability to sense the voltage wavforms of the BLDC motor, the commutation logic can be stated. This logic presents a mapping from the voltage states to the active MOSFETs. The delicate dance between transistors and current keeps the motor spinning. Although the method for determing the rotor's position can vary, the commutation logic is the same for both sensored and sensorless ESCs and is given by table 2.2.

Table 2.2: 6-step 120^o commutation intervals in an ESC and BLDC motor.

θ_e [deg]	Active Switches	v_{AN^*}	i_A	v_{BN^*}	i_B	v_{CN^*}	i_C
$0-60$	Q_1, Q_5	$+$	$+$	$-$	$-$	floating	0
$60-120$	Q_1, Q_6	$+$	$+$	floating	0	$-$	$-$
$120-180$	Q_2, Q_6	floating	0	$+$	$+$	$-$	$-$
$180-240$	Q_2, Q_4	$-$	$-$	$+$	$+$	floating	0
$240-300$	Q_3, Q_4	$-$	$-$	floating	0	$+$	$+$
$300-360$	Q_3, Q_5	floating	0	$-$	$-$	$+$	$+$

Commutating the rotor depends on the electrical angle θ_e of the motor, and is related to the mechanical rotation by equation 2.21. Commutation logic follows a very simple rule - when the voltage is high the current is high, and when the voltage is low the current is low. High or low refer to the values of the voltages and currents being either positive or negative.

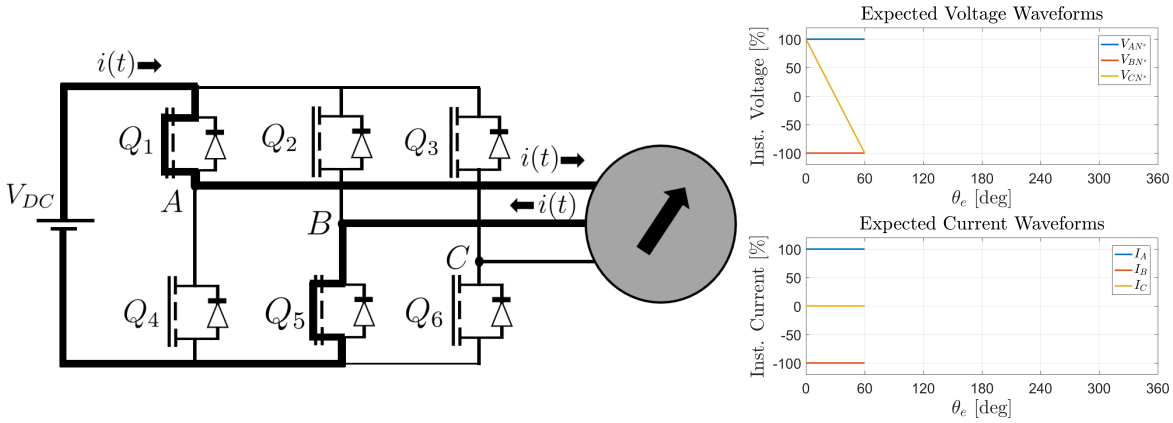

Figure 2.24: Commutating a BLDC motor with an ESC, $\theta_e = 0^o$ to 60^o.

Consider section $\theta_e = 0^o$ to 60^o of table 2.2 and the ESC diagram of figure 2.20. Having switch Q_1 open means positive voltage and current flows from the high side of the DC circuit into the motor. A second switch is required to connect the circuit to ground, which is Q_5 in this case. Positive current is defined when current is flowing into the motor, so for phase B this means a negative current is passing through the wire, since it is exiting the motor. A similar case can be said about the voltage of $v_{BN^*}(t)$, making this value negative. No switches are active for phase C, meaning no current flows in or out of this phase. The voltage is deemed floating, since the back-EMF is inducing a change in voltage from either positive to negative or vice versa. The direction of the change in back-EMF can be found by referencing the next sector. Switches Q_1 and Q_6 are active, meaning that current is exiting the motor through line C. This means that the voltage of C must be low, and that it would have needed to transition from positive to negative in the previous commutation interval. This sequence continues for the remaining intervals, and is represented pictorially in figures 2.25-2.29.

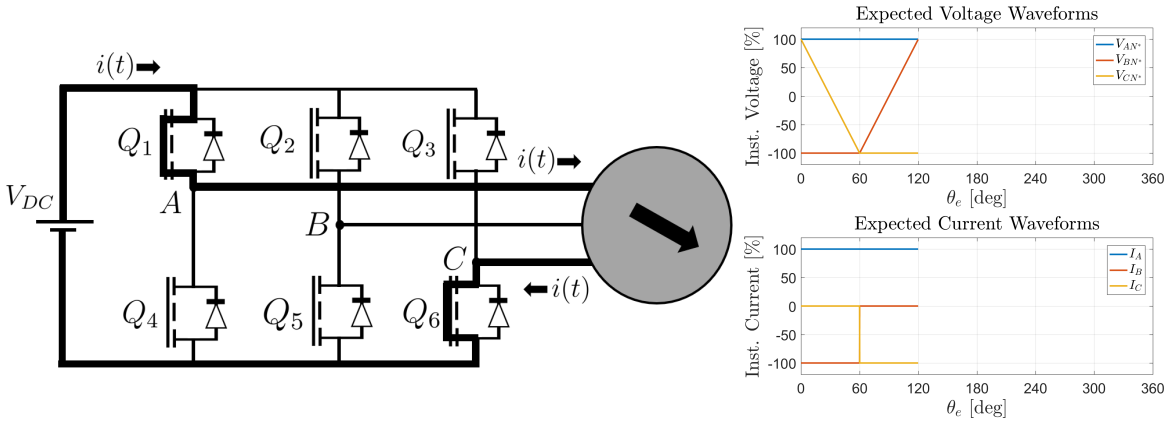

Figure 2.25: Commutating a BLDC motor with an ESC, $\theta_e = 60^o$ to 120^o.

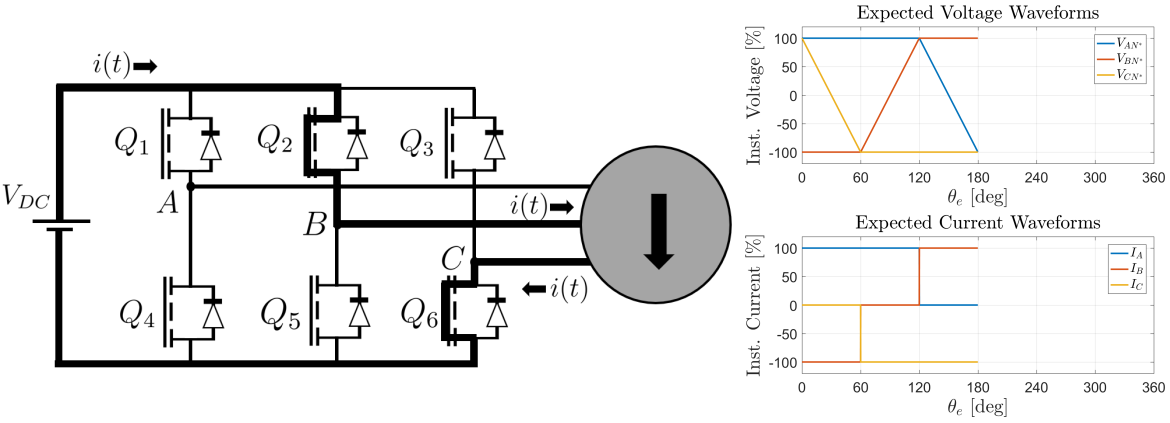

Figure 2.26: Commutating a BLDC motor with an ESC, $\theta_e = 120^o$ to 180^o.

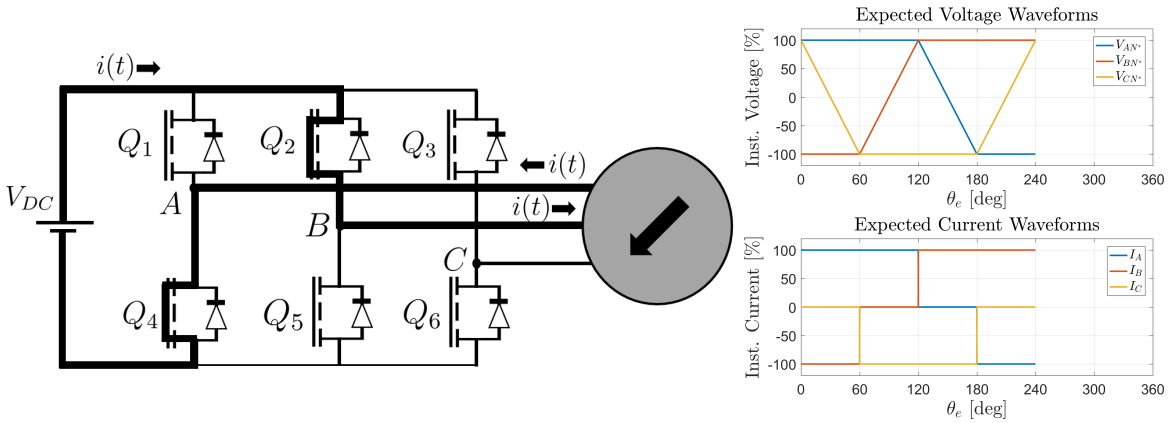

Figure 2.27: Commutating a BLDC motor with an ESC, $\theta_e = 180^o$ to 240^o.

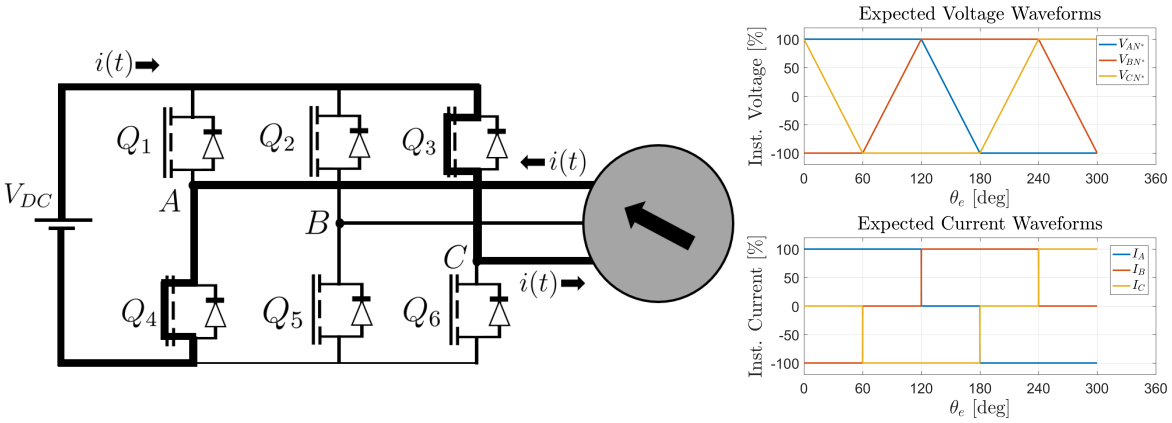

Figure 2.28: Commutating a BLDC motor with an ESC, $\theta_e = 240^o$ to 300^o.

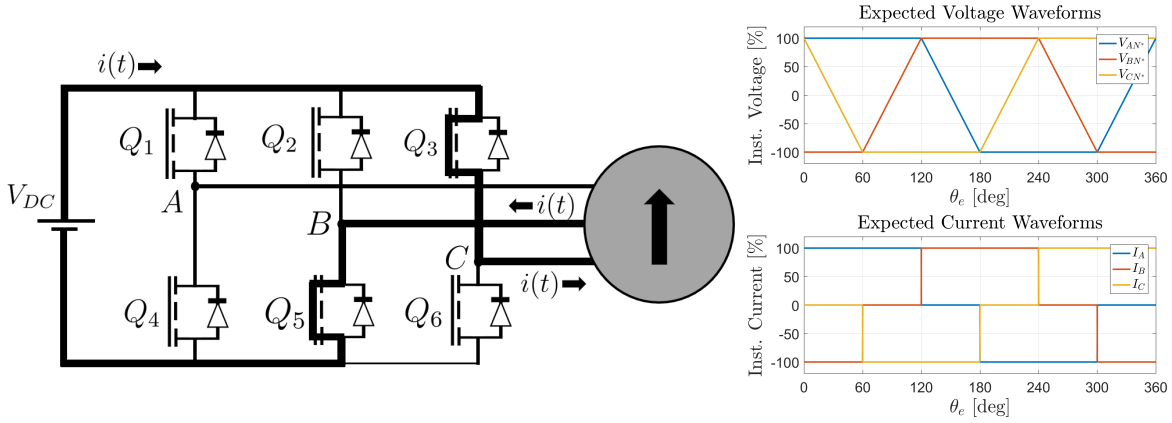

Figure 2.29: Commutating a BLDC motor with an ESC, $\theta_e = 300^o$ to 360^o.

This cycle repeats itself as long as the motor is spinning. Senorless feedback works well when the motor is spinning, but is ineffective at lower RPMs. Commutation timing is dependent on the rotor position, and mistiming commutation events results in a loss in performance. For sensorless ESCs, precise commutation timing is achieved using zero-crossing point (ZCP) detection schemes [18–20]. The exact moment of when to switch from one set of switches to the next is imperative for proper motor commutation. ZCP based methods work to detect when the floating

phase of the motor changes sign value. By recording the phase voltage of the floating signal, the microcontroller can detect when a ZCP occurs. By knowing the time between 2 ZCPs, and knowing they must have been 120^o electrical degrees apart, the speed of the electrical signal ω_e can be determined.

Operation of the ESC relies on accurate knowledge of the electrical angle to commutate the motor θ_e. Figures 2.25 to 2.29 depict the necessary steps to keep the rotation of the motor continuous. Additionally circuitry is required to sense the phase voltages, filter noise ripples, and freewheel voltage spikes. ESCs are fundamentally 6 switches, known as MOSFETs, which are the focus of the next section.

2.3.2 MOSFET Operation

The primary means of controlling induction motors are the MOSFETs. MOSFETs, function as electronic switches, that open or close rapidly based on a control signal. These MOSFETs can be combined into useful arrangements, to allow for precise control of the motor, such as an a H bidge or ESC configuration. To understand how MOSFETs work, we must first understand the basic working principle behind MOSFETs. A MOSFET consists of three terminals, shown in figure 2.30:

1. Drain - terminal connected to $+V_{DC}$
2. Source - terminal connected to load
3. Gate - terminal which controls if current is flowing between terminals

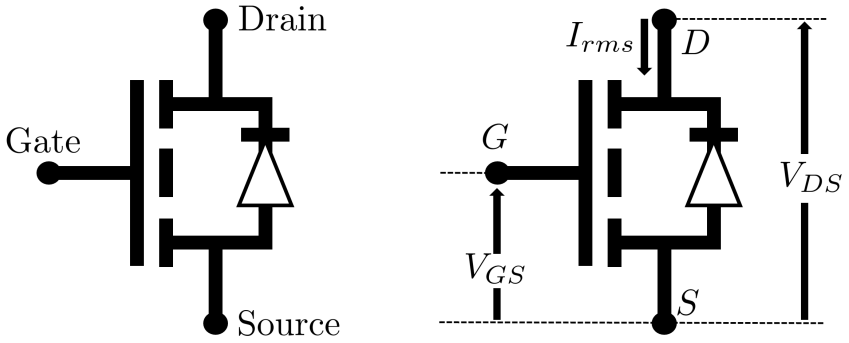

Figure 2.30: MOSFET model.

These names are based on the electron current definition, because when the MOSFET allows current to flow, electrons enter the source terminal and exit out through the drain terminal. However, this work discusses MOSFET operation using conventional current. For a standard NPN channel MOSFET, when no voltage is applied to the gate, no current is allowed to flow from the drain to the source.

To control current flow between MOSFET terminals, a voltage (typically $+5V$) is applied to the gate. The transistor allows current to flow as long as a voltage is applied to the gate, which is above some threshold value. To stop current flow, simply drop the gate voltage to 0. The use of a MOSFET is analogous to a switch,

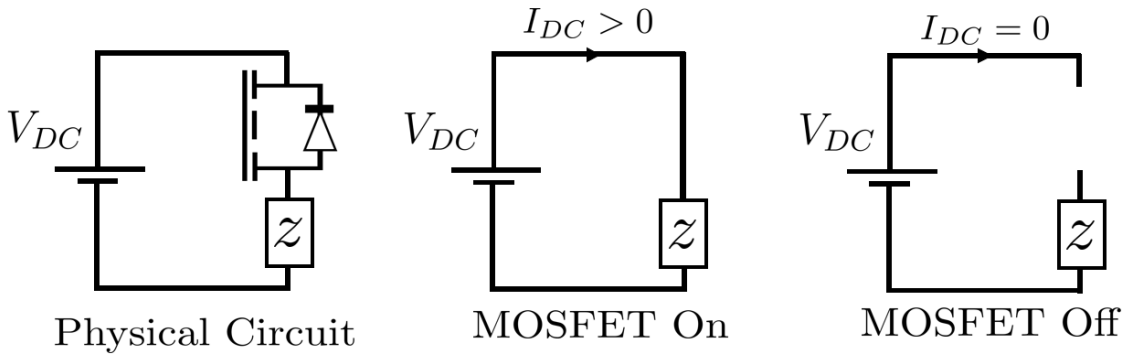

Figure 2.31: MOSFET model.

and can be used to augment the physical circuit into multiple equivalent circuits based on the state of the MOSFET, with a simple example shown in figure 2.31.

MOSFETs are useful when combined with additional circuitry that enables closed loop control of a particular system. A microcontroller, or some other type of MOSFET driver, is paired with a set of MOSFETs, and the controller regulates how much time the MOSFET is active. The controlling signal is typically a pulse width modulated (PWM) signal, with the length of time regulating the output voltage of the device.

Now consider if a microcontroller μC is added to the previously examined circuit, shown in figure 2.32. This microcontroller controls how long the MOSFET is open or closed, and sends a 50% duty cycle of $5V$ to the gate of the MOSFET. This

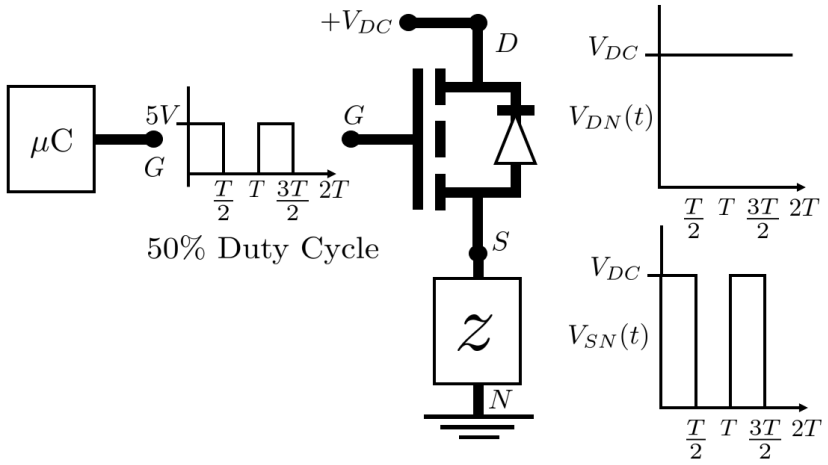

Figure 2.32: MOSFET circuit with a microcontroller μC.

input duty cycle is mimiced on the output of the MOSFET, where the same duty cycle waveform appears except with an augmeted amplitude. During on operation, the gate and drain are connected, meaning they share the same value of $+V_{DC}$.

During off operation, no voltage is dropped across the load z, meaning that the source is connected to ground and has a value of $0V$. The result is that the input duty cycle with an amplitude of $5V$ has been turned into a duty cycle with an amplitude of V_{DC}. This means that powerful circuits can be created.

An effective modeling tool is to consider the output voltage of the MOSFET as the average value of the source voltage over one waveform. The duty cycle ratio, or throttle, sets the effective output voltage of the circuit. In reality, the output of the MOSFET are voltage pulses between 0 and V_{DC}, however by modeling the output as the average value of voltage signal, a single simplified model can be determined.

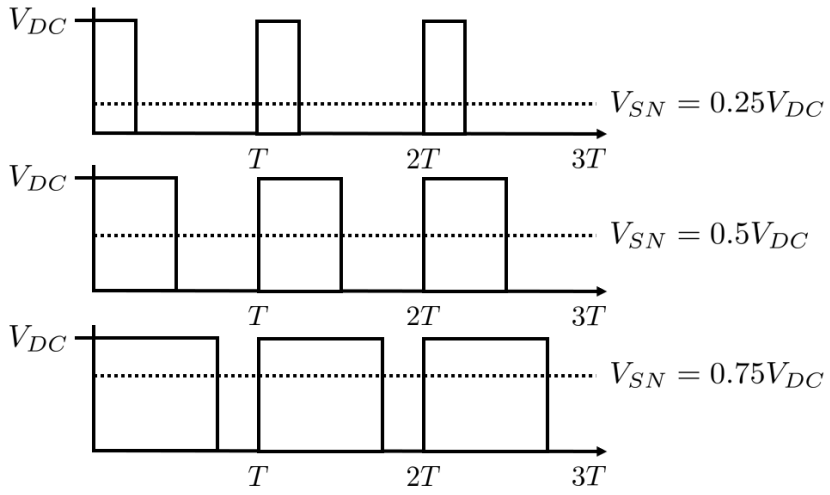

Figure 2.33: Output voltage of V_{SN} based off duty cycle duration.

At no throttle, the MOSFET is always off, meaning that no voltage is seen at the source terminal. At full throttle, the MOSFET is always on, meaning the source voltage is equal to the supply voltage. When the duty cycle is neither 0 or 100%, the output voltage is the combination of 'on' voltage and 'off' voltage. The average voltage of V_{SN} is given by equation 2.19. Common circuits involving MOSFETs

are switch mode power supplies, such as: DC-DC step up boost converters, DC-DC step down buck converters, and H-bridge topologies [21].

Combining MOSFETs with BLDC motors creates a complicated and exciting circuit to analyze. The voltage and current waveforms of a BLDC motor are trapezoidal and rectangular, respectively. The nonlinearity of the voltage waveform must be taken into account when designing BLDC motors. User throttle changes the duty cycle of the MOSFET, effectively scaling the output voltage in a controlled way. However, instead of seeing 0 to V_{DC} on the output of the MOSFET, one sees the back-EMF of the motor superimposed onto the MOSFET signal. An example of this is shown on the next pages in figures 2.34 and 2.35, which shows experimentally recorded waveforms of $v_{AN}(t)$ and $i_A(t)$. Recall that N is the DC ground of the system.

Consider the experimentally obtained voltage and current waveforms for a BLDC motor, figure 2.34. A snapshot of the instantaneous waveform over approximately 2 electrical cycles is shown in figure 2.35, for throttle settings of 40%, 70%, and 100%. When comparing individual waveforms, the most obvious result is there appears to be less noise in the waveforms as the throttle increases. For example, 40% throttle contains a large amount of electrical noise, resulting in a disorganized appearing waveforms. On the other hand, the 100% throttle waveforms look smooth and continuous.

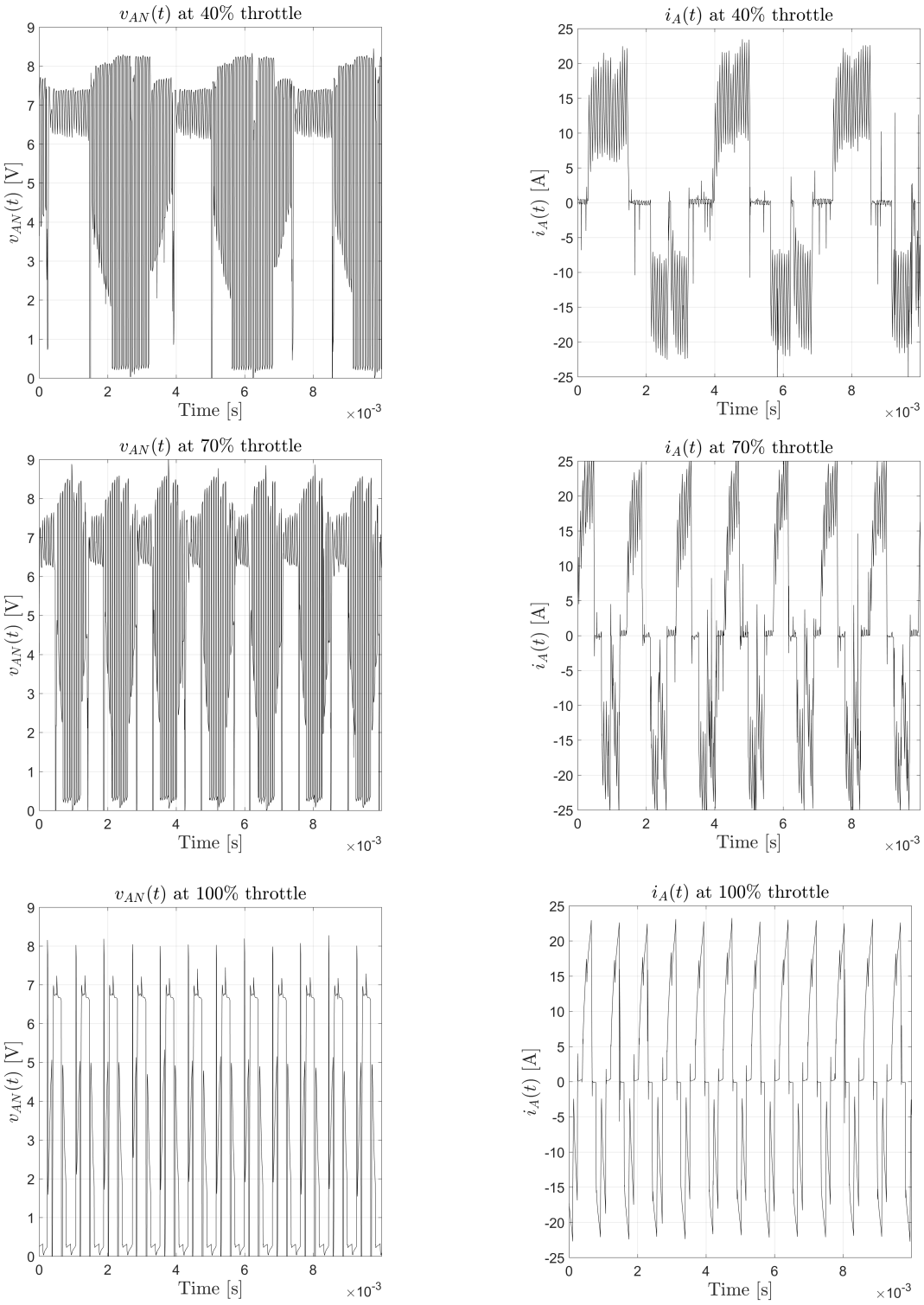

Figure 2.34: Instantaneous voltage and current waveforms over 1ms for a BLDC motor at $V_{DC} = 7.2V$.

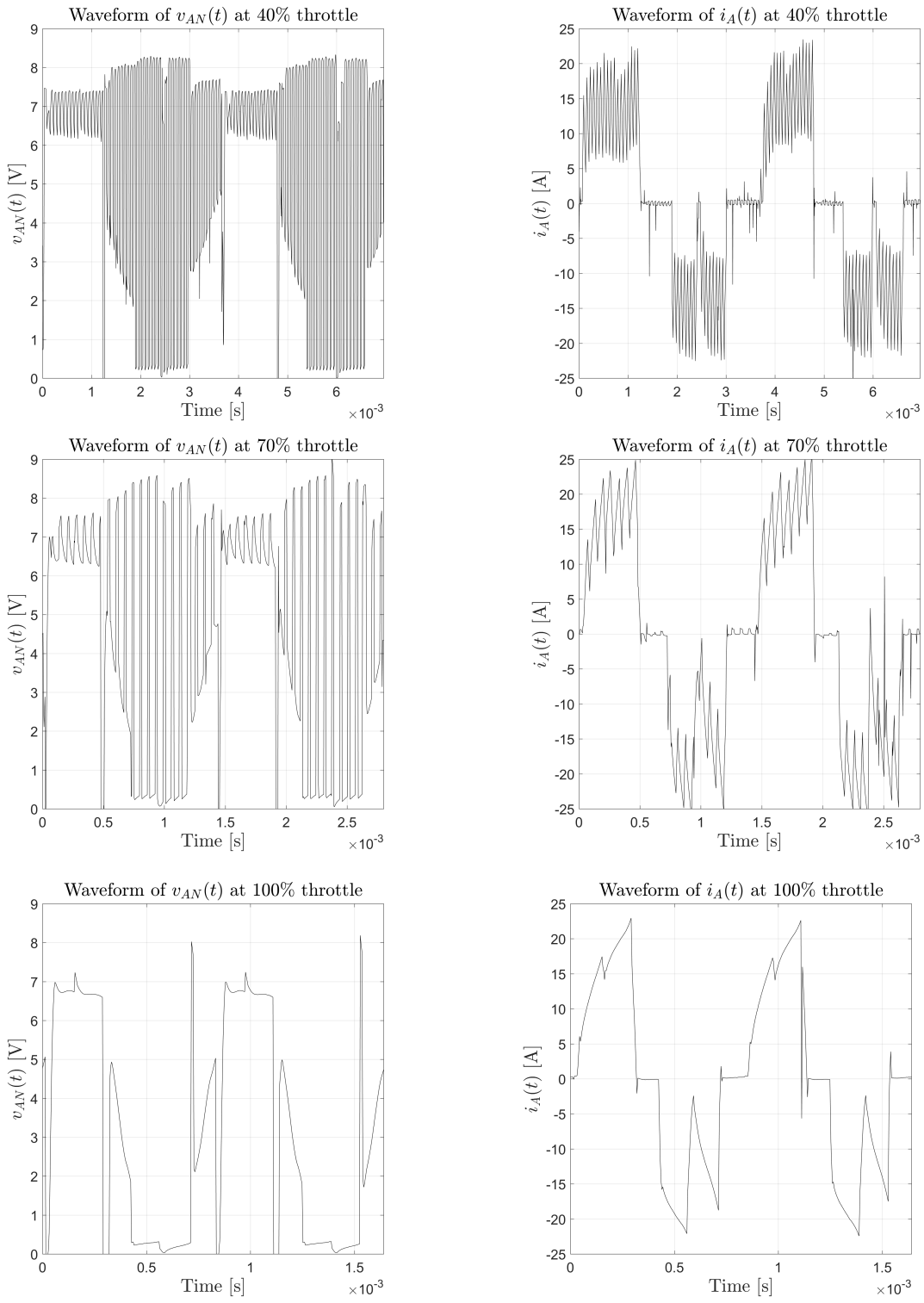

Figure 2.35: Instantaneous voltage and current waveforms over 2 cycles for a BLDC motor at $V_{DC} = 7.2V$. Note the difference in time between waveforms of different throttles.

The difference in appearance of these signals relates to the amount of time the MOSFETs are open. At a lower throttle setting, more switching occurs and thus the signal appears to be noisy in comparison to the 100% throttle setting. From this, 3 conclusions can be drawn:

1. Increase in throttle results in increased on time for a MOSFET, and thus fewer switching events for the same amount of time.

2. Increase in throttle increases effective motor voltage, which increases motor rotation speed

3. Waveforms are 'ideal-like' at 100% throttle

These results will be useful when determining the motor model in Chapter 4, and the ESC power loss model of section 4.2.4.

Careful examination of figure 2.35 shows large unaccounted spikes in voltage and current, which are most noticeable at 100% throttle. Additionally, the voltage spikes are larger than the supply voltage of 7.2V, meaning they must result from a different source. Also, these spikes appear to come in a repeatable fashion, indicating that it is not simply random noise. When examining the current waveform, a step response-like behavior appears. The voltage appears to change instantaneous, but the current contains some time-lag component before the current reaches its maximum value.

These voltage spikes are actually attributed to commutation events, when the rotor reaches a certain location to trigger a change in active MOSFETs. During this time, one MOSFET is turned off whereas a separate MOSFET turns on, and occurs

every 60 electrical degrees. A spike in voltage occurs whenever a commutation event occurs, due to the inductor discharging the energy stored in its magnetic field. The voltage across an inductor is [22]:

$$V_L(t) = L\dot{I}(t) \tag{2.22}$$

Just before commutation, current is flowing, whereas just after commutation, current no longer flows through that phase. This results in a large change in current $\dot{I}$, and thus a large spike in voltage acting across the inductor. Diodes are used to create a complete circuit path for the inductors to discharge, and so the resulting voltage spike is quickly dissipated. This process is referred to as freewheeling [13], and can be assisted by using additional MOSFETs to make the energy dissipation process more efficient.

The time-lag response of current can be explained by modeling a simple resistor-inductor circuit, shown in figure 2.36. At time $t = 0$, a change in voltage

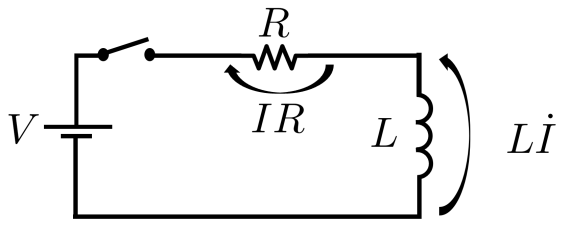

Figure 2.36: Simple RL circuit, switch closes at time = 0.

ΔV occurs which can be modeled as a step input. Kirchhoff's voltage law sums the voltages around the loop and can be used to expressed the set of differential

equations:

$$\Delta V = I(t)R + L\dot{I}(t) \tag{2.23}$$

This equation can be solved to find the current time response:

$$I(t) = \frac{\Delta V}{R}(1 - e^{-\frac{R}{L}t}) \tag{2.24}$$

For a given step input of voltage V, the current will reach a steady state value of V/R after some transient response occurs, and has a time constant of L/R. The larger the inductor value L, the longer it takes for the current to reach its steady-state value, shown in figure 2.37.

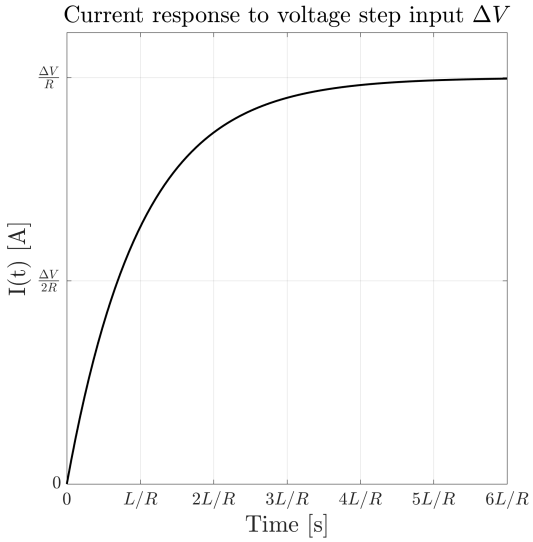

Figure 2.37: Output voltage of V_{SN} based off duty cycle duration.

Interestingly, this has a noticeable impact on the current waveforms for BLDC motors. For a large torque constant K_T, it is desirable to increase the number of turns in a coil to increase the strength of the magnetic field, from equation 2.2.

This large number of turns however, increases the inductance of each phase, which causes larger time delays. Additionally, more turns represents increased resistance, so the final value of steady state current V/R will be lower. This is consistent with needing less current to generate the same torque, as compared to a motor with a smaller K_T.

With the basic operation of DC motors and ESCs covered, the experimental setup to record motor and ESC performance can be explained.

Chapter 3: Experimental Setup

3.1 Dynamometer Overview

A dynamometer consists of a load varying device and sensors to monitor the motor's performance. Performance of commercial off the shelf motors and ESC is studied by recording the power at various points for a range of operating conditions.

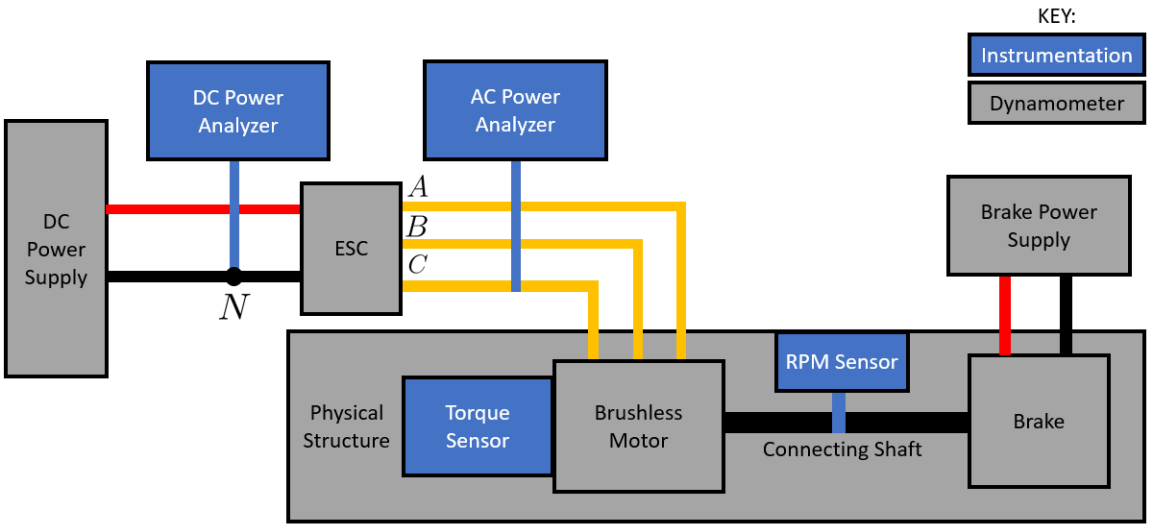

Figure 3.1: Basic components in a dynamometer for electric motors.

The centerpiece of this work was designing and fabricating a custom dynamometer using in-house resources. This involved creating custom hardware for

the power analyzers, constructing a versatile frame, and implementing a unique 2 data acquisition device (DAQ) LabView setup to properly record the system's performance. The final result is a highly customizable dynamometer, with a large amount of testing flexibility, in terms of ESCs, motors, and DC voltages.

To study BLDC motors and ESCs, the following components were used: a DC power supply, a DC power analyzer, an AC power analyzer, and a mechanical power analyzer, shown in figure 3.1. A breakdown of these items and their use can be found in table 3.1:

Table 3.1: Dynamometer component overview.

Item	Purpose
DC Power Supply	Provides DC electrical power to the ESC
DC Power Analyzer	Measures the power content of the DC signal
ESC	Modulates DC power to AC power for the BLDCM
AC Power Analyzer	Measures the power content of the AC signal
BLDCM	Converts AC power to mechanical power
Torque Sensor	Records the shaft torque of the motor
RPM Sensor	Records the shaft RPM of the motor
Brake	Varies load on the BLDCM
Brake Power Supply	Allows user to control operation of the brake

The critical component of any dynamometer is the brake, which is responsible for absorbing the motors mechanical output and should be controllable. The brake is physically connected to the output shaft of the motor and thus any change in load of the brake must be produced by the motor. Several types of brakes exist for dynamomemters [9]:

1. Friction Brakes: Mechanical devices impeded the rotation of the shaft, similar to an automobile's brakepad

2. Hydraulic Brakes: A working fluid, typically water, is compressed and expanded, which changes the load on the motor

3. Magnetic Brakes: Current flowing through a non rotating coil causes a magnetic interaction with a rotating magnet that produces a magnetic torque

For each of these types of brakes, the adsorbed energy must be dissipated as heat, and thus typically requires cooling for extended use. Additionally, the presence of rotating components inevitably causes wear on the system. For extended use, the number of these components must be minimized. A typical friction or hydraulic brake requires pistons, levers, pulleys or other moving components that are placed under cyclical stress. Both friction and hydraulic brakes consist of moving parts, whereas the primary action in the magnetic brake is a non-contacting magnetic interaction. For magnetic brakes, the only component subject to wear are the bearings. In addition, there are several other factors that make a magnetic brake desirable [23]:

1. Mechanical torque is only a function of the input current to the brake, $Q = f(I_{brake})$, and is easily controlled

2. Mechanical torque is independent of operational RPM

3. High degree of repeatability and controllability associated with ease of use

4. Long life cycle associated with low wear components

5. Smooth and quiet operation

The ability to control torque independent of RPM makes the magnetic hysteresis an attractive option for studying electric motor performance.

For this purpose, a Magtrol magnetic hysteresis brake (HB-10) was acquired to vary the load on the motor. The brake is rated for 10 in-oz at up to 20,000 RPM, however it was found that the load on the brake could go as high as 20 in-oz, for short term operation. The RPM limit is set by the maximum rated speed of the internal bearings used in the HB-10. Construction of the brake consists of a rotating pole structure and a coil, shown in figure 3.2. Energizing the stationary coil with DC current causes a magnetic interaction between the stationary coil and the moving magnets. This magnetic interaction causes a braking torque to develop, and thus the torque of the motor is changed. Controlling the DC current into the brake allows one to control the braking torque.

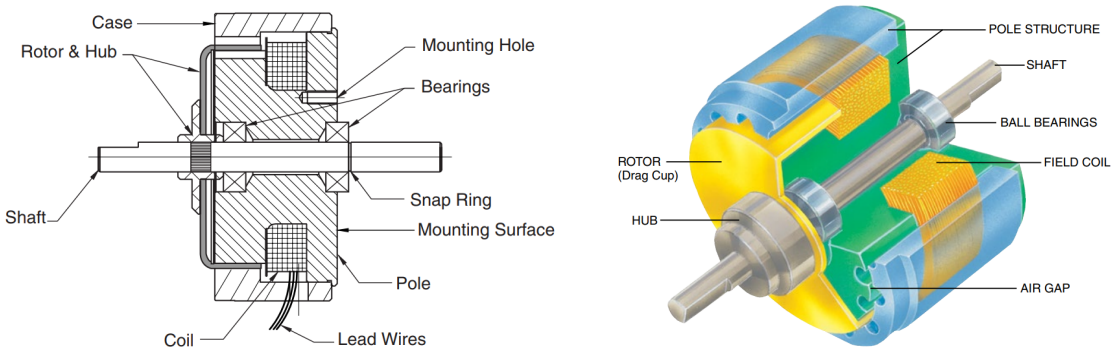

Figure 3.2: Exploded view of a magnetic hysteresis brake. Image on the left is from [24], image on the right is taken from [23].

As previously mentioned, the operation of the brake is only a function of the input current and is independent of RPM. Changing the output voltage of the brake's DC power supply allows the input current to the brake to be regulated, allowing for

control of the motor's torque. The input current to the brake and output current relationship can be found in figure 3.3.

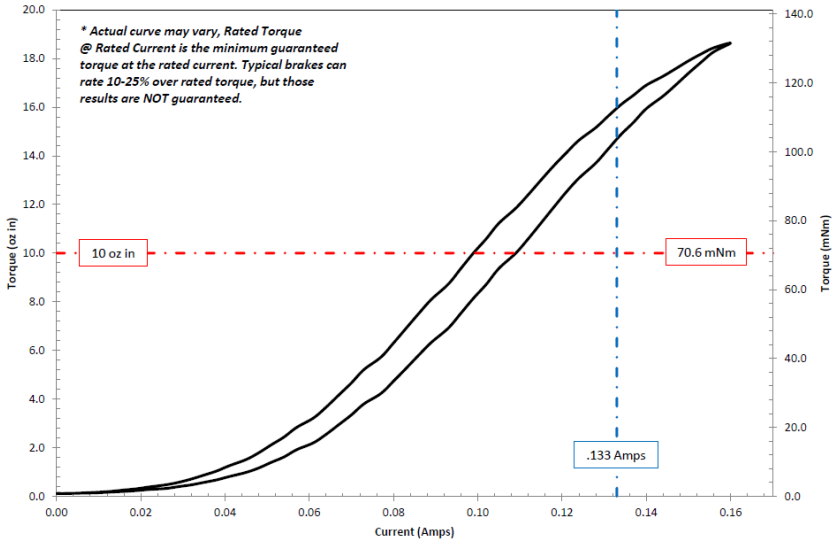

Figure 3.3: Input current vs output torque for the Magtrol HB-10 magnetic hystersis brake. Image taken from [25].

With the ability to regulate the motor's torque, the brake is the primary operational component in the dynamometer. Once the torque is varied, additional sensors record the performance of the motor at the various operating points. Once enough points at different throttles have been recorded, the motor and ESC parameters can be deduced.

Various sensors are used in the system's DC, AC, and mechanical power analyzers. A breakdown of the different sensors used is included in table 3.2. Each power analyzer uses a set of sensors to monitor the performance of the ESC and BLDC motor, each targeting a specific domain.

Table 3.2: Sensors used on the dynamometer.

Analyzer	Sensor	Quantity	Measurement	Rating
DC	DC Current Sensor	1	I_{DC}	+30A
	Voltage Sensor	1	V_{DC}	+15V
AC	AC Current Sensor	2	i_A, i_B	$+/-30$A
	Voltage Sensors	3	v_{AN}, v_{BN}, v_{CN}	+15V
Mechanical	Torque Sensor	1	Q	$+/-50$ *in-oz*
	RPM Sensor	1	ω	30,000 RPM

The remainder of this Chapter shall be devoted to exploring the 2 DAQ setup used to record the motor's performance and the power analyzers themselves. Special attention is given to the AC power analyzer as this requires an understanding of 3 phase electricity to implement. Derivations for the active power, apparent power, and power factor will be critical in the modeling efforts of Chapter 4.

3.2 Two DAQ Setup

To record DC, AC, and mechanical power, a DAQ system must have 2 features: a high number of input channels, and a data acquisition read rate high enough to properly sample the AC waveforms. Between the three analyzers, up to 10 analog input channels are required to record all necessary metrics. The National Instrument's (NI)-USB 6251 had a maximum channel capacity of 16 analog inputs. However running all inputs to 1 DAQ reduced the read rate to be 100 kHz.

Due to the number of input channels, and speed of the electrical signals, 2 Data Acquisition Devices (DAQs) were required to properly analyze the system's

performance. While originally using 1 DAQ, it was found that a slow sample rate had a detrimental effect on calculating the AC power. An insufficient sample rate resulted in nonphysical values for P_{AC}. To eliminate this issue, the maximum data rate for the system was increased by using a second DAQ. Each DAQ has a data limit, which is a function of the number of samples/sec and the number of samples collected.

The final sample rate of setup was 250 kHz, which appears adequate for sampling the electrical signals. The maximum RPM of the brake is 20,000 RPM and all motors studied contain 7 pole pairs, meaning that at 250 kHz sampling, each waveform contained a minimum of 107 samples. Such a high resolution is necessary to detect the large amount of MOSFET switching, shown in figures 2.34 and 2.35, which occurs during normal operation. Additionally, the ideal voltage and current waveforms contain six distinct steps over one cycle and can only be captured by rapid data acquisition. Note that at lower motor speeds, the number of samples per waveform is higher.

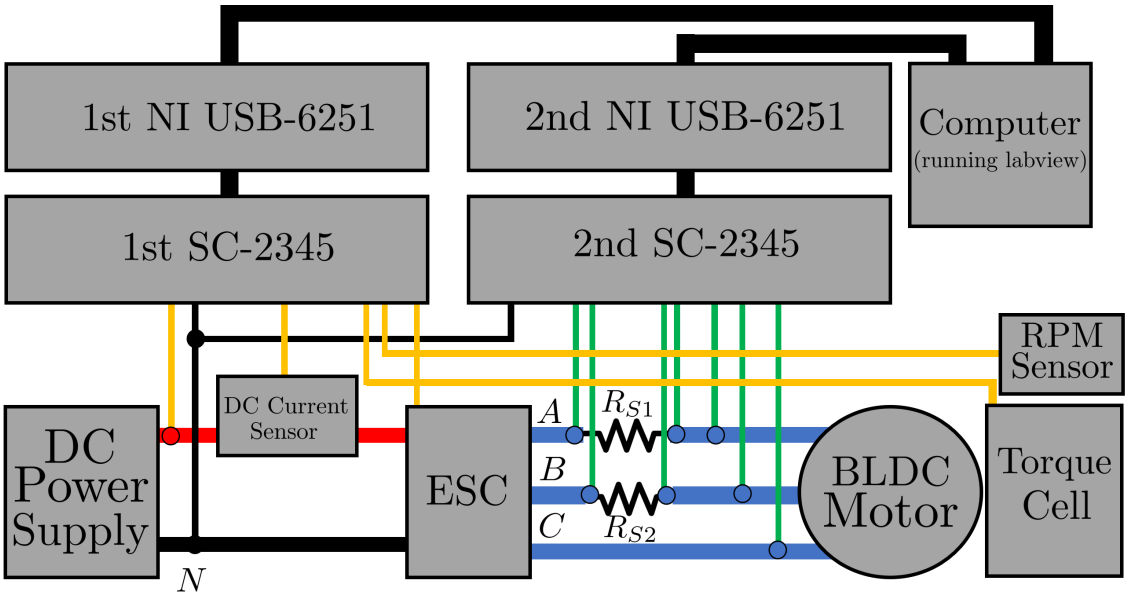

Figure 3.4: DAQ and sensor arrangement.

Use of two DAQs with in house power analyzers produced a dynamometer system that was completely customizable, and allowed for testing numerous motors and ESCs at different voltages. Figure 3.4 shows which signals were read into which DAQ. Due to the time sensitive nature of the AC power analyzer, all signals related the AC system were read into DAQ-2. Each DAQ contains 2 components: the NI-USB 6251 is the actual data sampling and collection device, and the SC-2345 functions as a breakout board for the NI-USB 6251. Measurements from motor were connected to the SC-2345 and transmitted to the labview environment via the NI-USB 6251. Both DAQs were read into the same labview program, streamlining data collection.

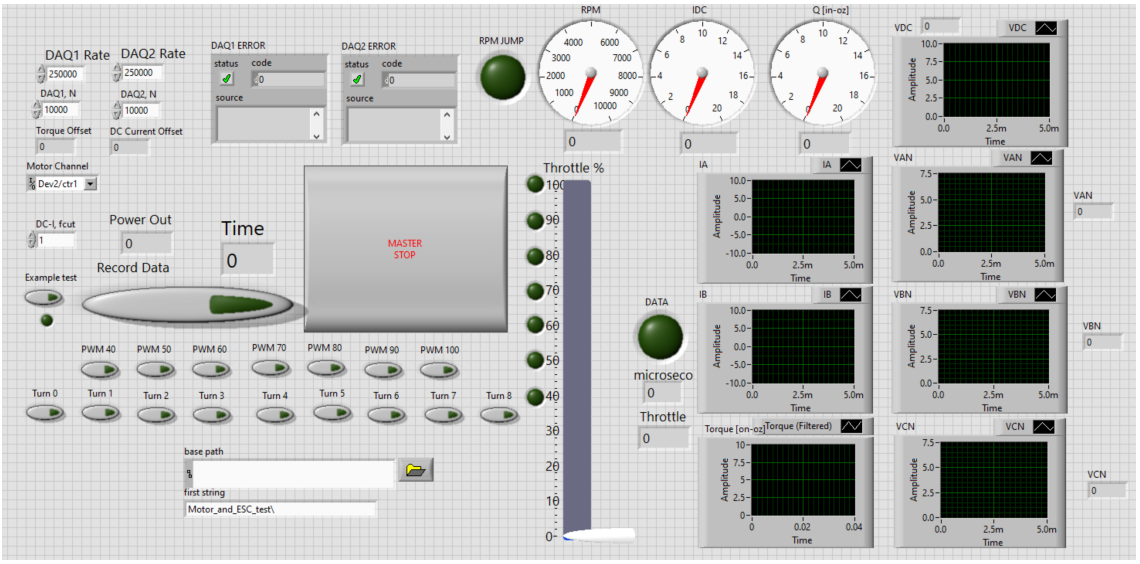

Figure 3.5: Screenshot of labview front panel with 2 DAQs.

All parameters related to system performance are monitored directly from the front panel of the labview setup, shown in figure 3.5, whereas the power calculations are done in post processing. Redcuing the number of calculations to a minimum keeps the labview setup as bare bones as possible, allowing for a 250 kHz read rate. The labivew program had certain custom additional features such as PWM signal generation, a robust file data saving network, and automatic zeroing of sensors before tests. The final two DAQ configuration is shown in figure 3.6.

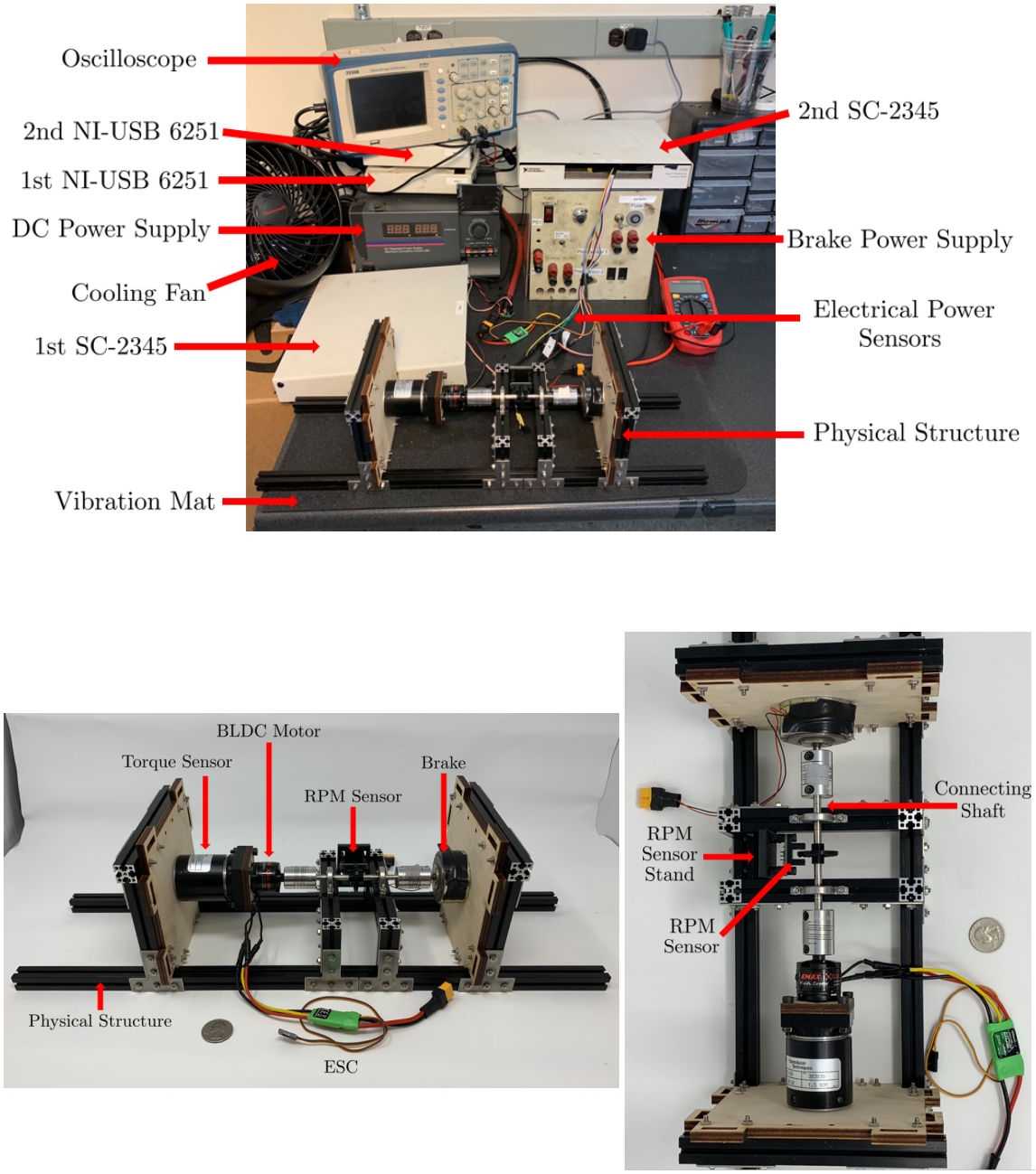

Figure 3.6: Final dynamometer configuration.

With an understanding of the dynamometer components, the focus shifts to examining the various power analyzers used to measure performance.

3.3 DC Power Analyzer

The DC power supply provides a constant DC voltage V_{DC} and a constant DC current I_{DC} to ESC. The DC power is [21, 22, 26]:

$$P_{DC} = I_{DC} V_{DC} \tag{3.1}$$

A noninvasive hall effect based current sensor was used to measure the value of the DC current, and deduces the strength of the DC current based off the current's magnetic field strength. The output of this sensor was a 0-5 V analog voltage signal, which was converted to the DC current value based of a simple factor of 133 mV/A. This sensor showed good agreement during use with the DC power supply's LED display, which showed the value of the instantaneous current while the motor was running. The voltage measurement was read into the DAQ directly for $V_{DC} < 10V$.

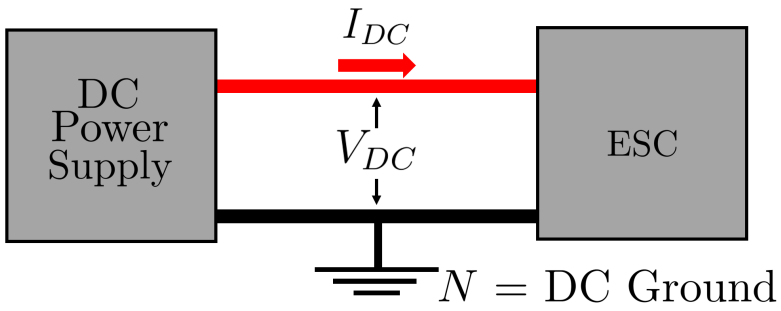

Figure 3.7: DC power occurs between the DC power supply and the ESC.

The DAQ has a 10 V hardware limit, meaning that for higher voltages a simple voltage divider was used to reduce the value to within 10 V. By sampling the voltage in the middle of two 500 Ω resistors in series, the signal's voltage is reduced by a

factor of 2, meaning that at the maximum $V_{DC} = 14.8$ V, only 7.4 V was being read into the DAQ. Calibration of the voltage divider is accomplished by reading in voltages between 0-10 V into the DAQ both before and after the voltage divider and then deducing the gain. Finally, a low pass filter was applied to both the voltage and current signals to smooth out any spikes from the power supply. Both sensors were placed before the ESC.

3.4 Mechanical Power Analyzer

A mechanical power analyzer was developed to measure the output performance of the motor. The mechanical power is [13, 27, 28]:

$$P_m = Q\omega \tag{3.2}$$

An infrared (IR) optical sensor was used to monitor RPM by counting the time between pulses. Mounted on the rotating shaft is a disk with slots, so as the shaft rotates the IR beam is interrupted periodically and the RPM can be deduced. For low speeds (less than 10,000 RPM) a 20 slot disk was used, whereas for high speeds (up to brake limit of 20,000 RPM) a 4 slot disk was used. Accuracy of the RPM measurement was verified with a hand held IR tachometer.

Torque measurements were made with a transducer techniques 50 in-oz torque sensor, consisting of a full strain gauge bridge. When a load is applied, the shaft deflects and outputs a voltage proportional to the deflection of the device. This voltage is amplified to between 0-2 V and then read into the SC-2345. To calibrate

this sensor, calibration weights were hung off the device at a known distance. This test was repeated several times before arriving on the calibration plot, shown in figure 3.8.

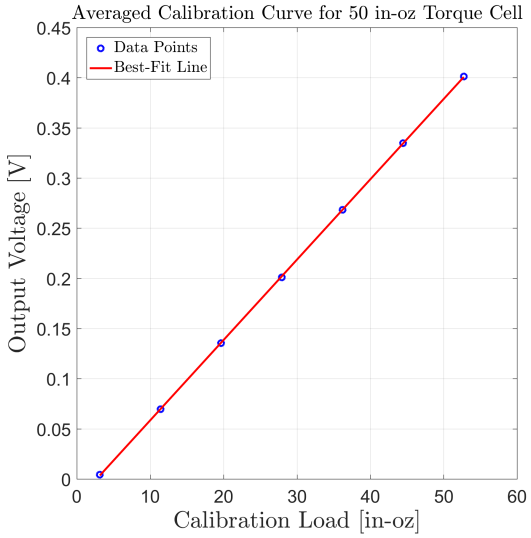

Figure 3.8: Calibration curve for the 50 in-oz torque cell.

During motor testing, it was found that the torque sensor is sensitive enough to pick up minor changes in the mass of the motor. Additionally, changes in the position of the sensor wire were found to augment the offset of the torque cell. As a result, a zeroing program was implemented in the LabView environment, which would zero out the sensors readings before the start of a test. This provided an effective strategy, as the brake required a repeatable 3.1 in-oz torque to overcome the cogging friction of the brake. The torque sensor was connected the BLDC motor via a short adapter piece. The sensor was then mounted to the remainder of the physical structure shown in figure 3.6.

DC and mechanical power measurements are straight forward to achieve, how-

ever AC power measurement requires additional circuit theory to implement.

3.5 AC Power

Before describing the custom AC power analyzer, an understanding of AC power is required. Basic power relations for AC systems, such as active power, apparent power, and the power factor, shall be expressed for a single phase sinusoidal AC system. Next these relations will be expanded to include polyphase and non-sinusoidal waveforms.

3.5.1 Single Phase AC Relations

When discussing AC circuits, it is common to explain the differences between DC and AC circuits by first considering a single phase AC circuit. Eventually, this analysis will be expanded to include additional phases. To start, consider a single phase AC system with sinusoidal voltage and current waveform:

$$v(t) = V_{pk}\cos(\omega_e t + \theta_v) \tag{3.3}$$

$$i(t) = I_{pk}\cos(\omega_e t + \theta_i) \tag{3.4}$$

where pk represents the peak value of the waveform and θ represents the initial phase shift of the signal. The user sets θ_v and the electrical frequency ω_e, and the load impedance z determines the amount of current and the current phase angle θ_i. Changing the impedance z can have two effects: changing the magnitude of the

current I_{pk}, or changing the phase lag between voltage and current $\theta_v - \theta_i$. This second point will be important when considering power transmission.

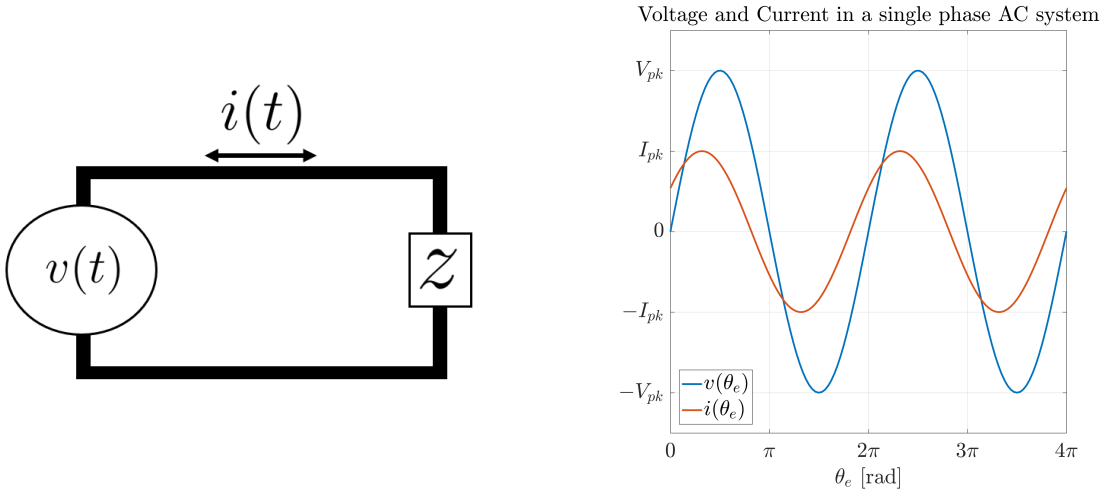

Figure 3.9: Left: Single phase AC system. Right: Voltage and current in a sinusoidal system.

The instantaneous power in any signal is simply the product of the instantaneous voltage $v(t)$ and the instantaneous current $i(t)$ [21, 22, 26]:

$$p_{inst}(t) = v(t)i(t) \tag{3.5}$$

$$p_{inst}(t) = [V_{pk}\cos(\omega_e t + \theta_v)][I_{pk}\cos(\omega_e t + \theta_i)]$$

$$p_{inst}(t) = \underbrace{\frac{V_{pk}I_{pk}}{2}\cos(\theta_v - \theta_i)}_{\text{non-ossicilating}} + \underbrace{\frac{V_{pk}I_{pk}}{2}\cos(2\omega_e + \theta_v + \theta_i)}_{\text{ossicilating}} \tag{3.6}$$

An important distinction of instantaneous power in an AC system is that it consists of an oscillating component and non-oscillating component. The steady component is found by the cosine difference of the phase angles whereas the oscillating component has a frequency of twice the driving frequency ω_e. Notice how the instantaneous

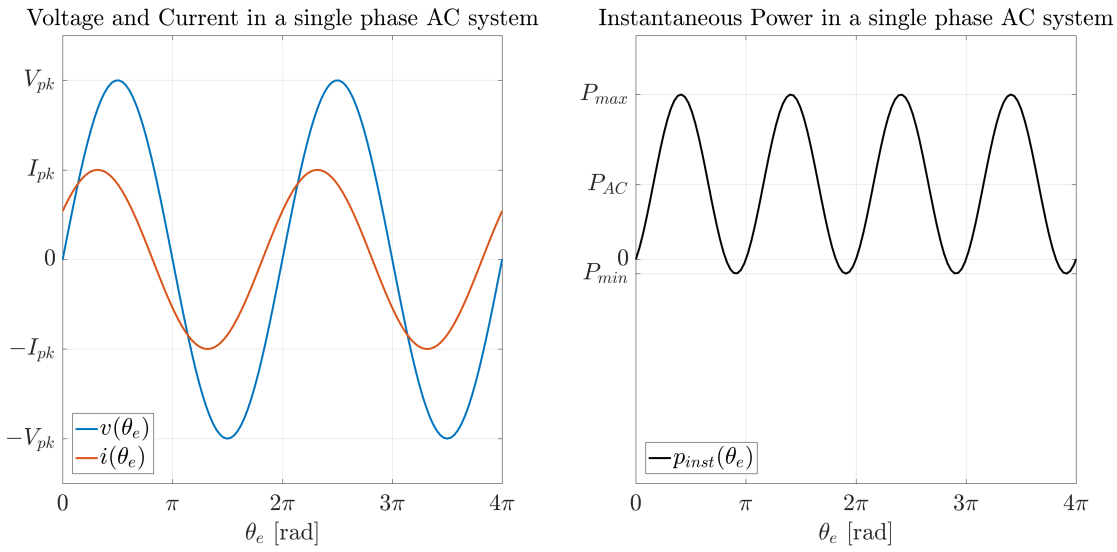

Figure 3.10: Left: Voltage and current in an AC system. Right: Instantaneous power in an AC system.

power p_{inst} oscillates between a maximum and minimum, and is offset by some average value in figure 3.10. To find the average power in the signal, it is simply the instantaneous power over a waveform:

$$P_{AC} = \frac{1}{T}\int_0^T v(t)i(t)dt \tag{3.7}$$

$$P_{AC} = \frac{1}{T}\int_0^T [\frac{V_{pk}I_{pk}}{2}[\cos(\theta_v - \theta_i) + \cos(2\omega_e + \theta_v + \theta_i)]]dt$$

Taking the integral over one waveform (2π radians) eliminates the oscillating component of the instantaneous power. This is a result of the fact that this component does no work on the system, as it both adds and subtracts power in an unusable manner. Hence, the term active power describes the mean power in the system, as this represents the net power transfer of the system. Active power is the power to spin motors, heat up wires, and do useful work. For efficiency metrics of the ESC

and motor, it is only proper to use the active power P_{AC}. This makes the active power for a single-phase sinusoidal system:

$$P_{AC} = \frac{V_{pk} I_{pk}}{2} \cos(\theta_v - \theta_i) \tag{3.8}$$

where term $\cos(\theta_v - \theta_i)$ is referred to as *the power factor*, pf. Power factor relates the leading or lagging of the voltage and current signals in the system. The important takeaway is that if the current and voltage signals are out of phase with one another, less real power can be transfered. This phase shift between current and voltage comes from the load impedance z. When inductors and capicators are present, a leading or lagging of the current signal occurs [22]. Some key notes about power factor and power transmission are:

1. Power factor has a range between $-1 \leq pf \leq 1$
2. $\theta_v > \theta_i$ relates to a lagging power factor, which is indicative of an inductive load. An example is a RL circuit.
3. $\theta_v < \theta_i$ relates to a leading power factor, which is indicative of a capacitive load. An example is a RC circuit.
4. $\theta_v = \theta_i$ has a power factor of unity, which is indicative of a purely resistive load. An example is a R or RLC circuit.
5. Higher power factor allows more work to be done on the system.
6. Increasing the peak current or voltage increases the active power.

To demonstrate the need for a high power factor, consider if voltage and current are completely out of phase with one another such that $\theta_v - \theta_i = \pi/2$. Here, the power factor is equal to 0, meaning even though voltage and current are flowing through the system, no power is transfered. An example of such a circuit is a source connected to only either a capacitor or a source connected to only an inductor. For maximum power transfer, a power factor of 1 is needed. The power factor can still be unity even with the presence of inductors capacitors are present in a load, as long as the values of the capacitors, inductors, and driving frequency are such that the net phase lag is 0.

The oscillating component of the active power is still useful for power analysis, as wires must be sized according to the maximum power in the system. To describe the "equivalent DC magnitude" of the AC voltage and current, the root-mean-square (rms) function is used. This is required since the average value of both the voltage and current is 0 in an AC system, by definition. The rms of any signal is defined as:

$$rms\{x(t)\} = \sqrt{\frac{1}{T}\int_0^T x^2(t)dt} \tag{3.9}$$

Thus the rms values for voltage and current are:

$$V_{rms} = rms\{v(t)\} = \sqrt{\frac{1}{T}\int_0^T v^2(t)dt}$$

$$V_{rms} = \frac{V_{pk}}{\sqrt{2}} \tag{3.10}$$

$$I_{rms} = rms\{i(t)\} = \sqrt{\frac{1}{T}\int_0^T i^2(t)dt}$$

$$I_{rms} = \frac{I_{pk}}{\sqrt{2}} \tag{3.11}$$

The ratio of the peak value to the rms value is the $\sqrt{2}$ for all single phase sinusoidal AC signals. Using equations 3.10 and 3.11 along with the active power equation 3.8 allows one to conclude:

$$P_{AC} = I_{rms}V_{rms}\cos(\theta_v - \theta_i) \tag{3.12}$$

The power factor relates the distortion from the $I_{rms}V_{rms}$ power to the active power. Consider again if the power factor is 0, meaning no active power is transferred. Voltage and current still flows through the system, and so $I_{rms}V_{rms}$ is nonzero. This quantity is important for determining how much effective power is in the line. The $I_{rms}V_{rms}$ power is defined as the apparent power S in the line:

$$S = I_{rms}V_{rms} \tag{3.13}$$

The ratio of active power to apparent power is an alternative way of defining the power factor:

$$P_{AC} = S\cos(\theta_v - \theta_i) = S\ pf$$

$$pf = \frac{P_{AC}}{S} \tag{3.14}$$

Apparent power S represents the maximum amount of power that can be used for work, whereas the power factor relates how much of the maximum power does work.

Typically the power factor angle is used to describe *the triangle of power*, figure 3.11, which are used to relate the active, reactive, and apparent power in a system.

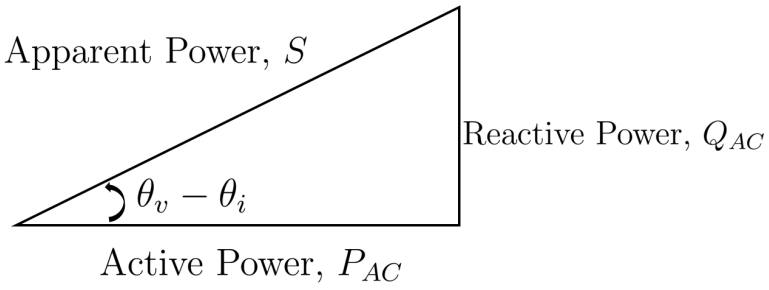

Figure 3.11: The Triangle of Power.

The final leg of the power triangle is the reactive power Q_{AC}, and is used as a modeling tool to describe the effect of the inductors and capacitors on a load. In an AC system, current and voltage are always changing which causes voltage and current to always be flowing across inductors and capacitors. The product of this current and voltage over these components would indicate that power is being lost. However, careful examination will show that this power is actually oscillating in nature. That is, it describes the second component of the instantaneous power relation from equation 3.6. Ideal inductors and capacitors are referred to as *loseless components*, in that they do no work. Their presence changes the distribution of power in a system, and is represented by Q_{AC}. Since P_{AC}, Q_{AC}, and S relate to legs of the triangle of power, the following relationship can be obtained:

$$S = P_{AC} + jQ_{AC}$$

$$S^2 = P_{AC}^2 + Q_{AC}^2 \tag{3.15}$$

where j is the complex quantity $\sqrt{-1}$, which is useful for determining the amount of reactive load in a circuit. Since voltage and current can be monitored, both the active and apparent power can be recorded by:

$$Q_{AC} = \sqrt{(I_{rms}V_{rms})^2 - (\frac{1}{T}\int_0^T v(t)i(t)dt)^2} = I_{rms}V_{rms}\sin(\theta_v - \theta_i) \tag{3.16}$$

The following relations were derived in the context of a single phase, sinusoidal voltage and current waveforms. The basic ideas of active, reactive, and apparent power hold even when the waveform is non-sinusoidal. The only term which is altered significantly is the definition of the power factor. The power factor still relates the lagging or leading of the voltage signal to the current signal, but is no longer defined in this manner when the signals are sinusoidal. Instead, the general definition for power factor, stemming from the triangle of power, as the ratio of active to apparent power must be used:

$$pf = \begin{cases} \frac{P_{AC}}{S} = \cos(\theta_v - \theta_i) & \text{for sinusoidal voltage and current} \\ \frac{P_{AC}}{S} \neq \cos(\theta_v - \theta_i) & \text{for non-sinusoidal voltage or current} \end{cases}$$

With the basics covered, these ideas can be expanded to include circuits with multiple phases and eventually brushless motors.

3.5.2 Polyphase AC Power Relations

The study of AC power analysis becomes more interesting when additional phases are added to the circuit. Typical power generation and distribution happens

using 3 phase electricity, as it will be shown in the following sections that the transfer of 3 phase power is constant. This is in stark contrast to the single phase system where power contains both a constant and oscillating term, equation 3.6. The remainder of this section discusses polyphase circuits, and the concepts can be applied to either sinusoidal or non-sinusoidal waveforms. Three phase non-sinusoidal waveforms are of importance for a brushless motors, as the voltage and current waveforms are trapezoidal and rectangular, respectively.

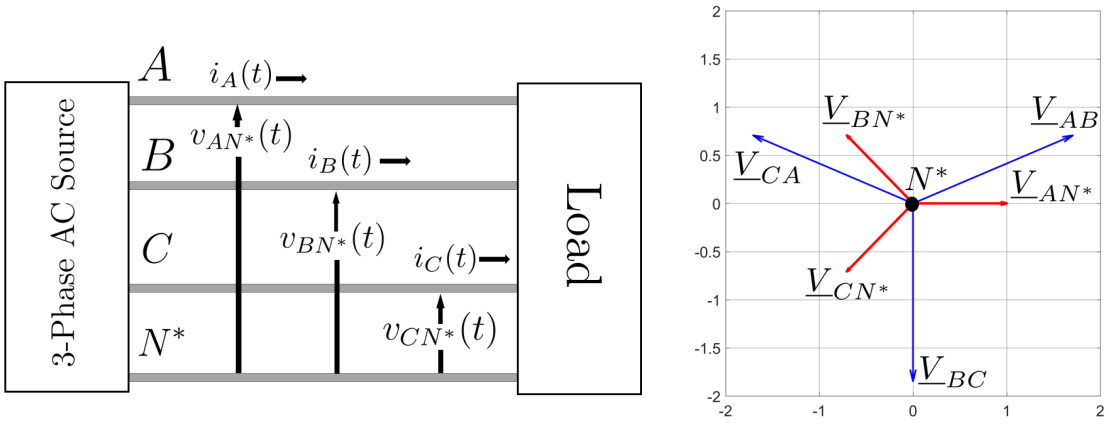

Figure 3.12: Left: Generic 3-phase AC system. Right: Phasor diagram for a 3 phase system. Each waveform is 120^o electrical degrees apart.

In an ideal three phase system, the voltage waveforms are 120^o apart from one another and is referred to as a *balanced* system. For a sinusoidal voltage and current, these waveforms take the following form:

$$v_{AN^*}(t) = V_{pk}\cos(\omega_e t + \theta_v) \tag{3.17}$$

$$v(t)_{BN^*}(t) = V_{pk}\cos(\omega_e t + \theta_v - 2\pi/3) \tag{3.18}$$

$$v(t)_{CN^*}(t) = V_{pk}\cos(\omega_e t + \theta_v - 4\pi/3) \tag{3.19}$$

$$i_A(t) = I_{pk}\cos(\omega_e t + \theta_i) \tag{3.20}$$

$$i_B(t) = I_{pk}\cos(\omega_e t + \theta_i - 2\pi/3) \tag{3.21}$$

$$i_C(t) = I_{pk}\cos(\omega_e t + \theta_i - 4\pi/3) \tag{3.22}$$

The goal is now to define the rms values for polyphase voltages and current, as this will be necessary when describing the motor model in Chapter 4. From figure 3.12, and the definition of a balanced load, the following relationship can be drawn [21]:

$$v_{AN^*}(t) + v_{BN^*}(t) + v_{CN^*}(t) = 0 \tag{3.23}$$

Which is equivalent to its phaser representation:

$$\underline{V}_{AN^*} + \underline{V}_{BN^*} + \underline{V}_{CN^*} = 0$$

When discussing polyphase circuits, it is important to bookmark the voltages. A voltage is described as a difference in a potential field, which means both the starting and final potentials must be taken into account. A *phase* voltage is a voltage measured with respect to the neutral point of the AC system (ex. v_{AN^*}, figure 3.12), whereas a $line-to-line$ voltage is a voltage from one phase measured with respect to another phase (ex. v_{AC}, figure 3.15). A neutral point N^* acts like an 'AC ground' for the system, and is used as a common measuring points for all phases.

This is similar to the DC ground, which is used as a common reference point for DC systems. It is important to note that the DC ground and the neutral point do not share the same voltage, and have a time varying value of $v_{N^*N}(t)$ from one another. A safe assumption is that all 3 phases have the same peak value and thus has the same rms value:

$$V_{AN^*} = V_{BN^*} = V_{CN^*} = V_{ph,rms} \tag{3.24}$$

The three phases are identical, only having been rotated 120^o electrical degrees from one another. With this in mind, voltages can be treated like positional vectors or phasers. Assuming a balanced voltage set, the line-to-line voltages can be calculated using [22, 26]:

$$\underline{V_{AB}} = \underline{V_{AN^*}} - \underline{V_{BN^*}}$$

$$\underline{V_{AB}} = V_{AN^*}[1 + j0] - V_{BN^*}[-\frac{1}{2} - j\frac{\sqrt{3}}{2}]$$

$$\underline{V_{AB}} = V[\frac{3}{2} + j\frac{\sqrt{3}}{2}]$$

$$V_{LL,rms} = \sqrt{3}V_{ph,rms} \tag{3.25}$$

which is also shown in figure 3.12. Circuit analysis depends on defining a complete circuit, and for 3-phase systems there are two ways to connect the circuit together.

AC circuits are connected in either a delta (Δ) or wye (Y) connection, depending on the power application. The derivation for the active power and apparent power depend upon the configuration.

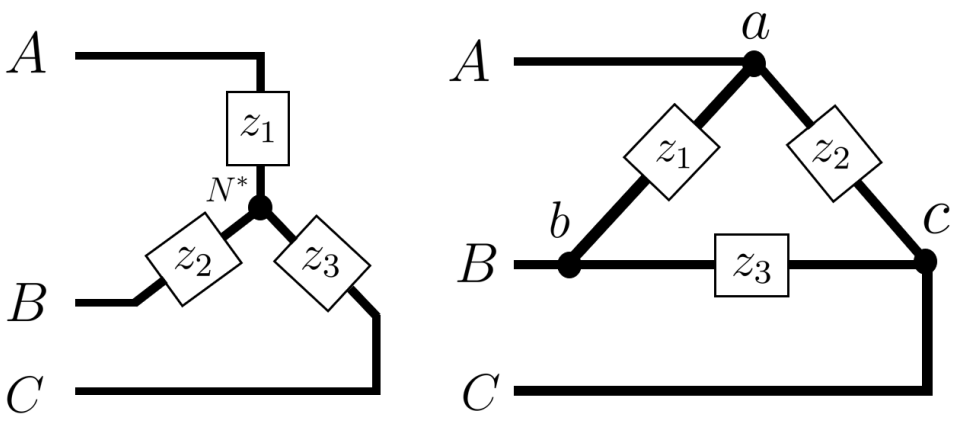

Figure 3.13: Y and Δ connected 3 phase circuits.

Y connected circuits have each input line connected together at a central point, referred to as the neutral point N^*. The Δ connection has each leg connected to the other 2 in a triangular formulation. The most notable difference between the 2 configurations is that a Δ connection does not have a neutral point.

When studying BLDC motors, the type of connection configuration can be thought of as the gearing. Y connected motors are favored for low speed/high torque applications, whereas the Δ motors are favored for high speed low torque conditions [29]. The relation for this can be stated as:

$$M_Y = \sqrt{3} M_\Delta \tag{3.26}$$

$$\omega_Y = \frac{1}{\sqrt{3}} \omega_\Delta \tag{3.27}$$

In fact, since most research and commercial electric aircraft use high RPM motors for propulsion, the majority of the commercial off the shelf products are Δ wound motors.

For an AC system, there are three principal ways of recording power in a 3 phase system: the 1-wattmeter, 2-wattmeter, and 3-wattmeter method [22, 30–32]. A wattmeter is a device that measures the voltage differential between two points and the current passing through the device. This is done for a DC system by measuring the DC current I_{DC} and DC voltage V_{DC}, with the DC power being simply $P_{DC} = V_{DC}I_{DC}$. With a DC system, the voltage differential between "high" and "low" volts makes sense, but how can this be applied to a polyphase time-varying system? To answer this, we shall first consider the 1-wattmeter method.

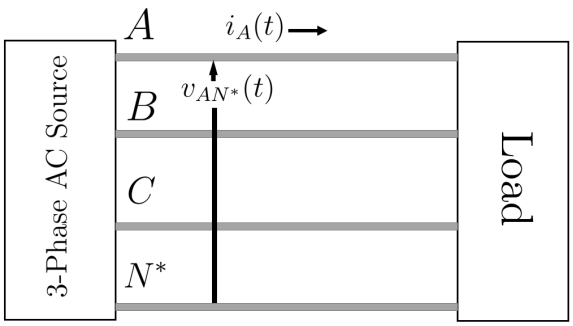

Figure 3.14: 1-wattmeter method for AC power measurement.

The 1-wattmeter method assumes that the neutral point of the system can be accessed. With this, then the definition of three phase power in the AC system is:

$$p_{inst} = p_A + p_B + p_C \tag{3.28}$$

$$p_A = v_{AN^*}(t)i_A(t) \tag{3.29}$$

$$p_B = v_{BN^*}(t)i_B(t) \tag{3.30}$$

$$p_C = v_{CN^*}(t)i_C(t) \tag{3.31}$$

$$P_{AC} = \frac{1}{T}\int_0^T p_{inst} \tag{3.32}$$

The 1-wattmeter method also assumes that each phase of the circuit carries the same power and so $p_A = p_B = p_C$. This allows for the following simplification:

$$p_{inst} = 3p_A = 3v_{AN^*}(t)i_A(t) \tag{3.33}$$

$$P_{AC} = \frac{3}{T}\int_0^T v_{AN^*}(t)i_A(t)dt \tag{3.34}$$

Which is simply the result of 3 times the single phase power, found from equation 3.7. An advantage of this method is that it is easy to implement, as only one phase voltage and current must be recorded. The disadvantage is that a neutral wire must be available to access, which is not possible as that point is either inside the motor (Y-wound motors) or does not exist (Δ-wound motors). To circumvent this, additional meters are required.

An alternative way to measure 3-phase power is with the 3-wattmeter method, shown in figure 3.12. Here the phase voltages are measured with respect to neutral, and each line current recorded. The instantaneous power is the $v(t)i(t)$ for each phase. Using equation 3.28 and the expressions for 3 phase voltage and current, equations 3.17 to 3.22, an expression for the instantaneous power using 3-wattmeters can be deduced. Combining terms and using trigonometric identities allows for the following expression for instantaneous power [22]:

$$p_{inst} = 3\frac{V_{pk}I_{pk}}{2}\cos(\theta_v - \theta_i) = constant \tag{3.35}$$

Here, for a 3 phase system the *instantaneous power* is constant, whereas for a single phase system it contained an oscillating component. Also note that the 3 phase active power $P_{AC,3p}$ is simply 3 times the single phase power $P_{AC,1p}$:

$$P_{AC,3p} = 3P_{AC,1p}$$

Power factor returns for 3 phase systems, and has the same meaning as it did for single phase systems. Recall, one wants to increase power factor for greater power transmission.

As with the 1-wattmeter method, the disadvantage of the 3-wattmeter method is that a neutral wire must be present. The major difficulty when dealing with 3 phase systems is that, in most cases, is that accessing the neutral point of the system is not possible. Why not measure the phases relative to the DC ground and repeat the analysis with v_{AN}? This is because there is some voltage differential $v_{N^*N}(t)$ between the DC ground and the neutral point. To calculate the 3 phase power when no neutral is available, the 2-wattmeter method is used.

3.5.3 2-Wattmeter Proof for Y-Circuits

Proof of the 2-wattmeter method depends upon the connection scheme, and so first the Y connection is analyzed. The goal is to calculate active and apparent power in this configuration, and then compare the results for a Δ connection in section 3.5.4 To begin, consider the Y connected circuit shown below:

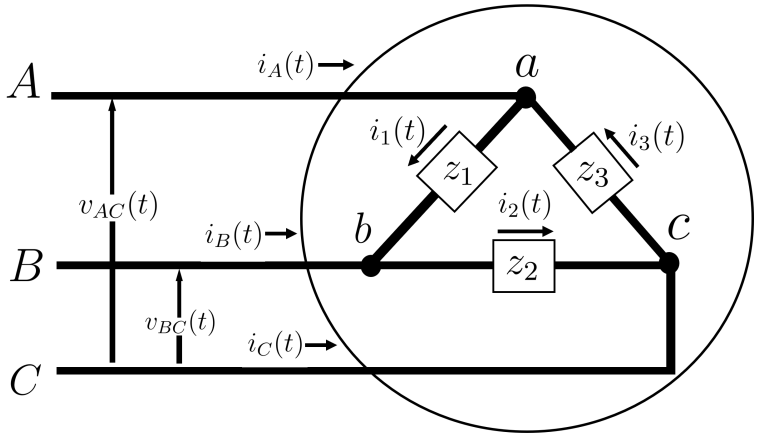

Figure 3.15: Y-connected circuit.

The AC power in a 3-phase circuit is given by equation 3.28, and is stated here again:

$$p_{inst} = v_{AN^*}(t)i_A(t) + v_{BN^*}(t)i_B(t) + v_{CN^*}(t)i_C(t) \tag{3.36}$$

In a Y configuration, the sum of currents at the neutral point N^* is 0 by Kirchoff's voltage law [22]:

$$i_A(t) + i_B(t) + i_C(t) = 0 \tag{3.37}$$

In this method, only $i_A(t)$ and $i_B(t)$ are measured, meaning the third current $i_C(t)$ can be deduced by:

$$i_C(t) = -i_A(t) - i_B(t) \tag{3.38}$$

Plugging equation 3.38 into equation 3.37 yields:

$$p_{inst,Y} = v_{AN^*}(t)i_A(t) + v_{BN^*}(t)i_B(t) + v_{CN^*}(t)[-i_A(t) - i_B(t)]$$

$$p_{inst,Y} = [v_{AN^*}(t) - v_{CN^*}(t)]i_A(t) + [v_{BN^*}(t) - v_{CN^*}(t)]i_C(t) \tag{3.39}$$

The advantage of the 2-wattmeter method is by referencing voltage differentials with respect to another phase, and taking advantage of equation 3.37, only 2-wattmeters are required. Both voltages for line A and B are referenced with respect to line C.

$$v_{AC}(t) = v_{AN^*}(t) - v_{CN^*}(t) \tag{3.40}$$

$$v_{BC}(t) = v_{BN^*}(t) - v_{CN^*}(t) \tag{3.41}$$

Plugging into equation 3.39 yields:

$$p_{inst,Y} = v_{AC}(t)i_A(t) + v_{BC}(t)i_B(t) \tag{3.42}$$

Note that because the same circuit was analyzed for the 3-wattmeter method, equation 3.35 and equation 3.39 are equal to one another, such that:

$$p_{inst} = v_{AC}(t)i_A(t) + v_{BC}(t)i_B(t) = 3\frac{V_{pk}I_{pk}}{2}\cos(\theta_v - \theta_i) = constant \tag{3.43}$$

indicating that AC power transmission is constant with the 2-wattmeter method as well. Integrating over a number of cycles yields the AC power for the Y-configuration:

$$P_{AC,Y} = \frac{1}{T}\int_0^T (v_{AC}(t)i_A(t) + v_{BC}(t)i_B(t))dt \tag{3.44}$$

To evaluate the power factor, the total apparent power in all three phases must

be evaluated. Recall that the power factor is the ratio of the active power to the apparent power in the circuit, and is expressed in equation 3.14.

The apparent power for a single phase AC circuit is given by equation 3.13, and must be expanded to include 3 phase circuits. Just like instantaneous power, apparent power is merely the sum of all single phase apparent powers:

$$S = S_A + S_B + S_C \tag{3.45}$$

with

$$S_A = rms\{v_{AN^*}(t)\}rms\{i_A(t)\} = V_{AN^*}I_A \tag{3.46}$$

$$S_B = V_{BN^*}I_B \tag{3.47}$$

$$S_C = V_{CN^*}I_C \tag{3.48}$$

Assume a balance loading condition, such that:

$$V_{AN^*} = V_{BN^*} = V_{CN^*} = V_{ph} = \frac{1}{\sqrt{3}}V_{LL,rms} \tag{3.49}$$

where the rightmost equation is given by equation 3.25. By definition, V_{AC} and V_{BC} are line-to-line rms voltages $V_{LL,rms}$, wheras V_{AN^*} and V_{BN^*} are rms phase voltages $V_{ph,rms}$. The line currents are all balanced as well, meaning:

$$I_A = I_B = I_C = I_{L,rms} \tag{3.50}$$

with $I_{L,rms}$ meaning rms line current. Plugging into equation 3.45 yields:

$$S = V_{AN^*}I_A + V_{BN^*}I_B + V_{CN^*}I_C = V_{ph,rms}(I_A + I_B + I_C)$$

$$S = 3V_{ph,rms}I_{L,rms} = 3(\frac{1}{\sqrt{3}}V_{LL,rms})I_{L,rms}$$

$$S = \sqrt{3}V_{LL,rms}I_{L,rms} \tag{3.51}$$

In reality, both line-to-line voltages V_{AC} and V_{BC} are not perfectly equal, and thus the average from the recorded values of S_A and S_B is used to compute the total apparent power:

$$S_Y = \frac{\sqrt{3}}{2}(V_{AC}I_A + V_{BC}I_B) \tag{3.52}$$

The ratio of equation 3.44 to equation 3.52 gives the power factor pf for the system:

$$pf_Y = \frac{P_{AC,Y}}{S_Y}$$

With the active and apparent power deduced for the Y configuration, the Δ configuration can be analyzed.

3.5.4 2-Wattmeter Proof for Δ-Circuits

Like the Y connection, the objective for the Δ connection analysis is to evaluate expressions for the active power, apparent power, and power factor. A Δ connected circuit is shown below:

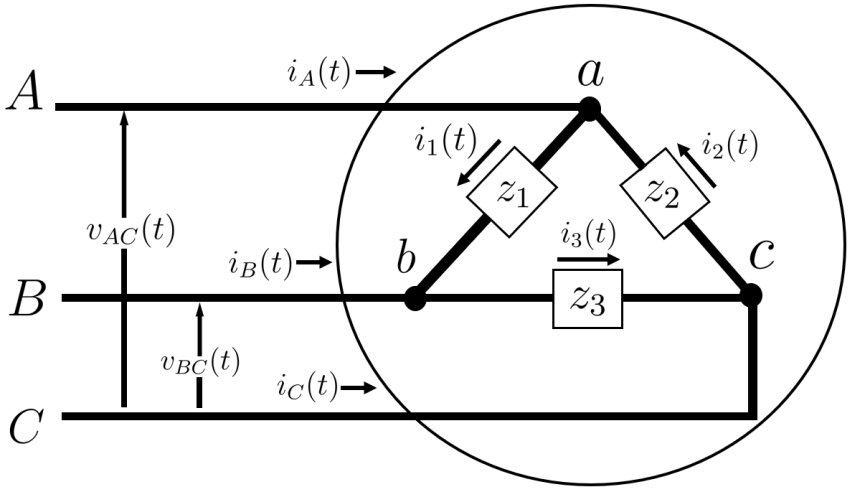

Figure 3.16: Δ-connected circuit.

The key difference between a Δ circuit and a Y circuit is that a Δ circuit does not have a neutral point N^*. The concept of a phase becomes nebulous, as there is no common reference point for the AC system. Instead, the voltages must be referenced to one another. For a Δ connection [22, 26, 32], the instantaneous power in the circuit is:

$$p_{inst} = v_{ab}(t)i_1(t) + v_{bc}(t)i_2(t) + v_{ca}(t)i_3(t) \tag{3.53}$$

where points a, b, and c represent different vertices of the Δ triangle. Kirkoff's node

law at points a, b, and c yield the following current relations:

$$i_A(t) = i_1(t) - i_3(t) \quad @ \quad point \quad a \tag{3.54}$$

$$i_B(t) = i_2(t) - i_1(t) \quad @ \quad point \quad b \tag{3.55}$$

$$i_C(t) = i_3(t) - i_2(t) \quad @ \quad point \quad c \tag{3.56}$$

It can also be stated that the voltages of A and a, B and b, as well as C and c are the same since they are physically connected. For a balanced, 3 phase Δ connection the following voltage relation can be stated:

$$v_{AB}(t) + v_{BC}(t) + v_{CA}(t) = 0 \tag{3.57}$$

which is pictorial represented in figure 3.12. With this, one can deduce:

$$v_{AB}(t) = -v_{BC}(t) - v_{CA}(t)$$

$$v_{AB}(t) = -v_{BC}(t) + v_{AC}(t) \tag{3.58}$$

From this, equation 3.53 can be expanded to:

$$p_{inst,\Delta} = [-v_{BC}(t) + v_{AC}(t)]i_1(t) + v_{BC}(t)i_2(t) + v_{CA}(t)i_3(t) \tag{3.59}$$

$$= -v_{BC}(t)i_1(t) + v_{AC}(t)i_1(t) + v_{BC}(t)i_2(t) - v_{AC}(t)i_3(t)$$

$$= v_{AC}(t)[i_1(t) - i_3(t)] + v_{BC}(t)[i_2(t) - i_1(t)]$$

$$p_{inst,\Delta} = v_{AC}(t)i_A(t) + v_{BC}(t)i_B(t) \tag{3.60}$$

$$P_{AC,\Delta} = \frac{1}{T}\int_0^T (v_{AC}(t)i_A(t) + v_{BC}(t)i_B(t))dt \tag{3.61}$$

which is the same as active power as the Y connection, equation 3.44.

The expression for apparent power is made on similar grounds as the instantaneous power. The total apparent power of the system is the sum of all S for each leg of the Δ:

$$S_\Delta = V_{ab}I_1 + V_{bc}I_2 + V_{ca}I_3 \tag{3.62}$$

Note that V_{ab}, V_{bc}, and V_{ca} are the line-to-line rms voltages and can be replaced with $V_{AB} = V_{BC} = V_{CA} = V_{AC} = V_{LL,rms}$. A relationship between the rms current and line currents can be found via an application of Kickoff's voltage law around the different legs of the Δ. The results are [22, 32]:

$$I_1 = I_2 = I_3 = I_\Delta = \frac{1}{\sqrt{3}}I_{L,rms} \tag{3.63}$$

where $I_{L,rms}$ represents the rms current in each line ($I_{L,rms} = I_A = I_B = I_C$). Thus the following relation can be found:

$$S_\Delta = V_{LL}(I_1 + I_2 + I_3) = 3V_{LL,rms}I_\Delta$$

$$S_\Delta = 3V_{LL,rms}(\frac{1}{\sqrt{3}}I_{L,rms})$$

$$S_\Delta = \sqrt{3} V_{LL,rms} I_{L,rms} \tag{3.64}$$

In reality, both line-to-line voltages V_{AC} and V_{BC} are not perfectly equal, and thus are averaged from the recorded values of S_A and S_B is used to compute the total apparent power:

$$S_\Delta = \frac{\sqrt{3}}{2}(V_{AC} I_A + V_{BC} I_B) \tag{3.65}$$

which is the same relation for the Y connection, equation 3.52.

Regardless of the connection scheme, the expressions for active power, apparent power, and power factor are the same. The strength of the 2-wattmeter method is that it does not require a neutral wire and is invariant of the connection type. These results can be summarized as:

$$P_{AC} = P_{AC,Y} = P_{AC,\Delta} = \frac{1}{T}\int_0^T (v_{AC}(t) i_A(t) + v_{BC}(t) i_B(t)) dt \tag{3.66}$$

$$S = S_Y = S_\Delta = \sqrt{3} V_{LL,rms} I_L \tag{3.67}$$

$$pf = pf_Y = pf_\Delta = \frac{P_{AC}}{S} \tag{3.68}$$

These results show another important proerty of Y and Δ circuits: that they can be transformed into one another. This transformation can write a Δ connection as an equivalent Y connection [21, 22, 26, 32], shown in figure 3.17. This is useful for motors, because this means a Δ connected motor, which has no neutral point N^*, can be represented as an equivalent Y circuit containing a neutral point N^*. The phase waveforms of a BLDC motor are most naturally defined in reference to

a neutral point, and are typically expressed in that manner.

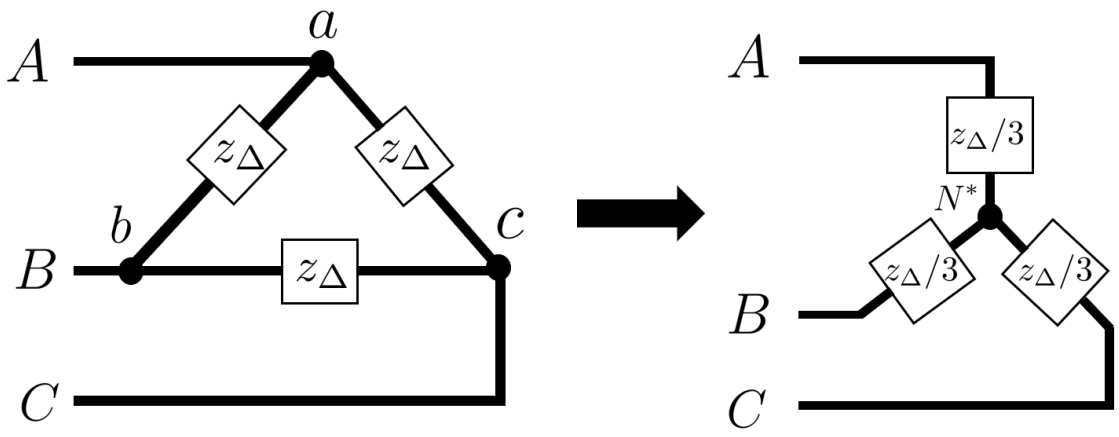

Figure 3.17: Conversion of a Δ connected circuit to an equivalent Y connected circuit.

To transform a 3 phase connected circuit into its evil twin, the following relation is used [26]:

$$z_{Y,1} = z_{Y,2} = z_{Y,3} = z_Y$$

$$z_{\Delta,1} = z_{\Delta,2} = z_{\Delta,3} = z_\Delta$$

$$z_Y = \frac{1}{3} z_\Delta \tag{3.69}$$

where z_Y and z_Δ are the impedances of each leg of the circuit. In the event that the impedances for each leg of the connection are not equal to one another, additional relations are used and are found in [26]. However, most models assume balanced voltages and impedances and therefore equation 3.69 is used.

Even though most commercial BLDC motors are Δ connected motors [29], the theory describing BLDC motors is typically given for Y connected motors. Y connected motors, and circuits, are less complicated to analyze, and contain a neutral

point, which is a logical point to reference phase voltages. However, it is important to remember that 3 phase active and apparent power are equal to one another, and hence makes this transformation valid.

Now that the proofs are completed, the system to record the performance of the AC system can be discussed.

3.5.5 AC Power Analyzer

The AC power analyzer uses the 2-wattmeter method for determining both the real and apparent power entering the motor. Because the DAQ had a 10 V limit, two separate setups were used to study the motors at different voltages.

Two types of AC power analyzers were employed to study the motors and ESCs; a low voltage ($V_{DC} < 10\ V$) and a high voltage setup ($10\ V < V_{DC} < 15\ V$). The NI-USB-6251 and SC-2345 DAQs used in the setups had a maximum voltage rating of 10 V, and so recording voltages higher than $10\ V$ required special attention. First the low voltage setup shall be described and then the high voltage setup.

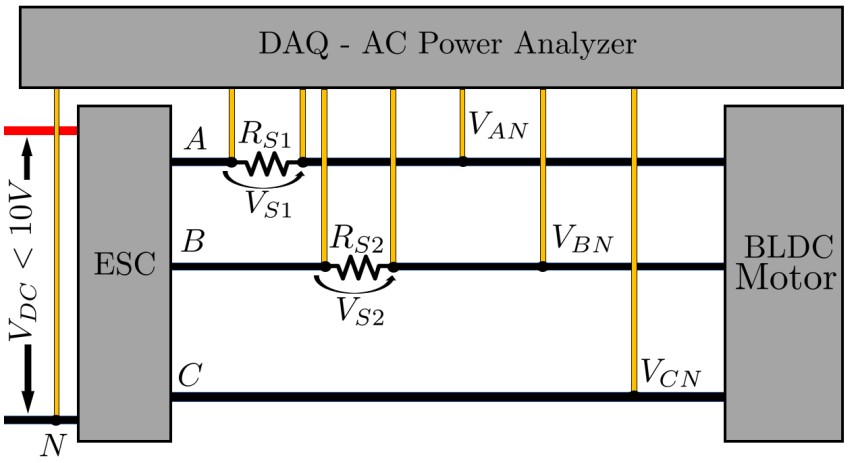

Figure 3.18: AC Power Analyzer connection scheme for $V_{DC} < 10\ V$.

The low voltage setup was the first AC power analyzer developed, shown in figure 3.18. Phase voltages below the DAQ's 10 V rating were read directly into the DAQ. For current measurements, a shunt resistor method was used and operates by measuring the voltage drop across a small, high tolerance, resistor. In this case $R_S = 0.005\ \Omega$ with a tolerance of 0.25% shown in figure 3.19. Once the voltage and resistance are known, ohms law is used to determine the current $i(t) = v(t)/R_S$. Accuracy of this measurement depends on two things: the accuracy of the resistor's known value, and the accuracy of the voltage measurement. The shunt resistor was shipped with a calibration certificate, indicating the calibrated resistor value and the test date.

Figure 3.19: 0.005 Ω shunt resistor and calibration certificate, used to sense current in the low voltage AC power analyzer.

The NI-USB-6251 DAQ has a high accuracy feature that allowed for all 16-bits of the DAQ to be focused into a specific region, which is ideal for differential voltage measurements. Accurate voltage measurements across the shunt resistors was accomplished by ensuring the voltage differential was less than $+/-100$ mV. This high-accuracy mode was sufficient for recording differential voltages of the

shunt resistor accurately, with the cost of running the DAQ channel in differential mode. This meant that 2 additional voltage measurements, 1 for line A and 1 for line B, were required to accurately measure the line currents, reducing the maximum read rate of the system to 250 kHz.

A high voltage setup was used to study systems between 10 V and 15 V. The 10 V lower limit comes from the DAQ's hardware upper limit and the 15 V comes from the maximum voltage of the DC power supply. In the dynamometer's current state, the setup employs two +/- 30 A bi-directional non-invasive current sensors (NICS) to measure the current pass through lines A and B. The voltage of each phase must be reduced by a voltage divider before being read into the DAQ.

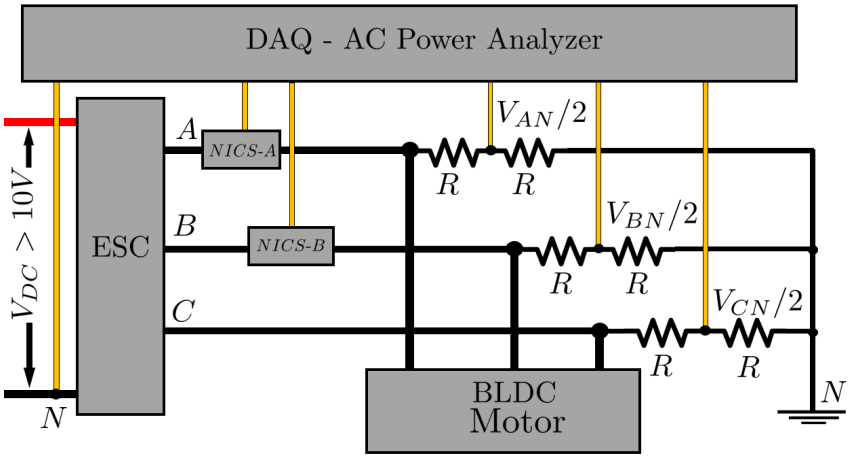

Figure 3.20: AC Power Analyzer connection scheme for $V_{DC} > 10\ V$.

Two 500 Ω resistors are used in series to drop the voltage of the phases to within the 10 V range of the DAQ. The estimate of power loss from the 3 voltage dividers at maximum voltage is 0.04 W, which is negligible compared to the 200 W DC input power. Two equally sized resistors means the phase voltage is dropped by half, meaning the sensed value $V_{AN,sens}$ must be multiplied by 2 to arrive at

the correct phase voltage V_{AN}. The bi-directional current sensors output an analog voltage between 0-5 V, proportional to the amount of current, similar to the DC current sensor described in section 3.3. The supplier provided the following relation between output voltage of the sensor $v_{NICS}(t)$ and current:

$$i(t) = \frac{1}{0.066}[v_{NICS}(t) - 2.5]$$

The sensor is centered at 2.5 V, meaning that if $V_{NCIS-A} > 2.5$ V current is flowing in the positive direction. If $V_{NCIS-A} < 2.5$ V, then current is flowing in the opposite direction. A key difference between this sensor and the shunt resistor is that it naturally contains a small amount of low pass filtering to the signals, with a cutoff frequency of 90kHz. This could be problematic with high pole count motors spinning at high RPM. Additionally the higher harmonic content of the current signal is attenuated by this filter.

The presence of a low pass filter in the non-invasive current sensor means that the AC current signals will be attenuated. To compensate, less filtering of the signals is done in post processing. A noticeable drop in the power factor is seen when studying motors at higher voltages, which is a result of this filtering. Additionally, the sensed AC power could be slightly lower than its actual value as a result of this sensor. For future setups, it is required that the DAQs are sized to handle the DC operating voltage so that the more accurate shunt method can be used exclusively.

To ensure that both setups are giving the same results for a given test, the same motor, ESC, and voltage were tested on both the low-voltage and high-voltage setup.

An EMAX 935 KV motor and a MultiStar 30A ESC were tested at $V_{DC} = 7.2V$. Results of the calibration test are shown on the next page in figure 3.21

The results of the calibration test show that the two setups are in agreement and produce the same results. Minor deviations in the x-crossing point of the lines are related to the fact that during the test not all throttle settings are the same (ex 49% vs 51% throttle). The important parameter is the slope of each line relative to the other setup, which seem to agree well. This test also determined the accuracy of the bi-directional current sensors, as it gave results that agreeme with the low voltage setup. However, when testing additional motors at higher voltages and faster RPMs, it was noticed that the noninvasive current sensor's filtering did have an impact on the recorded AC power values.

With the setup and power analyzers covered, we proceed to modeling the system in Chapter 4 and experiential results in Chapter 5.

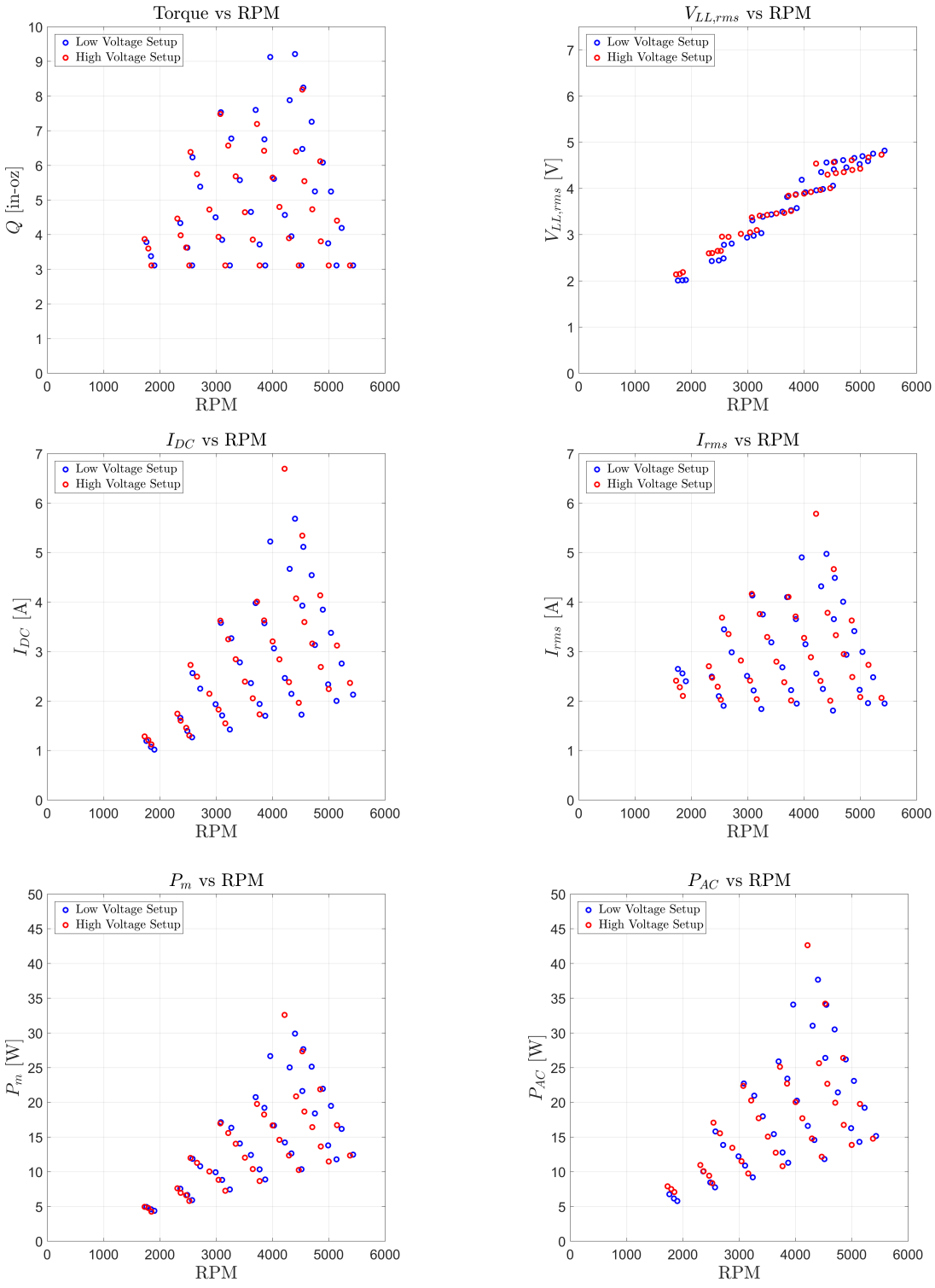

Figure 3.21: Calibration test for same conditions on both low and high voltage setup.

Chapter 4: BLDC Motor and ESC Modeling

A first principles based analytical model will be derived from the experimental results to represent BLDC motors and ESCs. The motor theory shall be presented as it was discovered, originally studying systems at $V_{DC} = 7.2$ V and then later expanded to cover higher voltage systems. Primary objectives for this model are:

1. Determination of an equivalent AC motor model, which relates the inputs $V_{LL,rms}$, I_{rms}, and T_R to the both the ESC's and BLDC motor's performance.
2. Prediction of the torque-RPM curve and mechanical output power.
3. Required AC power to run the motor.
4. ESC's DC to AC power conversion characteristics, ending with the steady state DC current draw out of the DC power supply.

First the BLDC motor shall be modeled in section 4.1, which describes the equivalent circuit model for the motor alone. Secondly, the ESC is modeled in section 4.2, with an emphasis being placed on MOSFET modeling and power transformation relations. The BLDC motor relies on an enhanced version of the DC motor model, presented in Chapter 2. However, in the BLDC model of section 4.1, the relevant motor parameters have been augmented into an equivalent AC circuit. For the ESC

model, a literature review of MOSFETs is given to identify the types of power losses that occur within an ESC.

Alternative models for BLDC motors exist, however, they typically are used with a time domain analysis [33, 34] and can include even a rotating mutual phase inductance [35]. This work seeks to model the steady state behavior of ESCs and BLDC motors, as they are determined with the dynamometer. A unique equivalent circuit model is to represent both the ESC and the BLDC motor.

By modeling the ESCs and the BLDC motors separately, a better understanding of power loss can be gained, with the goal of identifying unique parameters to describe different ESCs and BLDC motors. For example, in the DC model of Chapter 2, the ESC and BLDC motor are lumped into a single black box model. If the ESC was replaced with a different ESC, the system would have to be re-characterized before use. Characterizing the ESC and the BLDC motor separately allows for a more programmatic and discipled approach to aircraft design.

4.1 Brushless DC Motors

Brushless DC motors transform AC electrical power into mechanical power, and this section models the electromechanical interaction by using an equivalent circuit approach. The underlying equations for calculating AC power from instantaneous voltage and current measurements was presented in section 3.5 and are applied to the trapezoidal and rectangular waveforms of a BLDC motor. During motor testing, the active power as well as other key parameters related to AC power

are recorded:

$$V_{LL,rms} = \frac{V_{AB} + V_{BC} + V_{CA}}{3} \tag{4.1}$$

$$I_{rms} = \frac{I_A + I_B + I_C}{3}$$

$$I_{rms} = \frac{I_A + I_B}{2} \tag{4.2}$$

Equation 4.2 stems from the fact that only I_A and I_B are recorded for the 2-wattmeter method, and $I_C = I_A = I_B = I_{L,rms}$. It will be shown that $V_{LL,rms}$ maps to the motor's mechanical rotation ω, whereas I_{rms} relates to the motor's output torque. Both of these observations are consistent with the model presented in Chapter 2. By referring to the DC motor model of Chapter 2, this serves as a "sanity check", to verify that predictions with the presented AC motor model agree with previous work. An important distinction between the DC and AC motor model for BLDC motors is the evaluation of AC power in a 3-phase system. In the DC model, power to run the ESC and motor system is only DC, whereas in the presented AC motor model, only AC power is considered to run the motor. To start, let us consider evaluating AC power directly from the rms values of $V_{LL,rms}$ and I_{rms}, which requires evaluating the rms of the trapezoidal and rectangular waveforms.

4.1.1 Waveform RMS Evaluation

Waveforms entering a BLDC motor are time varying in nature, and are shown in figure 4.1. The derivation of the AC power entering a BLDC is built upon the following assumptions:

1. The voltage waveform is trapezoidal [12, 13, 15]

2. The current waveforms are rectangular [12, 13, 15]

3. Power, for any waveforms, can be calculated using the 2 wattmeter method [22]

By leveraging the fact that the exact waveform shapes are known, the AC power can be calculated from recorded rms values for $V_{LL,rms}$ and I_{rms}. Rms values are critical to the AC motor model as they will replace the DC values in the model from Chapter 2.

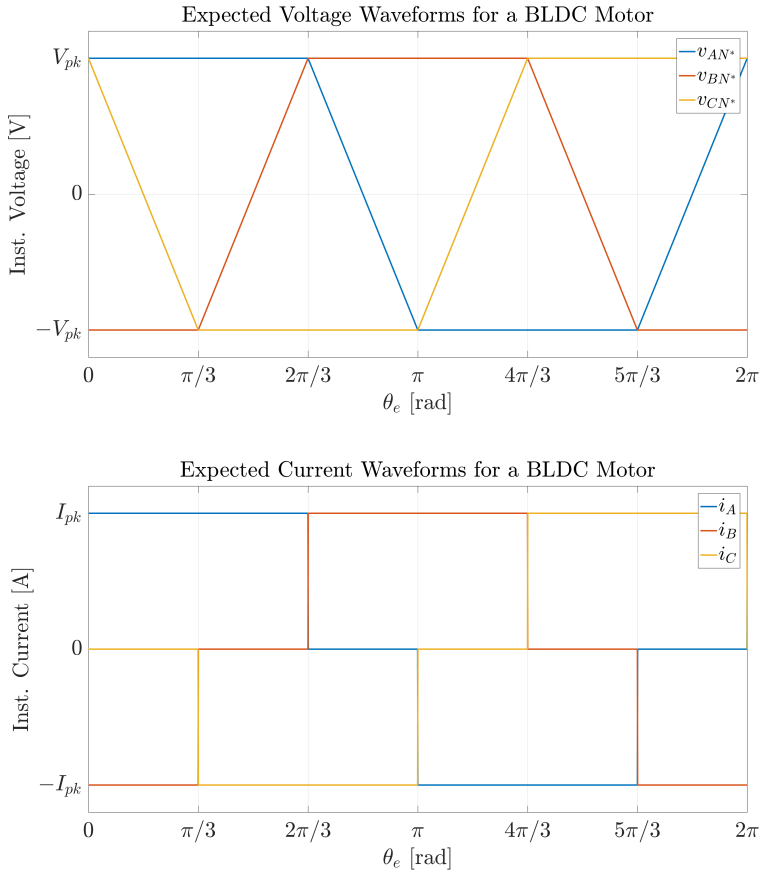

Figure 4.1: Expected voltage and current waveforms entering a BLDC motor.

A distinction must be made: during experiments AC power is calculated using

the 2-wattmeter method directly from time varying AC signals (ex. $v_{AN}(t)$, $i_B(t)$, *etc.*), whereas in the AC motor model predicts $V_{LL,rms}$ and I_{rms} values to determine AC power. It will be shown that determining P_{AC} from predicted $V_{LL,rms}$ and I_{rms} values is accomplished with the 2-wattmeter method as well. This relies upon subtracting waveforms from one another to arrive at an equation for the total instantaneous power that is similar to equation 3.66.

From figure 4.1, it can be seen that the waveforms oscillate back and forth between a peak voltage V_{pk} and a peak current I_{pk} value. To determine the AC power in these waveforms, first the waveforms for v_{AN^*}, v_{BN^*}, and v_{CN^*} will be mathematically defined and then subtracted from one another to find v_{AC} and v_{BC}. In a similar manner, the current waveforms i_A and i_B are explicity stated and then used to compute the AC power in the signal via the 2-wattmeter method.

All voltage waveforms follow the same trend, but are shifted by $2\pi/3$ radians from one another. Inspection of waveform v_{AN^*} from figure 4.1 shows the following intervals:

1. $+V_{pk}$ for $2\pi/3$ radians
2. A decreasing transition from $+V_{pk}$ to $-V_{pk}$ for $\pi/3$ radians
3. $-V_{pk}$ for $2\pi/3$ radians
4. An increasing transition from $-V_{pk}$ to $+V_{pk}$ for $\pi/3$ radians

With this, the piecewise waveform function for v_{AN^*} can be mathematically de-

scribed as:

$$v_{AN^*} = V_{pk} \begin{cases} 1 & \text{for } 0 \leq \theta_e < \pi/3 \\ 1 & \text{for } \pi/3 \leq \theta_e < 2\pi/3 \\ 5 - 6\theta_e/\pi & \text{for } 2\pi/3 \leq \theta_e < \pi \\ -1 & \text{for } \pi \leq \theta_e < 4\pi/3 \\ -1 & \text{for } 4\pi/3 \leq \theta_e < 5\pi/3 \\ 6\theta_e/\pi - 11 & \text{for } 5\pi/3 \leq \theta_e < 2\pi \end{cases} \tag{4.3}$$

Although there are only 4 unique regions, the waveform has been split into 6 regions in order to assist with determining v_{AC} and v_{BC}. Note that at the end of each 60^o interval, a commutation occurs and is shown in figures 2.25 to 2.29. A similar set of equations can be found for v_{BN^*} and v_{CN^*}, as they have the same waveform but are shifted $2\pi/3$ radians:

$$v_{BN^*} = V_{pk} \begin{cases} -1 & \text{for } 0 \leq \theta_e < \pi/3 \\ 6\theta_e/\pi - 3 & \text{for } \pi/3 \leq \theta_e < 2\pi/3 \\ 1 & \text{for } 2\pi/3 \leq \theta_e < \pi \\ 1 & \text{for } \pi \leq \theta_e < 4\pi/3 \\ 9 - 6\theta_e/\pi & \text{for } 4\pi/3 \leq \theta_e < 5\pi/3 \\ -1 & \text{for } 5\pi/3 \leq \theta_e < 2\pi \end{cases} \tag{4.4}$$

$$v_{CN^*} = V_{pk} \left\{ \begin{array}{ll} 1 - 6\theta_e/\pi & \text{for } 0 \leq \theta_e < \pi/3 \\ -1 & \text{for } \pi/3 \leq \theta_e < 2\pi/3 \\ -1 & \text{for } 2\pi/3 \leq \theta_e < \pi \\ 6\theta_e/\pi - 7 & \text{for } \pi \leq \theta_e < 4\pi/3 \\ 1 & \text{for } 4\pi/3 \leq \theta_e < 5\pi/3 \\ 1 & \text{for } 5\pi/3 \leq \theta_e < 2\pi \end{array} \right\} \tag{4.5}$$

Rms values for any piecewise waveform can be found using the following formula [21]:

$$V_{AN^*} = rms\{v_{AN^*}\} = \sqrt{\sum_{0}^{6} I_i^2} \tag{4.6}$$

$$I_i^2 = rms\{v_{AN^*}\}\Big|_{\theta_{e,i}}^{\theta_{e,i+1}} \tag{4.7}$$

where I_i represents the rms integral over the piecewise interval i from $\theta_{e,i}$ to $\theta_{e,i+1}$. Equation 4.6 states that sections of a piecewise function can be evaluated independently and then combined to find the total rms value over the entire interval. When evaluating V_{AN^*}, the expression can be simplified, after noting that only half of the waveform needs to be evaluated due to symmetry, and then multiplied by 2 to arrive at the final expression.

$$V_{AN^*} = \sqrt{I_1^2 + I_2^2 + I_3^2 + I_4^2 + I_5^2 + I_6^2}$$

$$I_1 = I_2 \quad I_1 = I_4 \quad I_2 = I_5 \quad I_3 = I_6$$

$$V_{AN^*} = \sqrt{4I_1^2 + 2I_3^2} \tag{4.8}$$

Likewise, integrals I_1, I_3 are evaluated using equation 3.9:

$$I_1^2 = \frac{1}{2\pi}\int_0^{\frac{\pi}{3}} V_{pk}^2 d\theta_e$$

$$I_1^2 = \frac{V_{pk}^2}{6} \tag{4.9}$$

$$I_3^2 = \frac{1}{2\pi}\int_{\frac{2\pi}{3}}^{\pi} V_{pk}^2 (5 - \frac{6\theta_e}{\pi})^2 d\theta_e$$

$$I_3^2 = \frac{V_{pk}^2}{18} \tag{4.10}$$

$$V_{AN^*} = \sqrt{4(\frac{V_{pk}^2}{6}) + 2(\frac{V_{pk}^2}{18})}$$

$$V_{AN^*} = V_{pk}\sqrt{\frac{7}{9}} \tag{4.11}$$

due to the balanced loading condition between $v_{AN^*},\ v_{BN^*}$, and v_{CN^*}, the rms values for all phase are equal to one another:

$$V_{AN^*} = V_{BN^*} = V_{CN^*} = V_{ph,rms} = V_{pk}\sqrt{\frac{7}{9}} \tag{4.12}$$

Note the similarities between trapezoidal and sinusodial waveform rms values:

$$V_{ph,rms} = \begin{cases} V_{pk}\frac{1}{\sqrt{2}} = 0.7071 V_{pk} & \text{for sinusodial waveforms} \\ V_{pk}\sqrt{\frac{7}{9}} = 0.8819 V_{pk} & \text{for trapezodial waveforms} \end{cases} \tag{4.13}$$

which is a 24.7% increase in rms value when compared to a sinusoidal waveform.

Line-to-line rms value $V_{LL,rms}$ can be found by evaluating the rms value of v_{AC}. However, first the analytical expression of v_{AC} is found by subracting equation 4.3 from equation 4.5:

$$v_{AC} = v_{AN^*} - v_{CN^*}$$

$$v_{AC} = V_{pk} \begin{Bmatrix} 1 \\ 1 \\ 5 - 6\theta_e/\pi \\ -1 \\ -1 \\ 6\theta_e/\pi - 11 \end{Bmatrix} - V_{pk} \begin{Bmatrix} 1 - 6\theta_e/\pi \\ -1 \\ -1 \\ 6\theta_e/\pi - 7 \\ 1 \\ 1 \end{Bmatrix}$$

$$v_{AC} = V_{pk} \begin{Bmatrix} 6\theta_e/\pi \\ 2 \\ 6 - 6\theta_e/\pi \\ 6 - 6\theta_e/\pi \\ -2 \\ 6\theta_e/\pi - 12 \end{Bmatrix} \tag{4.14}$$

By subracting two phase waveforms, the V_{pk}'s combine to yield $2V_{pk}$, but now occur with an interval of $\pi/3$ instead of $2\pi/3$. This can be visualized in figure 4.2.

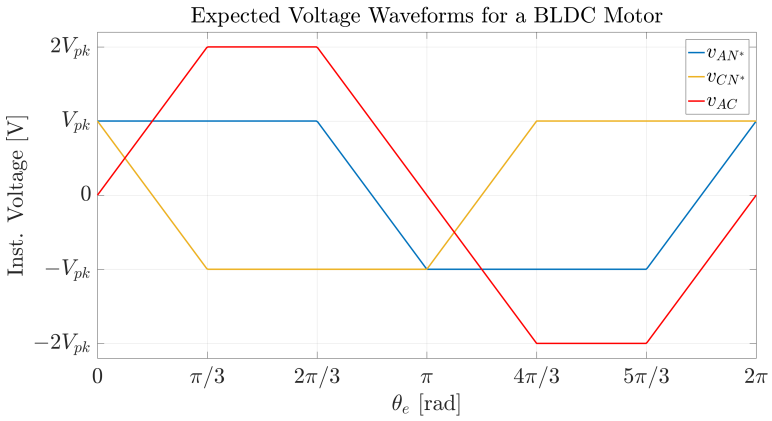

Figure 4.2: Voltage waveforms v_{AN*}, v_{CN^*} and v_{AC}.

The rms value of v_{AC} can be computed in a similar manner to v_{AN^*} by using equation 4.6 and identifying symmetrical patterns in the waveform:

$$V_{AC} = \sqrt{I_1^2 + I_2^2 + I_3^2 + I_4^2 + I_5^2 + I_6^2}$$

$$I_1 = I_4 \quad I_2 = I_5 \quad I_3 = I_6$$

$$V_{AC} = \sqrt{2(I_1^2 + I_2^2 + I_3^2)} \tag{4.15}$$

Integrals I_1, I_2, and I_3 are evaluated using equation 3.9:

$$I_1^2 = \frac{1}{2\pi} \int_0^{\frac{\pi}{3}} V_{pk}^2 (\frac{6\theta_e}{\pi})^2 d\theta_e$$

$$I_1^2 = \frac{2V_{pk}^2}{9} \tag{4.16}$$

$$I_2^2 = \frac{1}{2\pi} \int_{\frac{\pi}{3}}^{\frac{2\pi}{3}} V_{pk}^2 (2)^2 d\theta_e$$

$$I_2^2 = \frac{2V_{pk}^2}{3} \tag{4.17}$$

$$I_3^2 = \frac{1}{2\pi}\int_{\frac{2\pi}{3}}^{\pi} V_{pk}^2(6 - \frac{6\theta_e}{\pi})^2 d\theta_e$$

$$I_3^2 = \frac{2V_{pk}^2}{9} \tag{4.18}$$

$$V_{AC} = \sqrt{2((\frac{2V_{pk}^2}{9}) + (\frac{2V_{pk}^2}{3}) + (\frac{2V_{pk}^2}{9}))}$$

$$V_{AC} = V_{pk}\sqrt{\frac{20}{9}} \tag{4.19}$$

Due to the balanced loading condition between $v_{AB},\ v_{BC}$, and v_{CA}, the rms values for all phase are equal to one another:

$$V_{AB} = V_{BC} = V_{CA} = V_{LL,rms} = V_{pk}\sqrt{\frac{20}{9}} \tag{4.20}$$

Equation 4.20 can be extended to include any phase voltage subtracted from one another, the resulting rms value is the same as $V_{LL,rms}$. This is most notable for:

$$V_{LL,rms} = V_{AC} = V_{BC} \tag{4.21}$$

and will be useful when determining the AC motor model. Note the similarities between trapezoidal and sinusodial waveform rms values:

$$V_{LL,rms} = \begin{cases} \sqrt{3}V_{ph} = \sqrt{3}(\frac{V_{pk}}{\sqrt{2}}) = 1.2247V_{pk} & \text{for sinusodial waveforms} \\ \sqrt{\frac{20}{9}}V_{pk} = 1.4907V_{pk} & \text{for trapezodial waveforms} \end{cases} \tag{4.22}$$

which is a 21.7% increase in rms value when compared to a sinusoidal waveform. Additionally, the ratio of $V_{LL,rms}$ to $V_{ph,rms}$ for trapezoidal waveforms can be computed:

$$\frac{V_{LL,rms}}{V_{ph}} = \frac{\sqrt{\frac{20}{9}}V_{pk}}{\sqrt{\frac{7}{9}}V_{pk}} = \sqrt{\frac{20}{7}} \approx 1.6903 \neq \sqrt{3} \tag{4.23}$$

Interestingly, use of trapezoidal waveforms reduces the ratio of $V_{LL,rms}$ to V_{ph} by 2.4%, when compared to sinusoidal waveforms.

To continue the derivation of the AC power, we must produce the rms values for i_A and i_B. Inspection of waveform i_A from figure 4.1 shows the following intervals:

1. $+I_{pk}$ for $2\pi/3$ radians
2. 0 for $\pi/3$ radians
3. $-I_{pk}$ for $2\pi/3$ radians
4. 0 for $\pi/3$ radians

Only rms of i_A will be computed, since the procedure is the same for the other line currents. To start, consider the piecewise expression for the line current i_A:

$$i_A = I_{pk} \left\{ \begin{array}{ll} 1 & \text{for } 0 \leq \theta_e < 2\pi/3 \\ 0 & \text{for } 2\pi/3 \leq \theta_e < \pi \\ -1 & \text{for } \pi \leq \theta_e < 5\pi/3 \\ 0 & \text{for } 5\pi/3 \leq \theta_e < 2\pi \end{array} \right\} \tag{4.24}$$

The rms value of i_A can be computed in a similar manner to v_{AN^*}, by using equation

4.6 and identifying symmetrical patterns in the waveform:

$$I_A = rms\{i_A\} = \sqrt{I_1^2 + I_2^2 + I_3^2 + I_4^2}$$

$$I_1 = I_3 \qquad I_2 = I_4 = 0$$

$$I_A = \sqrt{2I_1^2} \tag{4.25}$$

Integrals I_1 is evaluated using equation 3.9:

$$I_1^2 = \frac{1}{2\pi}\int_0^{\frac{2\pi}{3}} I_{pk}^2 d\theta_e$$

$$I_1^2 = I_{pk}^2\frac{1}{3} \tag{4.26}$$

$$I_A = \sqrt{2(I_{pk}^2\frac{1}{3})}$$

$$I_A = I_{pk}\sqrt{\frac{2}{3}} \tag{4.27}$$

Note the similarities between trapezoidal and sinusodial waveform rms values:

$$I_{rms} = \begin{cases} I_{pk}\frac{1}{\sqrt{2}} = 0.7071 I_{pk} & \text{for sinusodial waveforms} \\ I_{pk}\sqrt{\frac{2}{3}} = 0.8165 I_{pk} & \text{for trapezodial waveforms} \end{cases} \tag{4.28}$$

which is a 15.4% increase when compared to a sinusoidal waveform. Table 4.1 contains the complied information on the rms differences between the relevant waveforms.

A great deal of effort has been made to identify the relevant sinusoidal electrical

Table 4.1: Relation between rms values for motor vs sinusoidal waveforms.

	BLDC motor	Pure Sinusoid	Difference [%]
$V_{ph,rms}$	$\sqrt{\frac{7}{9}}V_{pk} = 0.88V_{pk}$	$\frac{1}{\sqrt{2}}V_{pk} = 0.70V_{pk}$	+24.7
$V_{LL,rms}$	$\sqrt{\frac{20}{9}}V_{pk} = 1.49V_{pk}$	$\sqrt{\frac{3}{2}}V_{pk} = 1.22V_{pk}$	+21.8
$V_{LL,rms}$	$\sqrt{\frac{20}{7}}V_{ph,rms} = 1.69V_{ph,rms}$	$\sqrt{3}V_{ph,rms} = 1.73V_{ph,rms}$	−2.4
I_{rms}	$\sqrt{\frac{2}{3}}I_{pk} = 0.82I_{pk}$	$\frac{1}{\sqrt{2}}I_{pk} = 0.70I_{pk}$	+15.4

circuit theory, and then augment this model for BLDC motors. This is necessary as it properly encapsulates the correct waveforms for these devices. Now that a relation between peak values and rms values has been established for BLDC motors, a formulation for active and apparent power can be made.

4.1.2 Active Power from RMS Waveforms

Relation from AC power P_{AC} to rms motor values $V_{LL,rms}$ and I_{rms} is built upon the 2-wattmeter method, which states that the instantaneous power for a 3-phase AC system is given by equations 3.42 and 3.60, and is repeated here for convenience:

$$p_{inst} = v_{AC}i_A + v_{BC}i_B = p_{AC} + p_{BC}$$

where p_{AC} and p_{BC} are the wattmeter readings for lines A and B, respectively. It is important to emphasize that this is not the power flowing through line A and line B, since they are referenced to line C. It will be shown that the power entering the BLDC motor is constant, which is consistent with 3-phase electrical power transmission and equation 3.35.

Section 4.1.1 determined the relationship between peak values and rms values, whereas this section focuses on relating peak values to 3-phase active power. Overlaying the waveform equations on top on one another shows the instantaneous power of the system, shown in figure 4.3. To emphasize the connection between voltage and current waveforms to AC power, the relevant plots are shown on top of one another to visually aid in determining 3-phase active power.

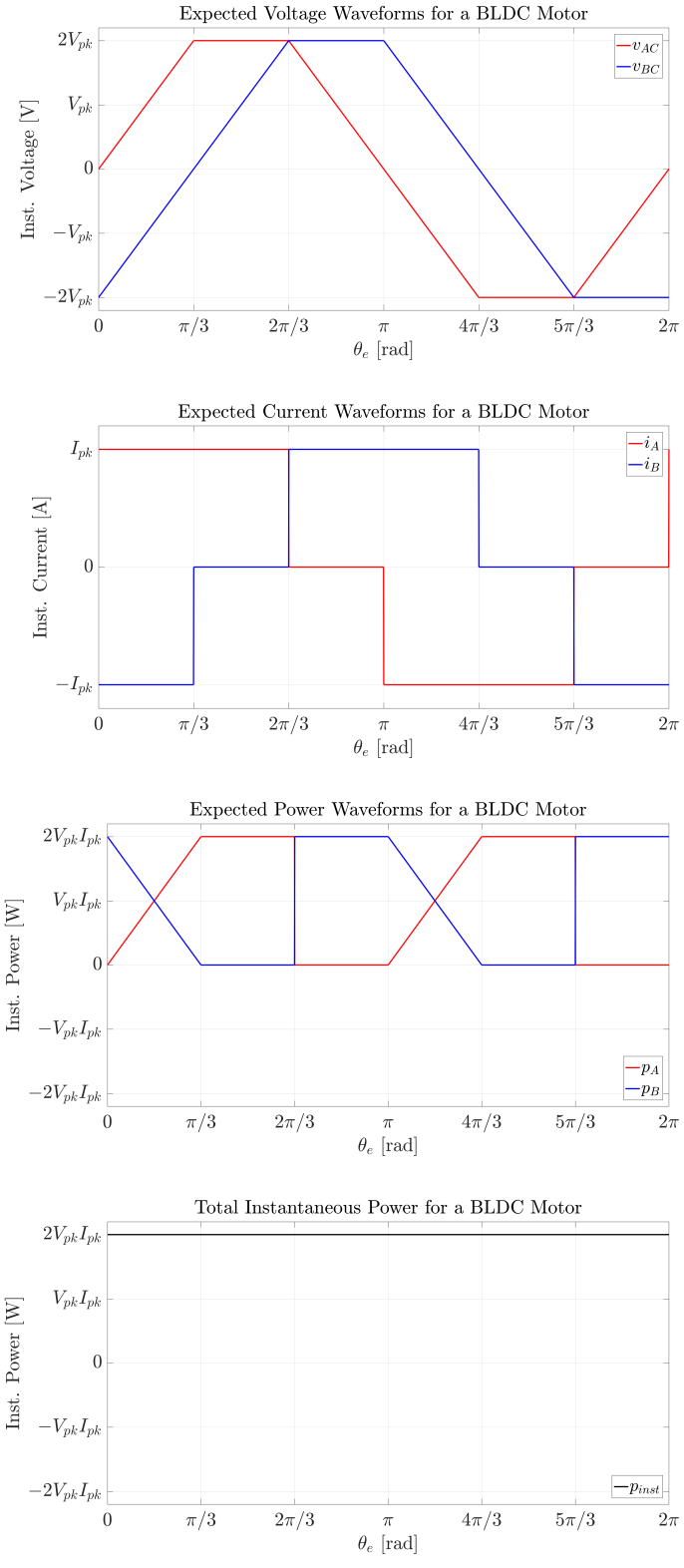

Figure 4.3: Total instantaneous power entering a BLDC motor.

From figure 4.3, the total instantaneous 3-phase power entering the BLDC motor from the ESC is:

$$p_{inst} = 2V_{pk}I_{pk} \tag{4.29}$$

and can be verified by combining the various mathematically defined waveforms from section 4.1.1. Using equation 3.66, the instantaneous power is integrated over one waveform cycle to determine the active power in the load:

$$P_{AC} = \frac{1}{2\pi}\int_0^{2\pi} p_{inst}d\theta_e$$

$$P_{AC} = \frac{1}{2\pi}\int_0^{2\pi} 2V_{pk}I_{pk}d\theta_e$$

$$P_{AC} = 2V_{pk}I_{pk} \tag{4.30}$$

Now that P_{AC} is written in terms of peak voltage and current values, table 4.1 from section 4.1.1 can be used to relate these quantities to $V_{LL,rms}$ and I_{rms} values.

$$V_{pk} = \sqrt{\frac{9}{20}}V_{LL,rms} \qquad I_{pk} = \sqrt{\frac{3}{2}}I_{rms}$$

$$P_{AC} = 2(\sqrt{\frac{9}{20}}V_{LL,rms})(\sqrt{\frac{3}{2}}I_{rms})$$

$$P_{AC} = \sqrt{\frac{27}{10}}V_{LL,rms}I_{rms} \approx 1.64V_{LL,rms}I_{rms} \tag{4.31}$$

Equation 4.31 is similar in nature to DC power $P_{DC} = V_{DC}I_{DC}$. For AC power, voltage and current must be evaluated as rms quantities, and the factor of $\sqrt{27/10}$ can be thought of as an exchange rate between rms values and active power. In DC

power, the peak value is equal to the rms value, meaning no conversion is required. AC power analysis has additional tools to evaluate the power content of a 3-phase system such as apparent power and the power factor.

4.1.3 Power Factor for a BLDC Motor

A question now arises if one can calculate the power factor for these waveforms. Recall that power factor is simply the ratio of the active power to the apparent power, expressed by:

$$pf = \frac{P_{AC}}{S}$$

The expressions for apparent power S, derived in section 3.5, must be modified for non-sinusoidal systems. In a standard AC system, changing the driving frequency ω_e changes the impedances of the line, and thus the balance of power in the circuit [22, 26, 31]. Augmenting the driving frequency for a sinusoidal circuit implies that the power factor is not constant, but a function of the components in a circuit.

For BLDC motors, the waveforms are actively controlled by the ESC, meaning that ω_e does not change the power distribution for a circuit, as evidenced in figure 2.35. Actively controlling the waveforms indicates that the apparent and active powers in a circuit are set by the commutation steps and the user throttle. Definition of 3-phase apparent power, equation 3.67, must be corrected for BLDC waveforms. Previously, total apparent power was found under the assumption of 3-phase sinusoidal system and required $V_{LL,rms} = \sqrt{3}V_{ph,rms}$, but must be revised for BLDC motors. This modification can be made by using the expressions in table

4.1 for an equivalent Y connected circuit:

$$S = V_{AN^*} I_A + V_{BN^*} I_B + V_{CN^*} I_C$$

$$S = 3 V_{ph,rms} I_{rms}$$

$$S = 3(\sqrt{\frac{7}{20}} V_{LL,rms}) I_{rms}$$

$$S = \sqrt{\frac{63}{20}} V_{LL,rms} I_{rms} \tag{4.32}$$

With apparent power S defined, and active power given by equation 4.31, the ideal power factor for a BLDC motor is found to be:

$$pf = \frac{\sqrt{\frac{27}{10}} V_{LL,rms} I_{rms}}{\sqrt{\frac{63}{20}} V_{LL,rms} I_{rms}}$$

$$pf = 92.6\% \tag{4.33}$$

Surprisingly, this result is independent of operating voltage, input throttle, rotational speed, and all other physical parameters. A constant power factor stems from the fact that the waveform shapes are set and controlled by the ESC. Passive RLC circuits do not have the ability to hold the power factor constant, and so the driving frequency ω_e effects the power factor. Figure 4.4 shows experimentally obtained data points for a BLDC motor's power factor vs the predicted 92.6%.

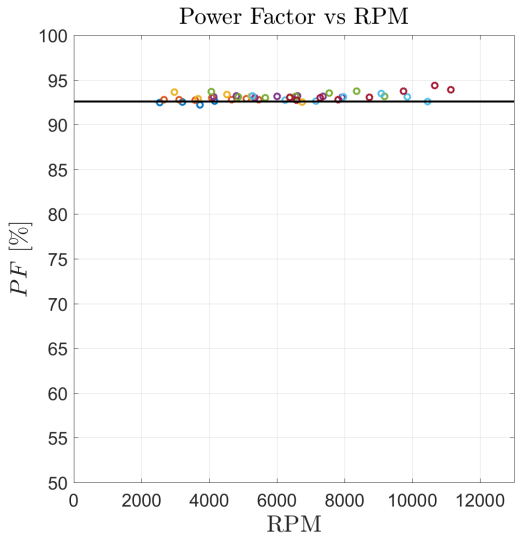

Figure 4.4: Power factor for the EMAX 1900KV motor. Black represents the predicted 92.6% value whereas each other color represents a different throttle.

Evaluation of active power from AC quantities, as well as the power factor, is useful as it allows one to relate rms values to active power. Next, an equivalent circuit is determined that includes the motor's performance.

4.1.4 Equivalent Motor Circuit

An equivalent motor circuit for BLDC motors and the ESCs can be found by modifying the existing DC motor model to include AC rms quantities. This augmented model serves to predict the performance metrics of the motor and the required AC and DC powers of the system. In the section 4.2, this motor model is expanded to include the ESC. Key points of the motor model include predicting the torque-RPM relation, properly capturing the torque-current relationship, and accurate prediction of the AC power required to run the motor. The model outlined in this work will be described as it was discovered, in a logical step-by-step manner.

To start, an actual motor and ESC are examined:

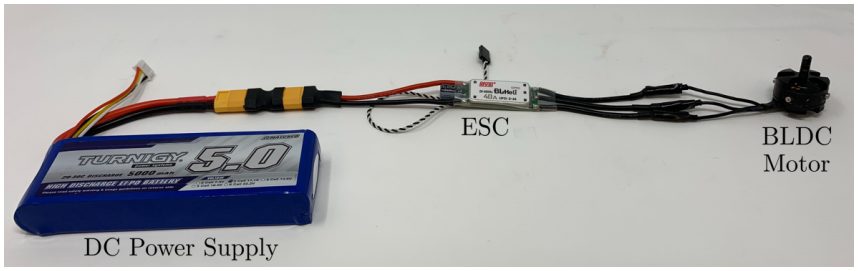

Figure 4.5: Components considered for equivalent circuit modeling.

Proper characterization of the system relies on 3 sets of equations:

1. AC motor equations, which relate input quantities such as V_{rms}, I_{rms}, and t to the motor's performance.

2. AC power equations, which determines the required amount of power drawn by the motor.

3. ESC transformer equations, relating the required AC power to the required DC current draw.

Equations relating DC, AC, and mechanical power will be derived in this Chapter, and then overlaid with the experimental tests in Chapter 5. To start, a component-by-component analysis of figures 4.5 and 2.21, is drawn:

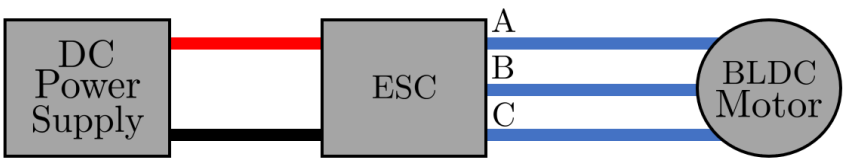

Figure 4.6: Components considered for equivalent circuit modeling.

An actual circuit for a BLDC motor requires 3-phases to commutate the motor. However, it has been shown that the AC power to run the motor is only related to $V_{LL,rms}$ and I_{rms}, meaning these values can be used to make a simplified 'quasi-single phase' circuit, like a DC circuit. With this, the AC motor model for brushless motors uses the following equivalent model for the ESC and motor:

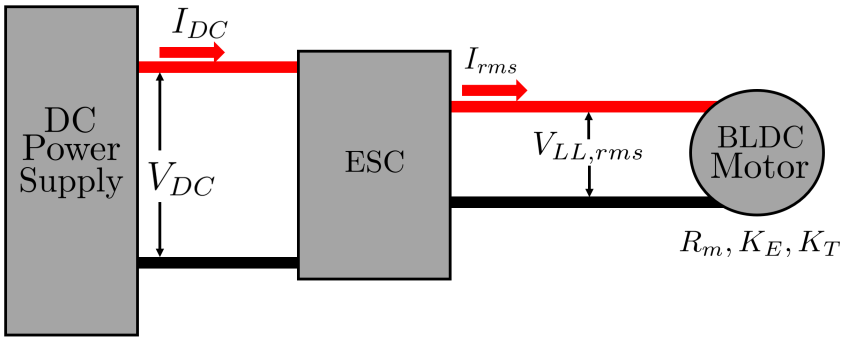

Figure 4.7: Equivalent BLDC and ESC circuit.

The equivalent model has the following features added: a motor resistance R_m, a back constant EMF K_E, and a motor torque constant K_T. By reducing the three phases system into an equivalent DC type circuit, the motor's complexity is reduced, and evaluating its performance can be referenced against the Chapter 2 model. A discussion on how AC electrical parameters influence the motor torque-RPM line starts by referring to the equivalent DC motor model that was presented in Chapter 2:

$$V_{DC}T_R = I_{DC}R_m + K_E\omega$$

$$Q = K_T(I_{DC} - I_{DC,o})$$

To work with solely the brushless motor, AC quantities are needed. This includes

the terms $V_{LL,rms}$ and I_{rms}, since they describe the power entering the motor. With this, the DC model is augmented to:

$$V_{LL,rms} = I_{rms}R_m + K_E\omega \tag{4.34}$$

$$Q = K_T(I_{rms} - I_o) \tag{4.35}$$

where $V_{LL,rms}$ is the line-to-line rms voltage entering the motor, I_{rms} is the input current to the motor, and I_o is the required rms current to overcome the static friction of the motor, all AC quantities. Equations 4.34 and 4.35 relate motor voltage to mechanical rotation, and rms current to output torque. Equation 4.35 is shown in figure 4.8 and is quite easy to verify with experimental data.

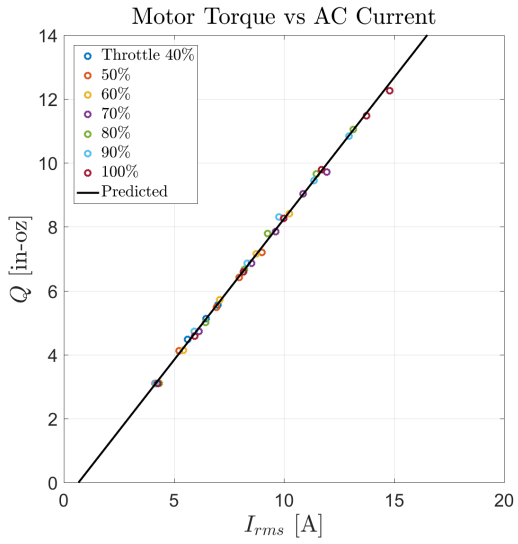

Figure 4.8: Q vs I_{rms} for an EMAX 1900KV motor and MultiStar 30A ESC at V_{DC} = 7.2 V.

Rms values for voltages and currents can be easily measured in an experiment, but how do these values relate to the DC voltage and the input throttle? One

expects a higher $V_{LL,rms}$ to be associated with a higher DC voltage and a higher input throttle, but by how much? To determine the link between rms voltage and input DC voltage and throttle, consider the following experimentally retrieved data on motor voltages, shown in figure 4.9.

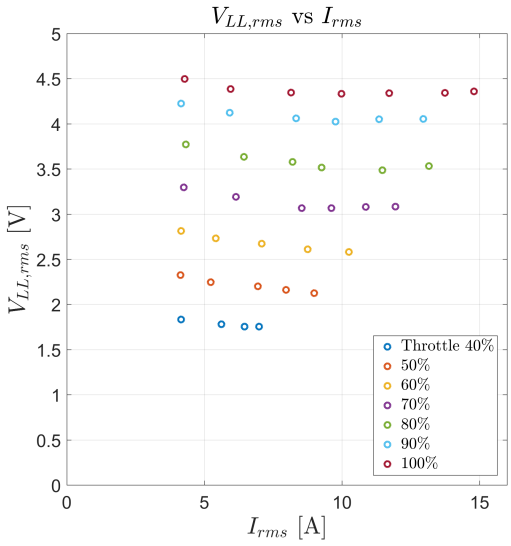

Figure 4.9: $V_{LL,rms}$ vs I_{rms} for an EMAX 1900KV motor and MultiStar 30A ESC at $V_{DC} = 7.2$ V. Note how all voltages are below V_{DC}.

From figure 4.9, it can be seen that for a given throttle setting t, all voltages following the same linear trend with I_{rms}:

$$y = b - mx$$

$$V_{LL,rms} = V_{LL,rms}\Big|_{I_{rms}=0} - R_{ESC} I_{rms} \tag{4.36}$$

where R_{ESC} is the equivalent ESC resistance. Phase voltages are measured directly at the output of the ESC, indicating that some voltage drop occurs across the ESC's internal resistance. Additionally changing the length of wire to the motor was found

to have no influence on R_{ESC}. These qualitative relations between $V_{LL,rms}$ vs I_{rms} can be summarized:

- Motor rms voltage $V_{LL,rms}$ is a function of throttle T_R, rms current I_{rms}, and the DC voltage V_{DC}.
- Initial offset rms voltage $V_{LL,rms}\Big|_{I_{rms}=0}$ is only a function of the DC Voltage V_{DC} and the input throttle T_R, and has a value less than V_{DC}.
- Equivalent ESC resistance R_{ESC} is the same for all throttles.

It was found from [13, 21], that the maximum rms output voltage depends on the connection and commutation setup, and the results and copied into table 4.2 for convenience.

Table 4.2: Relation between maximum rms values for BLDC, depedning on control scheme. Taken from [13].

Control Strategy	$V_{LL,rms}$	
Six step operation, with 180^o conduction in each transistor	$\frac{\sqrt{6}}{\pi}V_{DC}$	$0.780V_{DC}$
Six step operation, with 120^o conduction in each transistor	$\frac{3}{\sqrt{2}\pi}V_{DC}$	$0.675V_{DC}$
Limit of linear modulation in "sine/triangle" PWM	$\frac{\sqrt{3}}{2\sqrt{2}}V_{DC}$	$0.612V_{DC}$

The ESCs studied in this work are of six step, 120^o conduction commutation type, as displayed by figures 2.25 to 2.29. Therefore, the effective rms voltage offset of the motor is:

$$V_{LL,rms}\Big|_{I_{rms}=0} = \frac{3}{\sqrt{2}\pi}V_{DC}T_R \tag{4.37}$$

with this, the rms motor voltage can be stated:

$$V_{LL,rms} = \frac{3}{\sqrt{2}\pi} V_{DC} T_R - R_{ESC} I_{rms} \tag{4.38}$$

which satisfies the original stipulations for rms motor voltage. Overlaying the predicted $V_{LL,rms}$ values via equation 4.38 with the original experimentally obtained $V_{LL,rms}$ values from figure 4.9 results in the plot shown in figure 4.10.

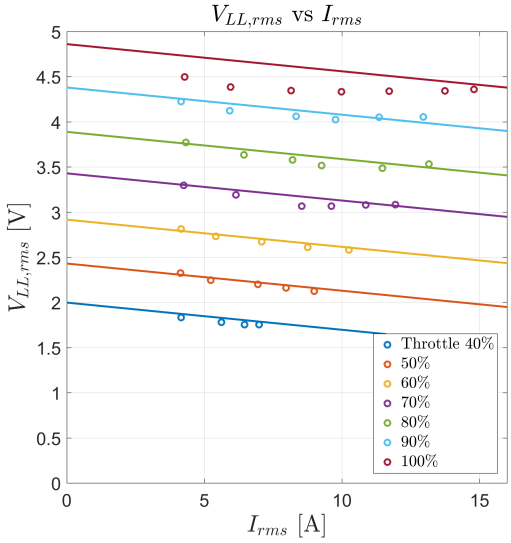

Figure 4.10: Predicted and experimentally obtained $V_{LL,rms}$ vs I_{rms} for an EMAX 1900KV motor and MultiStar 30A ESC at $V_{DC} = 7.2$ V.

Predicted values for $V_{LL,rms}$ agree well with experiment up to 90% throttle. Somewhere between 90% and 100% throttle, the ESC begins to saturate and can no longer provide the required $0.675 V_{DC} T_R$ voltage, and is believed to have happened because table 4.2 predicts the maximum theoretical rms voltage value. Saturation is a phenomenon that occurs at high control inputs, and takes place in this system between 90% and 100% throttle. Physically, this means that some DC voltage

cannot be converted into AC voltage due to inherit hardware limitations in the ESC.

As a result of this upper saturation limit, the model presented in this Chapter is only valid up to 90% throttle. In this region, no saturation occurs - meaning that equation 4.37 is valid. However, at 100% throttle a nonlinearity occurs, which means that equation 4.37 over predicts the amount of voltage available to the motor. An area of future work is to further explore the region between 90% and 100% throttle, because at 100% the absolute limits of the system's performance can be evaluated. However, within the non-saturated region, we can determine the torque-RPM relationship.

Throttle ranges between 0 and 90% are predicted well with this model, and are shown in Chapter 5. To determine the relationship between voltage, throttle, and RPM, equation 4.34 can be combined with equation 4.38:

$$(\frac{3}{\sqrt{2}\pi}V_{DC}T_R - R_{ESC}I_{rms}) = I_{rms}R_m + K_E\omega$$

$$\frac{3}{\sqrt{2}\pi}V_{DC}T_R = (R_{ESC} + R_m)I_{rms} + K_E\omega \tag{4.39}$$

which yields a more useful form of the AC motor equation. Here the influence of user throttle and DC voltage is linked to the physical parameters of the motor, and is similar to the brushed motor model, equation 2.15, in Chapter 2. This modified equivalent motor model is shown in figure 4.11, and has been updated to include the equivalent R_{ESC}.

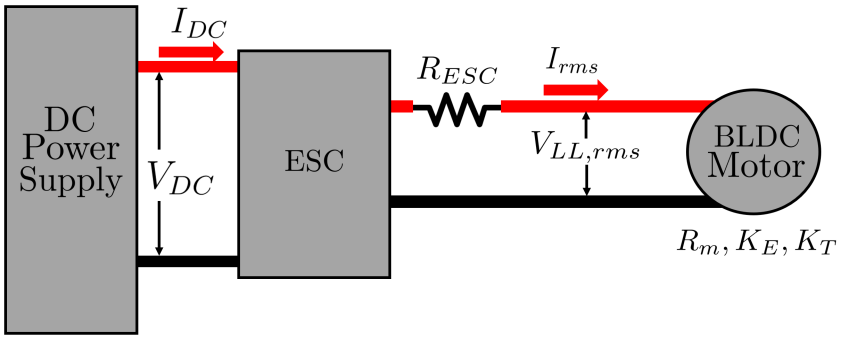

Figure 4.11: Equivalent BLDC and ESC circuit, updated to include R_{ESC}.

With the voltage-RPM relation and the torque-current relation defined, an expression relating torque to RPM can be found by combining equations 4.39 and 4.35:

$$Q = \frac{K_T}{R_m + R_{ESC}}[\frac{3}{\sqrt{2}\pi}V_{DC}T_R - I_o(R_m + R_{ESC})] - \frac{K_T K_E}{R_m + R_{ESC}}\omega \tag{4.40}$$

which is the same result as equation 2.7 for the equivalent brushed model. From equation 4.40, determining the motor's output power can be found:

$$P_m = Q\omega$$

$$P_m = \frac{K_T\omega}{R_m + R_{ESC}}[\frac{3}{\sqrt{2}\pi}V_{DC}T_R - I_o(R_m + R_{ESC})] - \frac{K_T K_E}{R_m + R_{ESC}}\omega^2 \tag{4.41}$$

Equations 4.40 and 4.41 are plotted against experimentally obtained data in figure 4.12. Again, the motor's output power is a concave down parabola, and has a peak power point at half the no-load speed of the motor. Without the output power of the motor defined, an expression for the required AC power to drive the motor can

be made. However, first an observation about the torque vs RPM line.

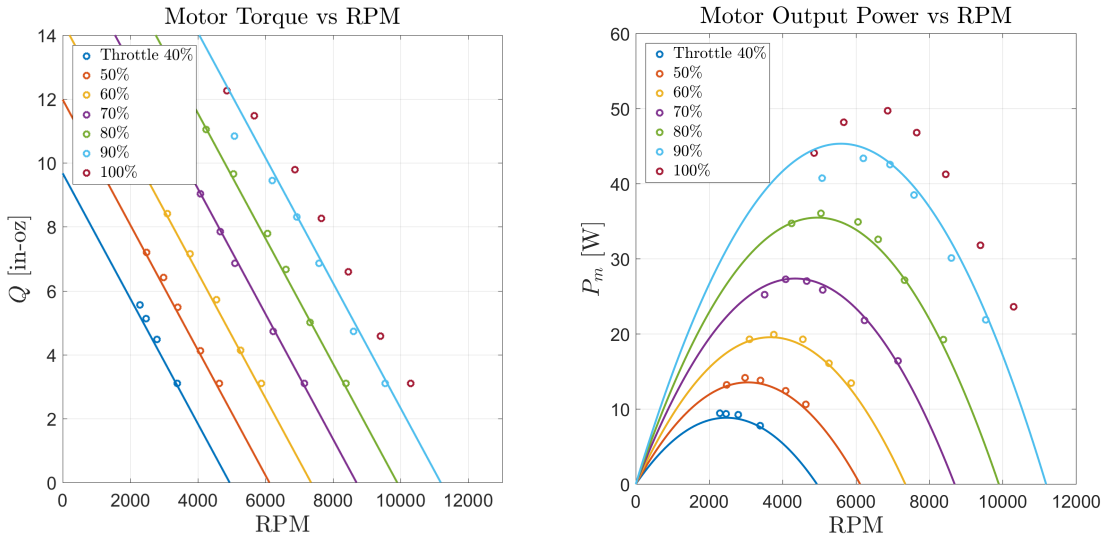

Figure 4.12: Predicted and experimentally obtained Q vs RPM curve for an EMAX 1900KV motor and MultiStar 30A ESC at $V_{DC} = 7.2$ V.

Careful examination of the torque vs RPM relation for a BLDC motor further demonstrates ESC saturation at high throttle. Consider the required RPM to generate 3.1 in-oz of torque, depicted as the lowest points for each throttle in figure 4.12. Between 40% and 90% throttle, each 10% increase in throttle has a consistent 1230 RPM increase in motor speed. However, the points between 90% throttle and 100% throttle only have 750 RPM increase, and stems from the fact that the ESC cannot produce the required rms voltage. Reduced voltage is attributed to slower rotational speeds by equations 2.7 and 4.40.

The strength of this equivalent motor model is that it combines easily with the AC power relations from section 4.1.2. Given a load Q and speed ω, the required voltage $V_{LL,rms}$ and current I_{rms} can be found, and are related to the active power P_{AC} in the circuit via their peak values. With the insight of figure 4.11 and equation

4.38, a modification to the AC power entering the motor is required to account for the impact of R_{ESC}. Power output from the ESC has an $I_{rms}R_{ESC}$ voltage drop associated with the ESC, and reduces the effective motor rms voltage. Therefore, power entering the BLDC motor sees an $I_{rms}^2 R_{ESC}$ power loss:

$$P_{AC} = \sqrt{\frac{27}{10}} V_{LL,rms} I_{rms}$$

$$P_{AC} = \sqrt{\frac{27}{10}} (\frac{3}{\sqrt{2}\pi} V_{DC} T_R - R_{ESC} I_{rms}) I_{rms} \tag{4.42}$$

$$P_{AC} = \frac{3}{\pi}\sqrt{\frac{27}{20}} V_{DC} I_{rms} T_R - \sqrt{\frac{27}{10}} I_{rms}^2 R_{ESC}$$

AC power for a BLDC motor contains 2 components: a positive $V_{LL,rms}I_{rms}$ and a negative $I_{rms}^2 R_{ESC}$ component. In reality, the $I_{rms}^2 R_{ESC}$ is a conductive power loss to the ESC, which will be explained further in section 4.2. As the rms current

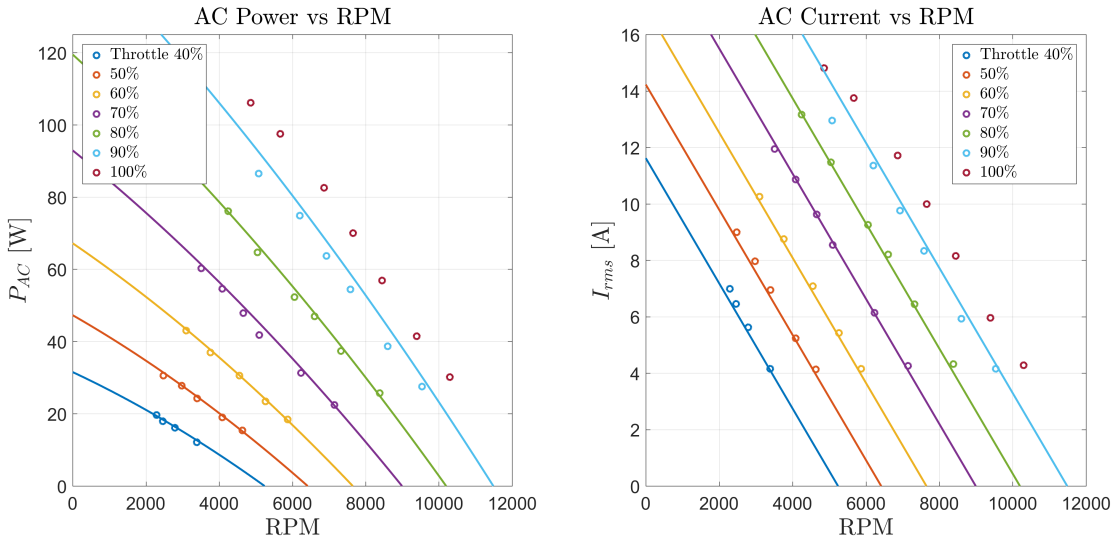

Figure 4.13: Predicted and experimentally obtained Q vs RPM curve for an EMAX 1900KV motor and MultiStar 30A ESC at $V_{DC} = 7.2$ V.

increases, less power is available to the motor. Predicted and experimental results

for the rms current and AC power are shown in figure 4.13.

Representing the BLDC motor as an equivalent AC circuit predicts the motor's performance well. As mentioned previously, this work was originally developed for 7.2 V motors, but later expanded to include 11.1 V and 14.8 V motors. Looking ahead: Chapter 4 continues with modeling the ESC, whereas Chapter 5 shows experimental results of motor and ESC testing overlaid with predicted results. The next section of work seeks to model the remainder of the propulsion system: the ESC.

4.2 Electronic Speed Controller

An ESC is responsible for properly modulating the DC power into the proper AC waveforms for a BLDC motor. A series of MOSFETs control the commutation interval, based on the rotor's position. The length of time that the MOSFETs are conducting controls the rms voltage to the motor. Objectives for ESC modeling are to determine:

1. DC current I_{DC} draw out of the DC power supply
2. Physical characteristics of the ESC which are invariant of the motor
3. Power loss of the ESC P_{ESC}

Traditionally, the ESC is neglected in formal analysis. However, this work seeks to determine a physics based model of the ESC, and to identify physical parameters that uniquely describe the ESC. Testing ESC models is complicated because different

motors bring about different test environments for the ESC, regarding RPM and current usage. To simplify this work, the following observations have been made about ESCs:

1. Power loss increases with DC Voltage V_{DC}.

2. Power loss increases with AC current I_{rms}.

3. Power loss decreases with throttle T_R.

Power losses for an EMAX 935 KV and MultiStar 30A ESC are shown in figures 4.14 and 4.15.

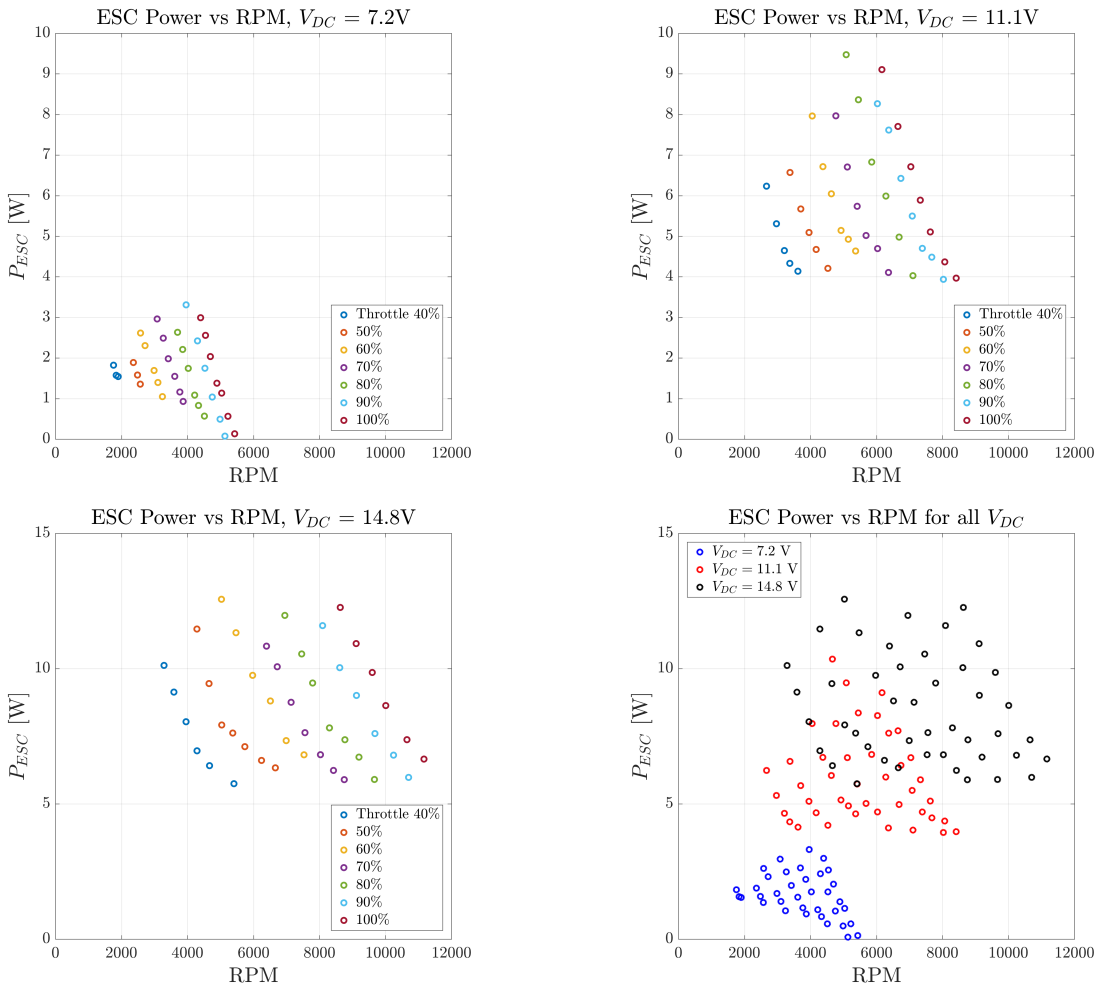

Figure 4.14: ESC power loss vs RPM for a MultiStar 30A ESC and EMAX 935 KV motor.

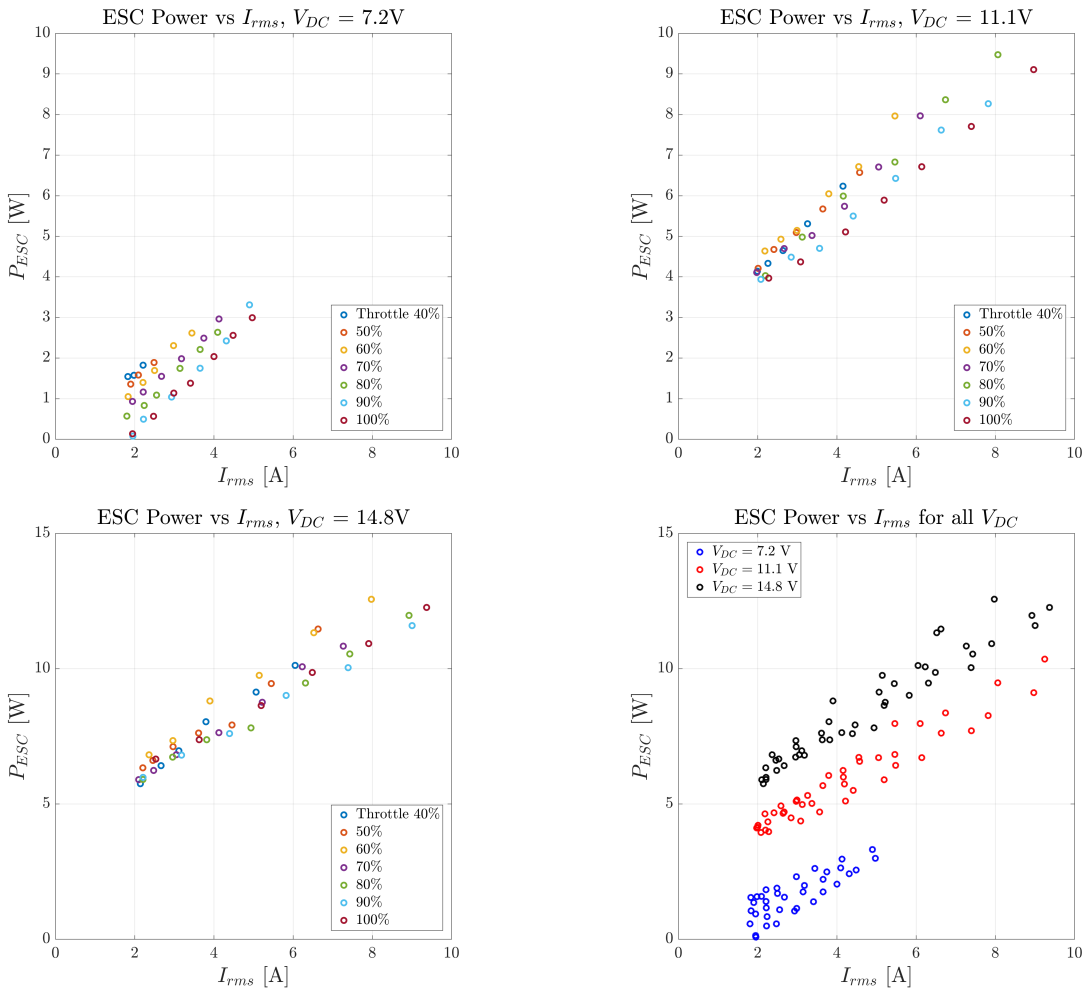

Figure 4.15: ESC power loss vs I_{rms} for a MultiStar 30A ESC and EMAX 935 KV motor.

ESC power loss shows a strong correlation with DC voltage, rms current, and throttle. Before modeling an ESC, first MOSFET power loss literature is reviewed.

4.2.1 MOSFET Power Losses

As was explained in section 2.3 and 2.3.2, an ESC is comprised of 6 MOSFETs that are responsible for commutating the brushless motor. Two MOSFETs control a commutation event and alternating the two out of six MOSFETs, the rotor is kept spinning. Both the act of switching the MOSFET on and off, as well as the act of allowing current to flow results in power losses. Results show that the power loss of a MOSFET contains two primary components [36–40]:

1. A linear I_{rms} component - related to the rapid switching on and off of the MOSFET. Referred to as switching losses
2. A quadratic I_{rms}^2 component - related to the conductive power loss of any physical component. Referred to as conduction losses

Ideally, these losses can be written as:

$$P_{MOSFET} = P_{sw} + P_{cond} \tag{4.43}$$

$$P_{sw} = \frac{1}{2} V_{DC} I_{rms} (t_{on} + t_{off}) f_{sw} \tag{4.44}$$

$$P_{cond} = I_{rms}^2 R \tag{4.45}$$

where t_{on}, t_{off}, and f_{sw} are the time to switch on in seconds, time to switch off in seconds, and switching frequency in Hz, respectively. This relates how long each MOSFET switches to how many switches occur each second. Switching losses originate with a changing voltage and current acting across the MOSFET. Resistive

losses are evident in all physical conducting elements. Diode losses and capacitive effects have also been included in some models [37, 40]. Favorable qualities to have in a MOSFET are fast swtiching times, low forward voltage drop, low on resistance, and high breakdown voltage [41].

To better understand the physical nature of switching losses, consider the following diagram of a MOSFET:

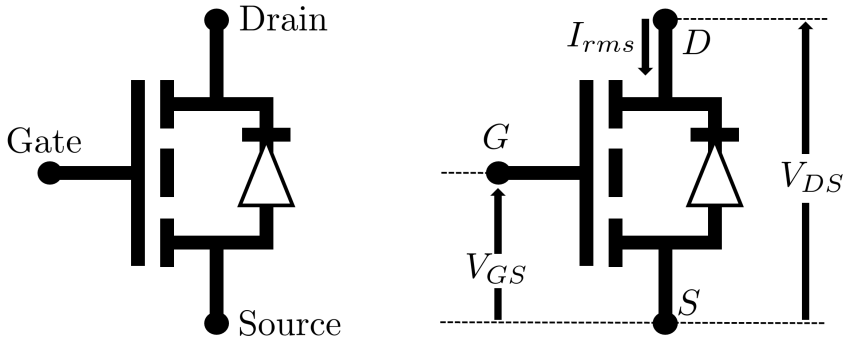

Figure 4.16: MOSFET model.

As explained in section 2.3.2, MOSFETs have three terminals: a drain, a gate, and a source. When a sufficient voltage is applied between the source and gate, the MOSFET will allow current I_{rms} to flow from the drain to the source. However, this transition from no current flowing to current flowing takes some time. Changes in waveforms during this switching event is what causes the switching power loss. A typical MOSFET waveform during switching is shown in figure 4.17.

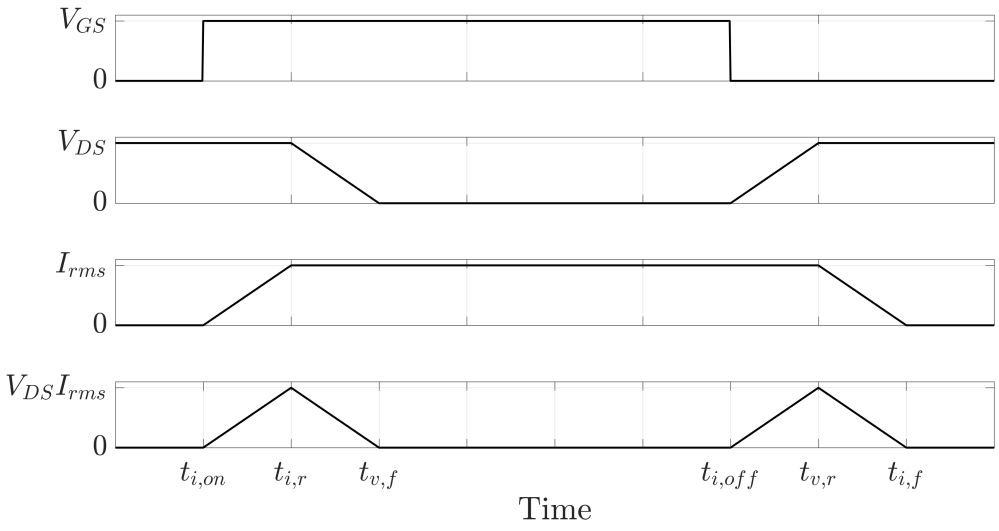

Figure 4.17: MOSFET switching waveforms for on and off operation.

Switching, as the name applies, occurs when the MOSFET is switched from on (i.e. non-conducting to conducting) and off (i.e. conducting to non-conducting). First, switching on losses shall be considered [37], which occurs between the initial on time $t_{i,on}$ and the voltage falling time $t_{v,f}$. At $t_{i,on}$, V_{GS} is pulled high, which allows current to start flowing through the MOSFET. A linear transition between 0 to I_{rms} concludes at the time of maximum current rise $t_{i,r}$. After this, the voltage difference between drain and source V_{DS} drops from it's maximum value to 0. The MOSFET is fully on at $t_{v,f}$, when there is no voltage difference between the drain and source. Energy consumed during the on transition is the area under the $V_{DS}I_{rms}$ curve:

$$E_{sw,on} = \frac{1}{2} V_{DS} I_{rms} (t_{v,f} - t_{i,on})$$

$$t_{on} \triangleq t_{v,f} - t_{i,on}$$

$$E_{sw,on} = \frac{1}{2} V_{DS} I_{rms} t_{on} \tag{4.46}$$

Energy lost during the on transition per second $P_{sw,on}$ can be found by:

$$P_{sw,on} = E_{sw,on} \times (number\ of\ switches\ each\ second)$$

$$P_{sw,on} = \frac{1}{2} V_{DS} I_{rms} t_{on} f_{sw} \tag{4.47}$$

where f_{sw} is the switching frequency, or the number of switches each second.

Similar logic is used to determine the switching off losses. When V_{GS} changes from high to low, the MOSFET begins the off transition at $t_{i,off}$. At this time, V_{DS} linearly rises to block the flow of current and reaches its maximum value at time $t_{v,r}$. After this, the current I_{rms} linearly decreases to 0. The MOSFET is fully off at $t_{i,f}$, when there is no current flowing from the drain to the source. Energy consumed during the off transition is the area under the $V_{DS} I_{rms}$ curve:

$$E_{sw,off} = \frac{1}{2} V_{DS} I_{rms} (t_{i,f} - t_{i,off})$$

$$t_{off} \triangleq t_{i,f} - t_{i,off}$$

$$E_{sw,off} = \frac{1}{2} V_{DS} I_{rms} t_{off} \tag{4.48}$$

Energy lost during the off transition per second $P_{sw,off}$ can be found by:

$$P_{sw,off} = \frac{1}{2} V_{DS} I_{rms} t_{off} f_{sw} \tag{4.49}$$

With the switching on and off power modeled, the total switching loss can be computed:

$$P_{sw} = \frac{1}{2} V_{DS} I_{rms} (t_{on} + t_{off}) f_{sw} \tag{4.50}$$

Conduction losses occur between $t_{v,f}$ to $t_{i,off}$, that is: when the MOSFET is conducting. Total power loss during MOSFET operation is the sum of the switching and conductive losses, and is stated as:

$$P_{MOSFET} = \frac{1}{2} V_{DS} I_{rms} (t_{on} + t_{off}) f_{sw} + I_{rms}^2 R \tag{4.51}$$

A single MOSFET contains both a linear and quadratic component of power loss with the rms current. If there were only one MOSFET to block the entire supply voltage, then $V_{DS} = V_{DC}$. Recall from figure 2.21, that a micro controller controls the rate at which switching occurs, and is by user throttle. That is, the user controls the amount of switching. From equation 4.51, it is evident that minimizing switching losses occurs when $f_{sw} = 0$, indicating that the MOSFET only has conductive losses. In an ESC, the switching frequency f_{sw} shows a strong correlation to the input throttle. Before determining a power loss model for an ESC, first an ideal DC to AC transformer is considered.

4.2.2 Ideal DC to AC Transformer

ESCs invert the steady DC waveforms into AC waveforms for the brushless motor, acting as transformers, changing DC power into AC power by rapidly switching

MOSFETs in a specific sequence. It was shown in the previous section that MOSFETs contain some power loss related to switching and conduction, however this section presents an experiment to evaluate ESC behavior. It will be shown that by identifying ideal ESC behavior, and tracking actual ESC behavior, the difference between these models relates to the ESC power.

Figure 4.18 shows a diagram that relates the input power to the output power. Here V_{DC} and I_{DC} are augmented into $V_{LL,rms}$ and I_{rms}. Based on the equivalent motor circuit: $V_{LL,rms}$, I_{rms}, and V_{DC} are known, whereas the DC current draw I_{DC} is unknown.

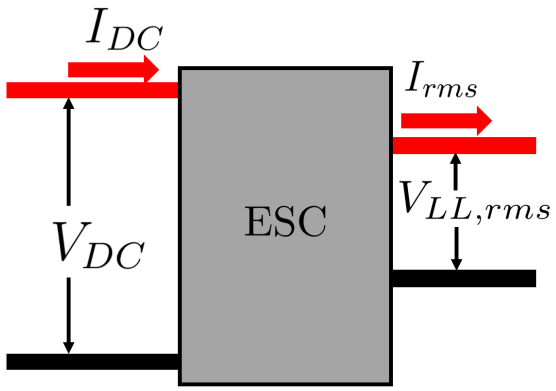

Figure 4.18: ESC transformer diagram.

Converting DC power P_{DC} into AC power P_{AC} requires some power P_{ESC}, which is lost to the environment as heat. A power balance relates these quantities:

$$P_{DC} = P_{ESC} + P_{AC} \tag{4.52}$$

which states that the DC power is lost to either the ESC or is converted into AC power to run the motor. From equation 4.52 and 1.1, the efficiency of the ESC can

be reformulated as:

$$\eta_{ESC} = \frac{P_{AC}}{P_{DC}}$$

$$\eta_{ESC} = 1 - \frac{P_{ESC}}{P_{DC}} \tag{4.53}$$

Increasing ESC efficiency indicates that power lost to the ESC P_{ESC} should be minimized. However, what if the power lost to the ESC P_{ESC} was exactly 0? Here, an ESC is operating in an ideal state with an efficiency of 100%. An ideal ESC implies that DC and AC powers are equal to one another:

$$P_{DC} = P_{AC} \tag{4.54}$$

To explore how DC current is converted into AC current, we will first examine an ideal transformer and then generalize this work to an non-ideal transformer. A key concept in the transmission of electrical power, or any power, is that the input and output power must remain accounted for. For electrical systems [41], a reduction in voltage requires an increase in current such that if $V_{out} < V_{in}$ then it is guaranteed that $I_{out} > I_{in}$. Exchanging voltage for current stems from the fact that power must remained balanced, and the electromagnetic system will work to achieve this. Power cannot be created or destroyed, but merely changes form. This logic can be extended for an ideal ESC, by using the relations for DC and AC power from equations 3.1 and 4.42 respectively:

$$V_{DC}I_{DC} = \sqrt{\frac{27}{10}}(\frac{3}{\sqrt{2}\pi}V_{DC}T_R - \cancelto{0}{R_{ESC}}I_{rms})I_{rms}$$

$$V_{DC}I_{DC} = \frac{3}{\pi}\sqrt{\frac{27}{20}}V_{DC}T_R I_{rms} \tag{4.55}$$

For an ideal ESC, the equivalent resistance $R_{ESC} = 0$, meaning that no voltage is dropped across the inverter. Equation 4.55 can be further simplified into a more useful form:

$$I_{DC} = \frac{3}{\pi}\sqrt{\frac{27}{20}}T_R I_{rms}$$

$$\frac{I_{DC}}{I_{rms}} = \frac{3}{\pi}\sqrt{\frac{27}{20}}T_R \approx \frac{10}{9}T_R \tag{4.56}$$

which states that for a given amount AC current I_{rms}, the required DC current draw I_{DC} out of the power supply is dependent upon the throttle alone and is independent of the DC voltage. It is also worth noting that at 90% throttle, the ratio $I_{DC}/I_{rms} = 1$. Equation 4.56, referred to as the ideal transformer relation, is plotted in figure 4.19 for all throttles.

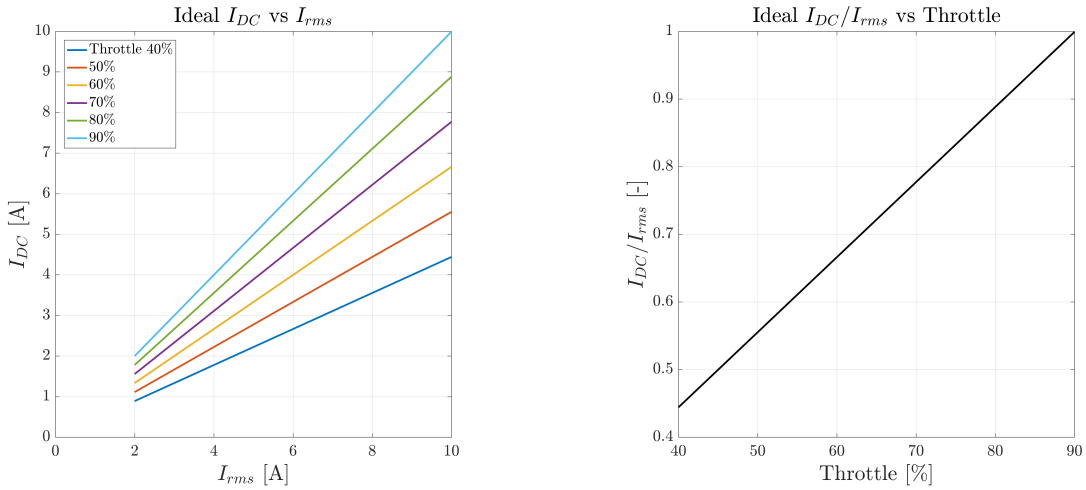

Figure 4.19: Ideal I_{DC} and I_{rms} relationship.

Note that this I_{DC}/I_{rms} relationship is a straight line with regions above and below the line. If an actual ESC produced a I_{DC}/I_{rms} curve above the ideal line, then

more DC current is required for the same amount of rms current when compared to the ideal relationship. Deviating above the ideal line demonstrates a nonideal transformer, with $\eta_{ESC} < 1$. It is nonphysical for an ESC to occupy the region below the ideal line, as that would suggest $\eta_{ESC} > 1$. Determination of the exact location of an ESC transformation curve will allow a designer to determine the exact amount of power lost to the ESC as heat and the DC current draw out of the battery.

4.2.3 DC Current Draw for an ESC

The concept of an ideal transformer must be extended to include losses. Experimentally obtained plots for rms current vs DC current is shown in figure 4.20, and reveals plots similar to the ideal transformer plots shown in figure 4.19. In both figures, for a given throttle, it appears all DC currents line on the same line, originating from 0. When the throttle changes, the slope of the line changes and all I_{DC} follow the same trend. The higher the throttle, the more the ratio of DC current to rms current becomes closer to 1.

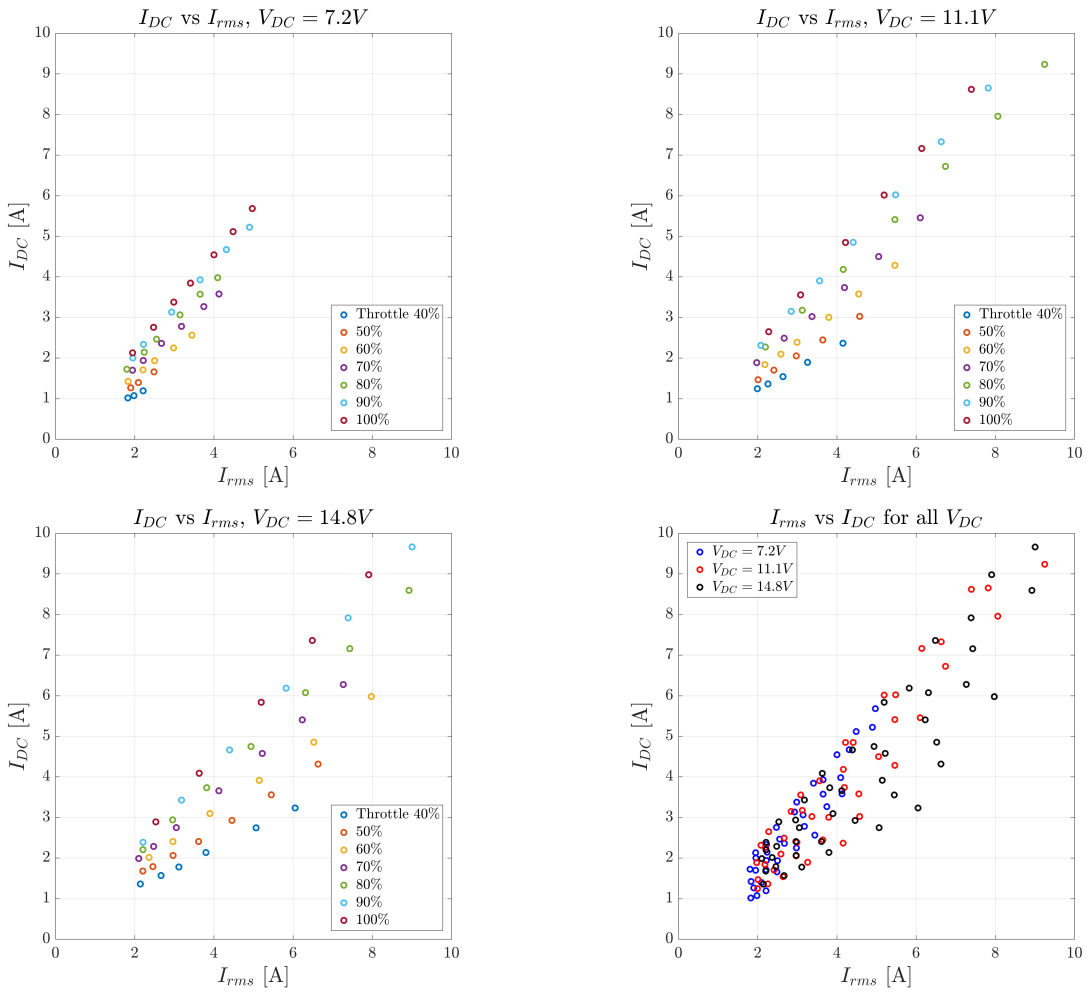

Figure 4.20: I_{DC} vs I_{rms} for a MultiStar 30A ESC and EMAX 935 KV motor.

Figure 4.20 implies that the ratio of DC current to rms current does not depend on voltage, which was first shown in the ideal transformer relation, by equation 4.56. Experimentally observed ratio of I_{DC}/I_{rms} is the same regardless of the operating voltage and are located on the same line for a given throttle. The goal now is to determine an expression for the current ratio, and then deduce an expression for ESC power. By plotting the ratio of I_{DC}/I_{rms} vs throttle at different voltages for this motor/ESC combination in figure 4.21, it is apparent that these points lie above the ideal transformer relation.

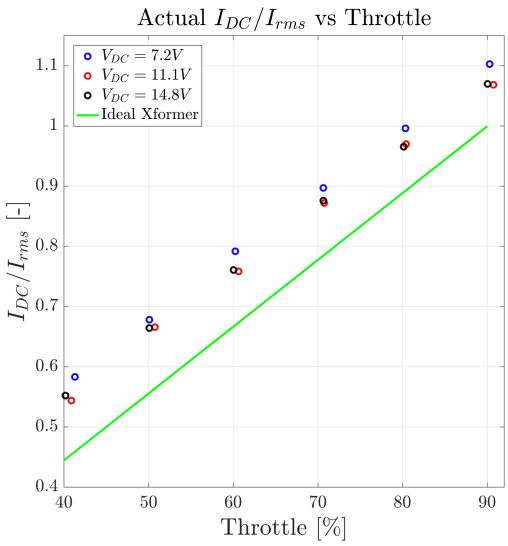

Figure 4.21: ESC transformer diagram for the MultiStar 30A ESC.

For all voltages, the grouping of the points is consistent. To describe the actual ratio of points, a simple linear expression is required:

$$\frac{I_{DC}}{I_{rms}} = C_1 T_R + C_0 \tag{4.57}$$

$$I_{DC} = (C_1 T_R + C_0) I_{rms} \tag{4.58}$$

where C_1 and C_0 are coefficients that describe the transformation from DC to AC current. Note that $C_1 = 10/9$ and $C_0 = 0$ for an ideal transformer. Both $C_1 > 0$ and $C_0 > 0$, to make physical sense. One expects a more efficient ESC to have a smaller value of C_0, meaning the actual ESC transformer curve lies close to the ideal curve. Transformation coefficients C_1 and C_0 are easy to find in post processing by using a best fit approximation. In section 4.2.4, it will be shown that C_1 and C_0 are related to the MOSFET switching frequency f_{sw}. Combining the motor model with

equation 4.57 is shown in figure 4.22.

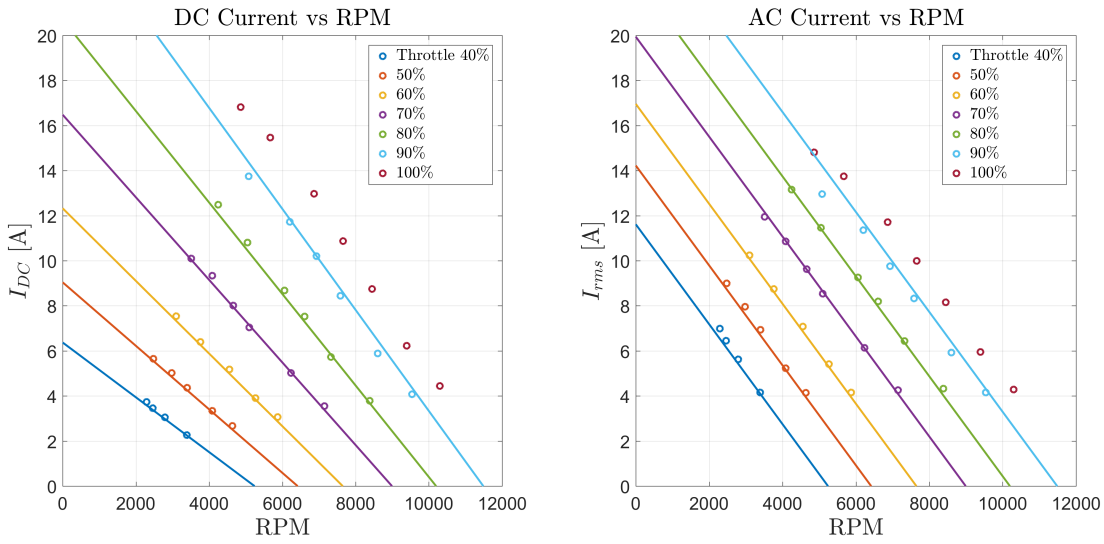

Figure 4.22: Predicted and experimentally obtained Q vs RPM curve for an EMAX 1900KV motor and MultiStar 30A ESC at $V_{DC} = 7.2$ V.

Combining the ESC transformer relations with the equivalent motor model allows one to determine the required DC current/power. Using the rms current, throttle, and equation 4.57, the DC power can be evaluated:

$$P_{DC} = V_{DC} I_{DC}$$

$$P_{DC} = V_{DC}(C_1 T_R + C_0) I_{rms} \tag{4.59}$$

which shows that the DC power is correlated to both the throttle and the rms current. Recall that throttle sets the speed of the motor and the rms current sets the torque of the motor. Therefore, it makes sense that both variables appear in the final DC power equation. With AC and DC power determined, an expression for ESC power is made.

4.2.4 ESC Power Losses

An ESC is a non ideal component, indicating that power must be lost as current conducts across the device. Section 4.2.1 showed the literature review of MOSFET power losses, revealing that MOSFETs contain both conductive and switching power losses. The goal of this section is to arrive at an ESC power loss equation which contain both a switching loss and a conduction loss, similar to equation 4.51. From section 4.1.4, the motor model has already identified an $I_{rms}^2 R_{ESC}$ conductive power loss across the ESC. The remaining item to quantify is the ESC's switching losses.

Considering again the diagram in figure 4.11, a power balanced can be used to relate the DC and AC power to the power lost to the ESC P_{ESC}:

$$P_{DC} = P_{ESC} + P_{AC}$$

It was shown in the previous sections, that the AC power can be found from the motor parameters and the operating point, whereas the DC power is determined based on the ESC transformer relations. With P_{DC} and P_{AC} defined, the difference in power is the ESC power:

$$P_{ESC} = P_{DC} - P_{AC} \tag{4.60}$$

Combining equations 4.42 and 4.59 with equation 4.60, the ESC power can be

determined:

$$P_{ESC} = V_{DC}(C_1 T_R + C_0) I_{rms} - \sqrt{\frac{27}{10}}(\frac{3}{\sqrt{2}\pi} V_{DC} T_R - I_{rms} R_{ESC}) I_{rms}$$

$$P_{ESC} = \underbrace{V_{DC} I_{rms}((C_1 - \frac{3}{\pi}\sqrt{\frac{27}{20}})T_R + C_0)}_{\text{switching losses}} + \underbrace{\sqrt{\frac{27}{10}} R_{ESC} I_{rms}^2}_{\text{conduction losses}} \tag{4.61}$$

Equation 4.61 contains both switching losses and conduction losses, mimicking the power loss form of a single MOSFET, equation 4.51. The result of this analysis is that each ESC can be represented as a single equivalent MOSFET, with some modifications. In an ESC, two MOSFETs are active at any one time, meaning that each MOSFET $V_{DS} = V_{DC}/2$. Having two connected in series means that the total voltage of both MOSFETs is $V_{DS,1} + V_{DS,2} = V_{DC}$. The equivalent MOSFET model contains this, as $2V_{DS,equiv} = V_{DC}$. Additionally, the switching frequency decreases as the throttle increases, and is consistent with the results displayed in figure 4.15, which shows lower power poss P_{ESC} for the same I_{rms}. Mathematically, this result can be represented by:

$$2P_{MOSFET,sw} = P_{ESC,sw}$$

$$V_{DC} I_{rms}(t_{on} + t_{off}) f_{sw} = V_{DC} I_{rms}((C_1 - \frac{3}{\pi}\sqrt{\frac{27}{20}})T_R + C_0)$$

$$(t_{on} + t_{off}) f_{sw} = (C_1 - \frac{3}{\pi}\sqrt{\frac{27}{20}})T_R + C_0 \tag{4.62}$$

Recall that for a MOSFET, t_{on} and t_{off} are set by the physical characteristics of the device, whereas f_{sw} is controlled via the duty cycle to the gate of the MOSFET. The microcontroller of the ESC, shown in figure 2.21, regulates the amount of

switching to keep the motor commutating based of the phase voltages and the user throttle.

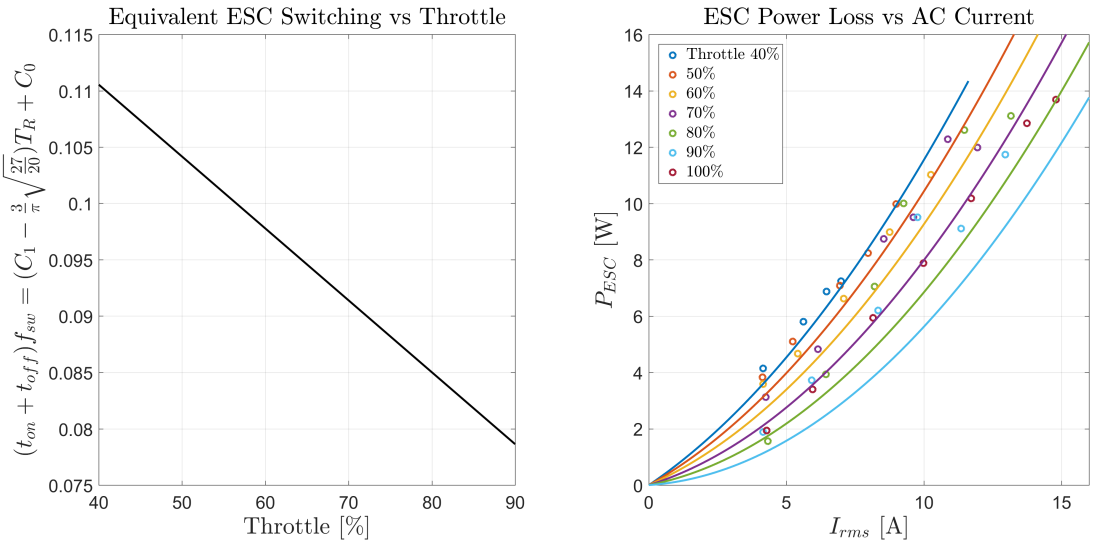

Figure 4.23: Left: ESC transformer diagram for a MultiStar 30A ESC ($C_1 = 1.02$, $C_0 = 0.16$). Right: Predicted and experimentally obtained P_{ESC} vs I_{rms} curve for an EMAX 1900KV motor and MultiStar 30A ESC at $V_{DC} = 7.2$ V.

Plotting equation 4.62 vs throttle shows how the C_1 and C_0 describe a decreasing switching frequency with an increased throttle. It was shown in figures 2.34 and 2.35 in section 2.3.2, that increasing the throttle linearly decreases the number of switching events. Similarly, the conduction losses are modeled as having an equivalent resistance $R = \sqrt{\frac{27}{10}}R_{ESC}$. The factor $\sqrt{\frac{27}{10}}$ is consistent with having defined the R_{ESC} in the previous motor modeling section and needing to convert to active AC power.

A linear transformation relation, specifically equation 4.57, seems well suited to describe the conversion between DC and AC current and is critical to model correctly, as time of flight estimates for electric aircraft are dependent upon the total DC current drawn from the battery. With the AC motor model and the transfor-

mation relations, the designer is well equipped to answer many design challanges. Equations 4.57 and the AC motor equations match experimental results well for all voltages, but further work is required for the ESC model.

Experimental results show that this model for ESC works well for $V_{DC} = 7.2$ V, but contains some inconsistencies at higher voltages, which are not easily explained. At higher voltages, the expression for ESC power, equation 4.61, both under-predicts and over-predicts the power loss of the ESC. Additionally, there is a noticeable offset in P_{ESC}, which remains unaccounted for in the current model, shown in figure 4.24. It appears that conduction losses are overly pessimistic, as there is an widening gap between experimental and expected results, even at moderate I_{rms}.

This result is surprising, considering both the DC power and AC power are accurately predicted, and that the final form of the ESC power equation agrees, in theory, with the MOSFET power loss equations 4.61 and 4.51. The ESC power loss discrepancy results in an over-estimation of cooling requirements for an ESC on board an electric aircraft. However, the important prediction of DC current draw remains matches with experimental results, which is important as this determines an aircraft's endurance.

Figure 4.24: ESC modeling results for a MultiStar 30A ESC and EMAX 935 KV motor with the high voltage setup.

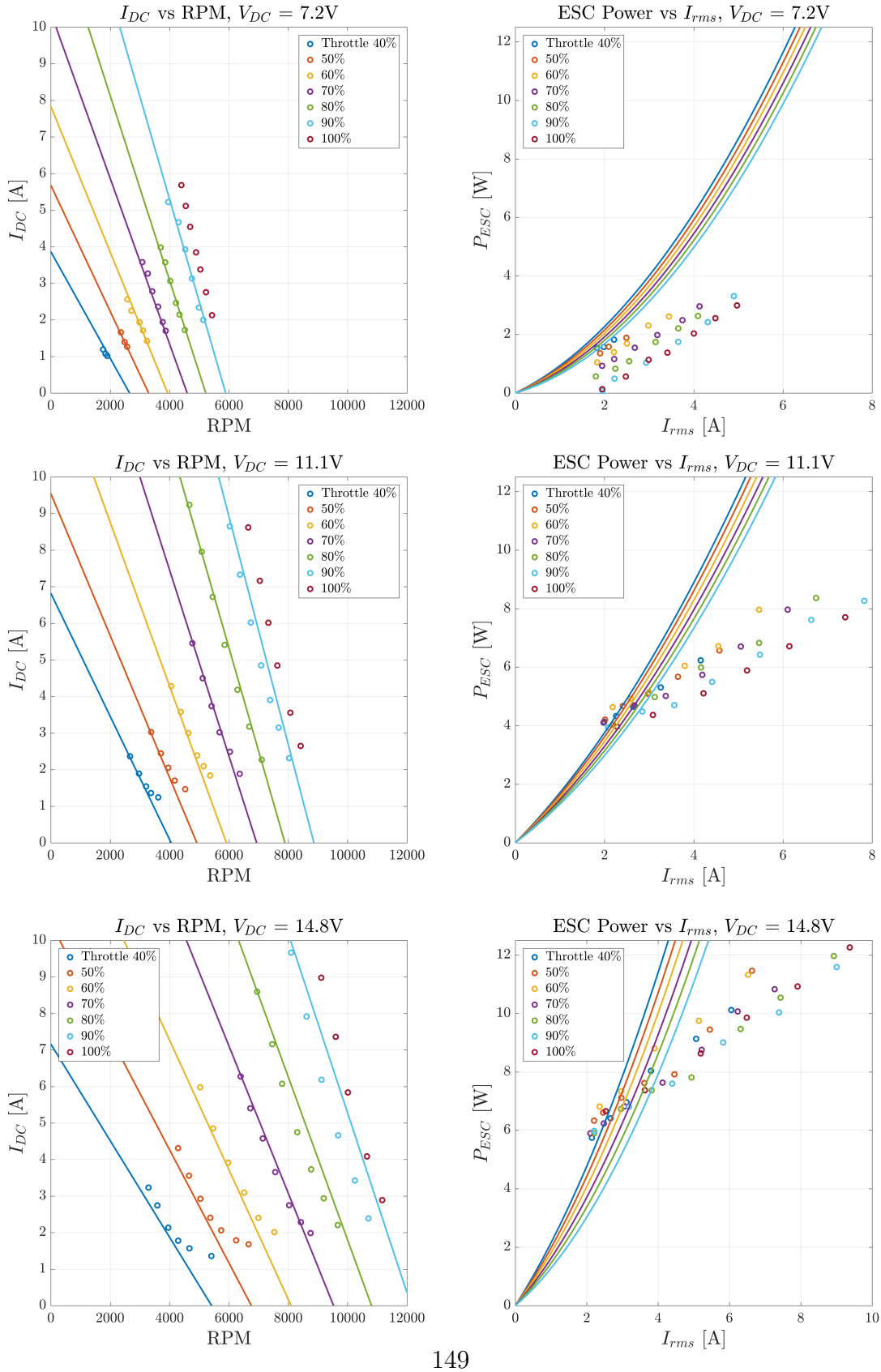

It is believed that some of this inaccuracy between model and experimental results is attributed to the high voltage experimental setup. In section 3.5.5, it was described how a different current measurement technique was used, and contains some inherent low pass filtering. At higher RPMs, the effect of this filtering is believed to augment the power content of the signals, indicating that experimental results may contain some inaccuracies.

Additionally, it will be shown in the next Chapter that using equation 4.61 to predict ESC efficency reveals a linear decrease in ESC efficiency, something that was first observed in [42]. Figure 4.25 shows on the left a plot of efficiency vs torque

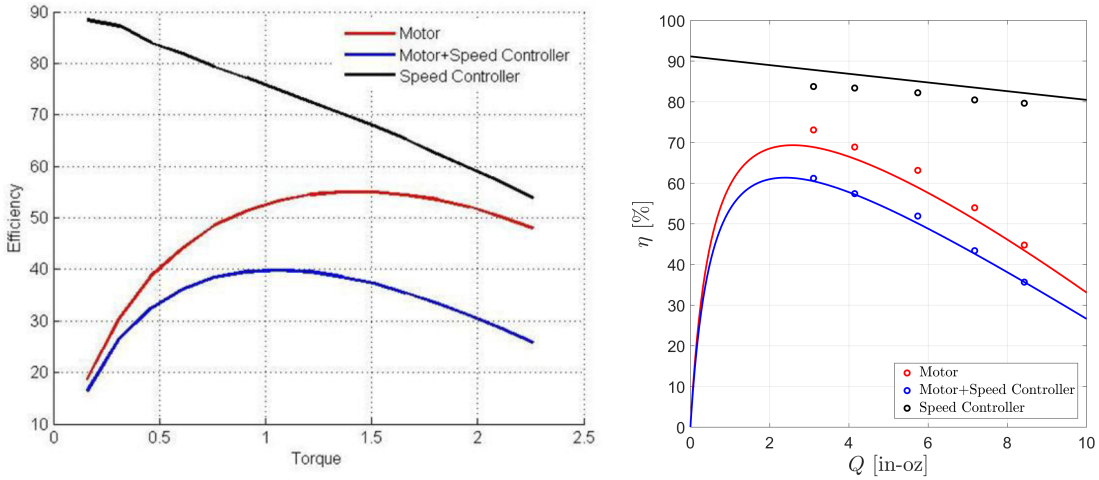

Figure 4.25: System efficiency vs load, image on the left was taken from [42] and image on the right was produced by this thesis. Note the linear decrease in ESC efficiency.

from [42], and on the right information collected and predicted on ESC, motor, and system performance from this thesis. It is believed that the P_{ESC} prediction is correct because it matches observations from external authors. This further supports the idea that the high voltage setup contains some error in recording AC power.

Future work consists of further refining the AC power analyzers to allow for

only current shunt resistors to be used for all voltages. Shunt resistors are favorable to non-invasive hall effect sensors because shunts allow for nearly instantaneous capturing of the current signal, and do not contain any filtering. Nevertheless, this model is applied to all BLDC motor and ESC tests, and the results are shown in Chapter 5.

Chapter 5: Experimental Results

Experimental tests were conducted with the dynamometer to study the performance of different combinations of BLDC motors and ESCs under different DC voltages. Motors between 920 KV to 2500 KV, 7 pole pairs, and at voltages of 7.2 V (2S), 11.1 V (3S), and 14.8 V (4S) were tested. Basic parameters of the motors are outlined in table 5.1 and the motors are shown in figure 5.1. For each BLDC motor, L_{AB} represents the total non-rotating inductance measured between lines A and B with a precision inductance meter in mili-henries, and Rec. Prop. is the manufacturer recommended rotor diameter in inches.

Table 5.1: BLDC motors tested using the custom dynamometer.

Motor	KV [RPM/V]	Mass [g]	N_p [-]	V_{DC} [V]	Rec. Prop [in]	L_{AB} [μH]
DJI 2212	920	50	7	7.2, 11.1, 14.8	8-12	29.5
EMAX 2213	935	55	7	7.2, 11.1, 14.8	8-12	30.6
EMAX ECO2306	1700	32	7	7.2, 11.1	3-5	17.6
EMAX MT2206	1900	35	7	7.2, 11.1	3-5	16.0
EMAX RS2205	2300	31	7	7.2, 11.1	3-5	10.4
Samguk Series	2500	36	7	7.2	3-5	8.2

Not all motors could be tested at higher voltages due to the magtrol magnetic

hysteresis brake's 20,000 RPM limit. This effects higher KV motors, as using 14.8 V on a 2500 KV (or RPM/V) motor results in a no-load speed of 37,000 RPM, nearly double the brake's limit. Additionally, motors with low KV rating quickly saturated the brake's torque rating, and so motors with rating below 800 KV could not be tested.

Figure 5.1: BLDC motors tested using the custom dynamometer.

ESC selection was restricted by the inherent nature of using a magnetic brake, as it contained a repeatable static 3.1 in-oz cogging torque [24]. All motors and ESCs must produce a sufficient initial torque to overcome this cogging torque before the motor could start spinning. Senorless ESCs use the back EMF from the motor's phases to commutate the motor. As discussed in section 2.3, this is a problem for slowly spinning motors as the back EMF ($V_E = K_E\omega$) is not large enough for the ESC to detect.

Table 5.2: ESCs tested using the custom dynamometer.

ESC	Max Cont. I_{DC} [A]	Voltage Range	Mass [g]
SpiderLite Series	18	2-4S	11
Turnigy MultiStar	30	2-4S	23
DYS BlHeliOpto	40	2-6S	27

In the event of a stalled rotation, modern ESCs stop commutating the motor in order to prevent an electrical short. Therefore, not all ESCs could begin spinning when there was already a substantial load on the motor. It is important to note that this is not a defect of the ESC, but rather a result of using a sensorless ESC in an environment for which it was not designed.

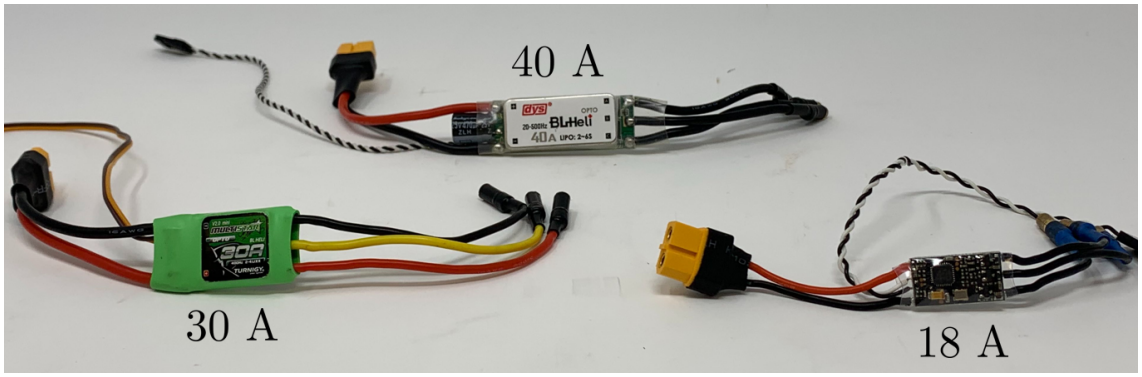

Figure 5.2: ESCs tested using the custom dynamometer.

ESCs that were able to start the motor under the 3.1 in-oz static cogging torque were tested, and shown in table 5.2 and figure 5.2. These ESCs have a max continuous DC current rating of 18 A, 30 A, and 40 A, a voltage range of 2S - 6S, and a mass between 11 g to 27 g. Note how manufacturers provide few details related to the physical parameters of ESCs. Identifying key performance parameters for ESCs is a main focus point of this work.

Sections 5.1 to 5.3 shows the experimental results at different voltages. Section 5.4 describes how system parameters (K_T, R_m, etc.) can be extracted directly from experimental results, and displays these results for all test in tables 5.4 to 5.9. Over the course of experimental testing, additional questions arose related to variation in motors as well as pairing motors to rotors. These topics are covered in sections 5.5 and 5.6.

When plotting the motor performance data, dots represent experimentally obtained data points using the dynamometer, whereas solid lines represent predicted performance curves using the model outlined in the previous Chapter.

5.1 Tests at 7.2V

Figure 5.3: Performance plots - DJI 920 KV - SpiderLite 18A - 7.2V

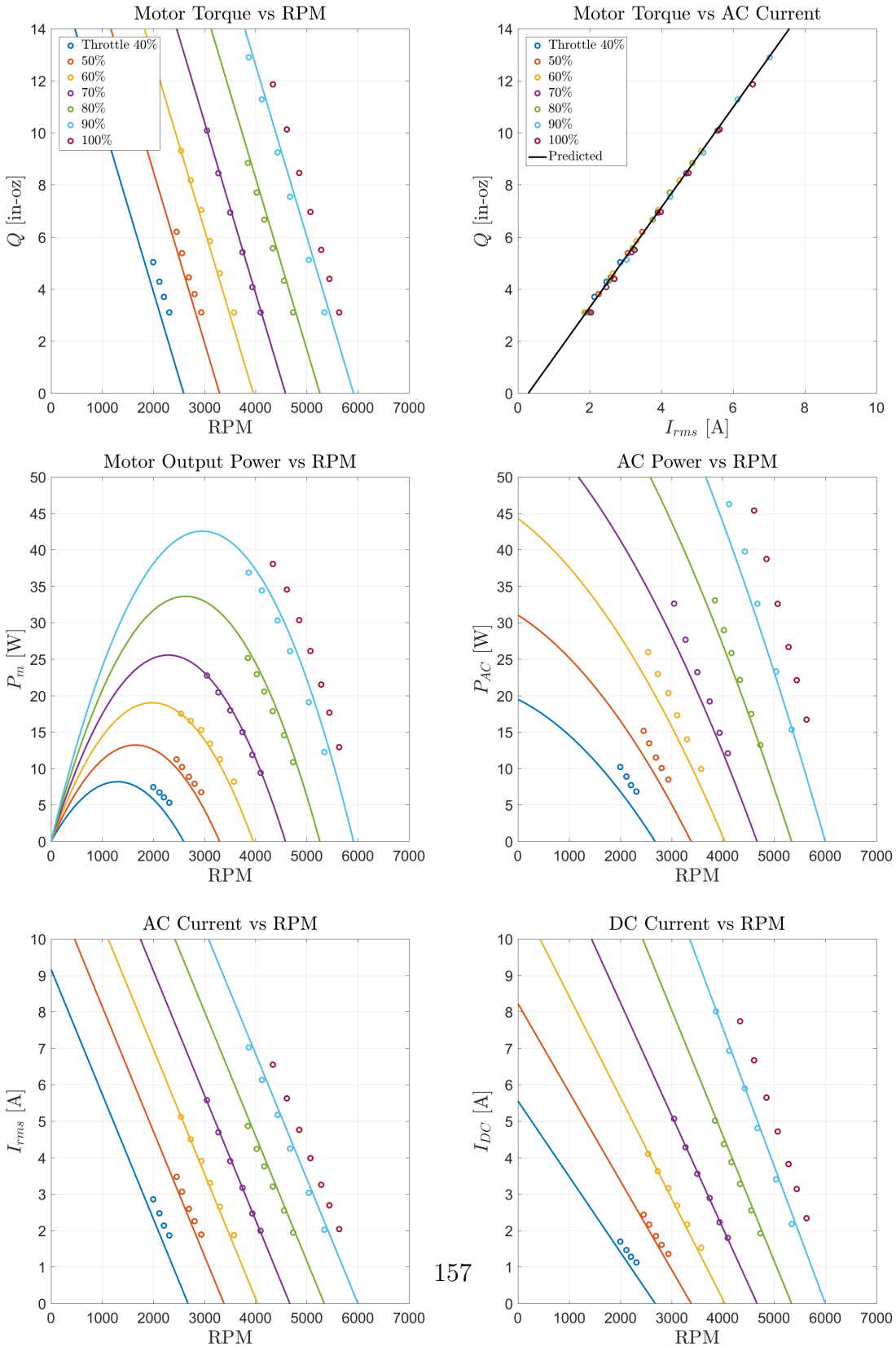

Figure 5.4: Efficiency plots - DJI 920 KV - SpiderLite 18A - 7.2V

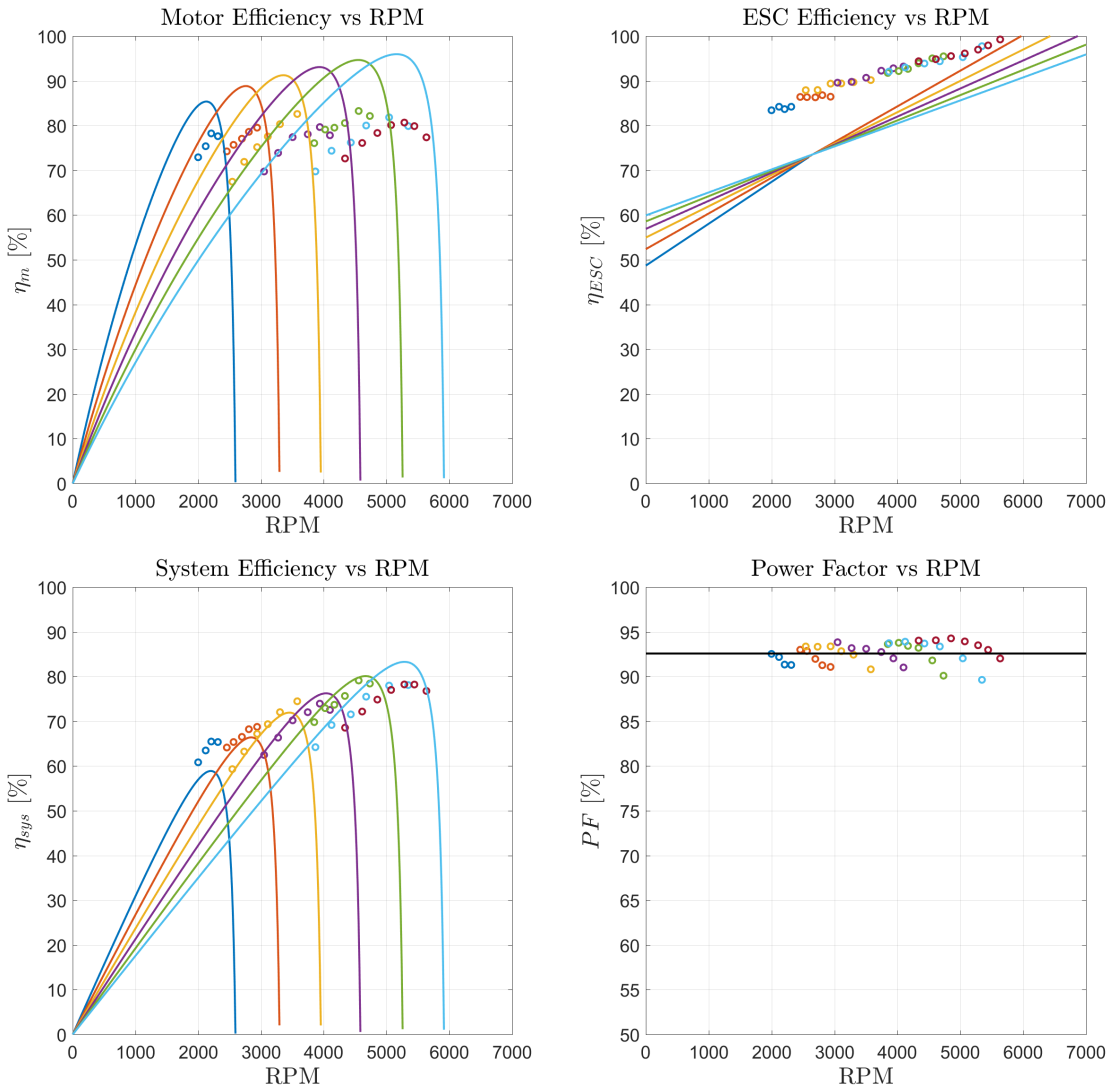

Figure 5.5: Performance plots - DJI 920 KV - MultiStar 30A - 7.2V

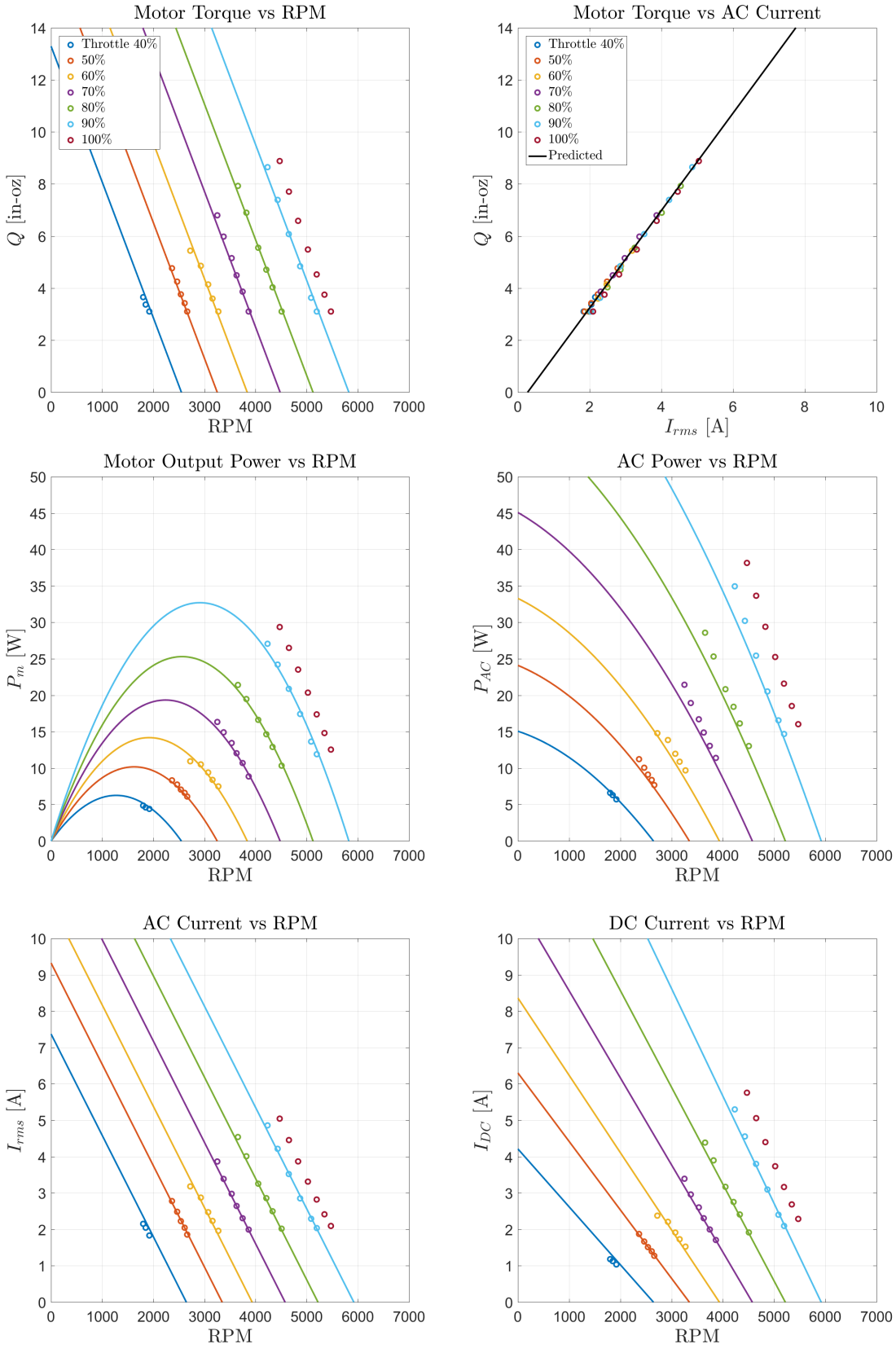

Figure 5.6: Efficiency plots - DJI 920 KV - MultiStar 30A - 7.2V

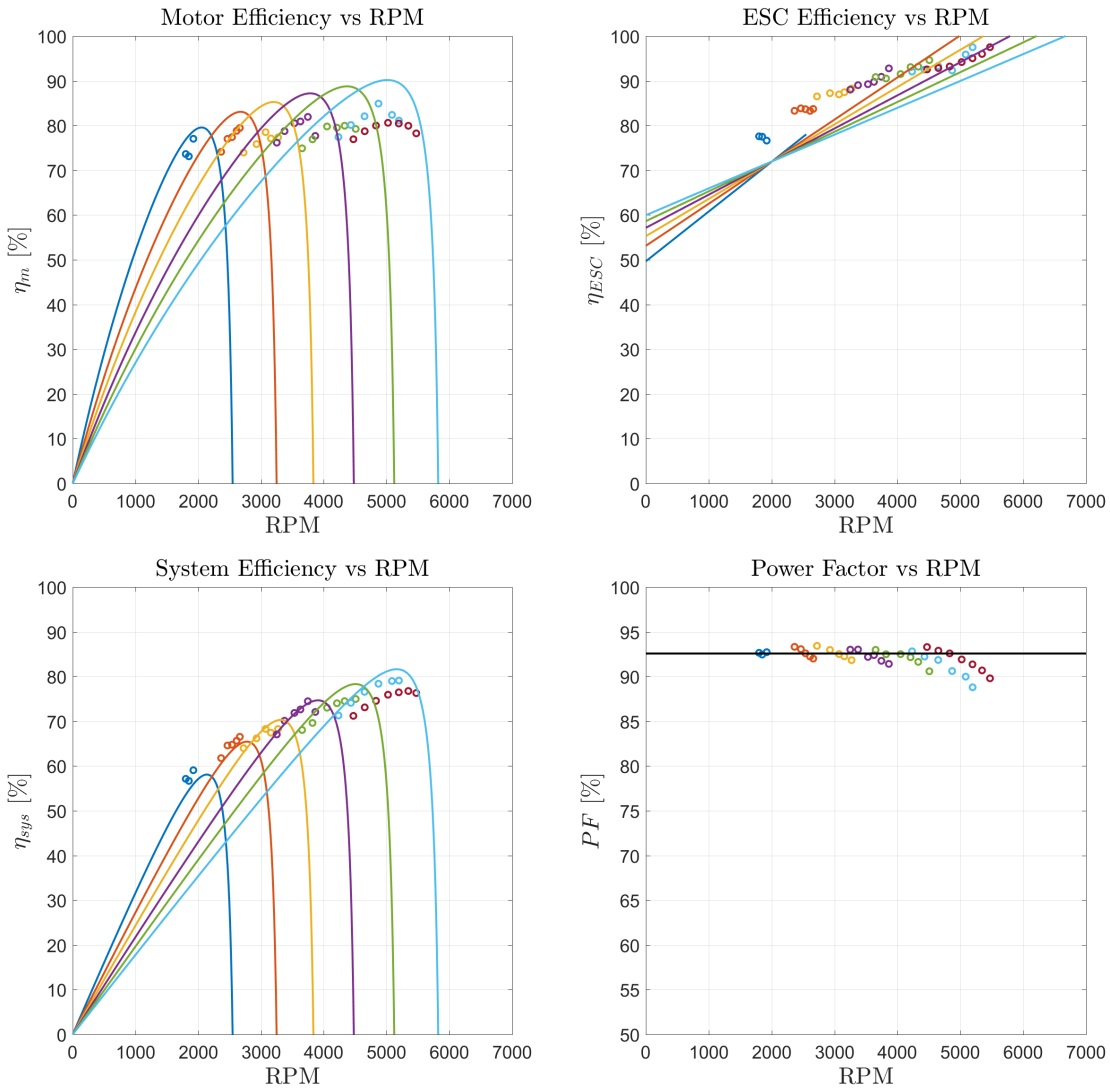

Figure 5.7: Performance plots - DJI 920 KV - DYS BlHeliOpto 40A - 7.2V

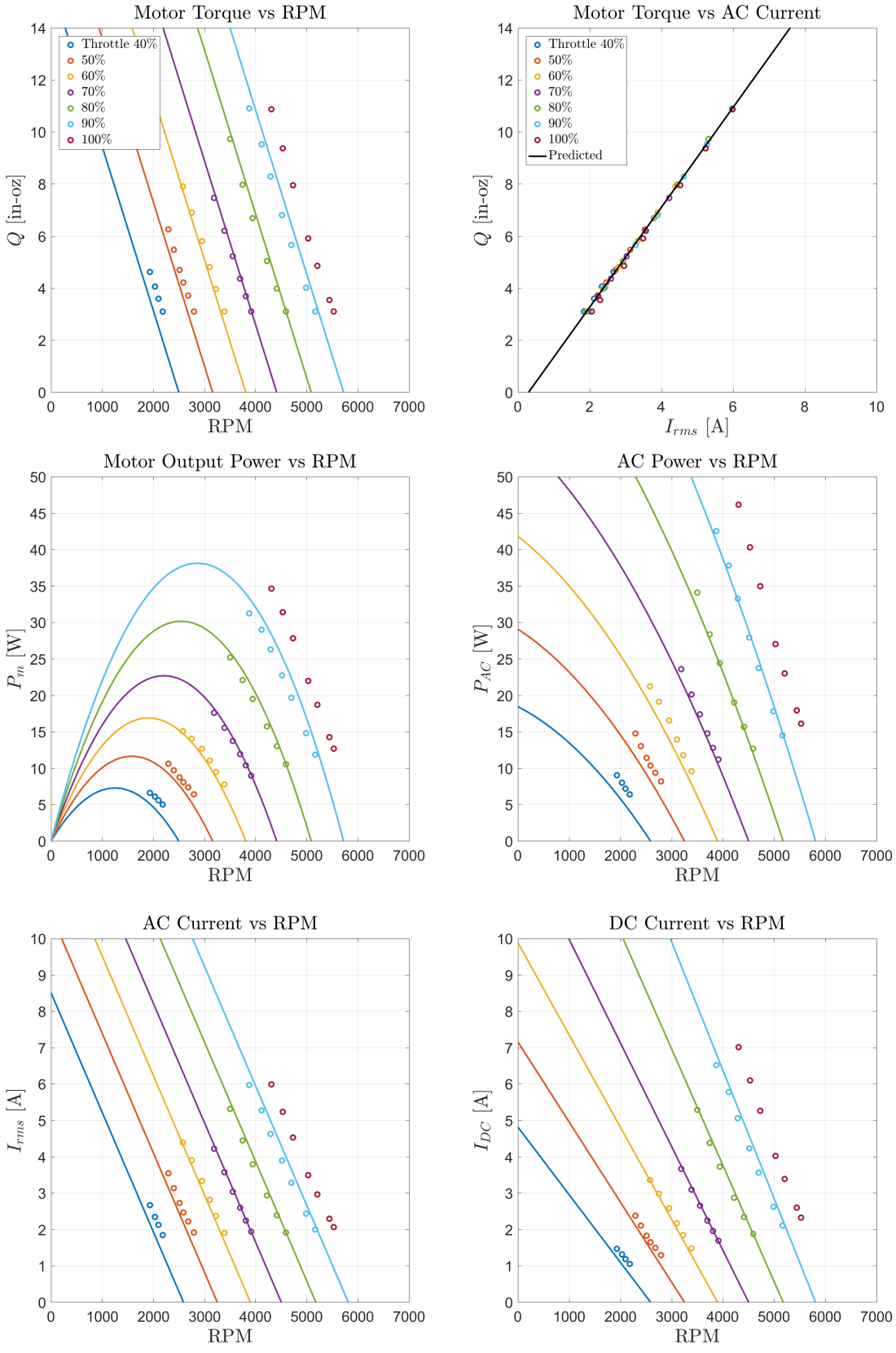

Figure 5.8: Efficiency plots - DJI 920 KV - DYS BlHeliOpto 40A - 7.2V

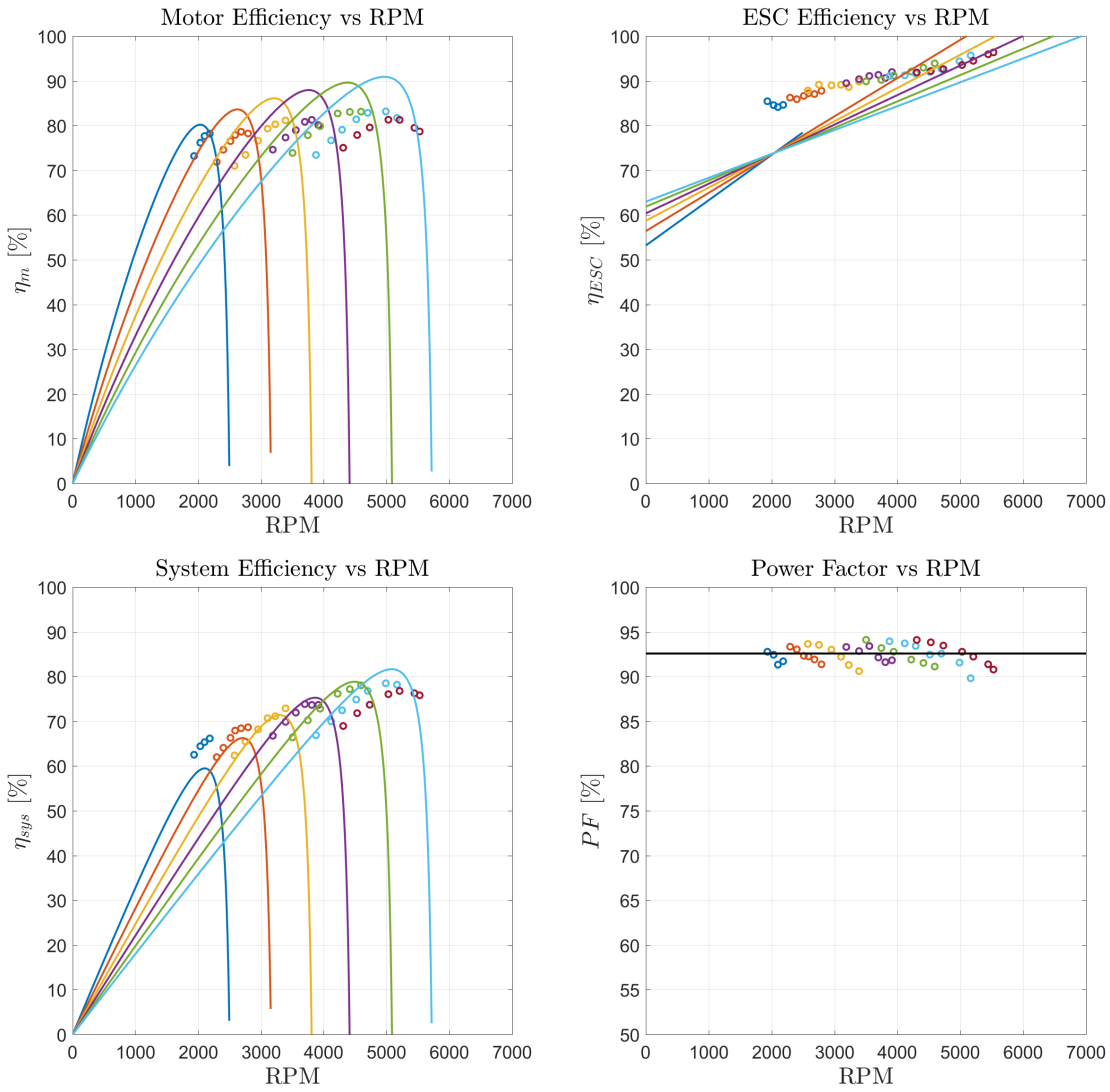

Figure 5.9: Performance plots

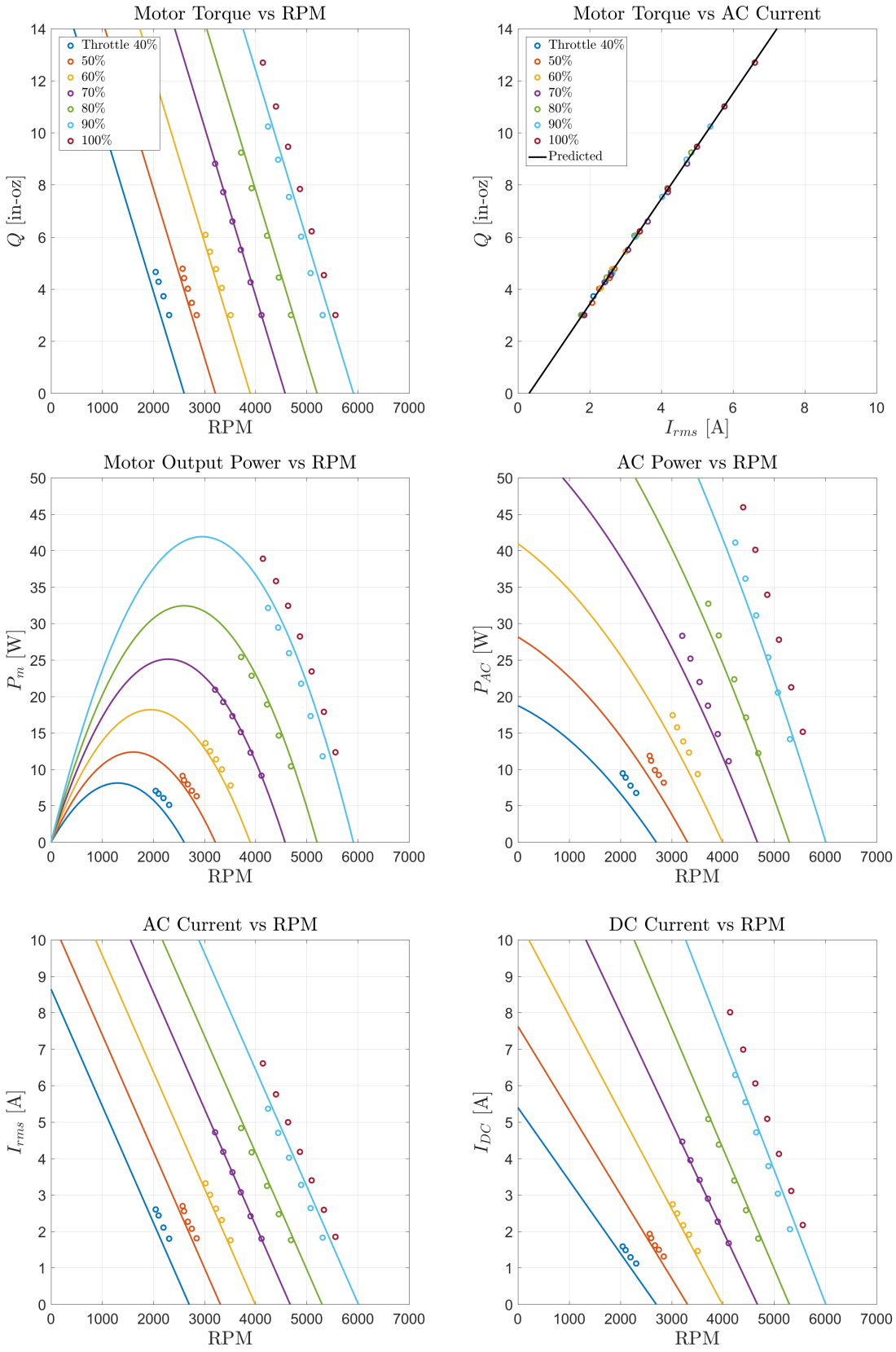

Figure 5.10: Efficiency plots - EMAX 935 KV - SpiderLite 18A - 7.2V

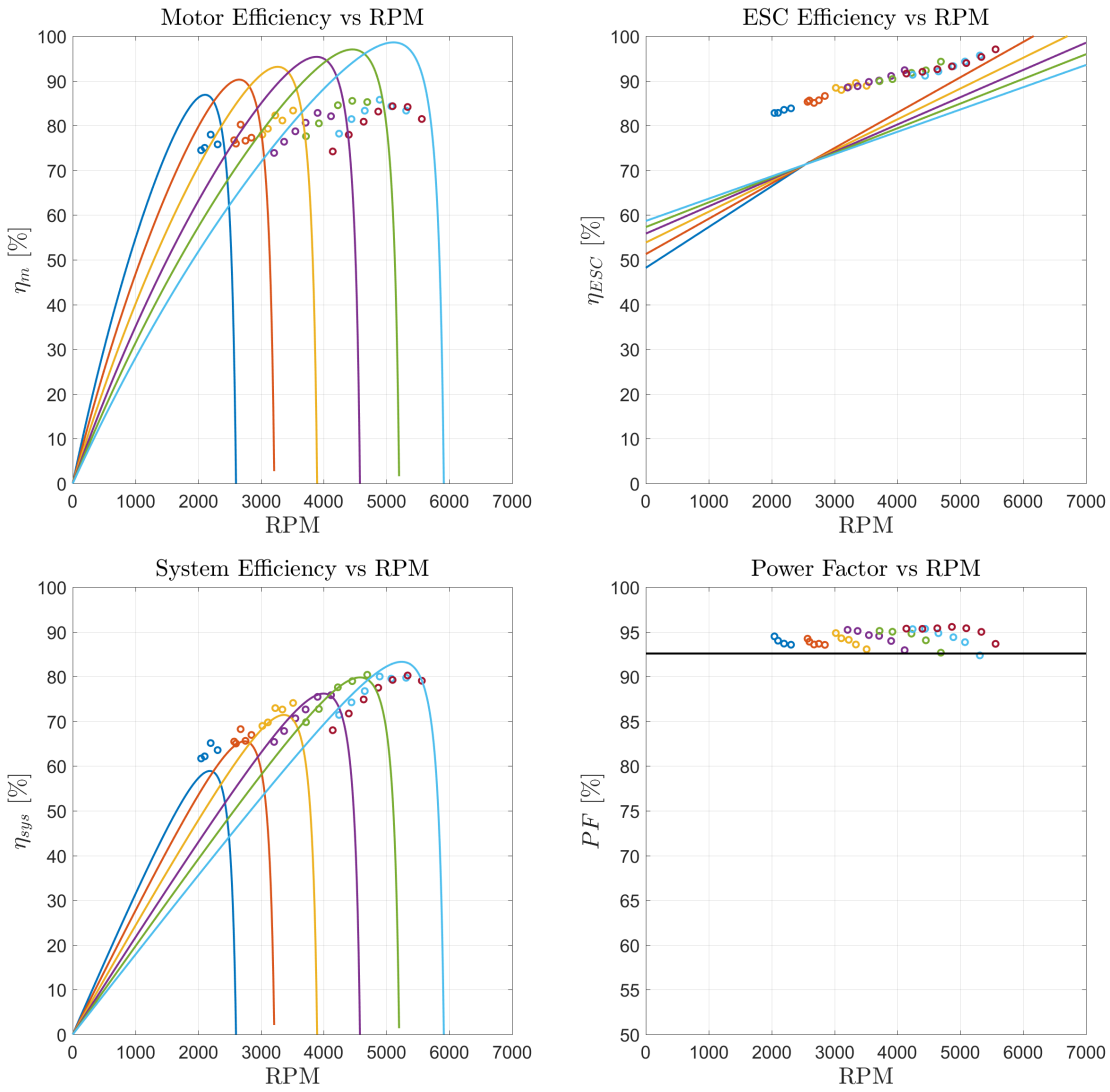

Figure 5.11: Performance plots - EMAX 935 KV - MultiStar 30A - 7.2V

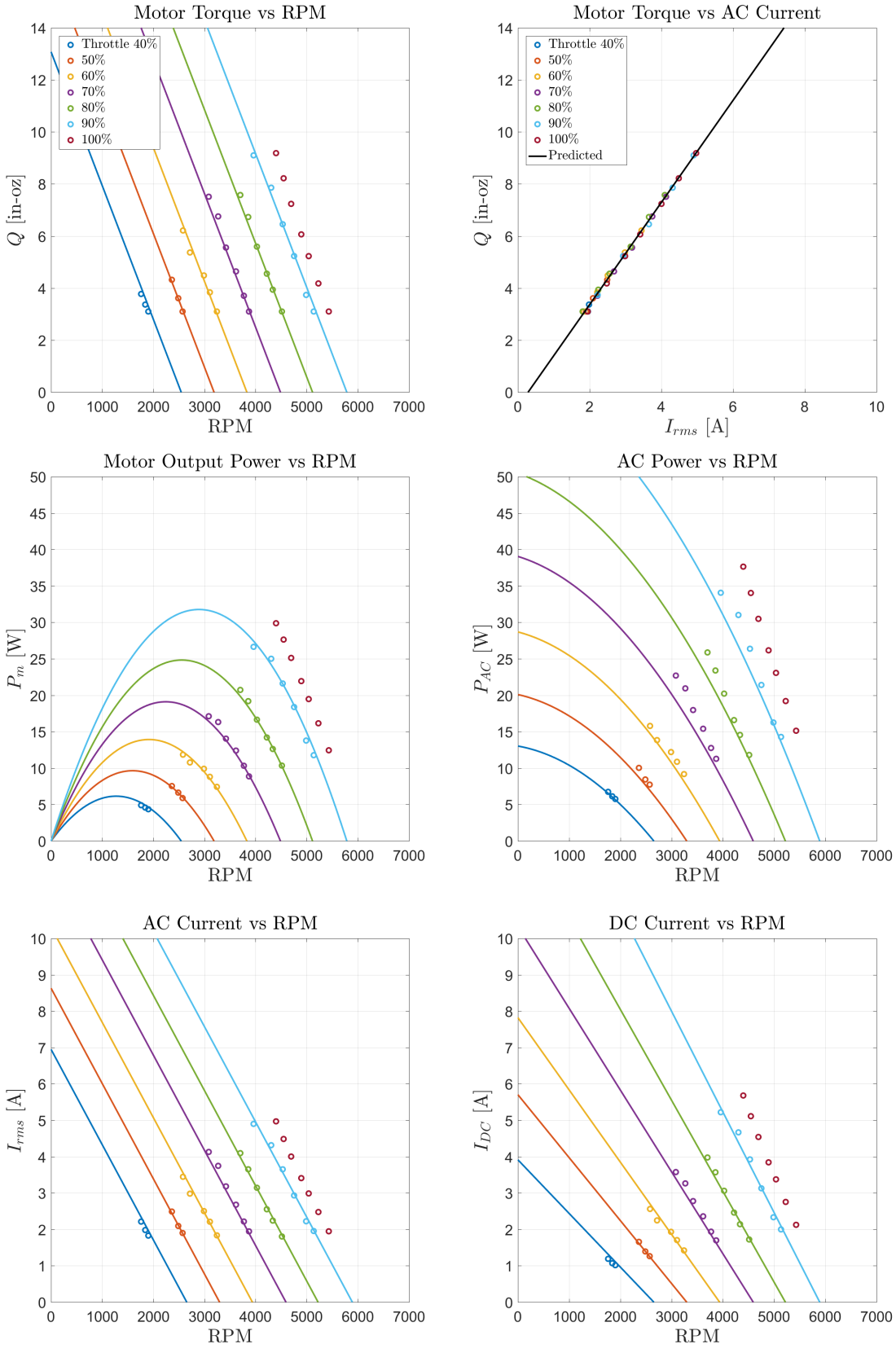

Figure 5.12: Efficiency plots - EMAX 935 KV - MultiStar 30A - 7.2V

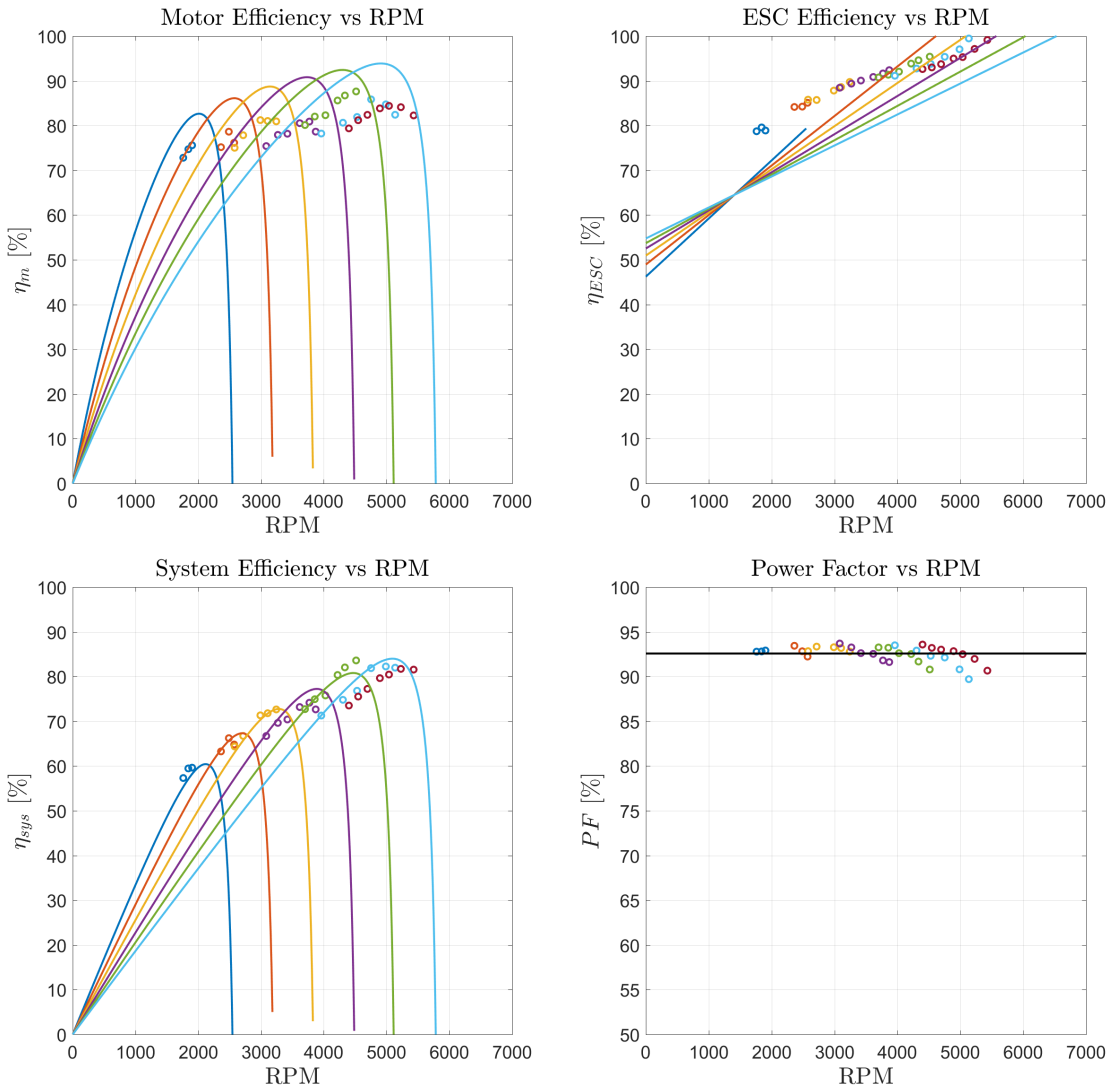

Figure 5.13: Performance plots - EMAX 935 KV - DYS BlHeliOpto 40A - 7.2V

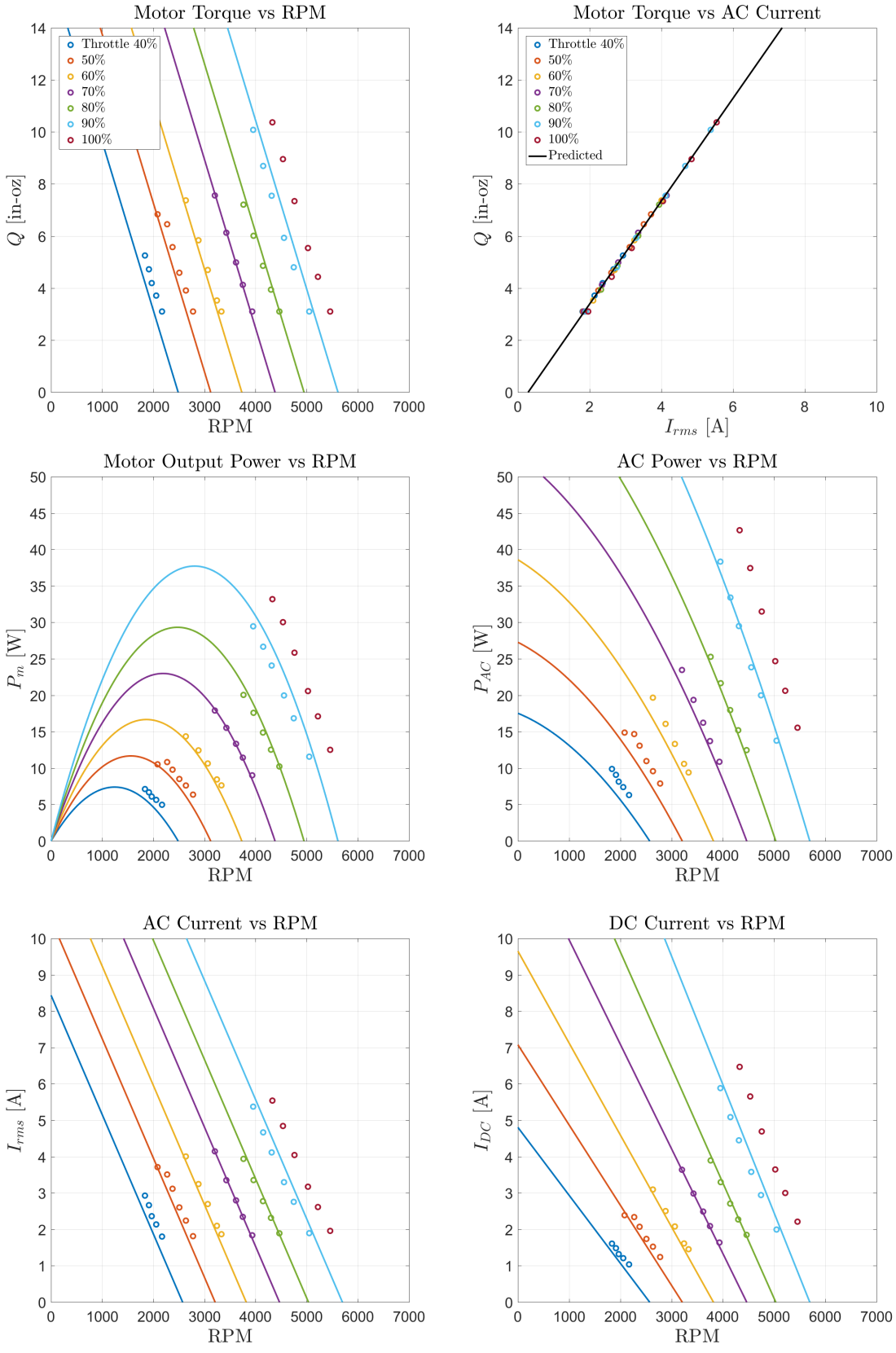

Figure 5.14: Efficiency plots - EMAX 935 KV - DYS BlHeliOpto 40A - 7.2V

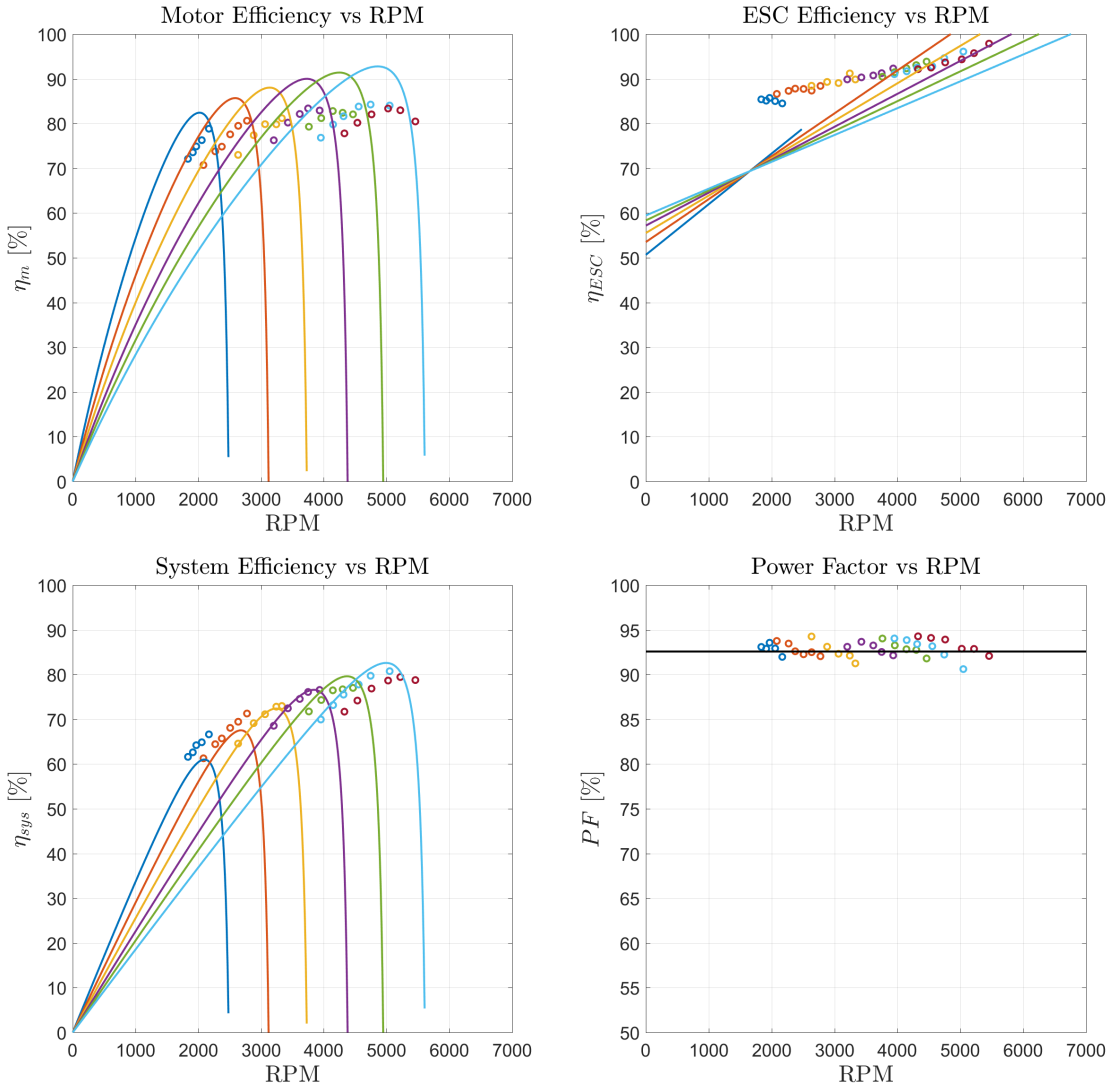

Figure 5.15: Performance plots - EMAX 1700 KV - SpiderLite 18A - 7.2V

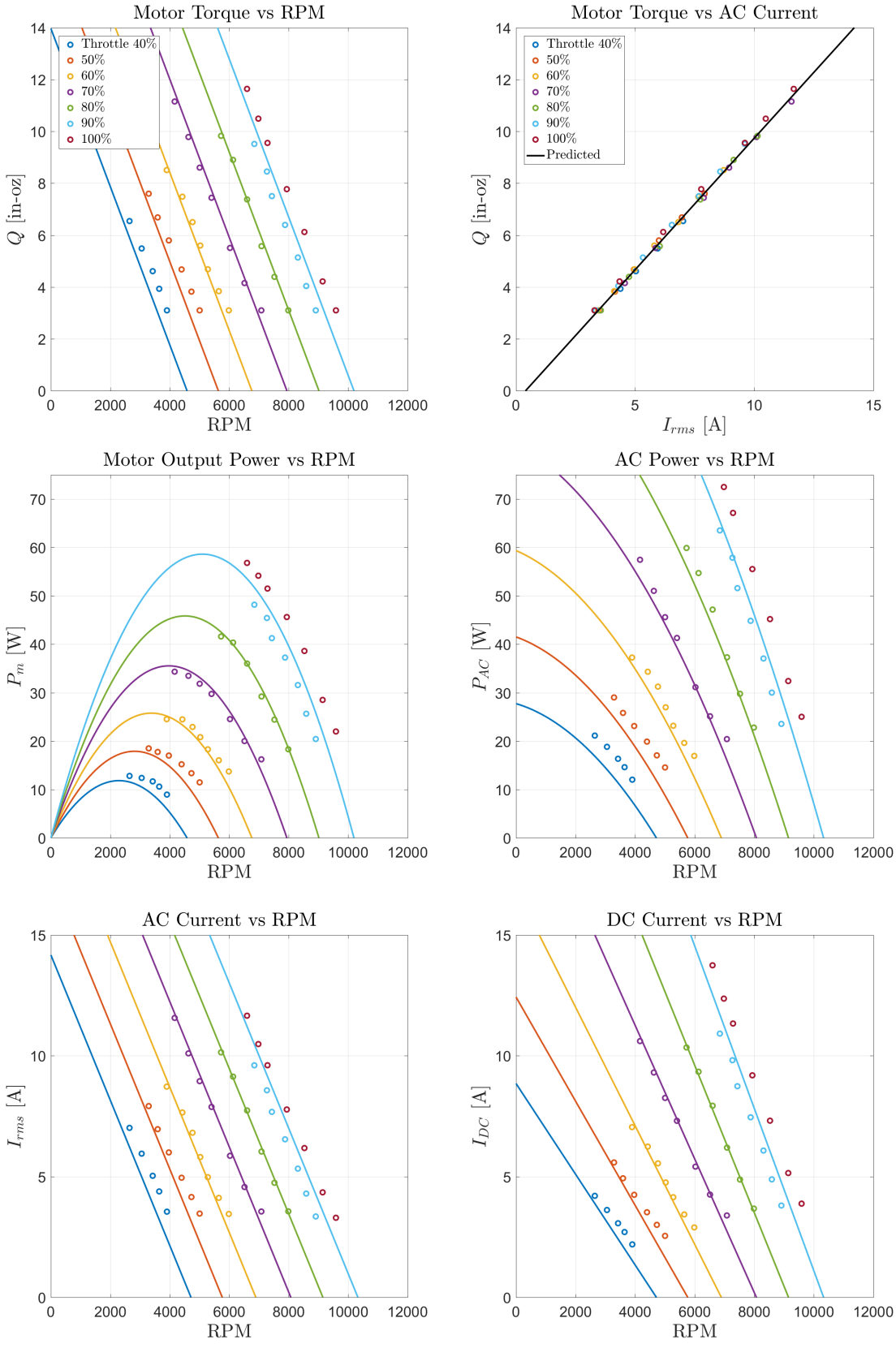

Figure 5.16: Efficiency plots - EMAX 1700 KV - SpiderLite 18A - 7.2V

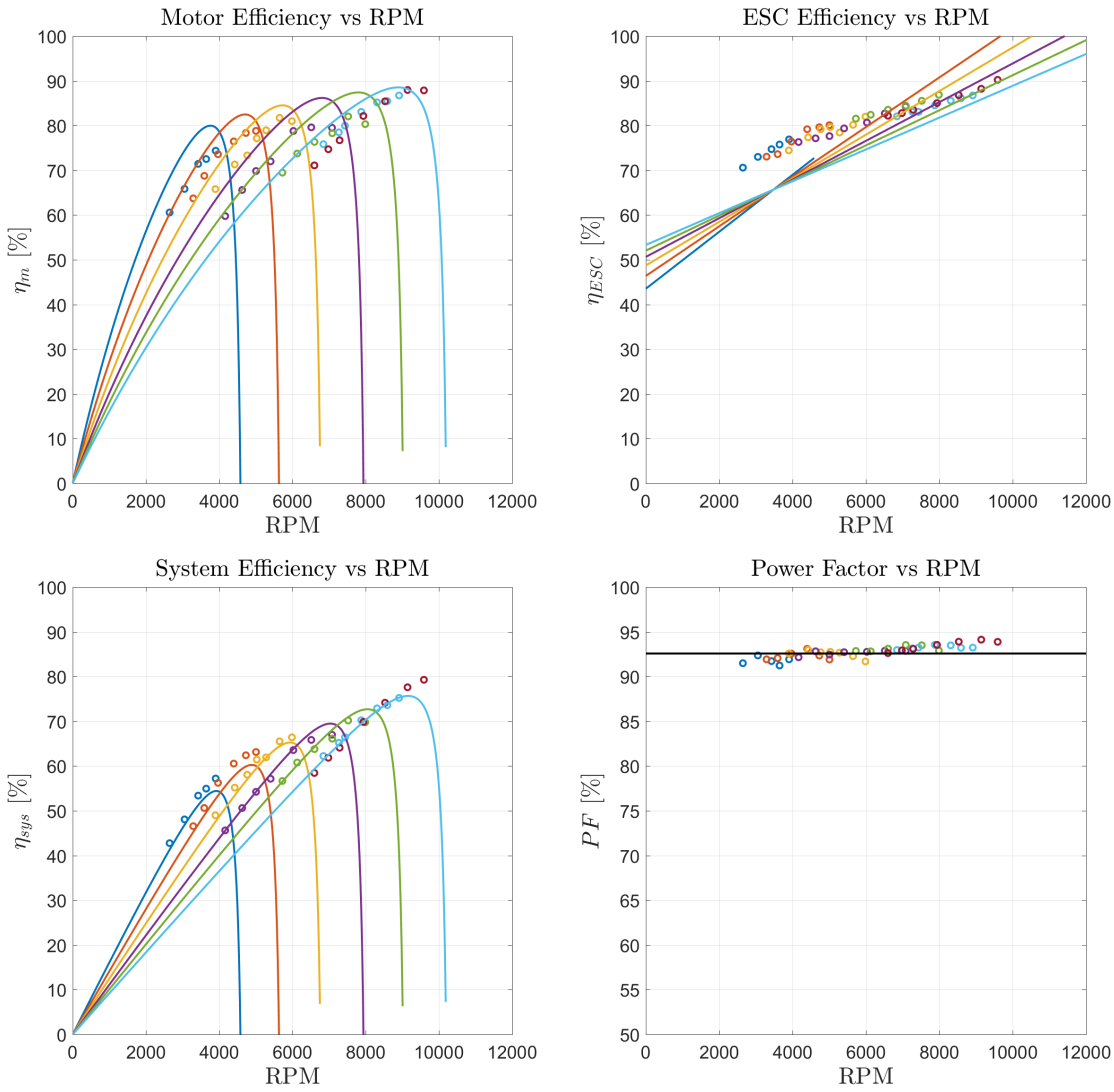

Figure 5.17: Performance plots - EMAX 1700 KV - MultiStar 30A - 7.2V

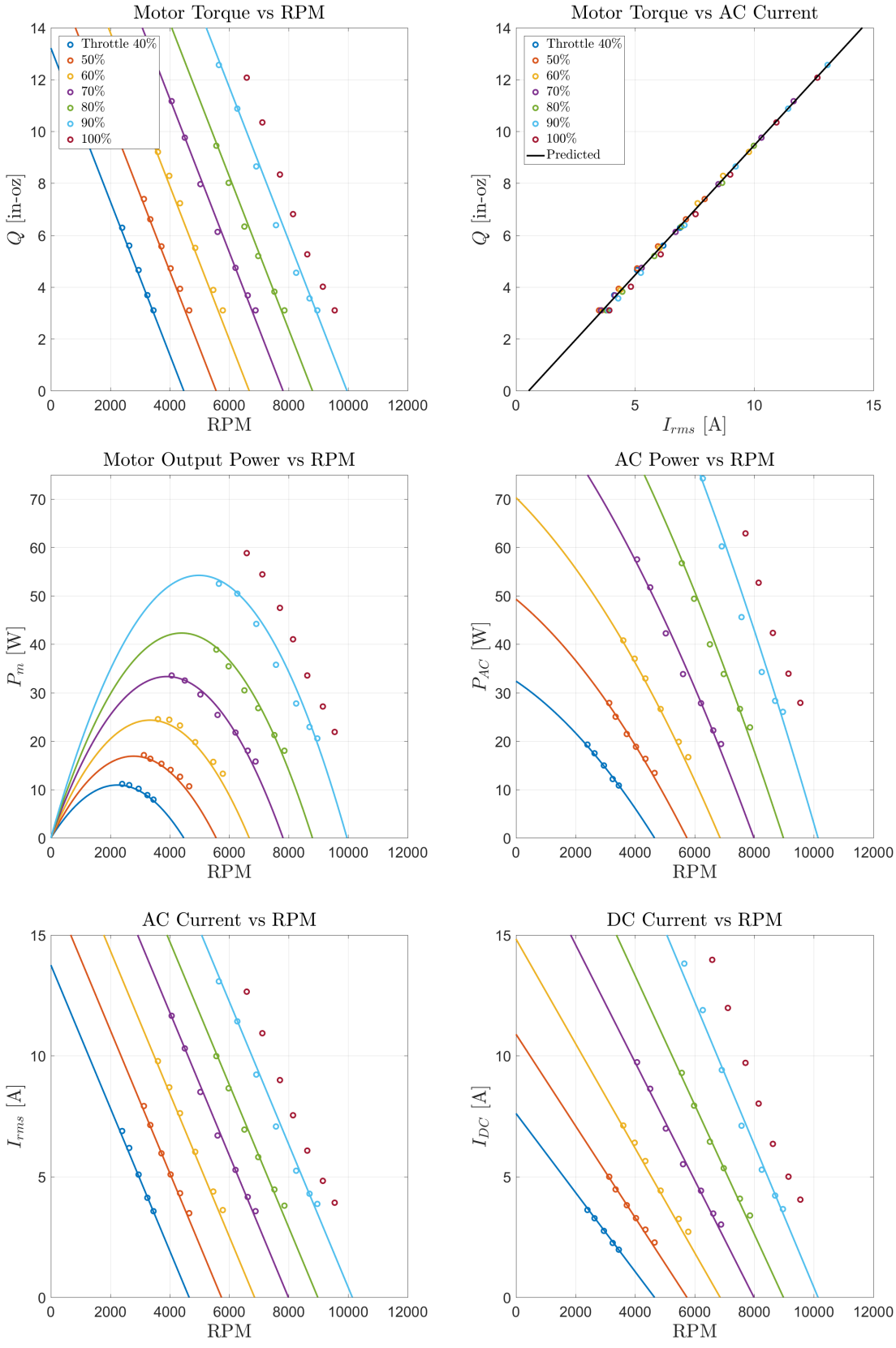

Figure 5.18: Efficiency plots - EMAX 1700 KV - MultiStar 30A - 7.2V

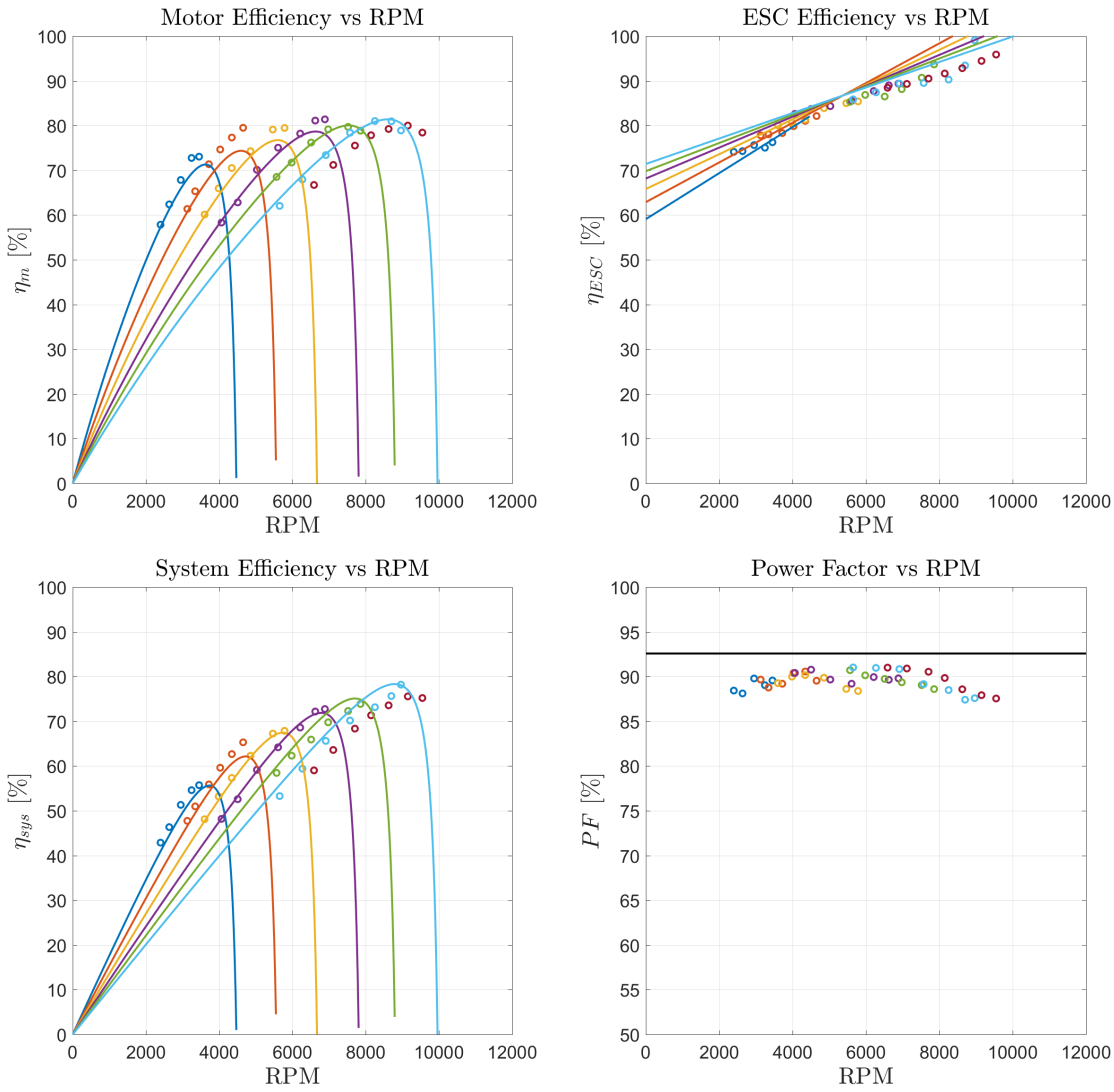

Figure 5.19: Performance plots - EMAX 1700 KV - DYS BlHeliOpto 40A - 7.2V

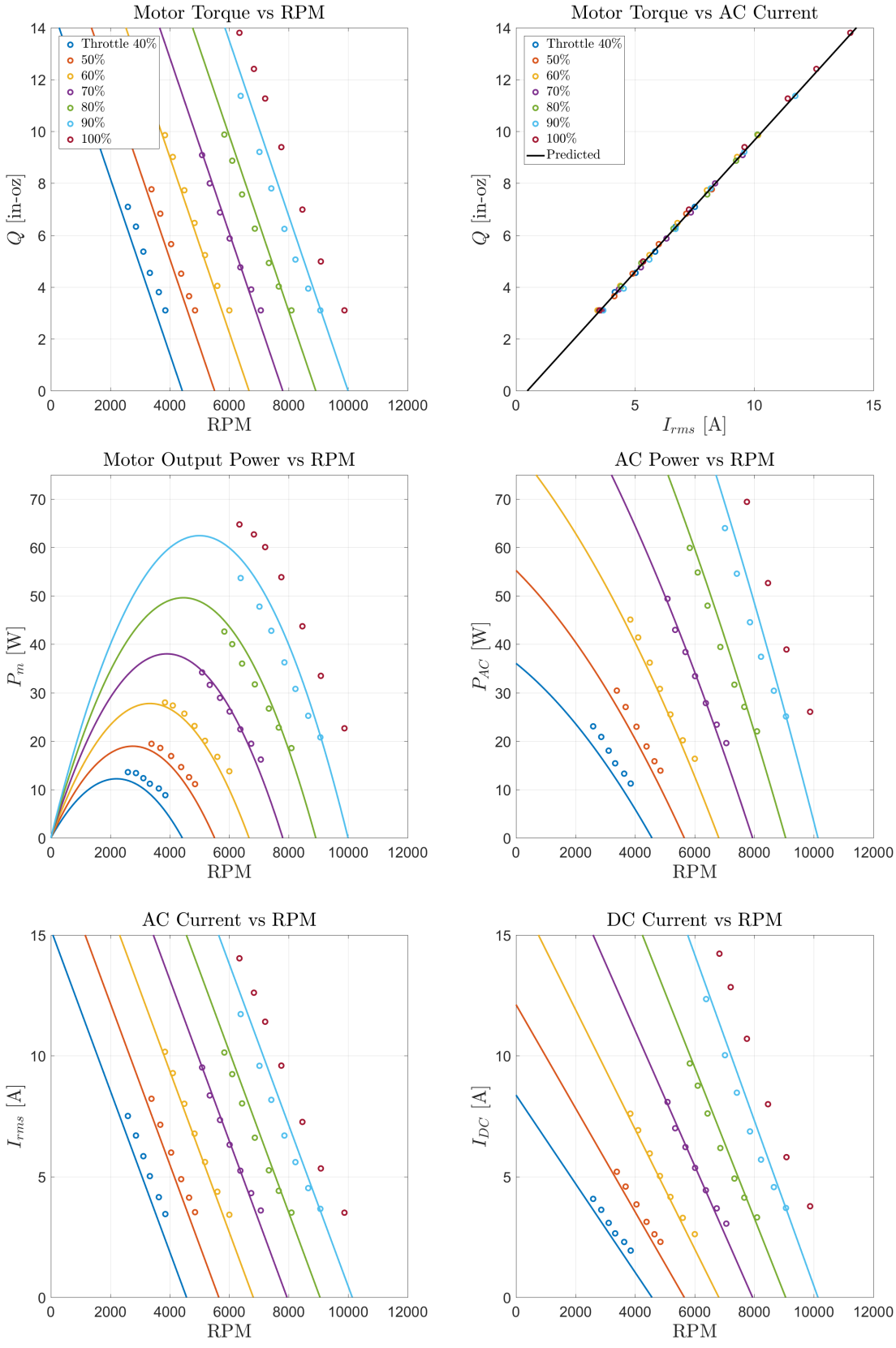

Figure 5.20: Efficiency plots - EMAX 1700 KV - DYS BlHeliOpto 40A - 7.2V

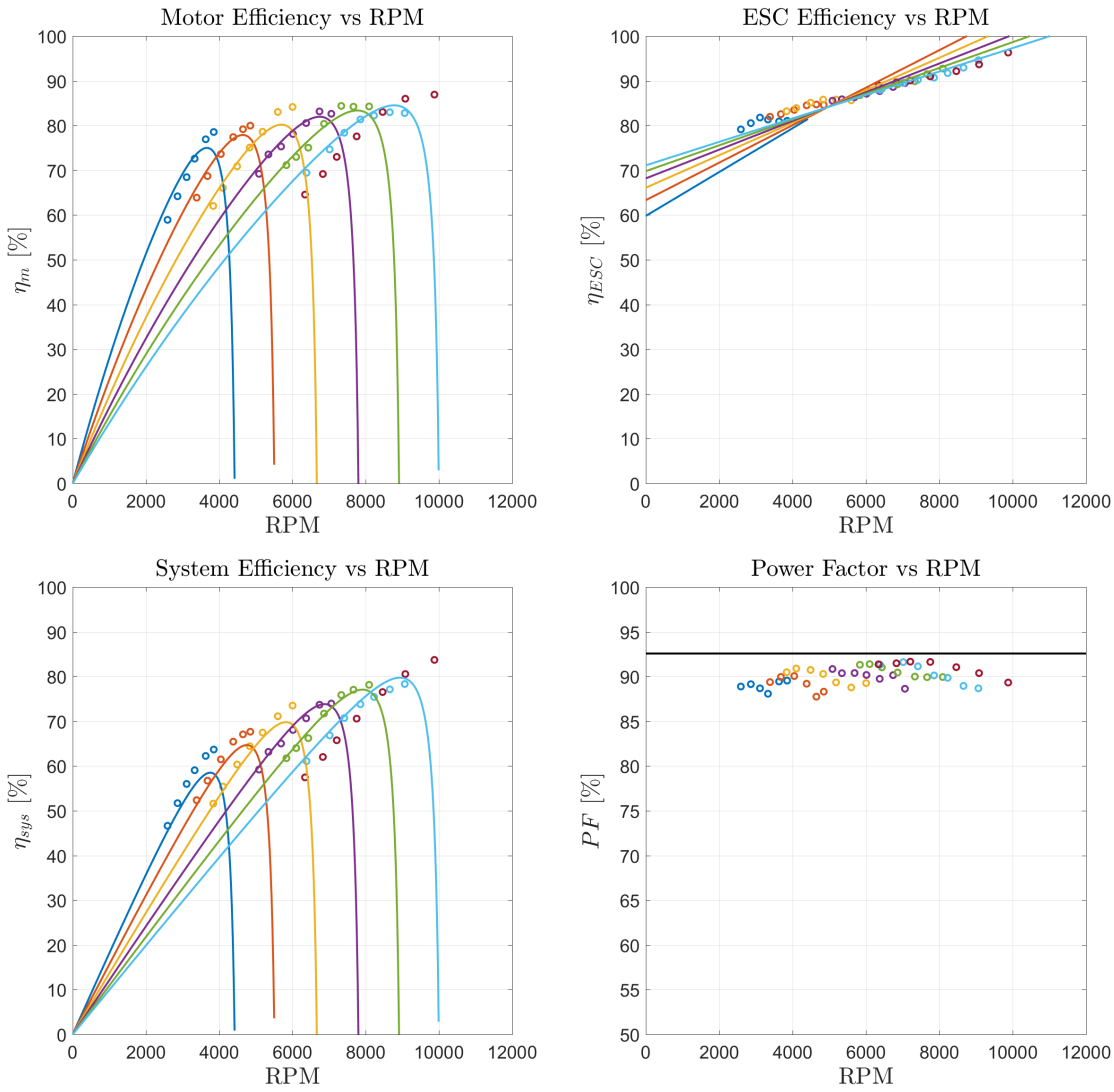

Figure 5.21: Performance plots - EMAX 1900 KV - SpiderLite 18A - 7.2V

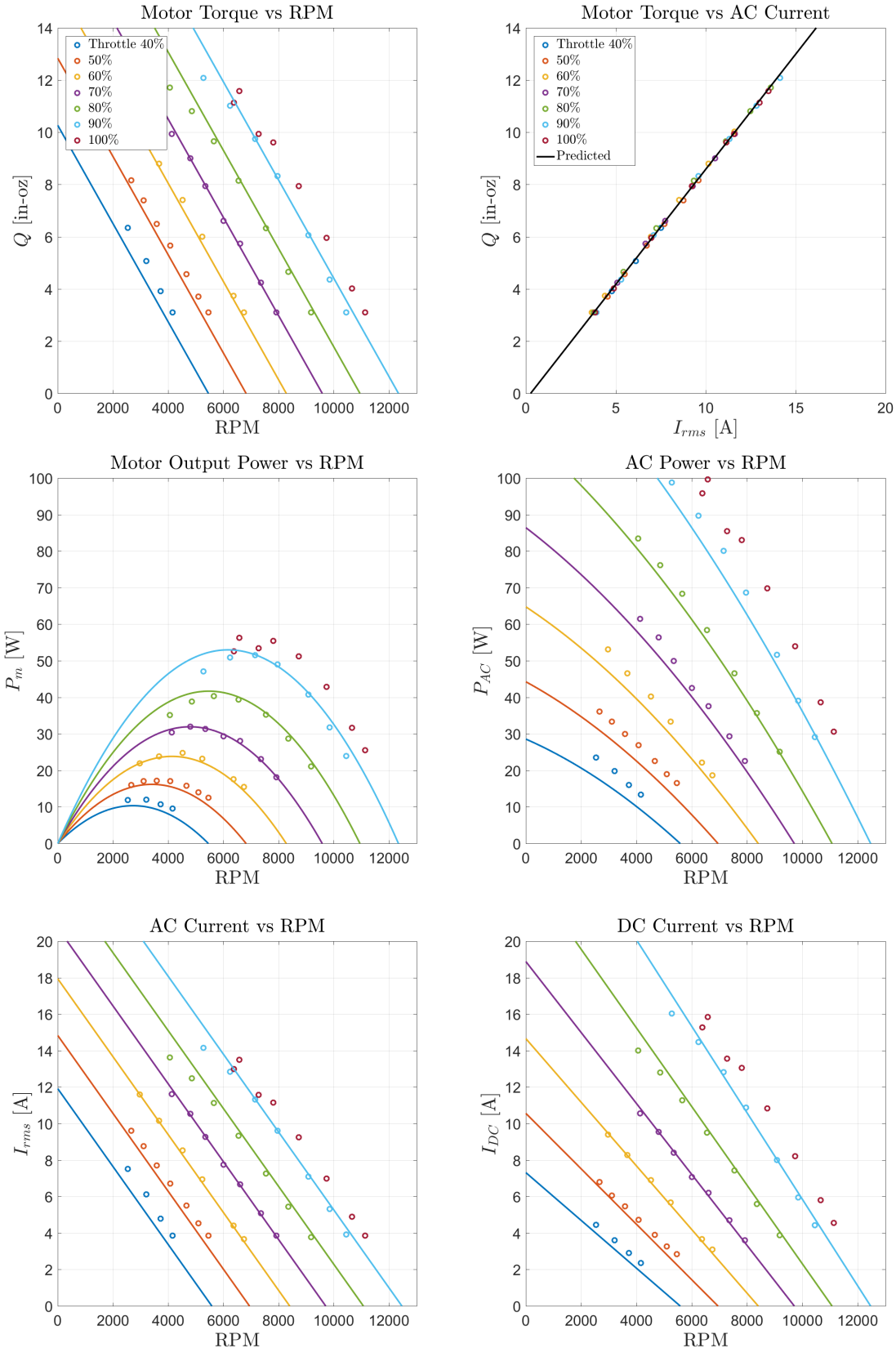

Figure 5.22: Efficiency plots - EMAX 1900 KV - SpiderLite 18A - 7.2V

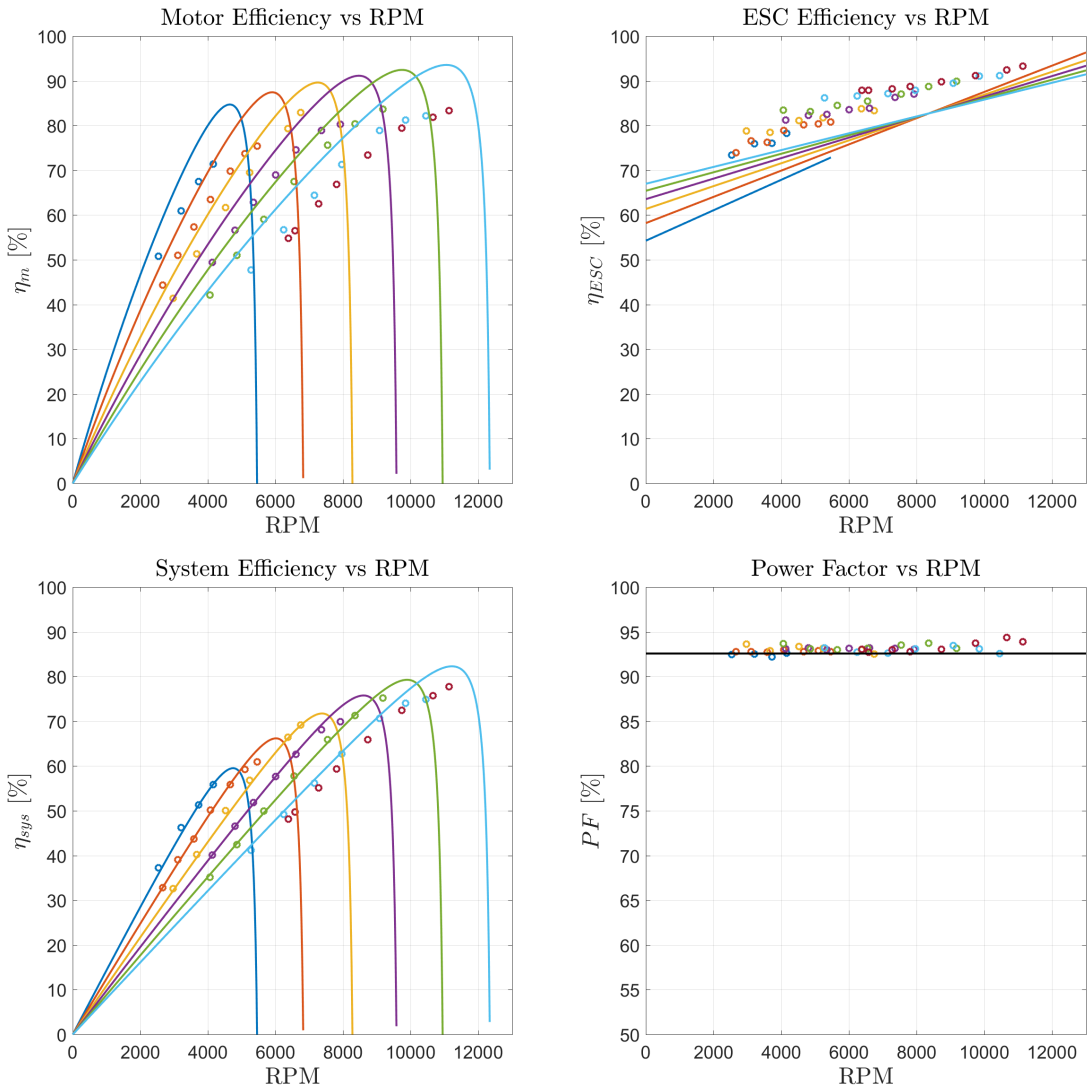

Figure 5.23: Performance plots - EMAX 1900 KV - MultiStar 30A - 7.2V

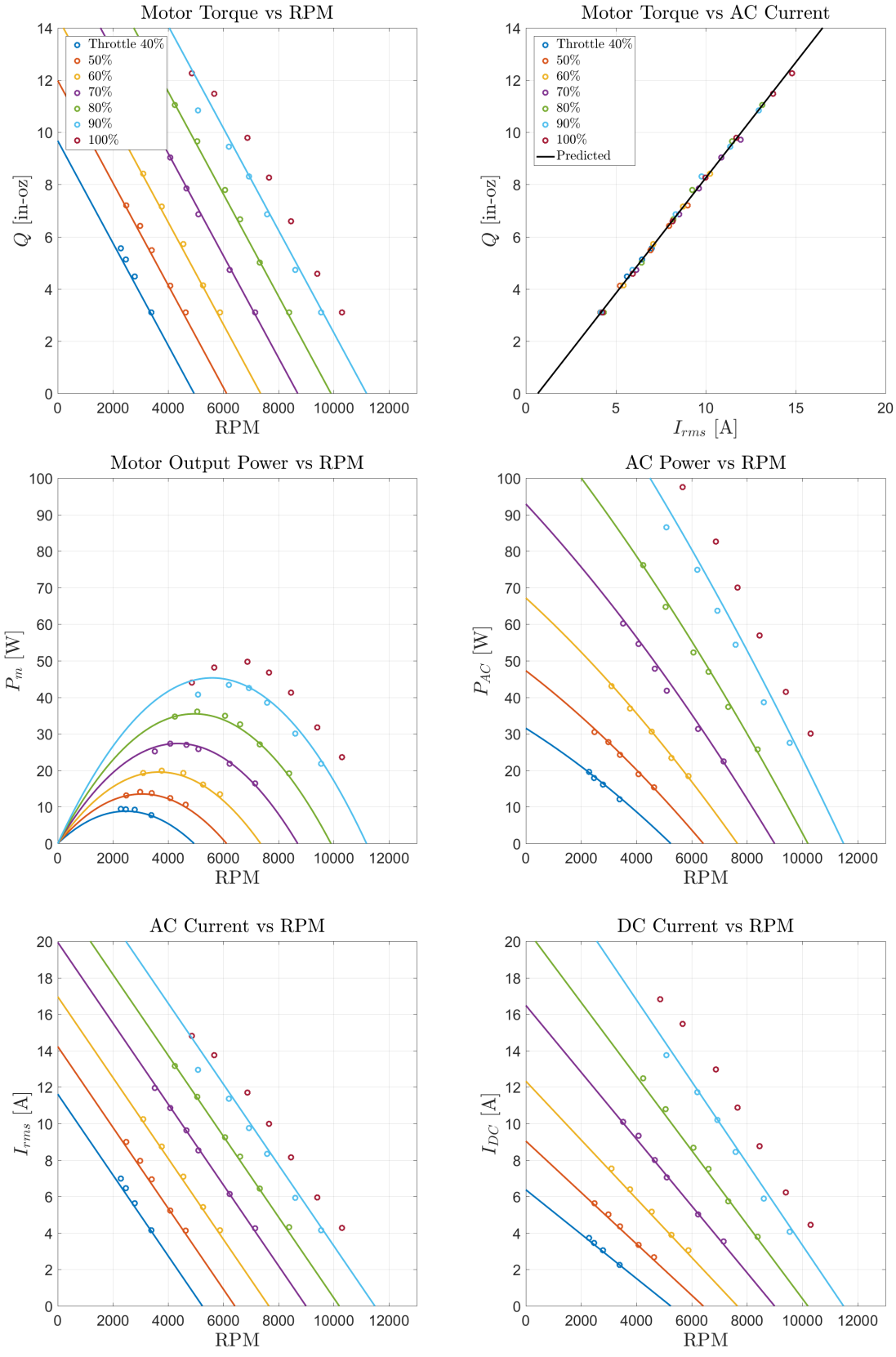

Figure 5.24: Efficiency plots - EMAX 1900 KV - MultiStar 30A - 7.2V

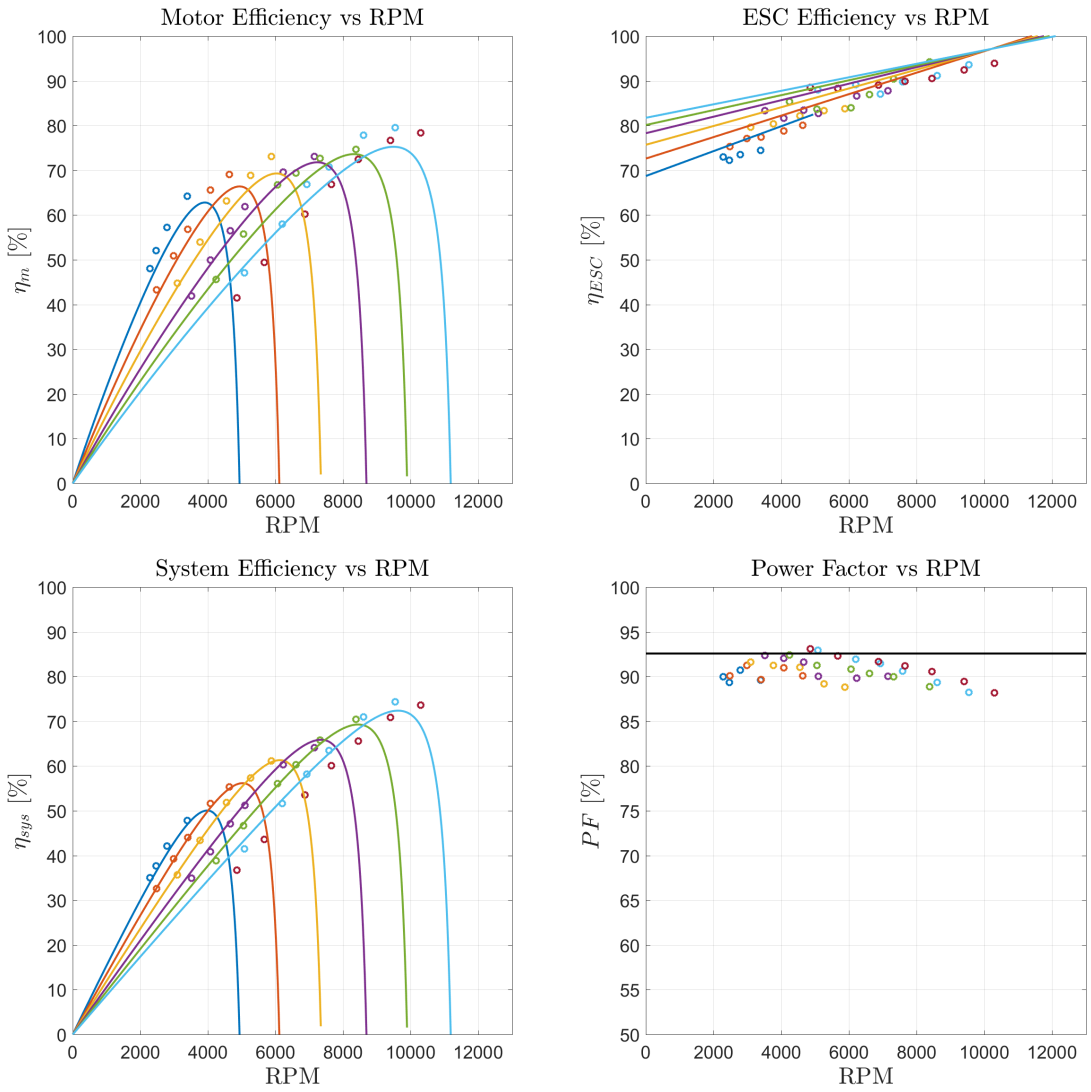

Figure 5.25: Performance plots - EMAX 1900 KV - DYS BlHeliOpto 40A - 7.2V

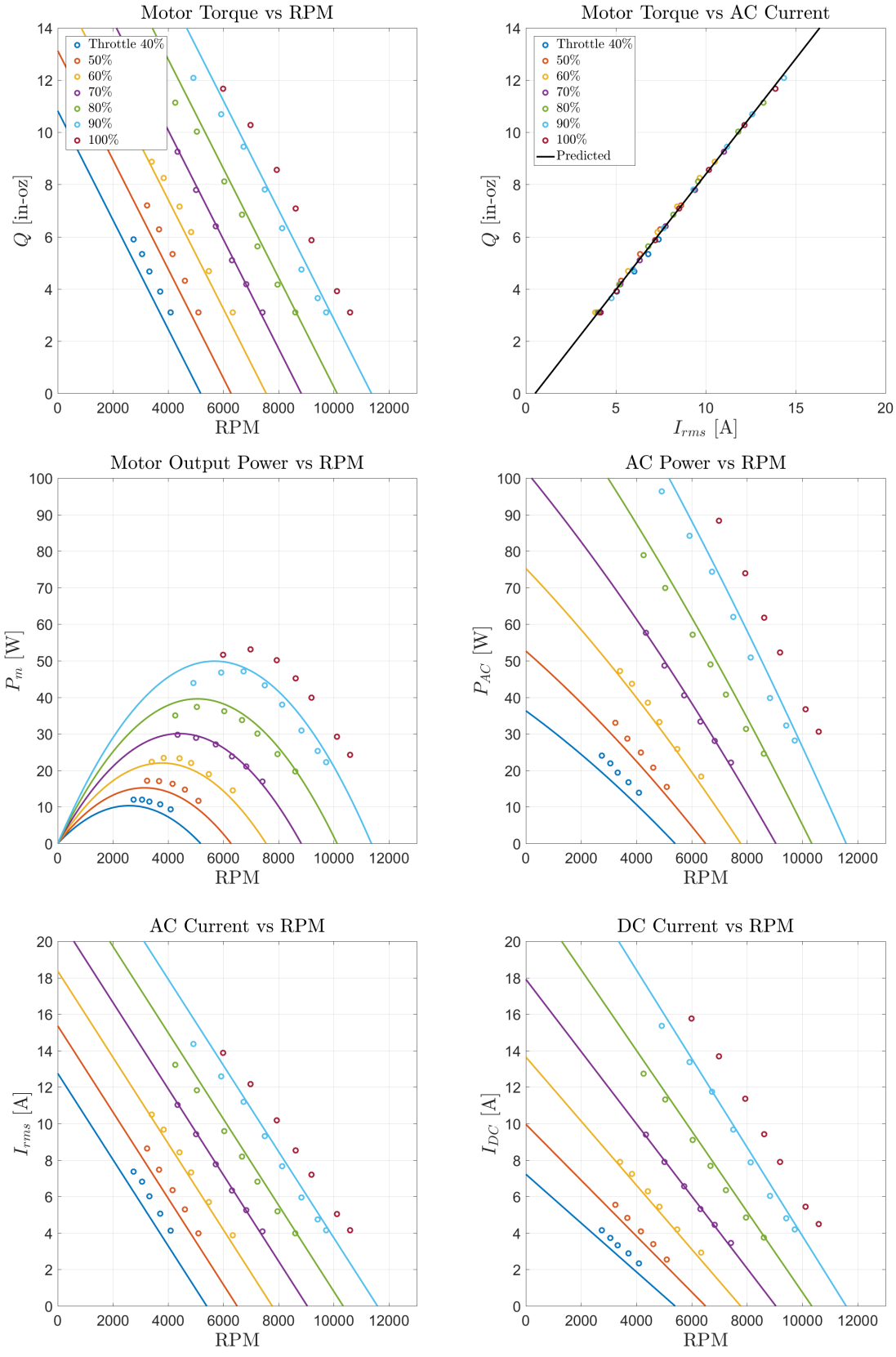

Figure 5.26: Efficiency plots - EMAX 1900 KV - DYS BlHeliOpto 40A - 7.2V

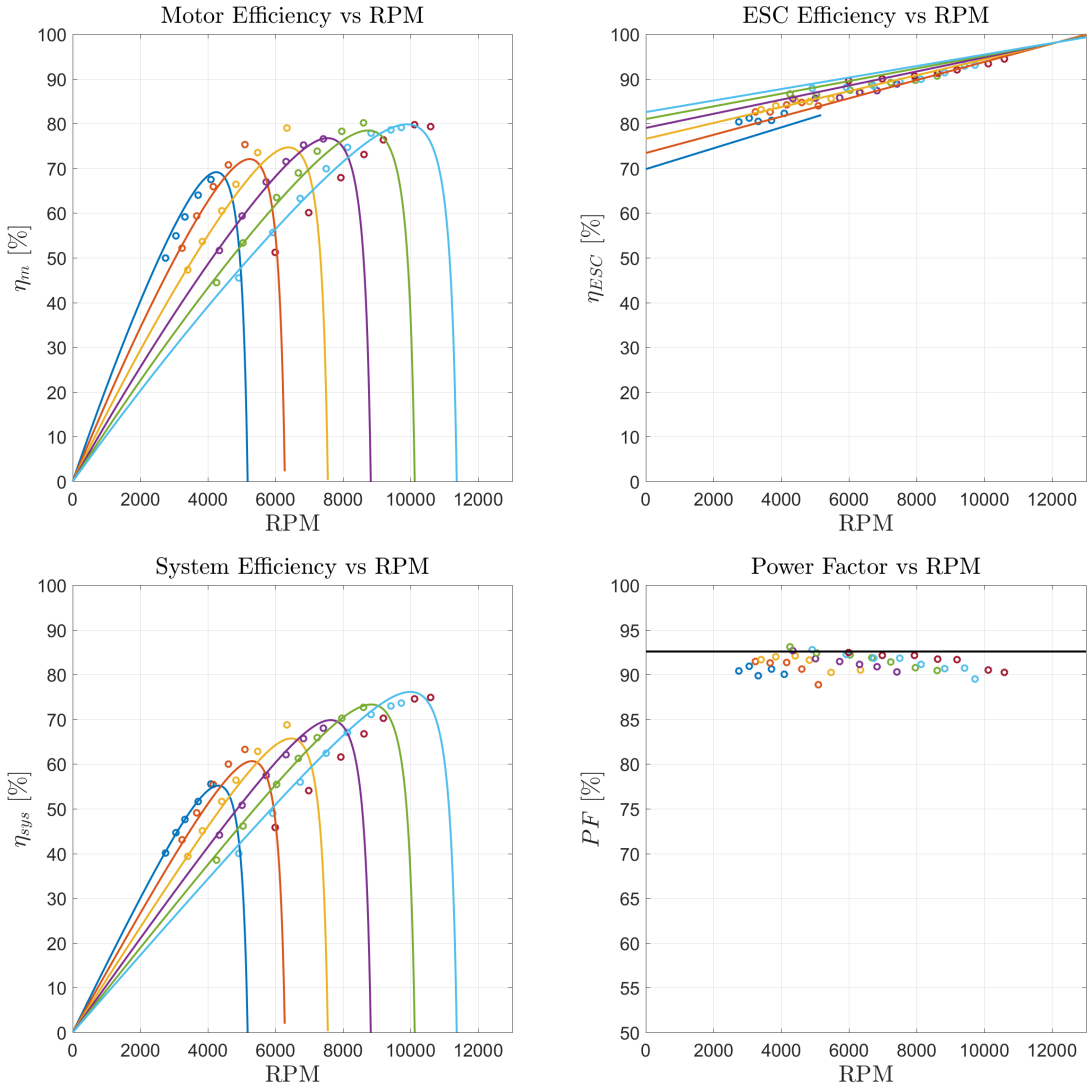

Figure 5.27: Performance plots - EMAX 2300 KV - SpiderLite 18A - 7.2V

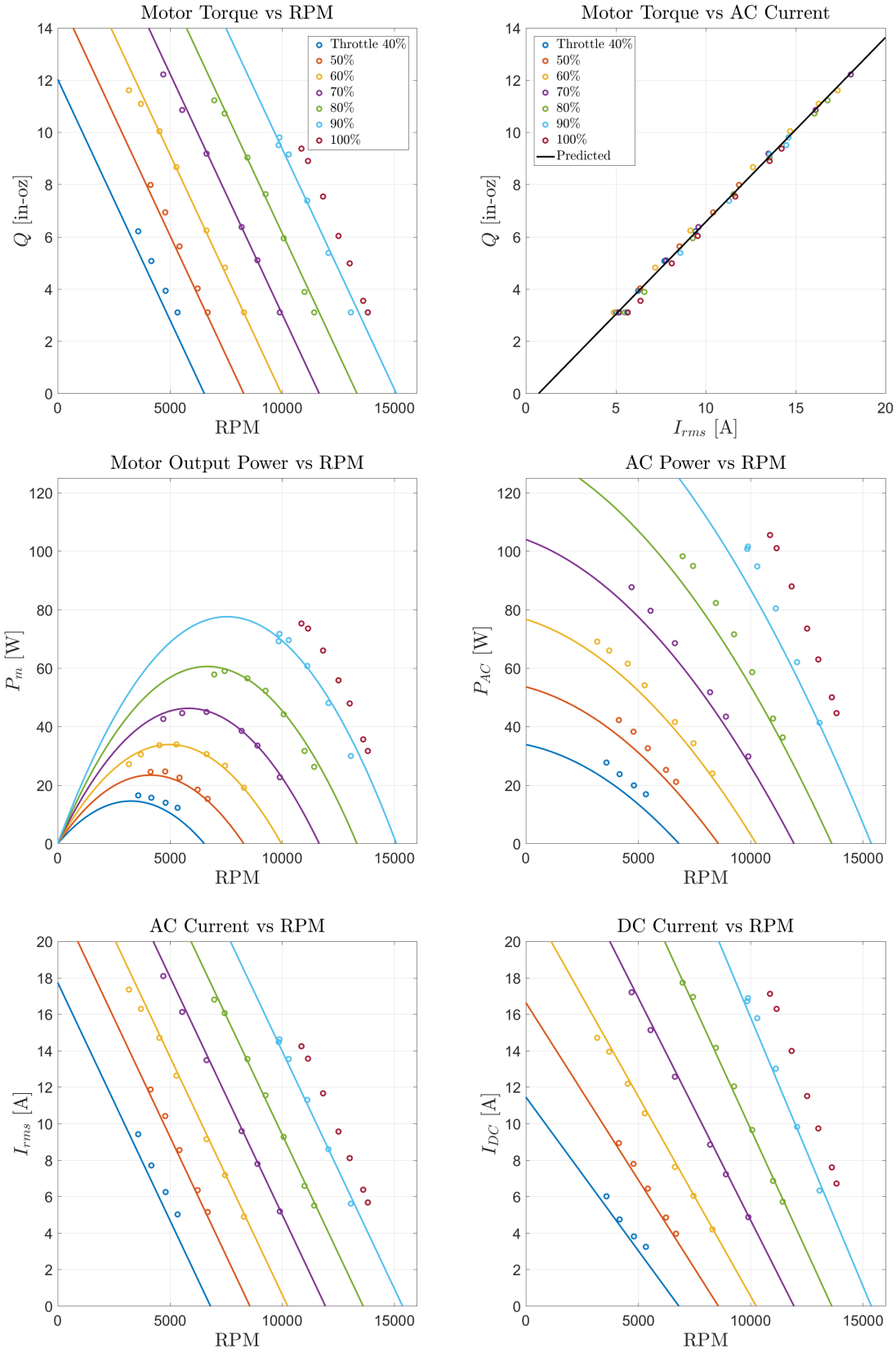

Figure 5.28: Efficiency plots - EMAX 2300 KV - SpiderLite 18A - 7.2V

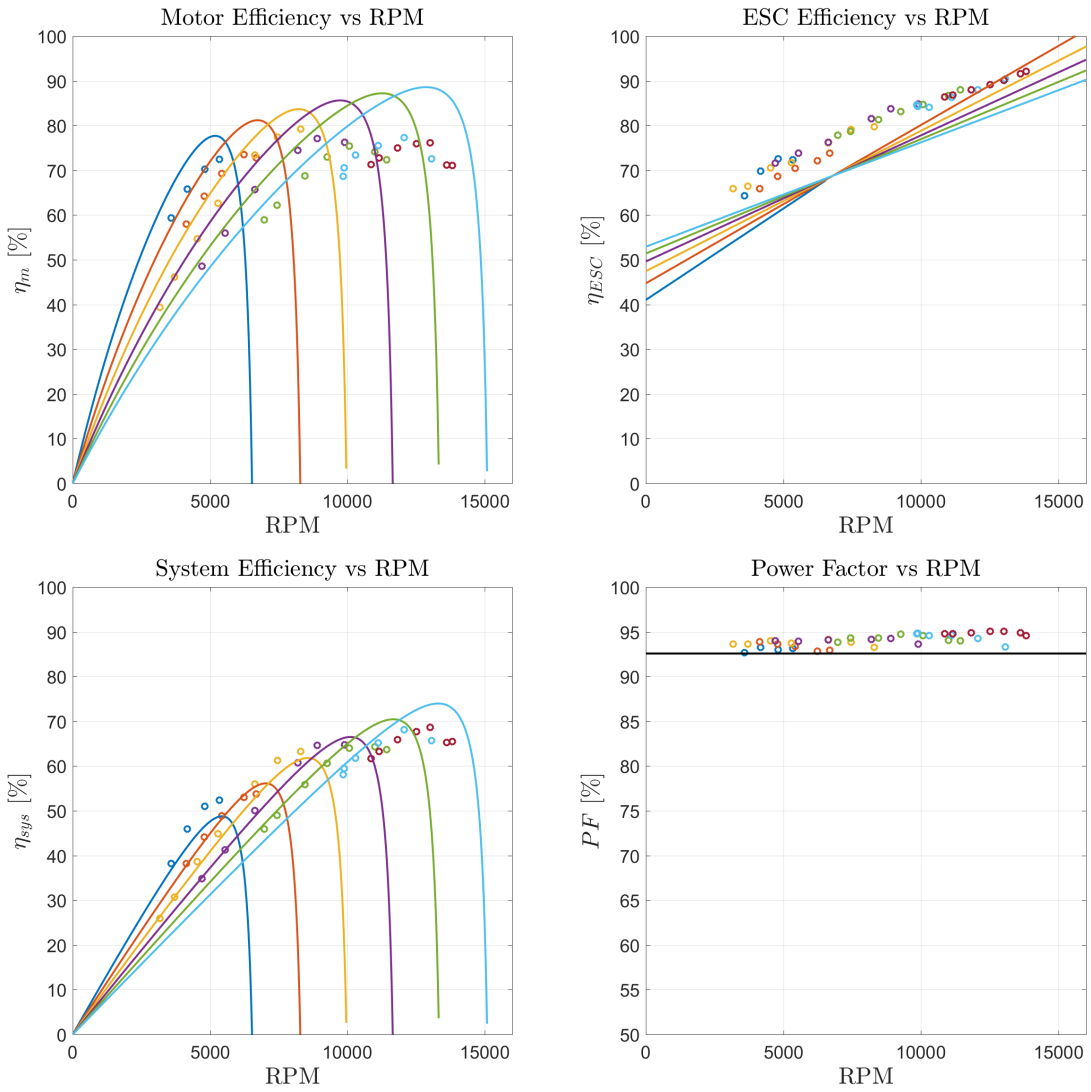

Figure 5.29: Performance plots - EMAX 2300 KV - MultiStar 30A - 7.2V

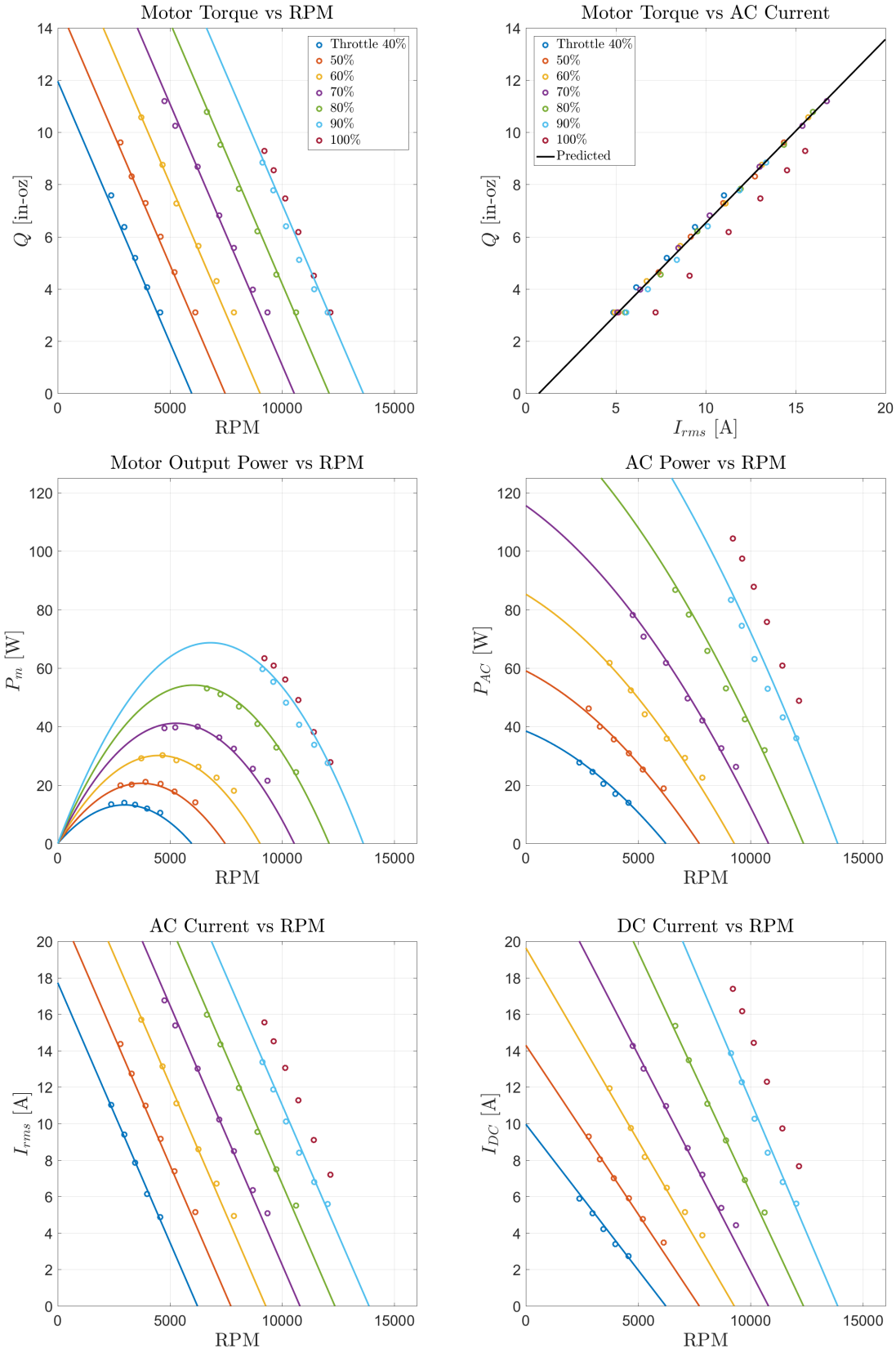

Figure 5.30: Efficiency plots - EMAX 2300 KV - MultiStar 30A - 7.2V

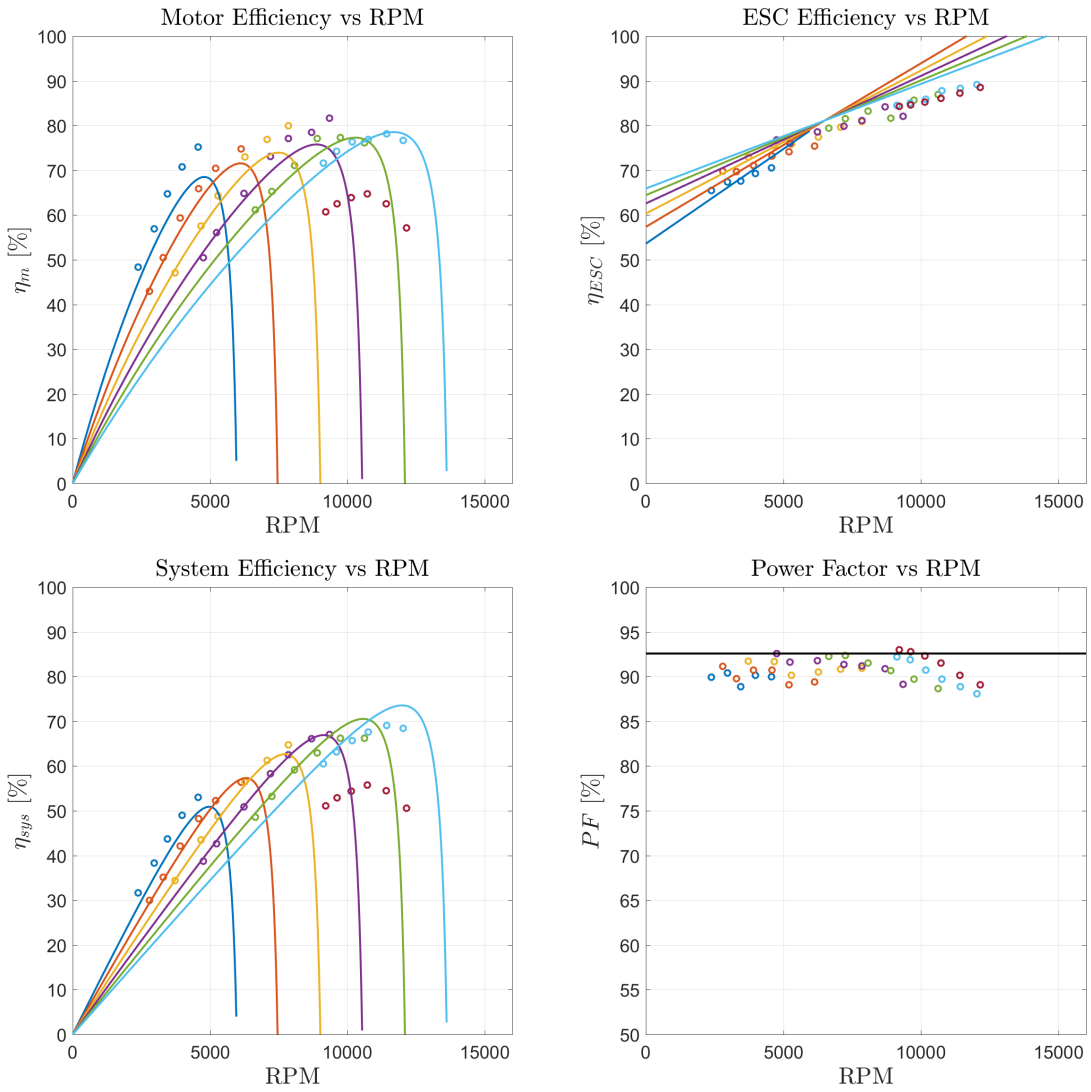

Figure 5.31: Efficiency plots - EMAX 2300 KV - DYS BlHeliOpto 40A - 7.2V

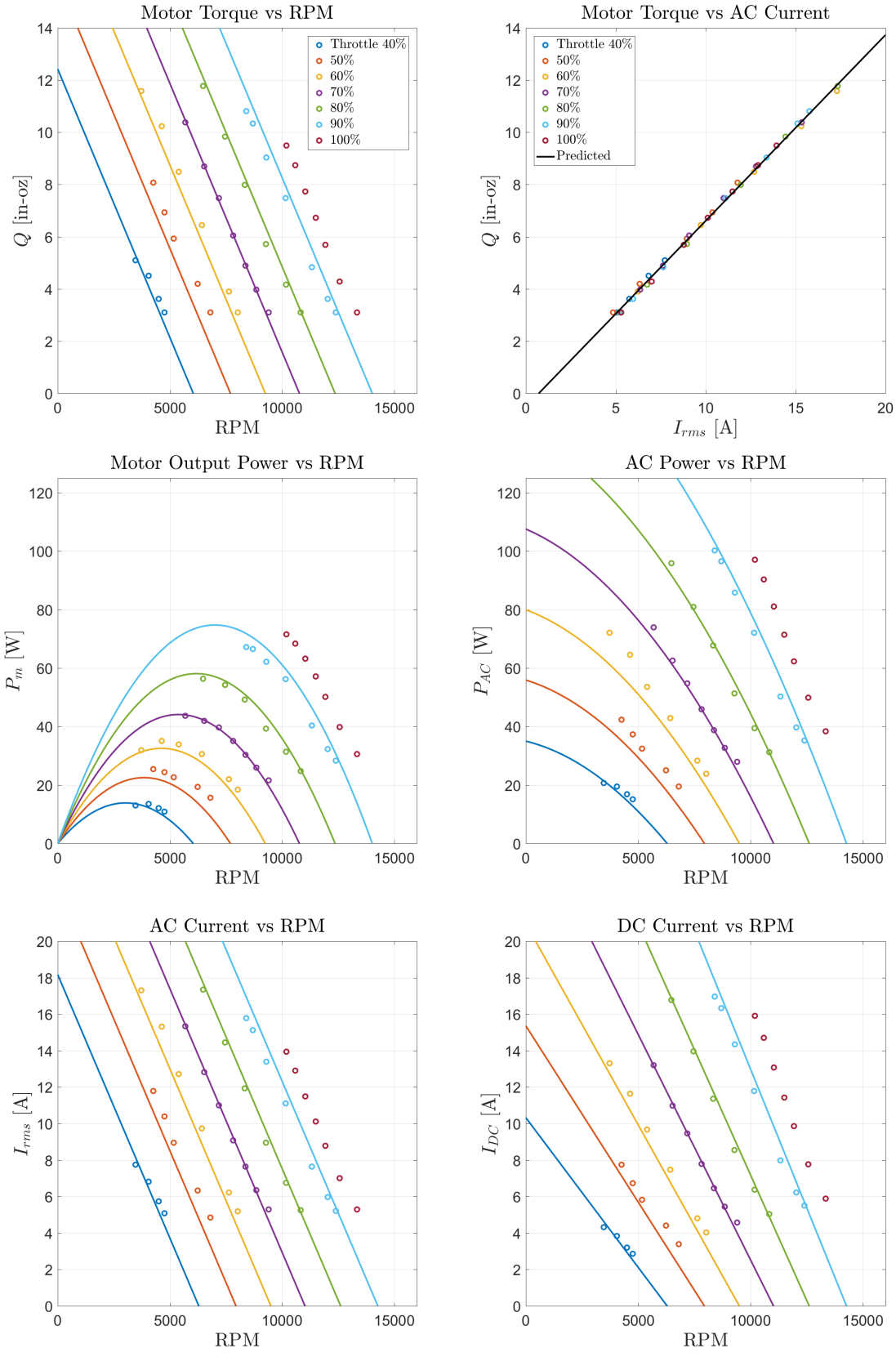

Figure 5.32: Efficiency plots - EMAX 2300 KV - DYS BlHeliOpto 40A - 7.2V

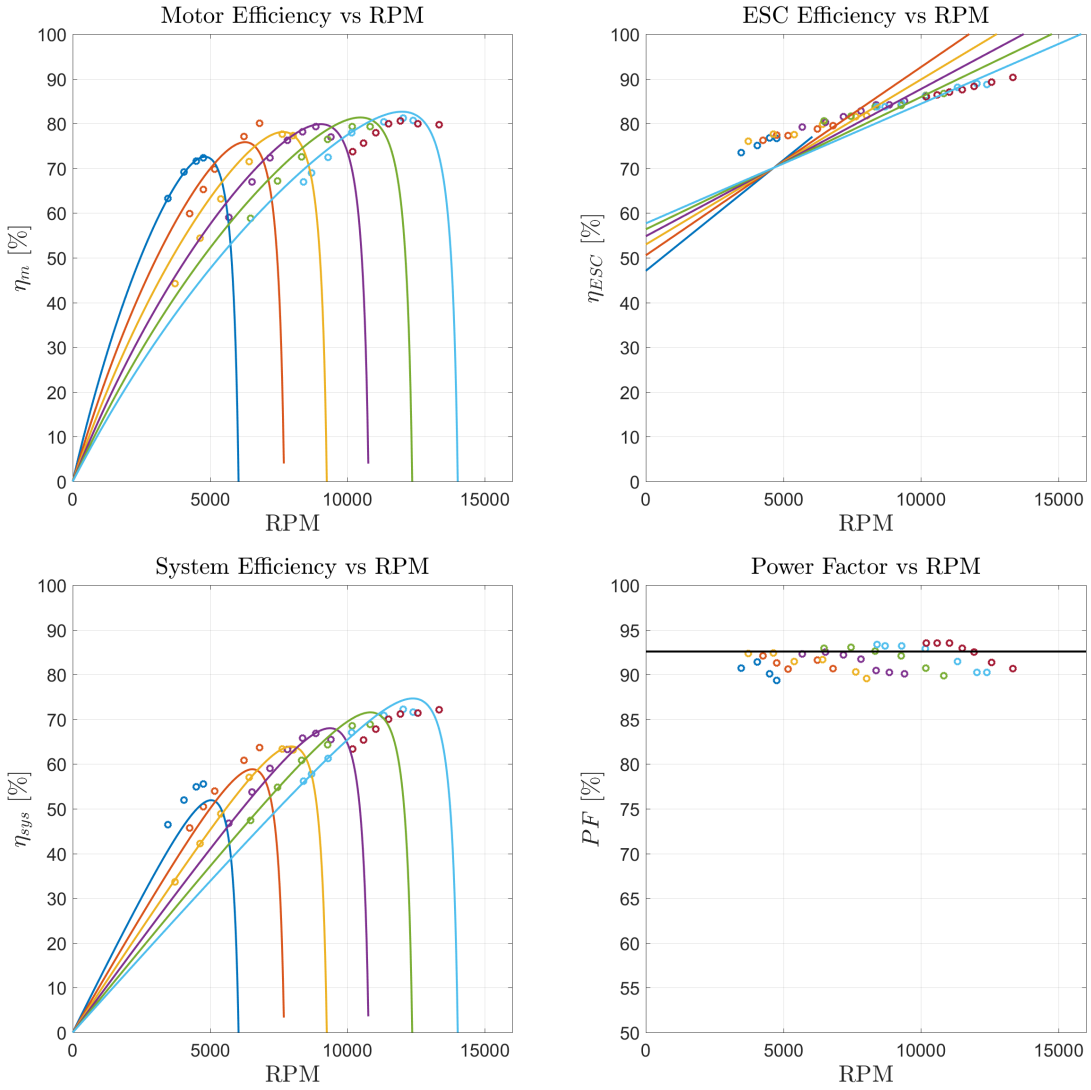

Figure 5.33: Performance plots - Samguk 2500 KV - SpiderLite 18A - 7.2V

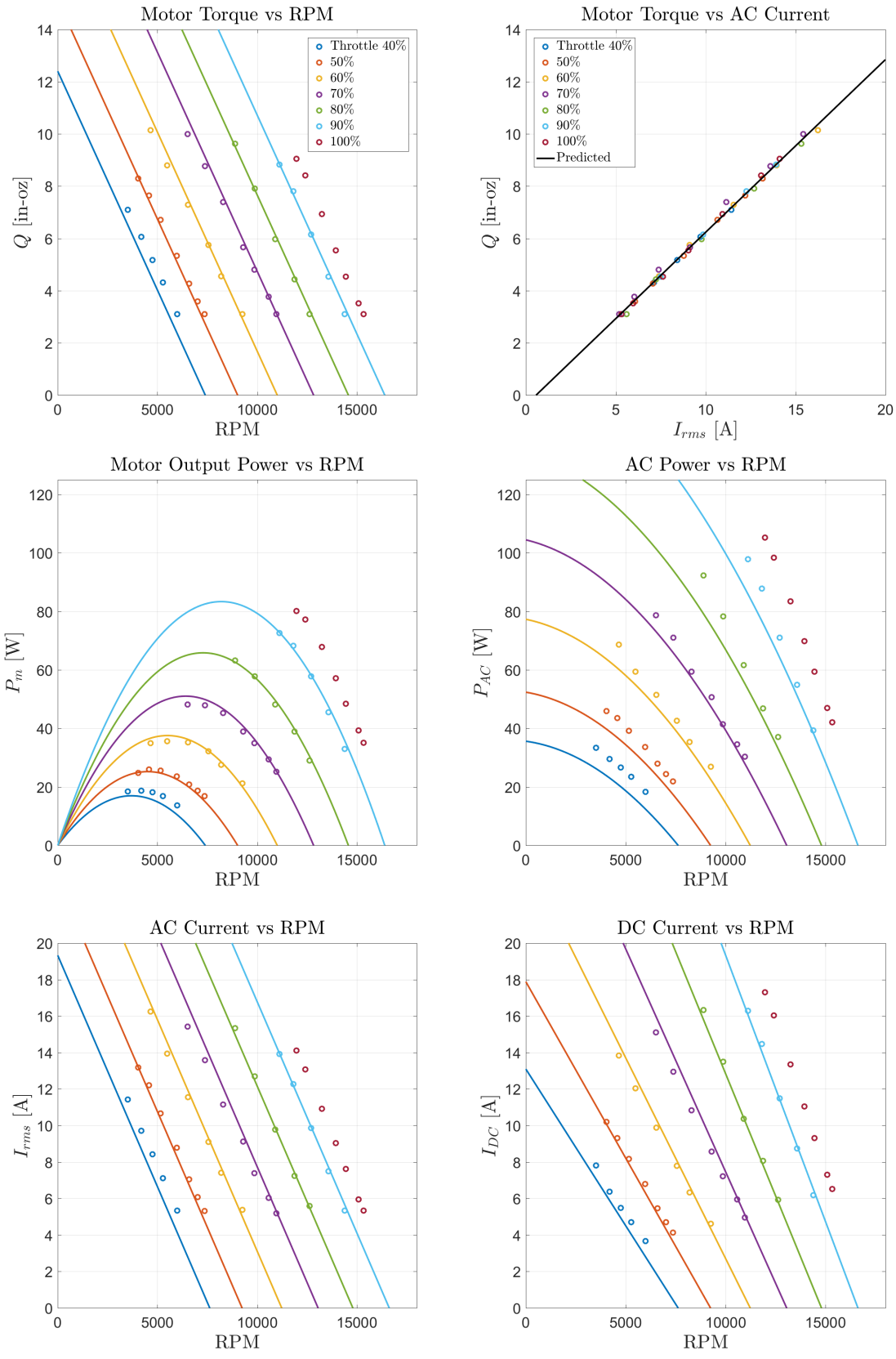

Figure 5.34: Efficiency plots - Samguk 2500 KV - SpiderLite 18A - 7.2V

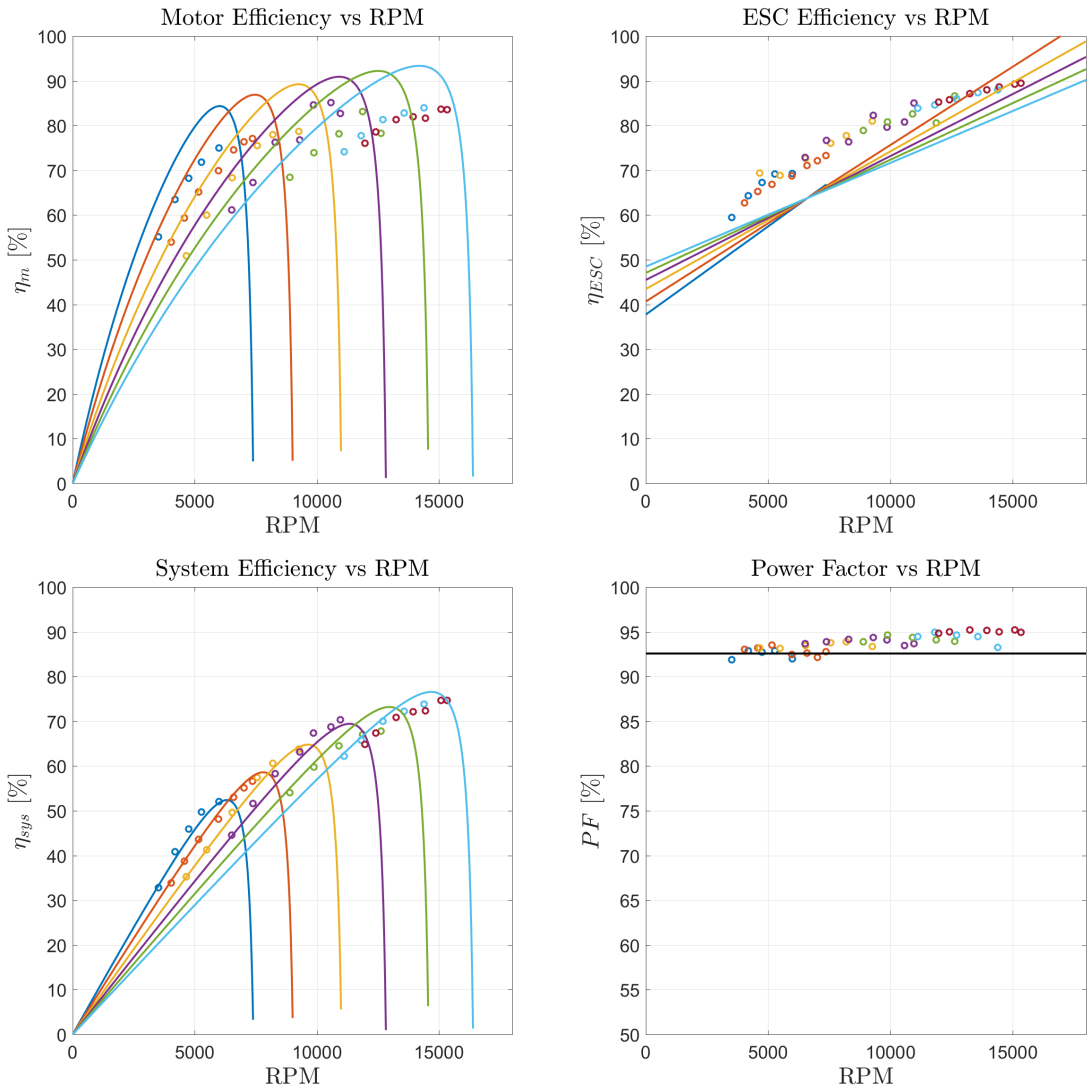

Figure 5.35: Performance plots - Samguk 2500 KV - MultiStar 30A - 7.2V

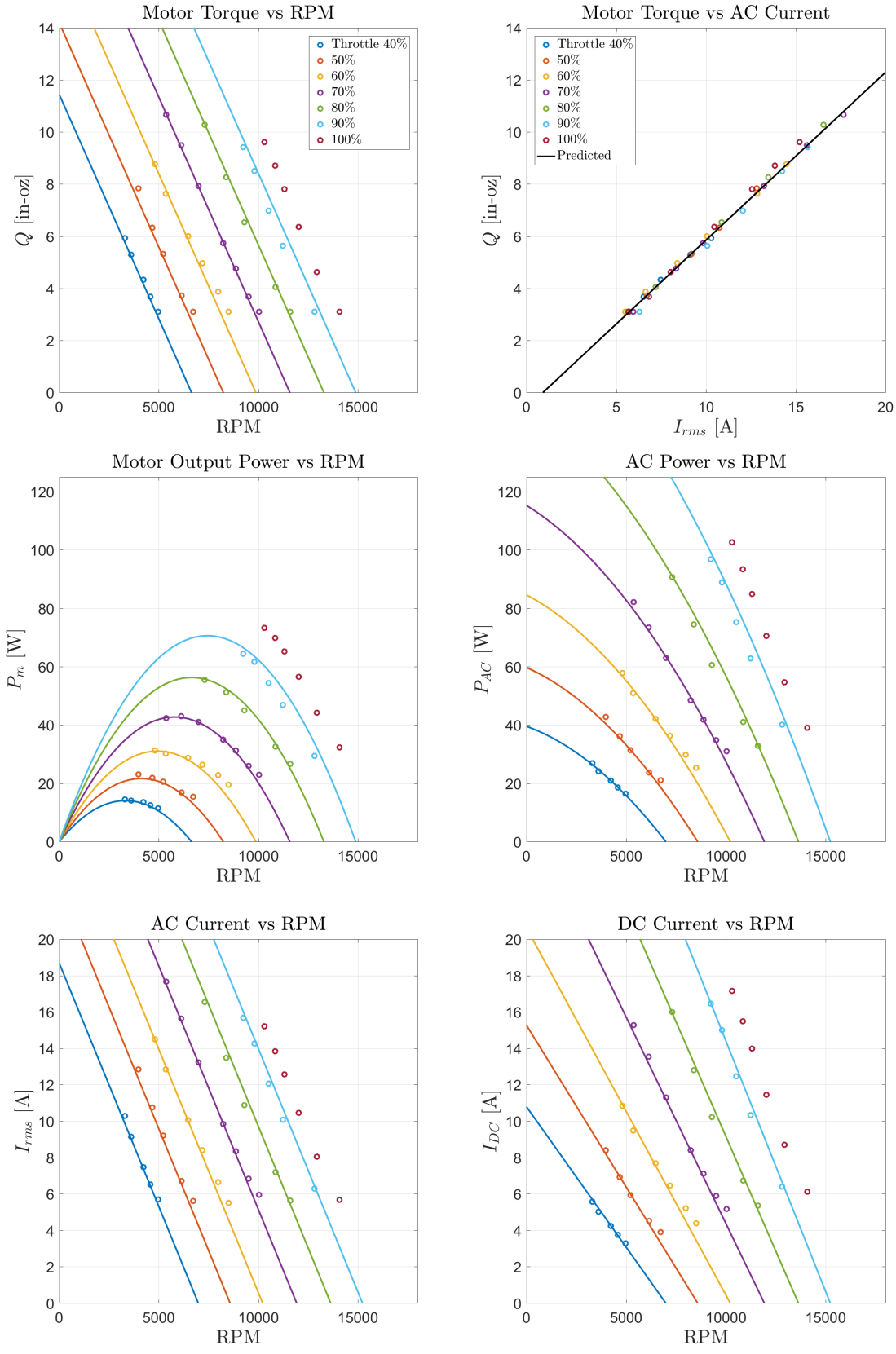

Figure 5.36: Efficiency plots - Samguk 2500 KV - MultiStar 30A - 7.2V

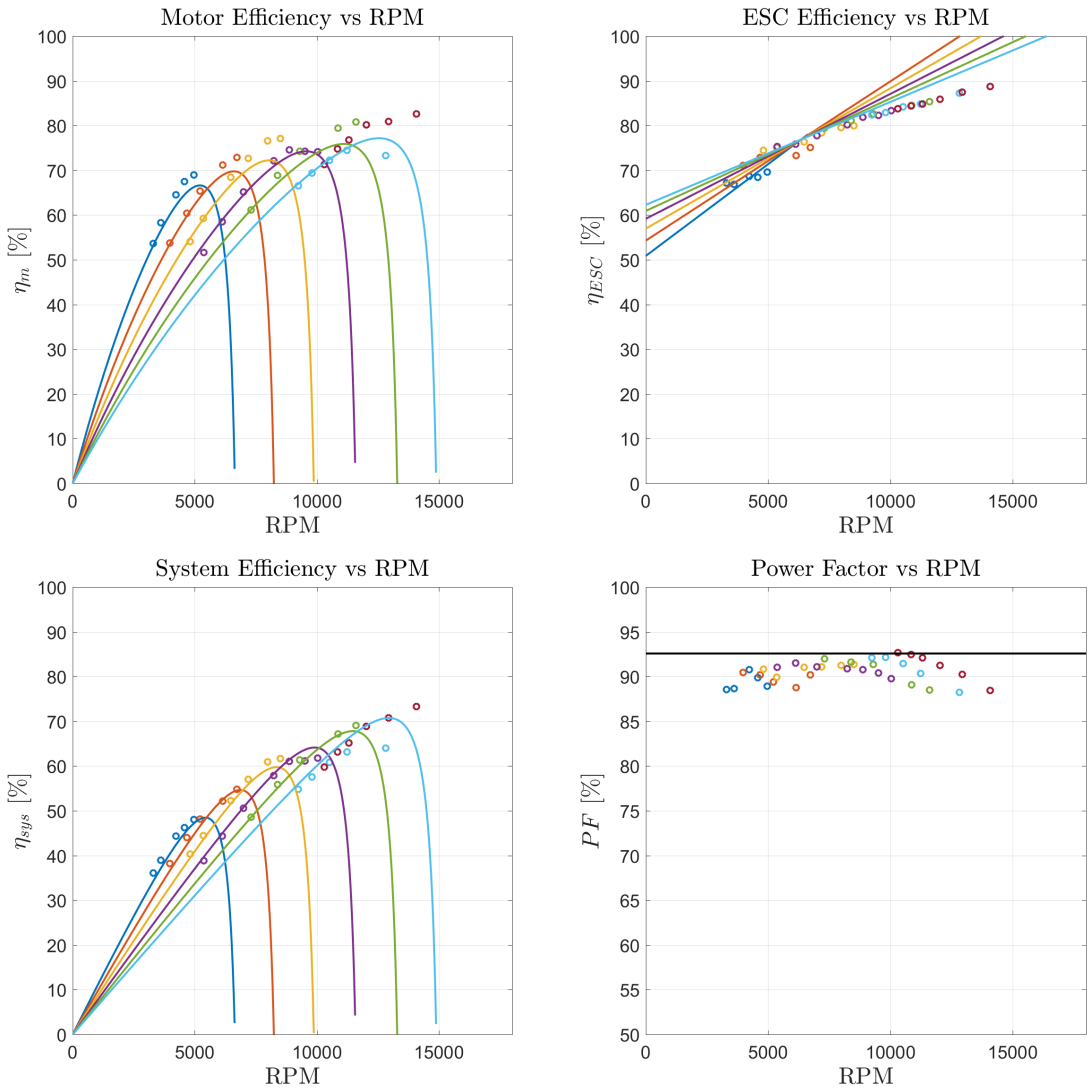

Figure 5.37: Performance plots - Samguk 2500 KV - DYS BlHeliOpto 40A - 7.2V

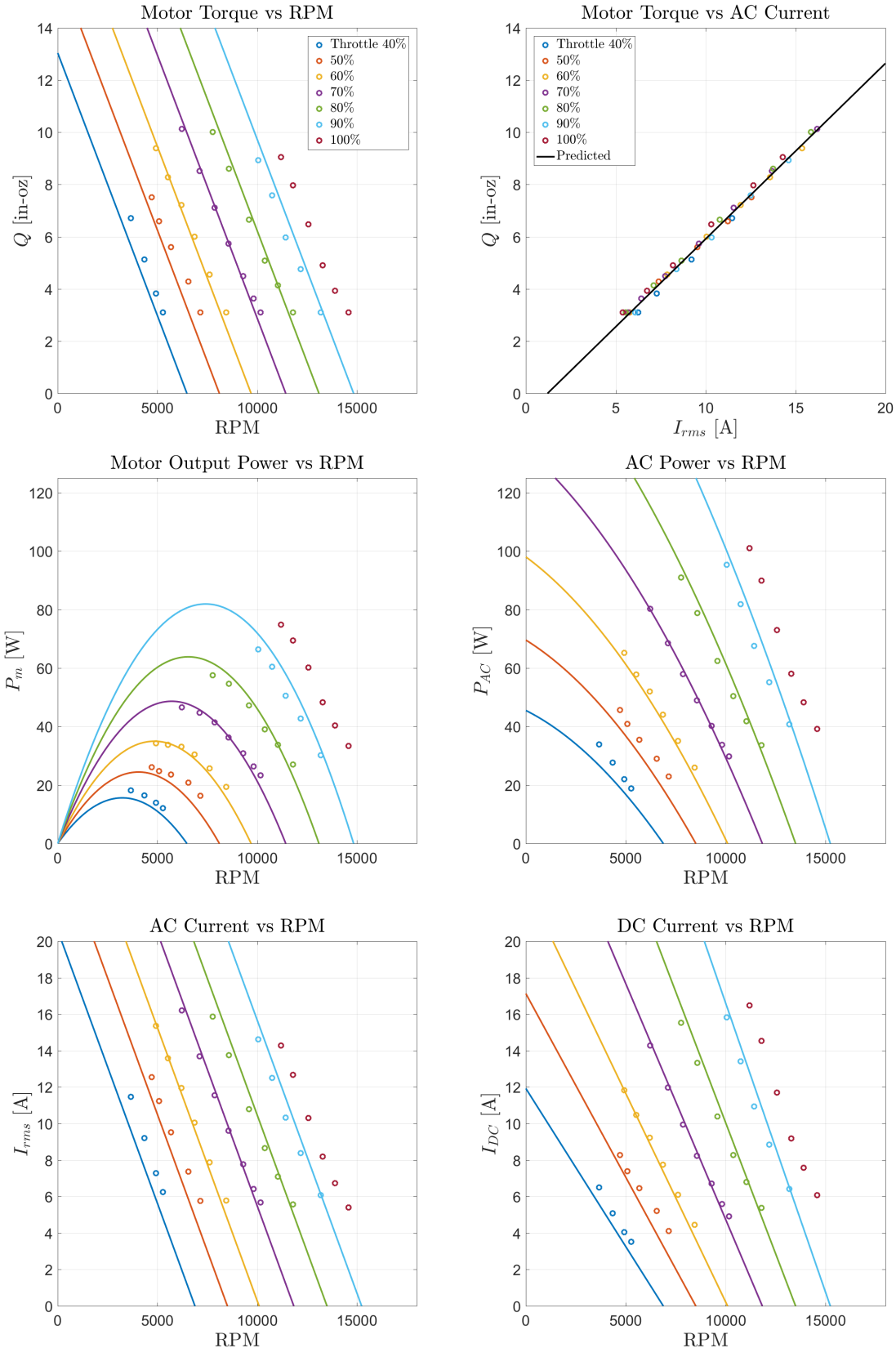

Figure 5.38: Efficiency plots - Samguk 2500 KV - DYS BlHeliOpto 40A - 7.2V

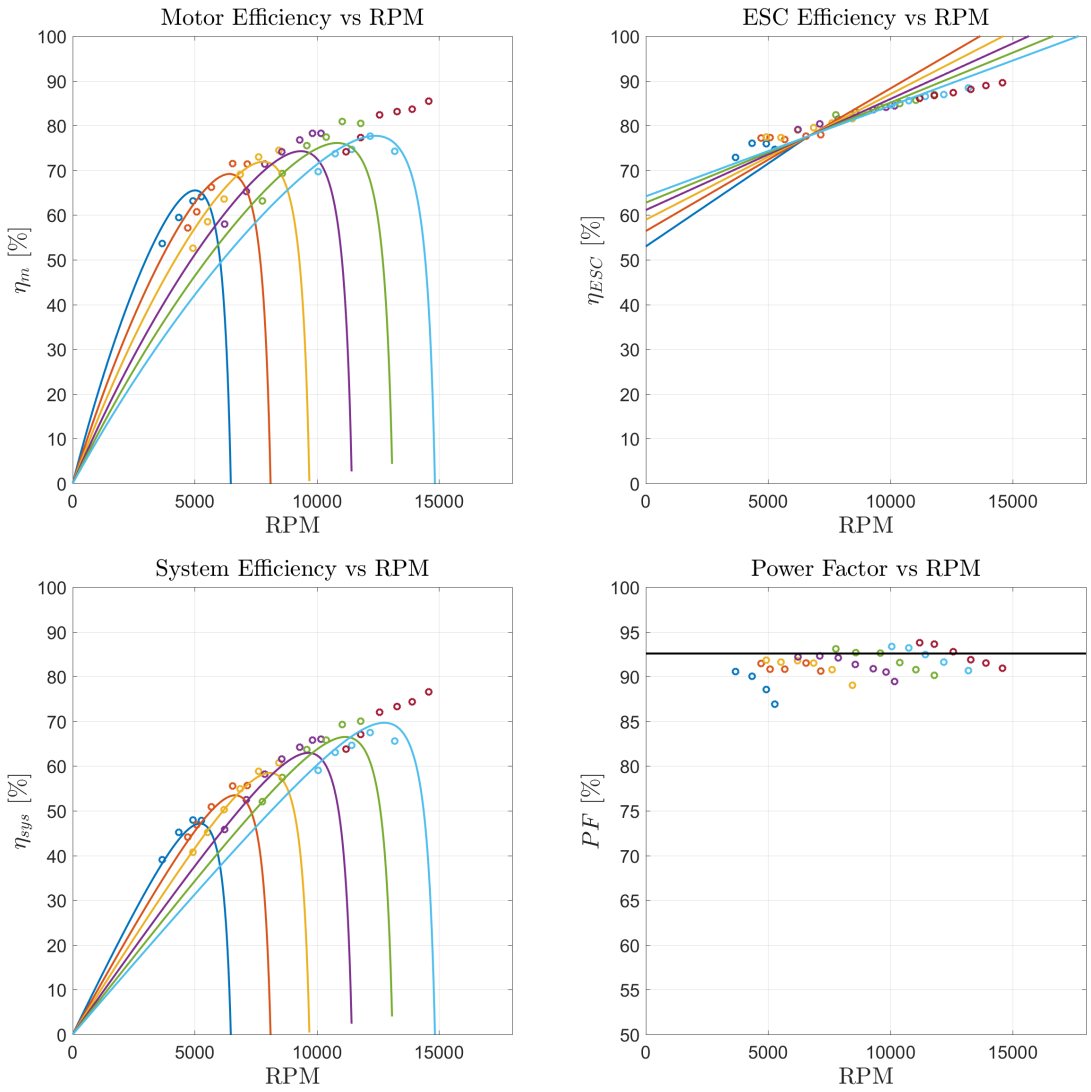

5.2 Test at 11.1V

Figure 5.39: Performance plots - DJI 920 KV - SpiderLite 18A - 11.1V

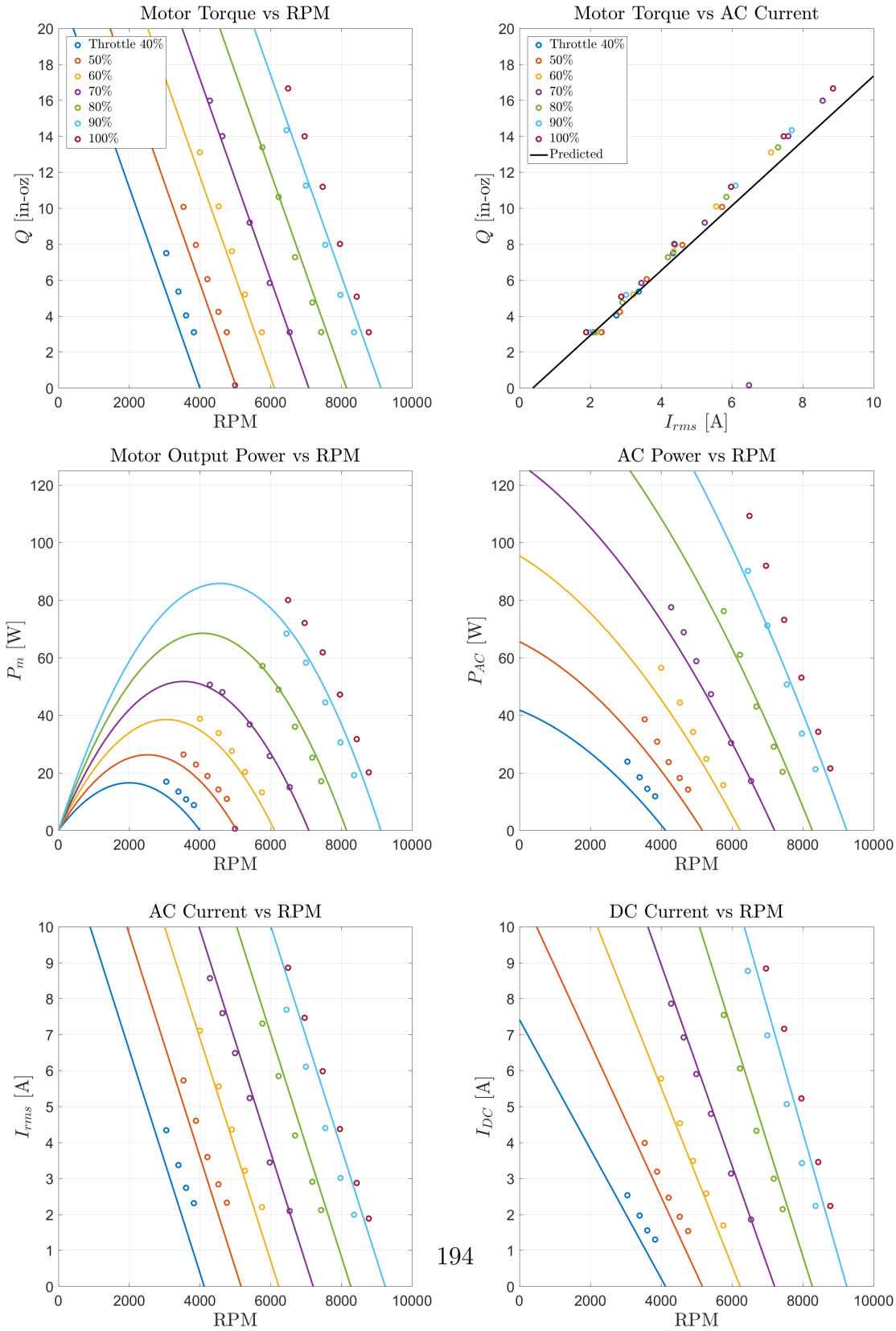

Figure 5.40: Efficiency plots - DJI 920 KV - SpiderLite 18A - 11.1V

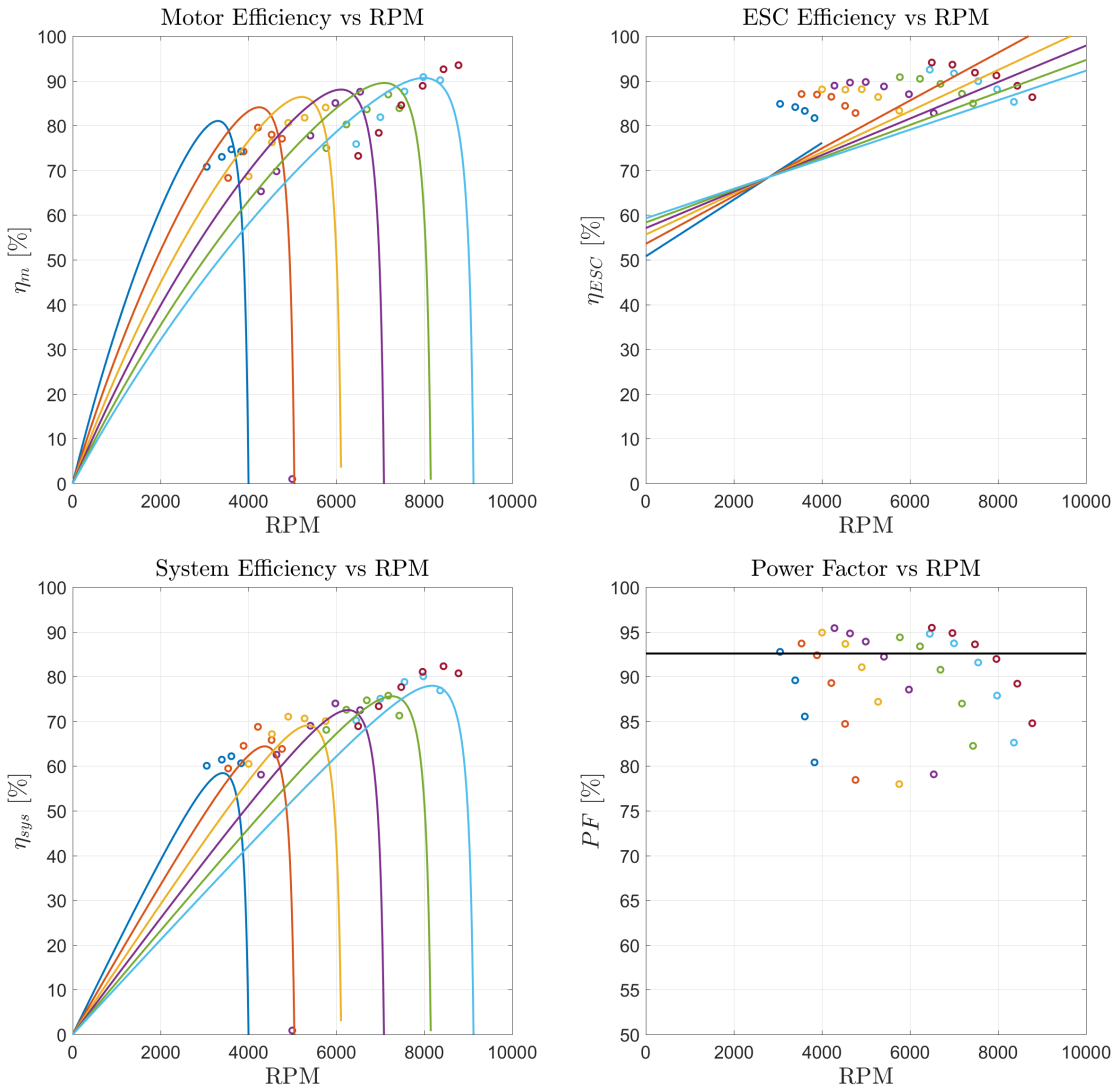

Figure 5.41: Performance plots - DJI 920 KV - MultiStar 30A - 11.1V

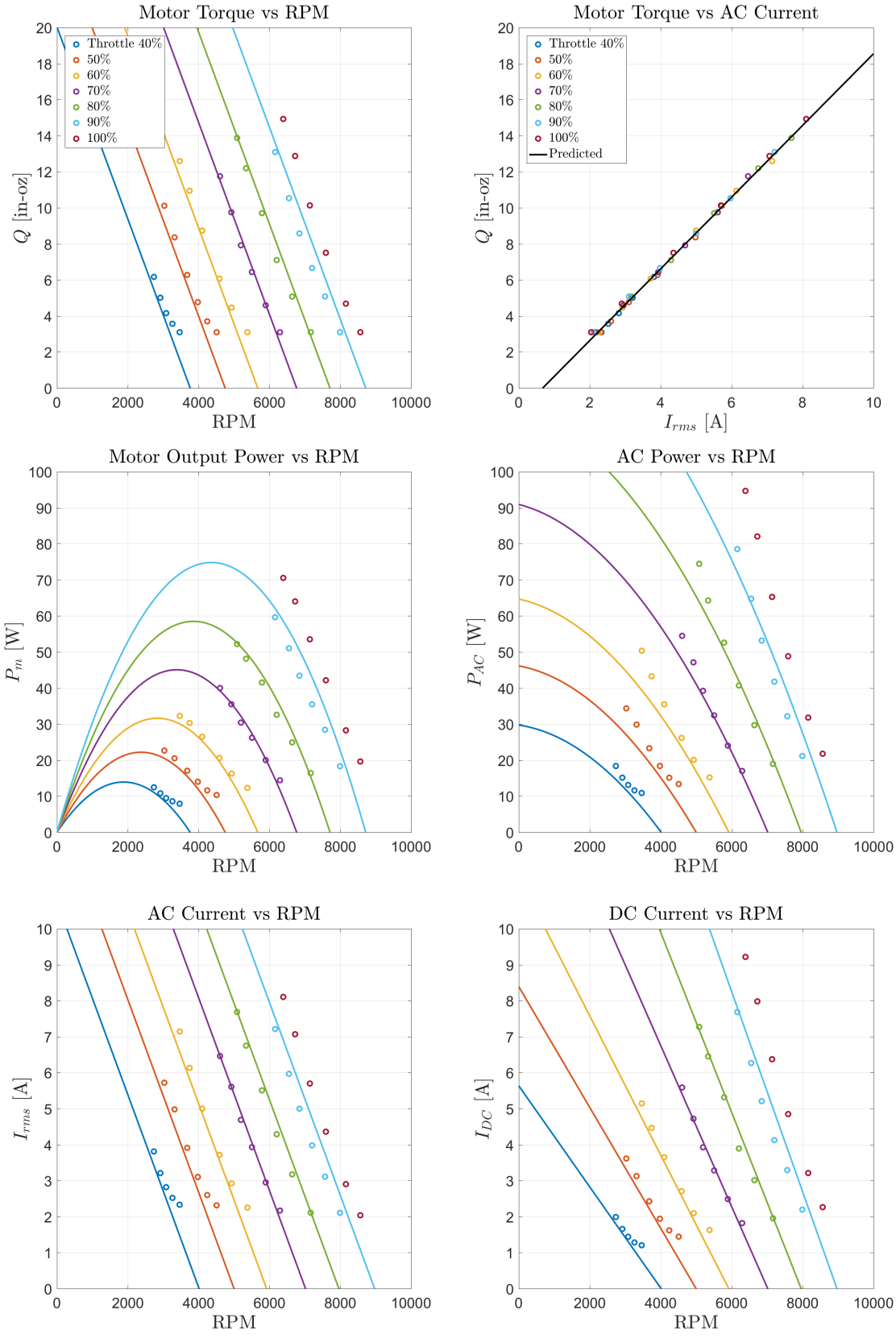

Figure 5.42: Efficiency plots - DJI 920 KV - MultiStar 30A - 11.1V

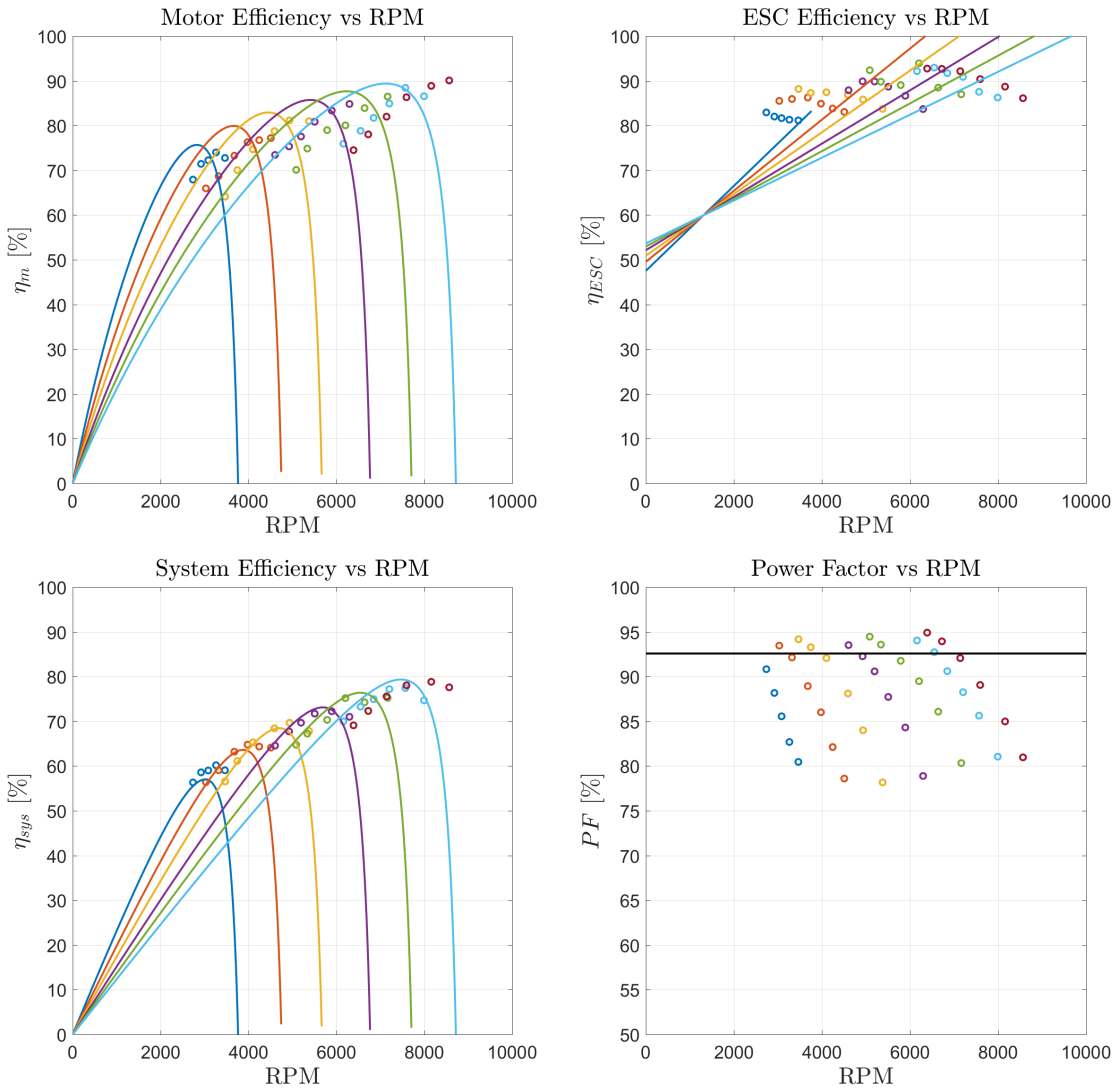

Figure 5.43: Performance plots - DJI 920 KV - DYS BlHeliOpto 40A - 11.1V

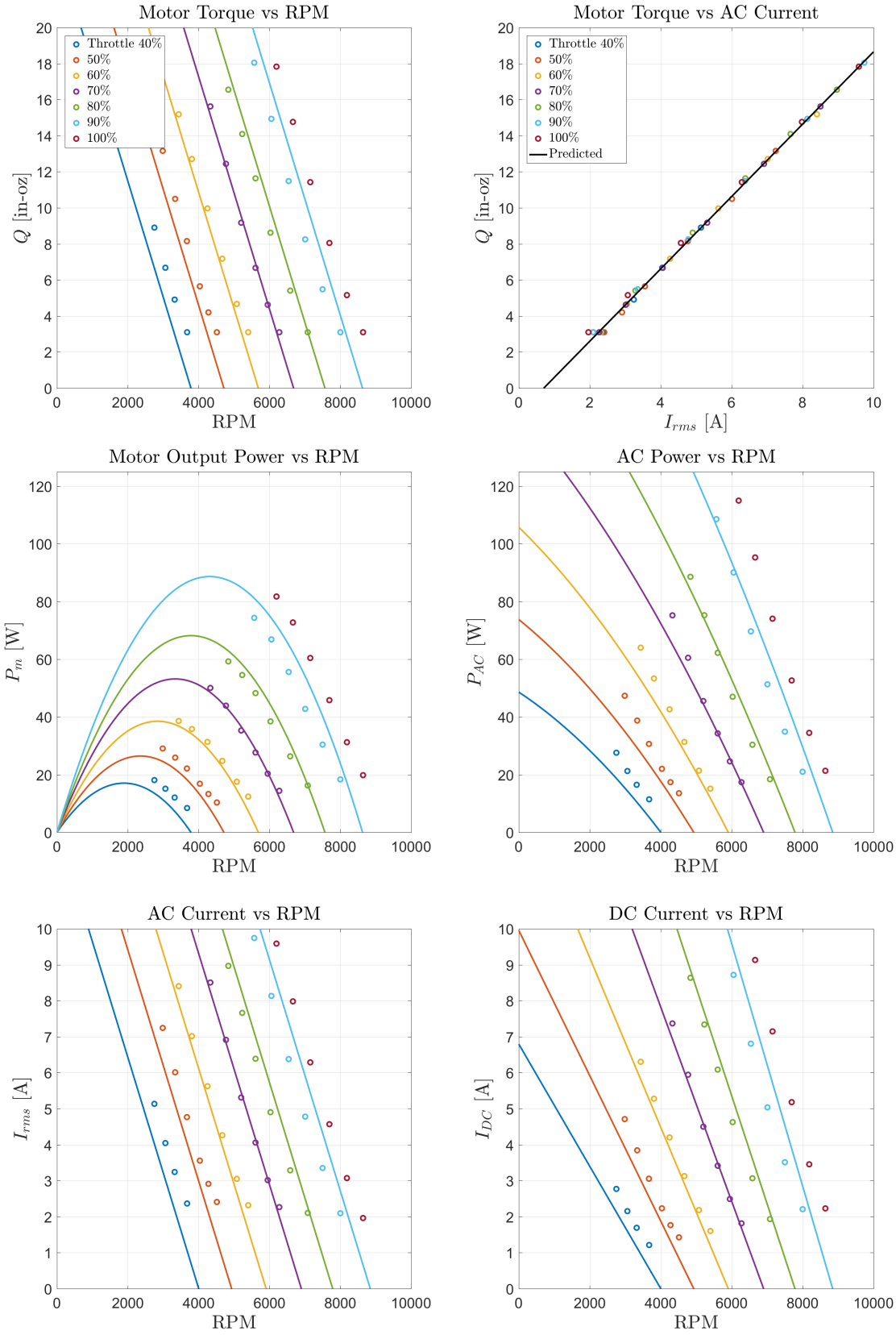

Figure 5.44: Efficiency plots - DJI 920 KV - DYS BlHeliOpto 40A - 11.1V

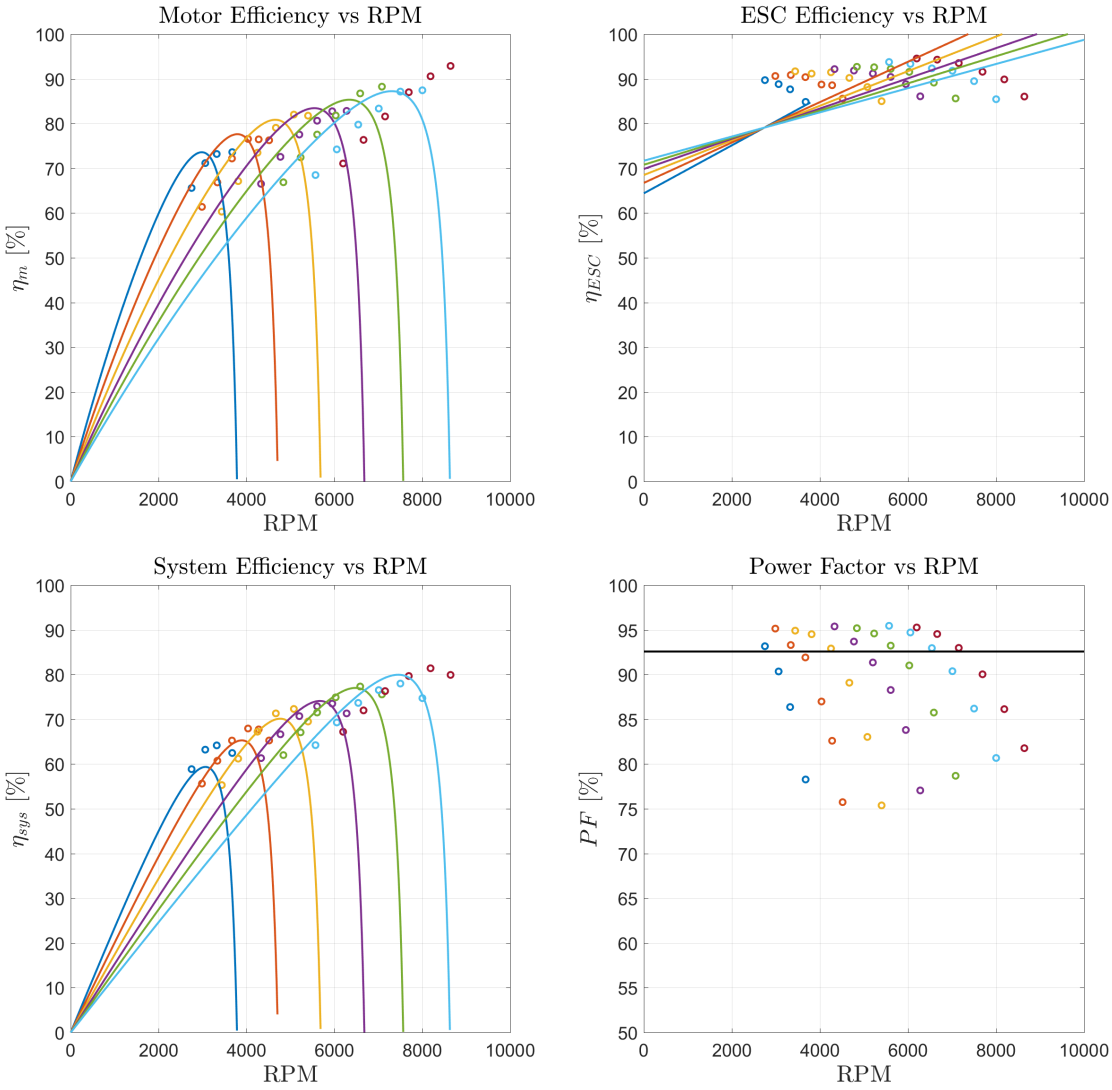

Figure 5.45: Performance plots - EMAX 935 KV - SpiderLite 18A - 11.1V

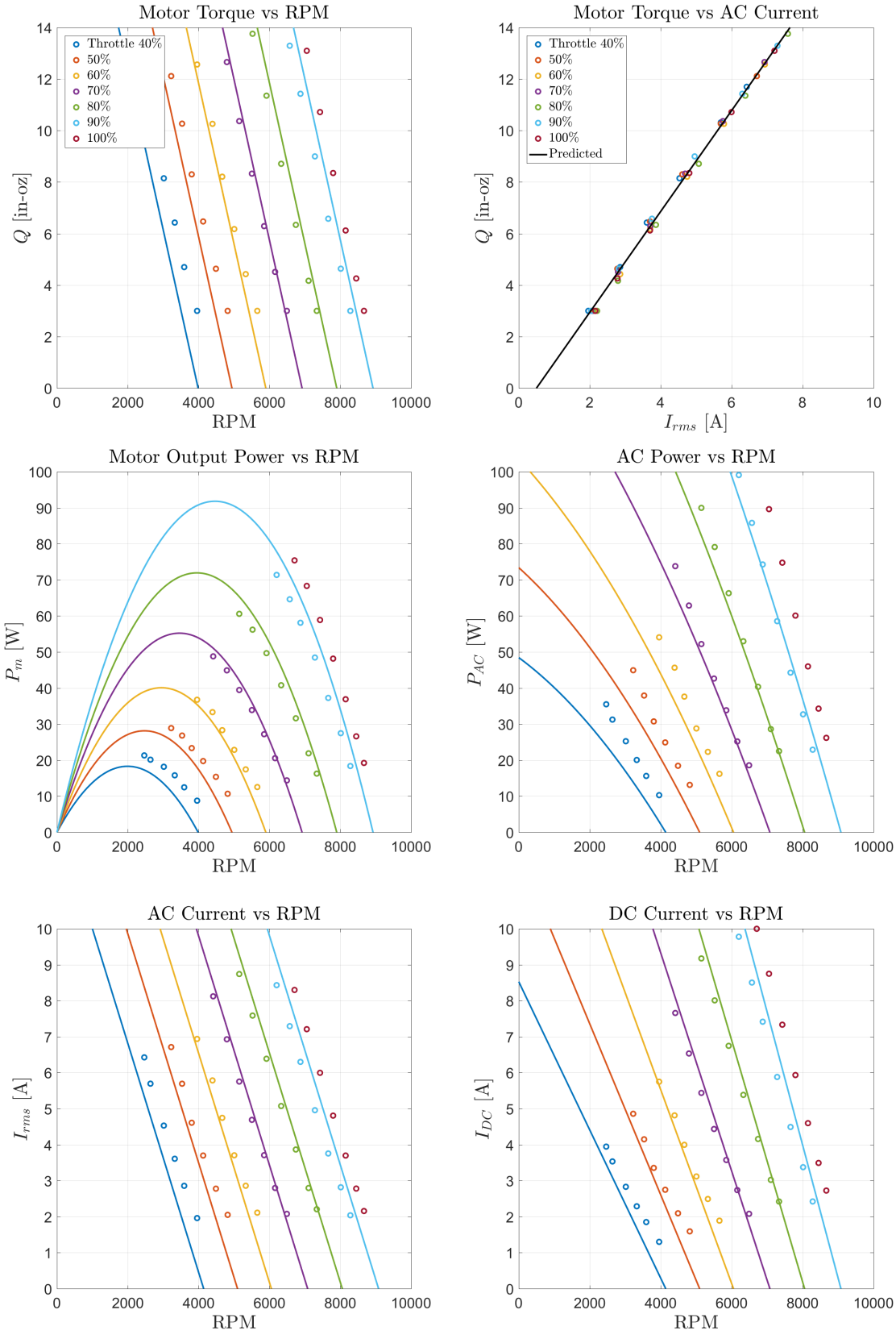

Figure 5.46: Efficiency plots - EMAX 935 KV - SpiderLite 18A - 11.1V

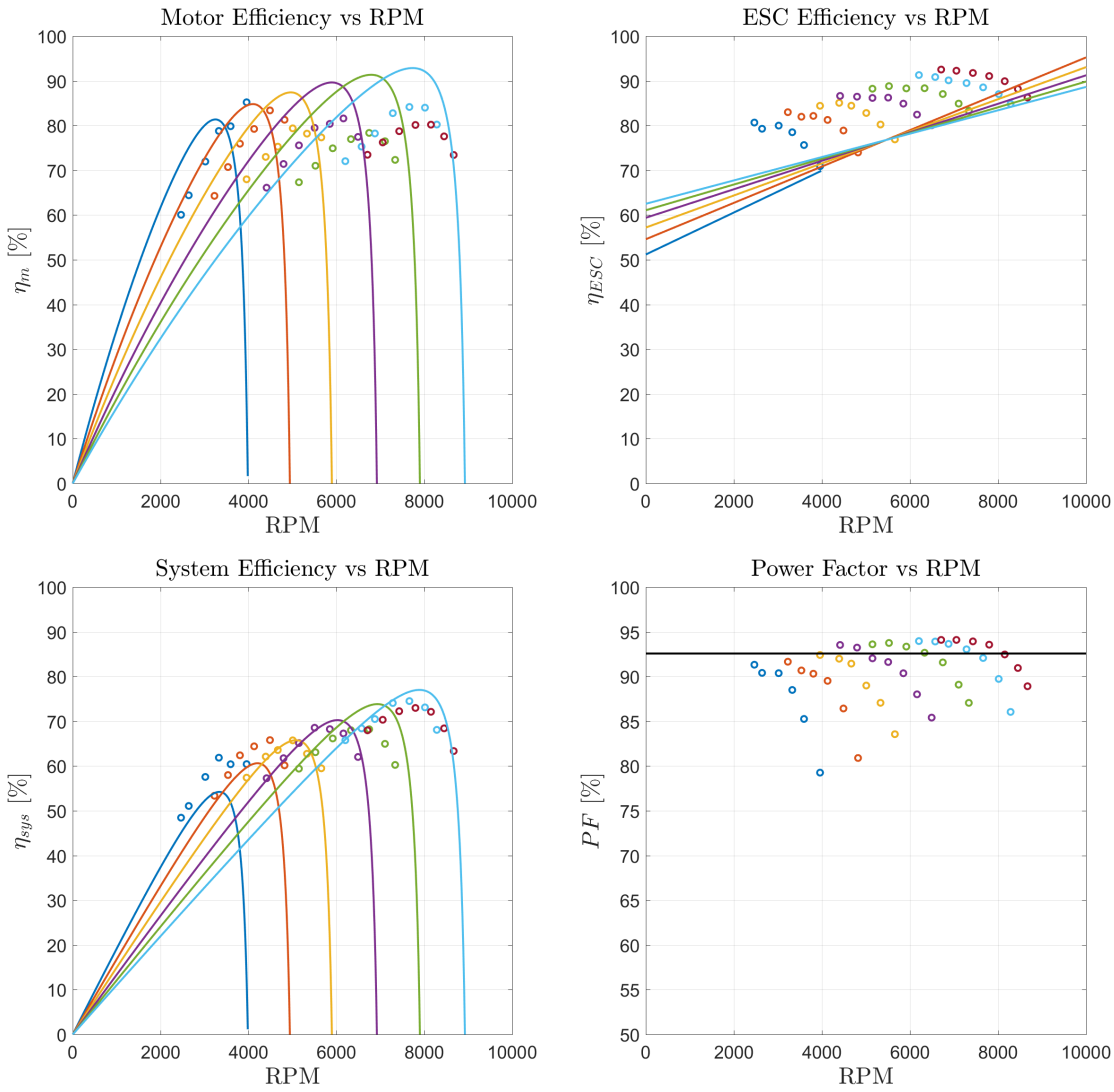

Figure 5.47: Performance plots - EMAX 935 KV - MultiStar 30A - 11.1V

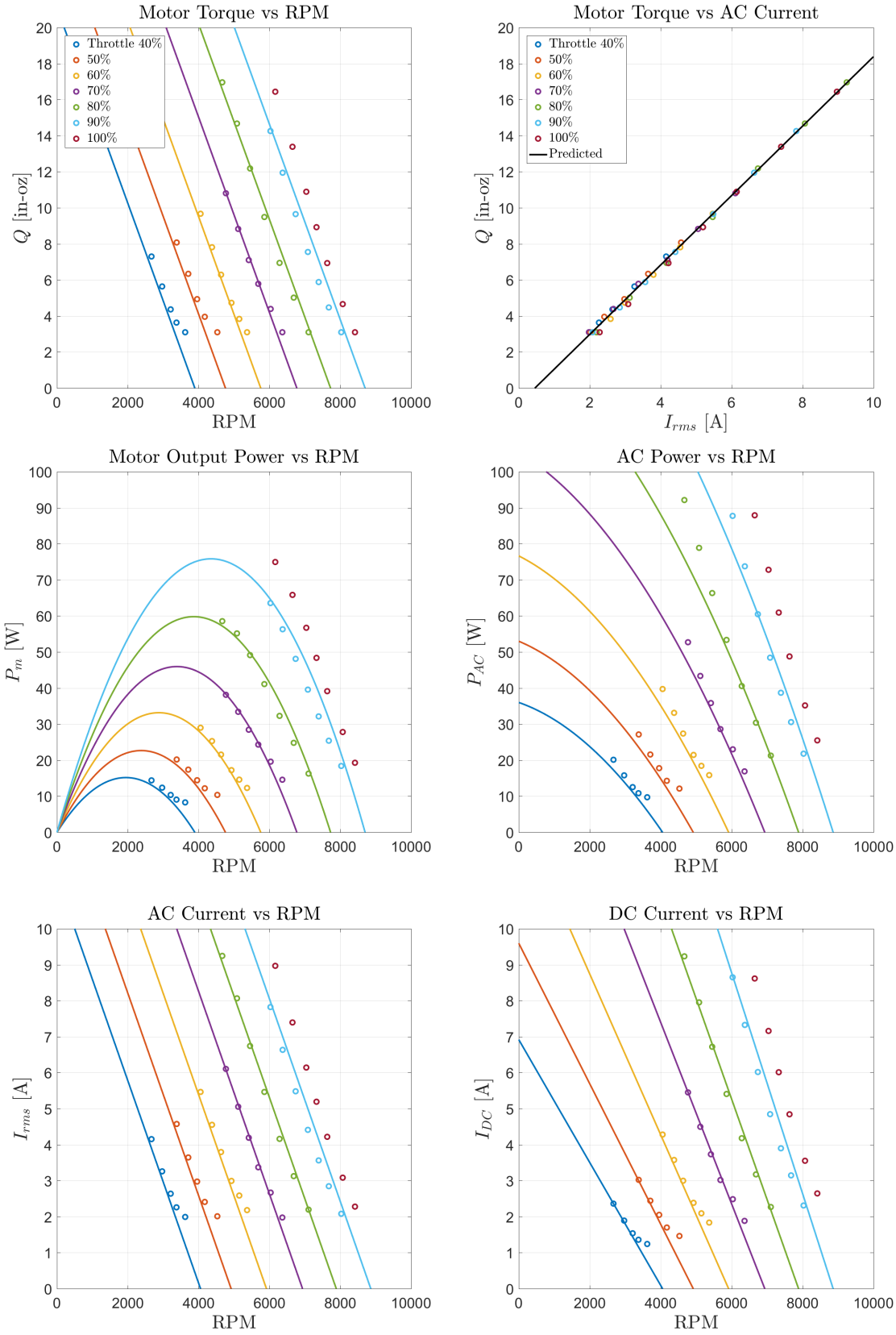

Figure 5.48: Efficiency plots - EMAX 935 KV - MultiStar 30A - 11.1V

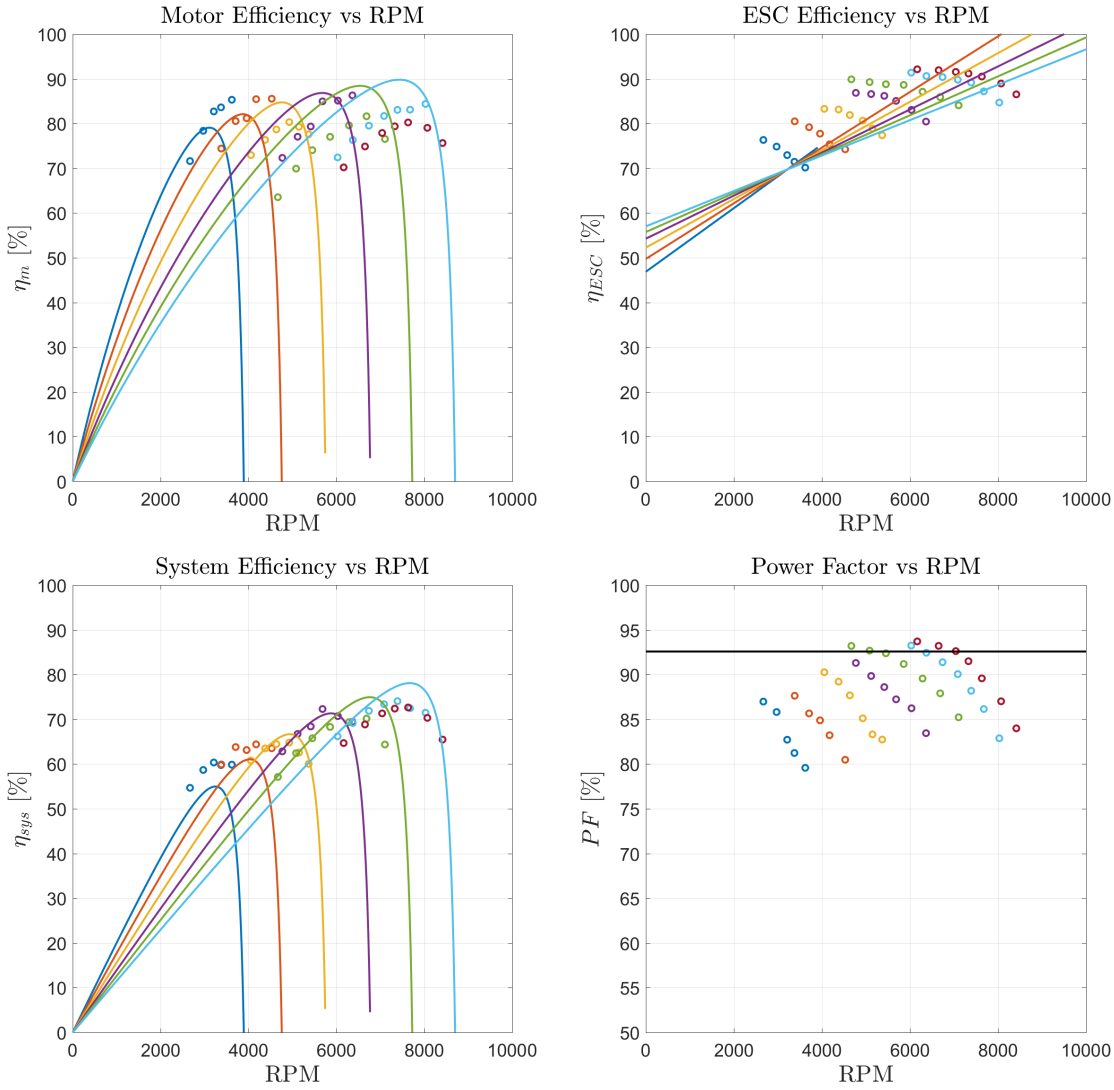

Figure 5.49: Performance plots - EMAX 935 KV - DYS BlHeliOpto 40A - 11.1V

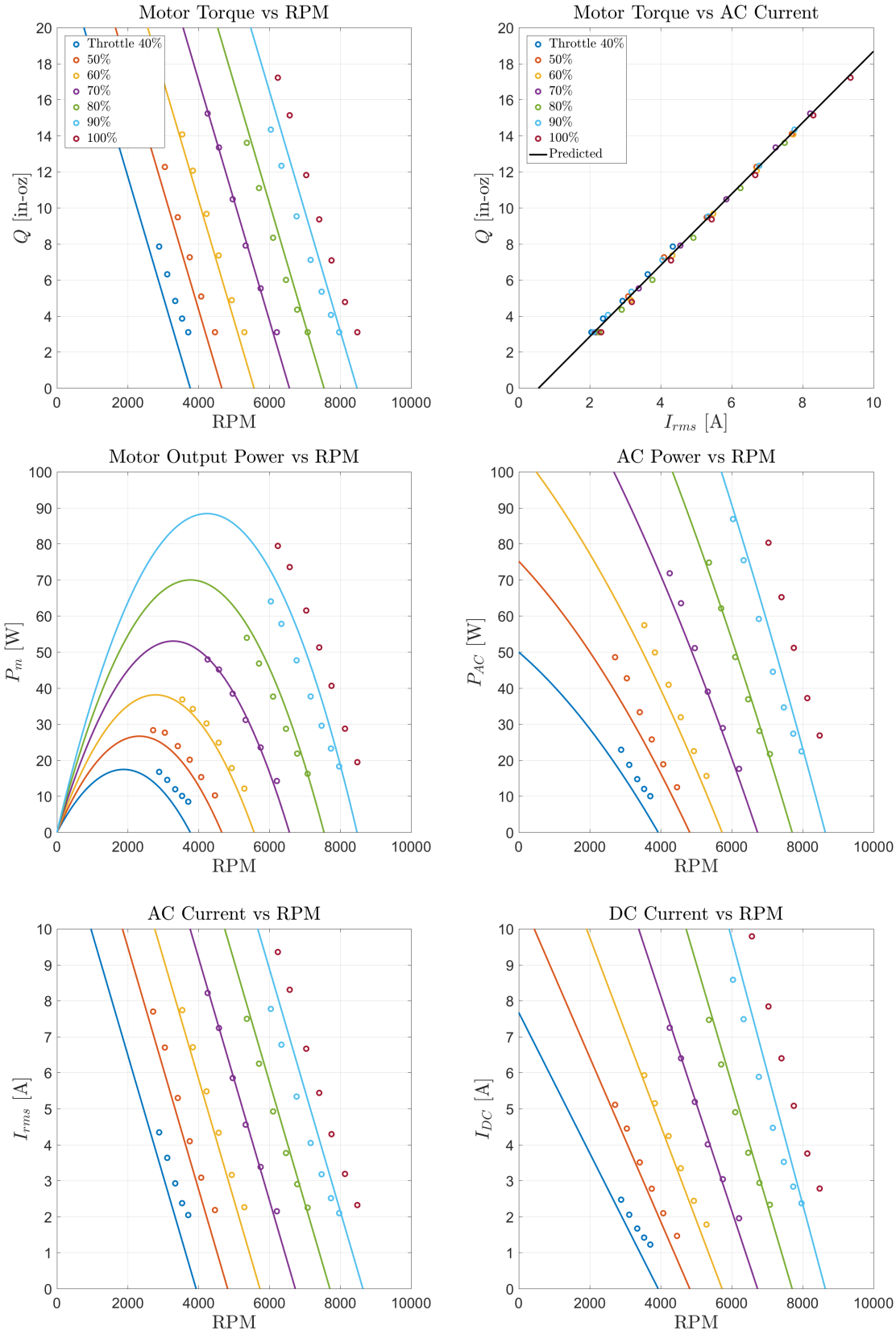

Figure 5.50: Efficiency plots - EMAX 935 KV - DYS BlHeliOpto 40A - 11.1V

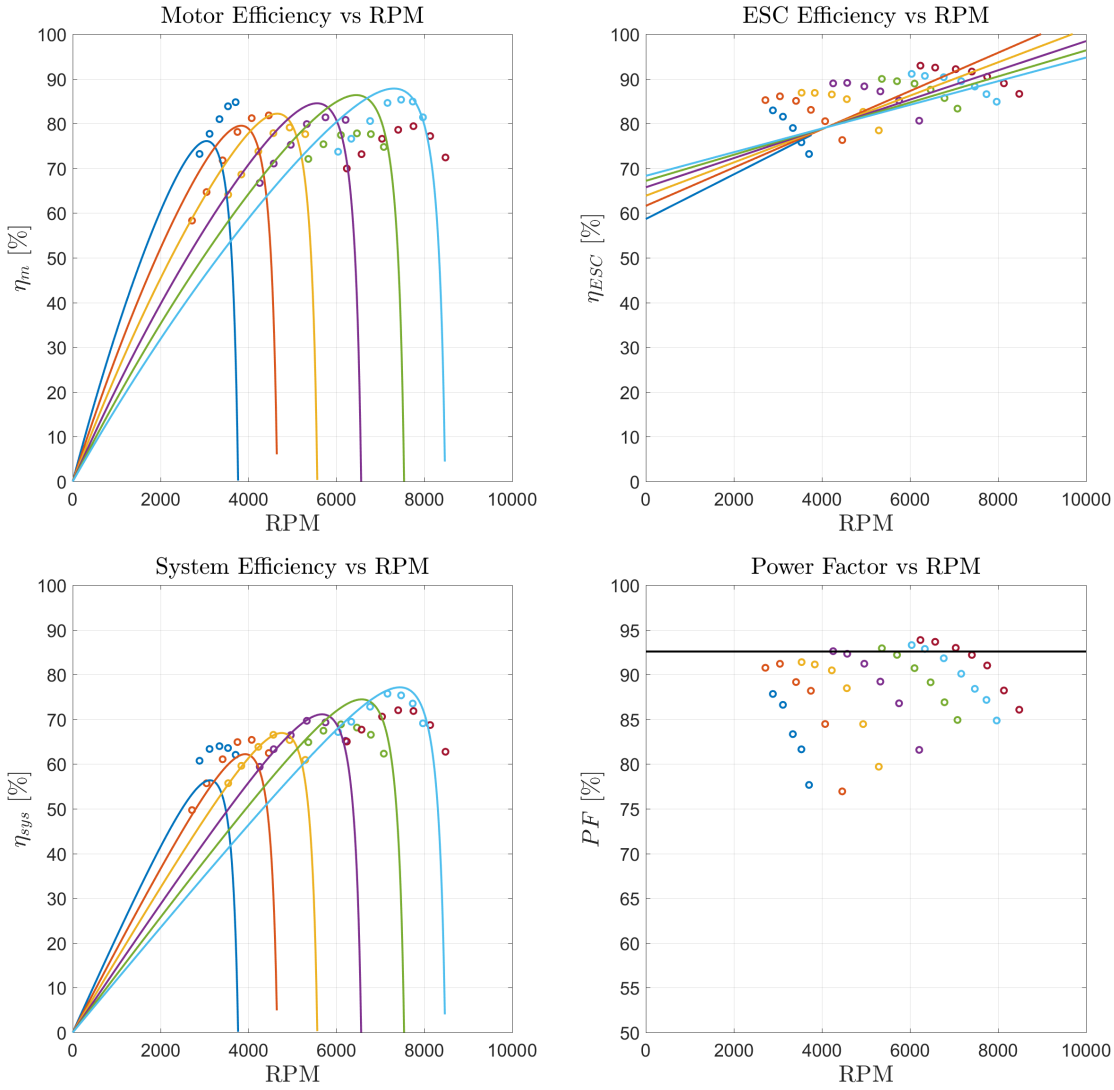

Figure 5.51: Performance plots - EMAX 1700 KV - SpiderLite 18A - 11.1V

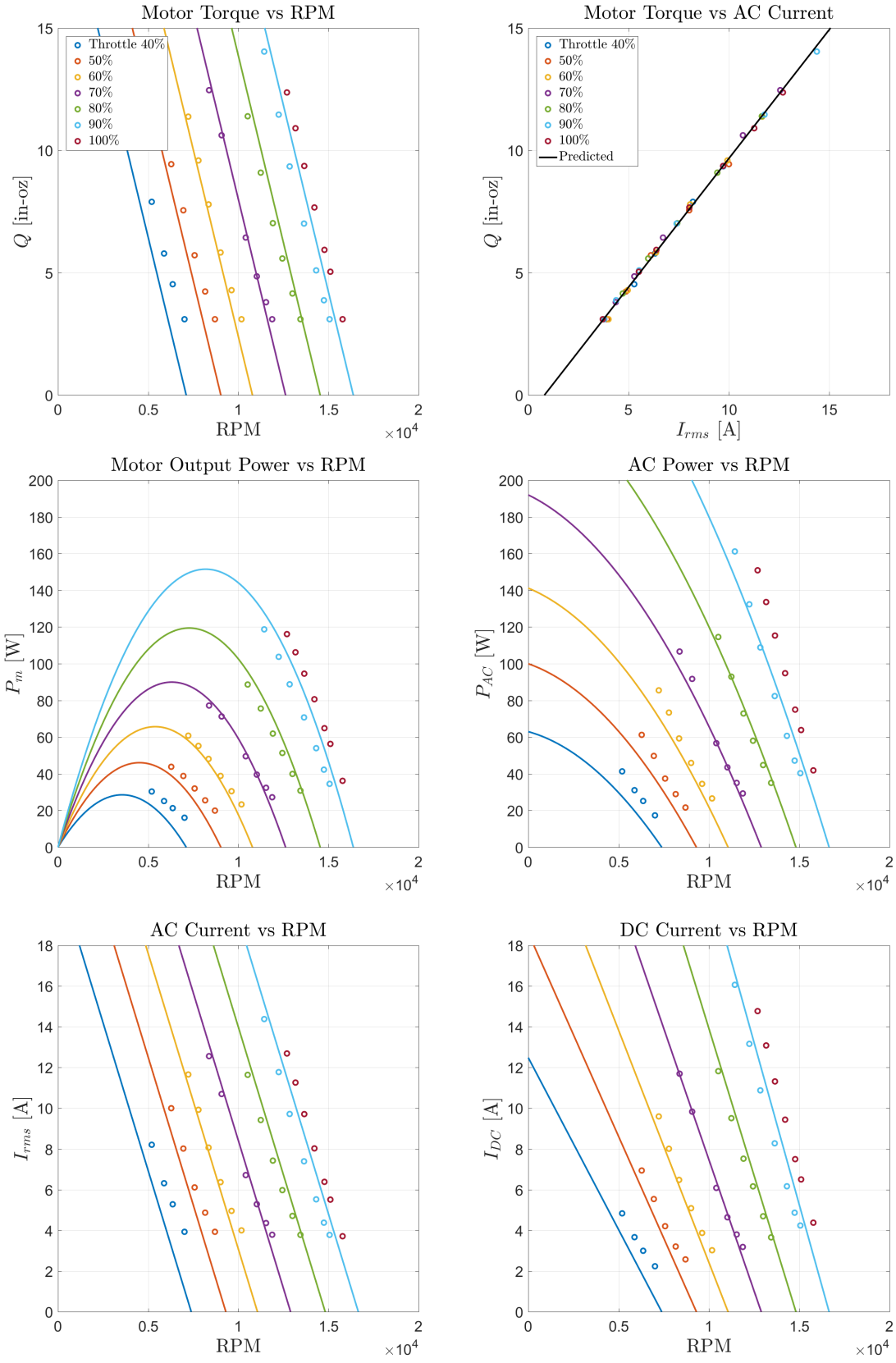

Figure 5.52: Efficiency plots - EMAX 1700 KV - SpiderLite 18A - 11.1V

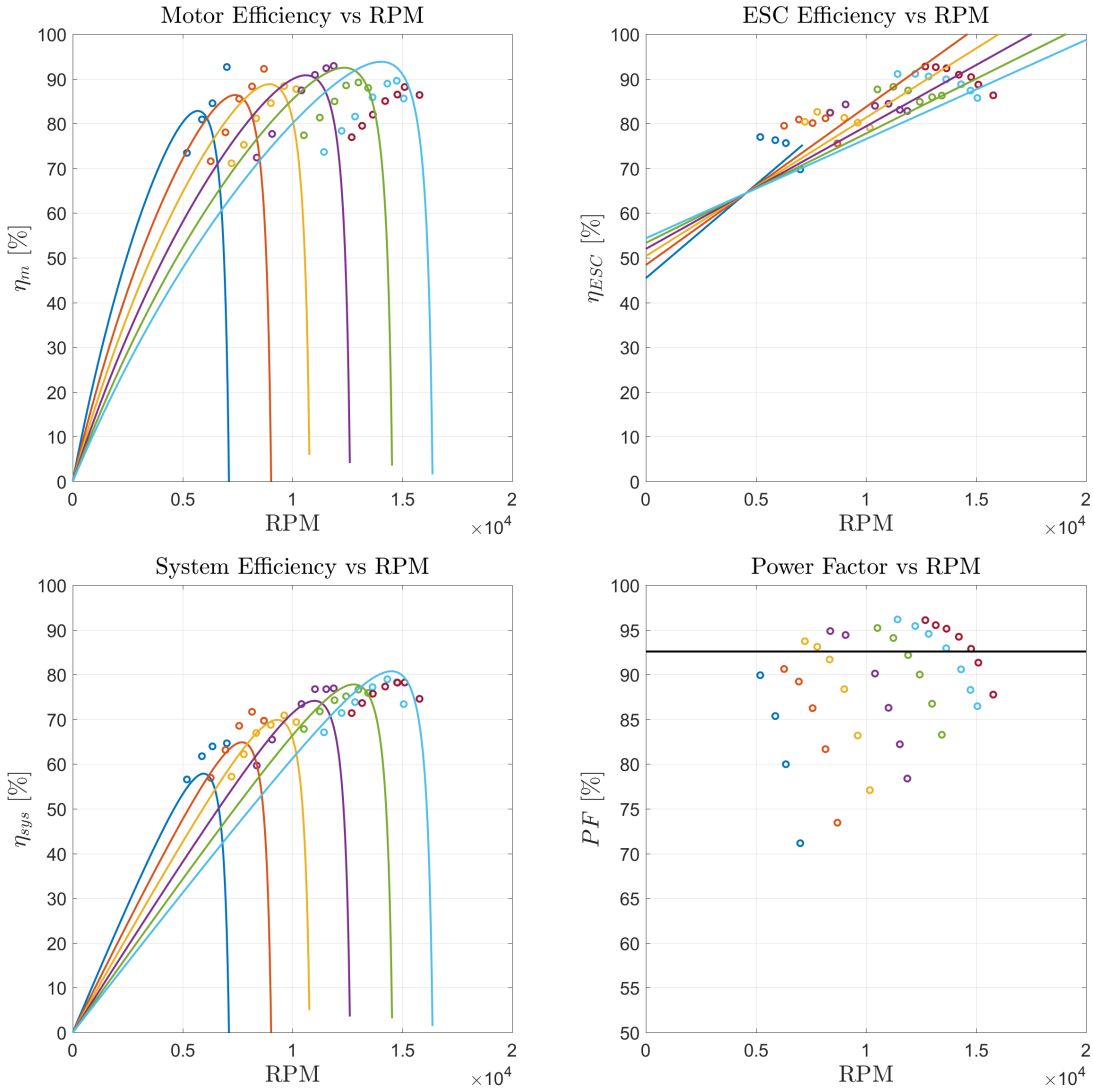

Figure 5.53: Performance plots - EMAX 1700 KV - MultiStar 30A - 11.1V

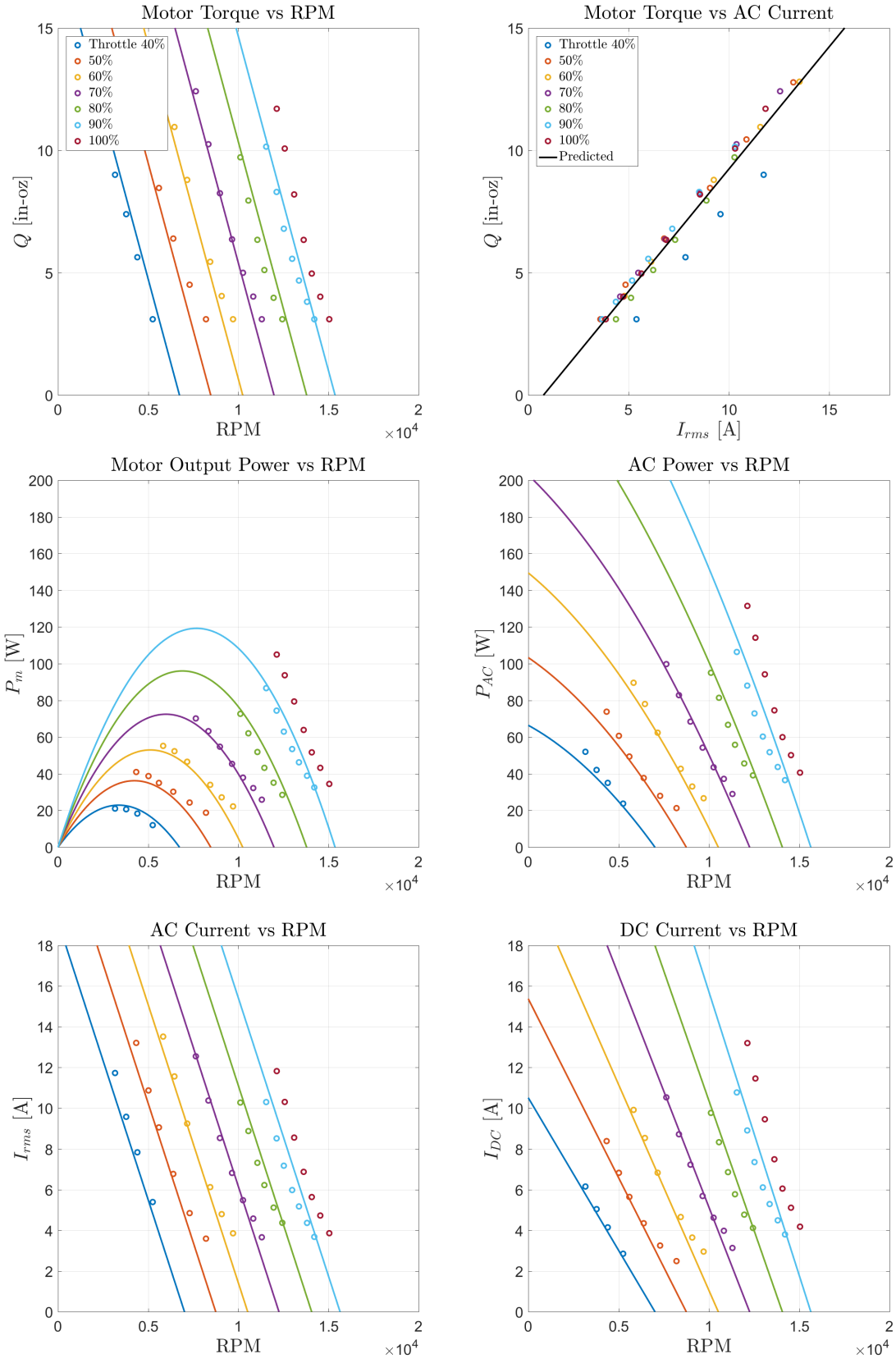

Figure 5.54: Efficiency plots - EMAX 1700 KV - MultiStar 30A - 11.1V

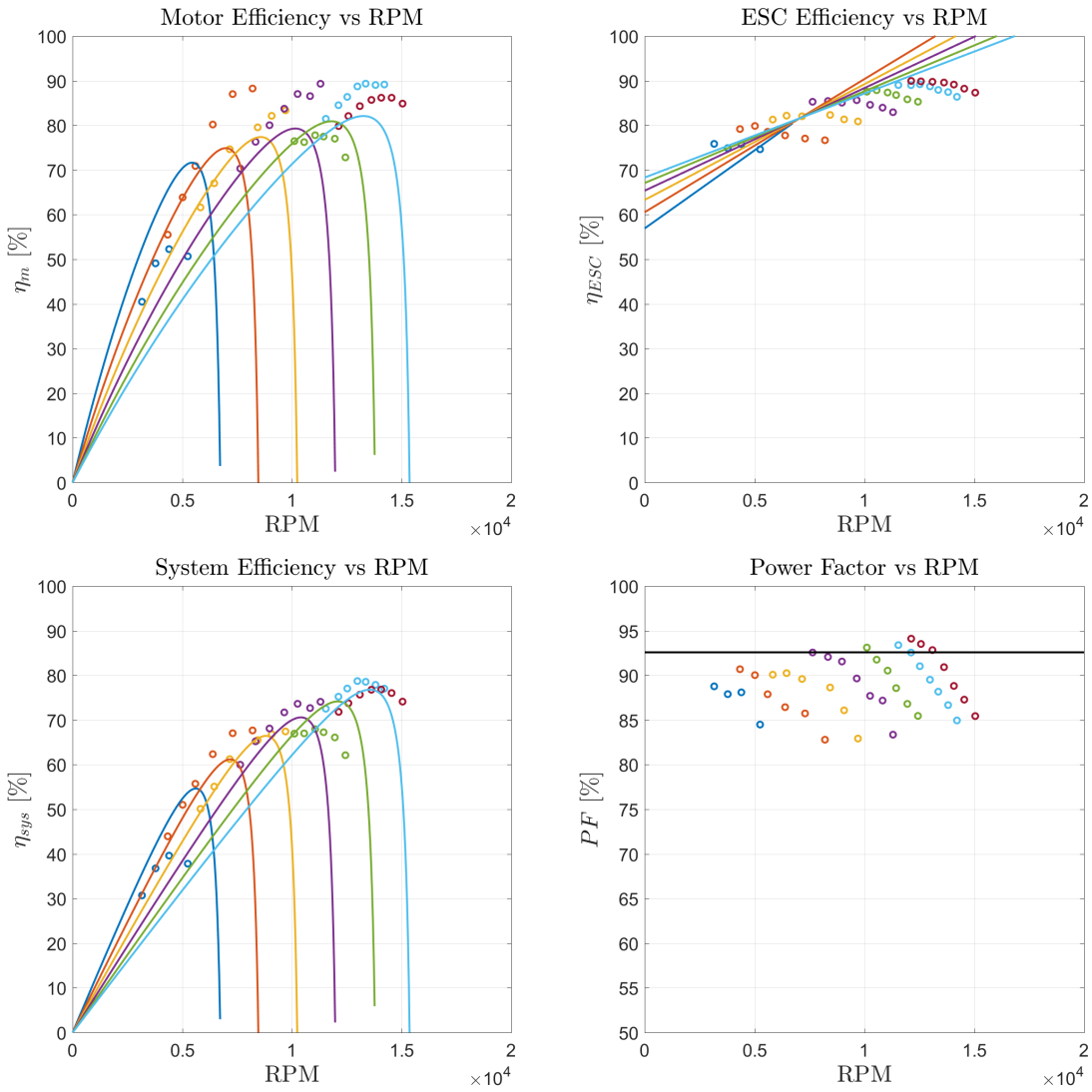

Figure 5.55: Performance plots - EMAX 1700 KV - DYS BlHeliOpto 40A - 11.1V

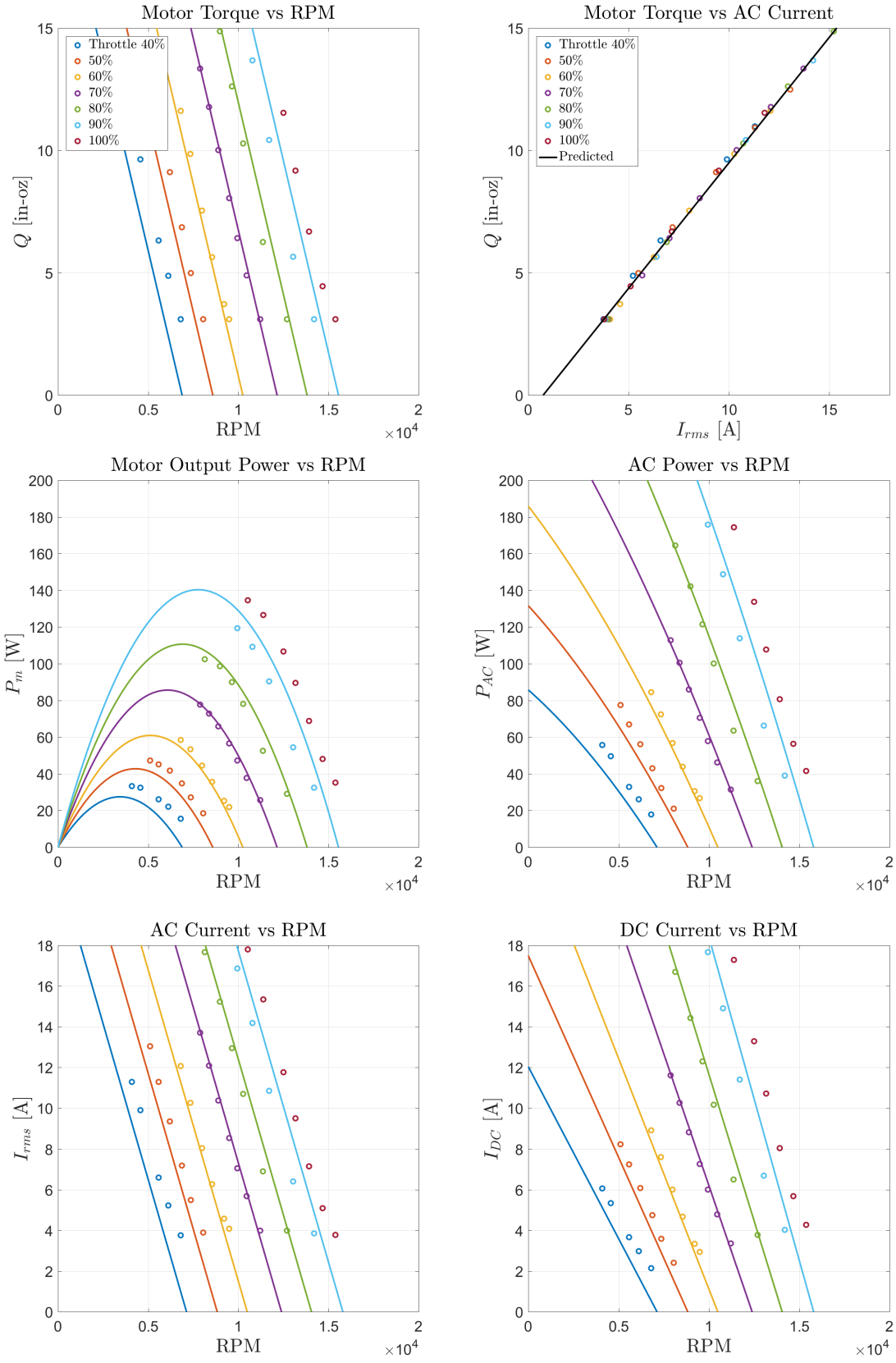

Figure 5.56: Efficiency plots - EMAX 1700 KV - DYS BlHeliOpto 40A - 11.1V

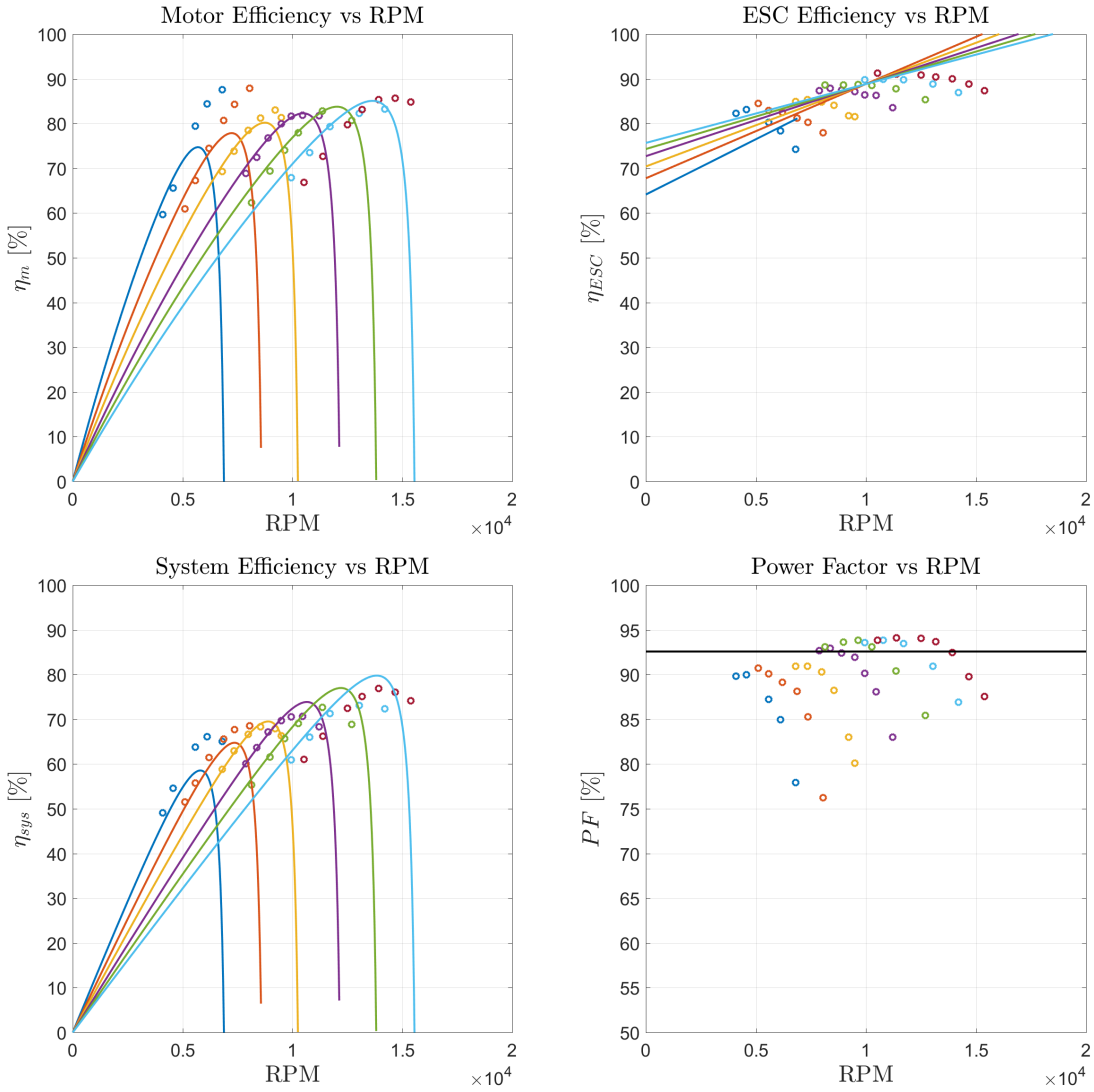

Figure 5.57: Performance plots - EMAX 1900 KV - MultiStar 30A - 11.1V

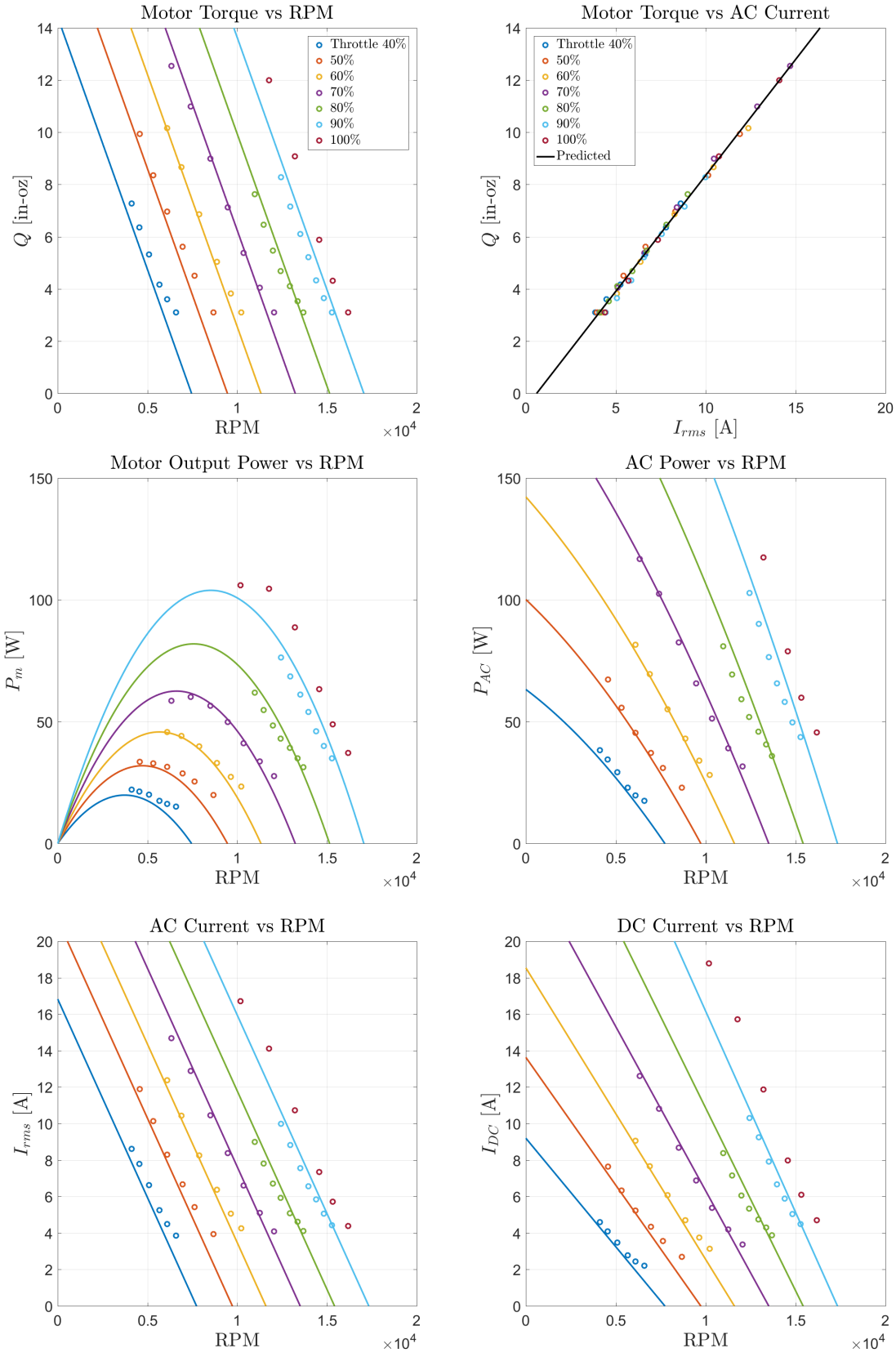

Figure 5.58: Efficiency plots - EMAX 1900 KV - MultiStar 30A - 11.1V

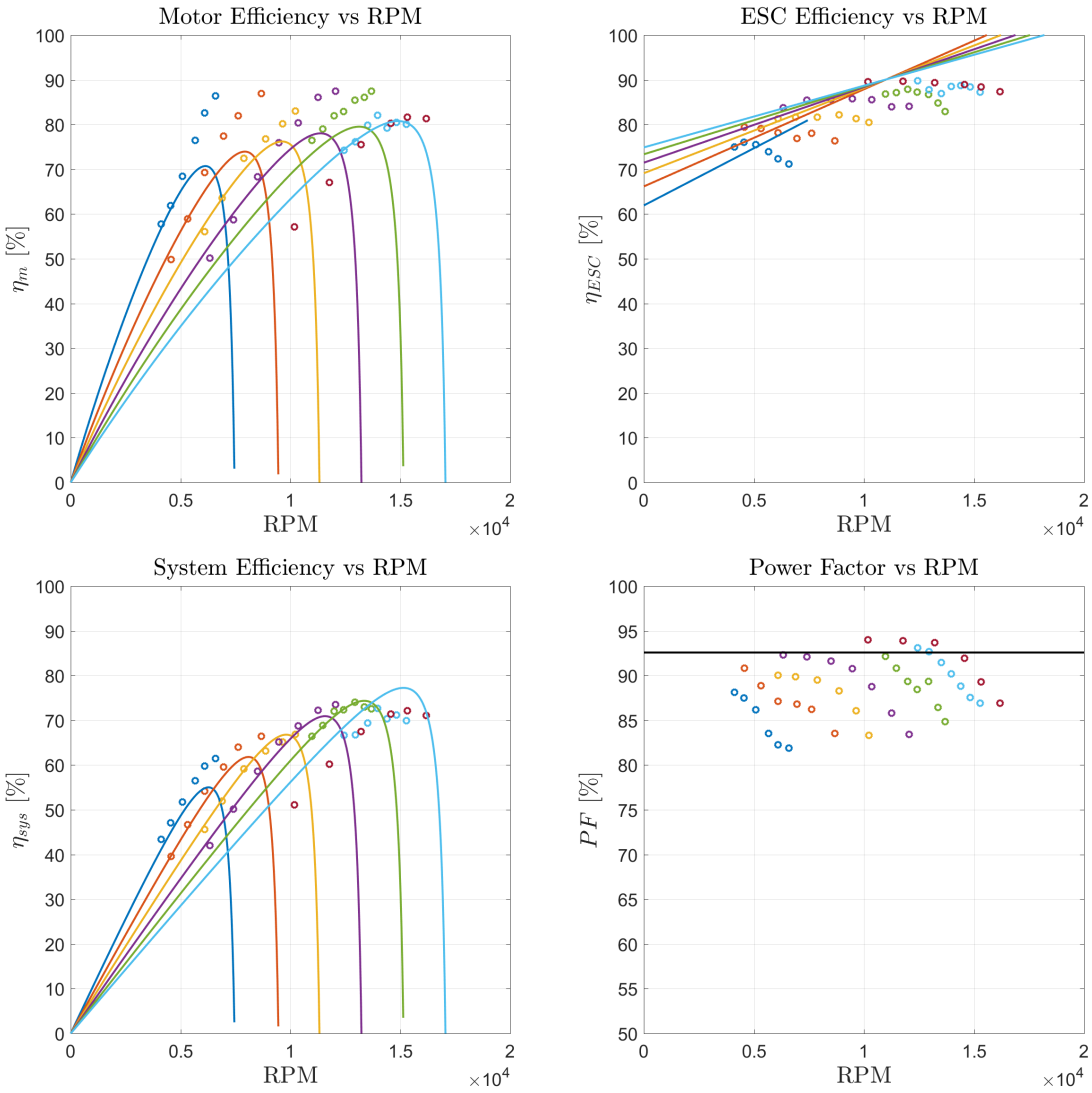

Figure 5.59: Performance plots - EMAX 1900 KV - DYS BlHeliOpto 40A - 11.1V

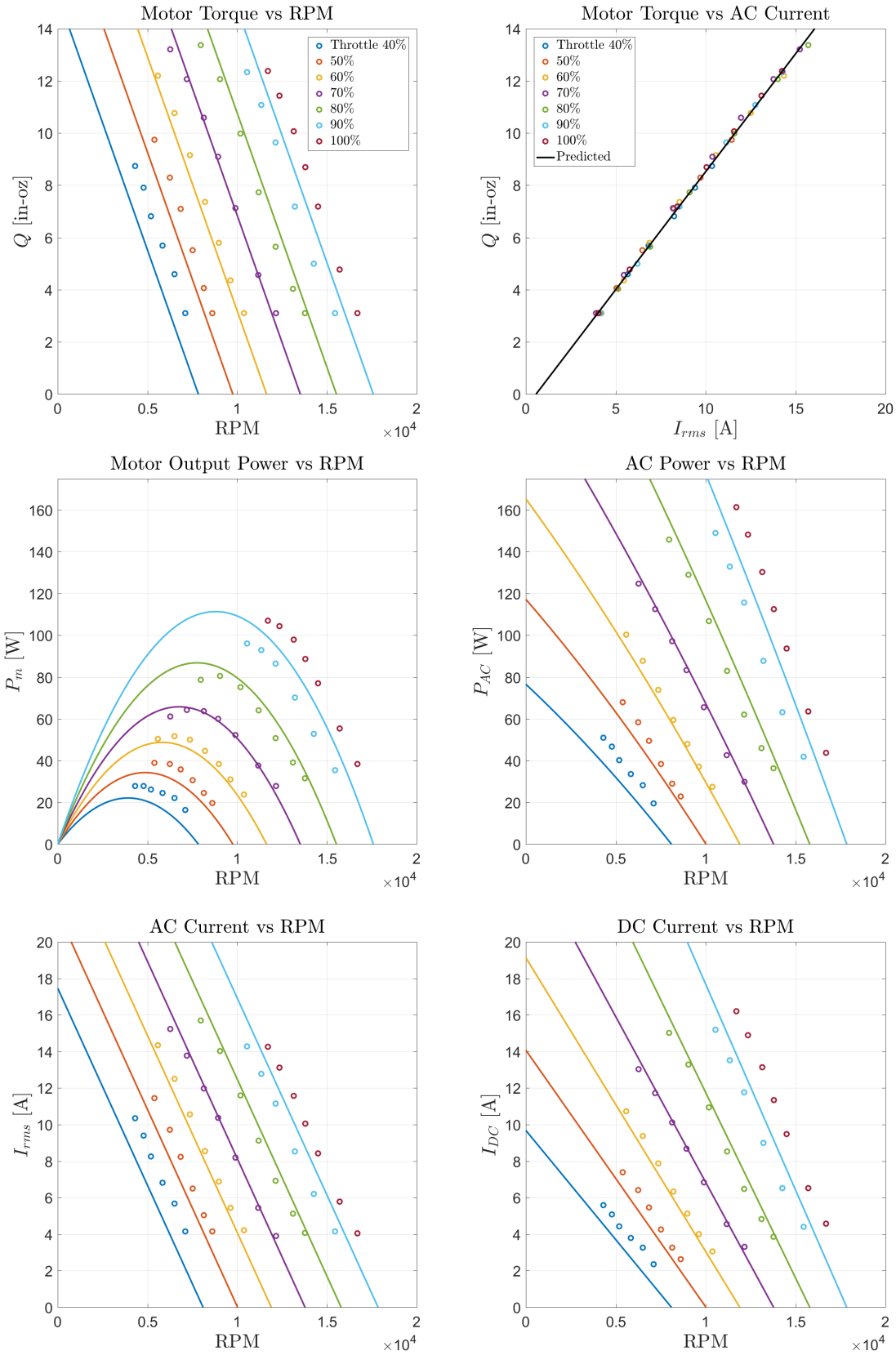

Figure 5.60: Efficiency plots - EMAX 1900 KV - DYS BlHeliOpto 40A - 11.1V

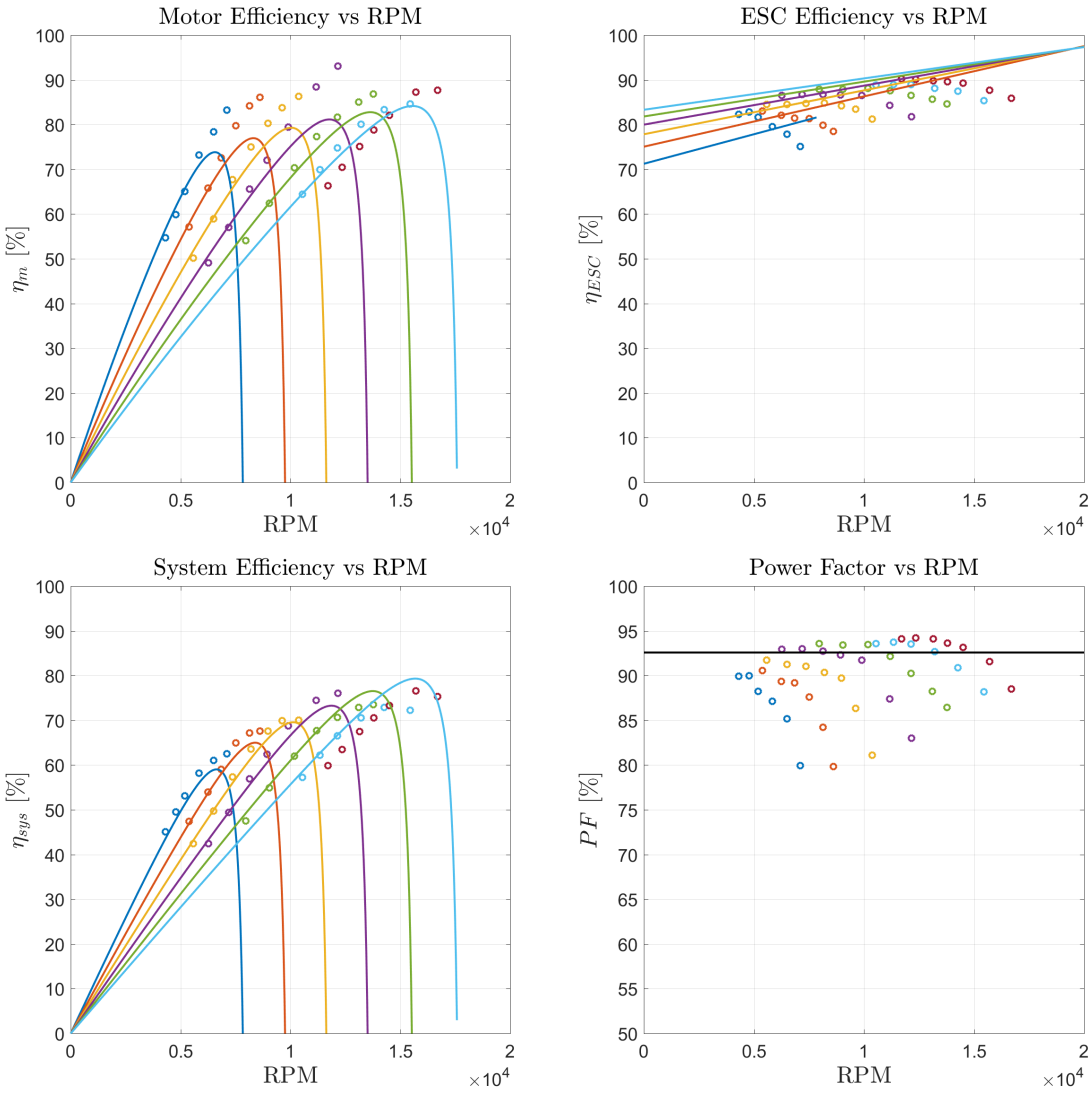

5.3 Tests at 14.8V

Figure 5.61: Performance plots - DJI 920 KV - SpiderLite 18A - 14.8V

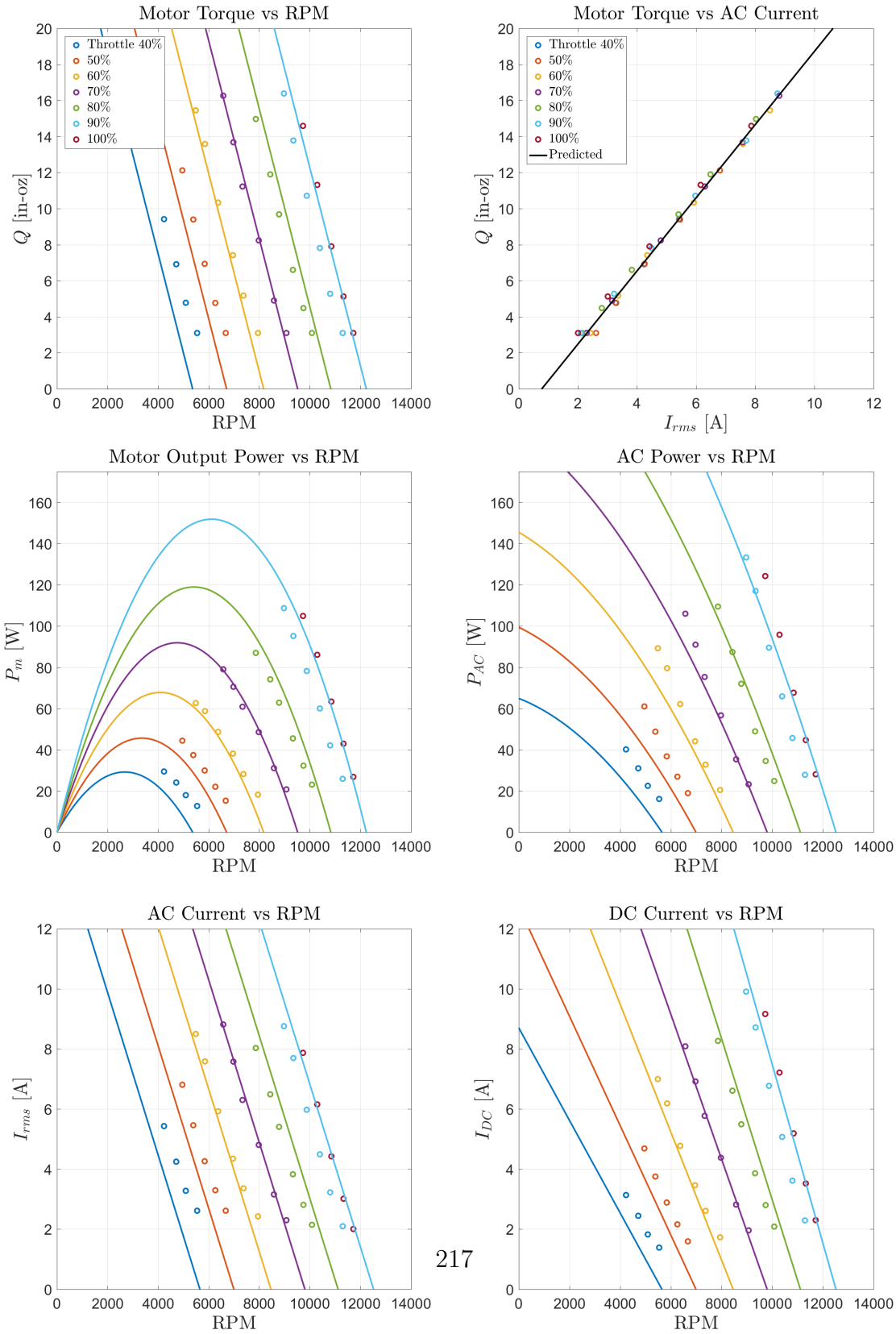

Figure 5.62: Efficiency plots - DJI 920 KV - SpiderLite 18A - 14.8V

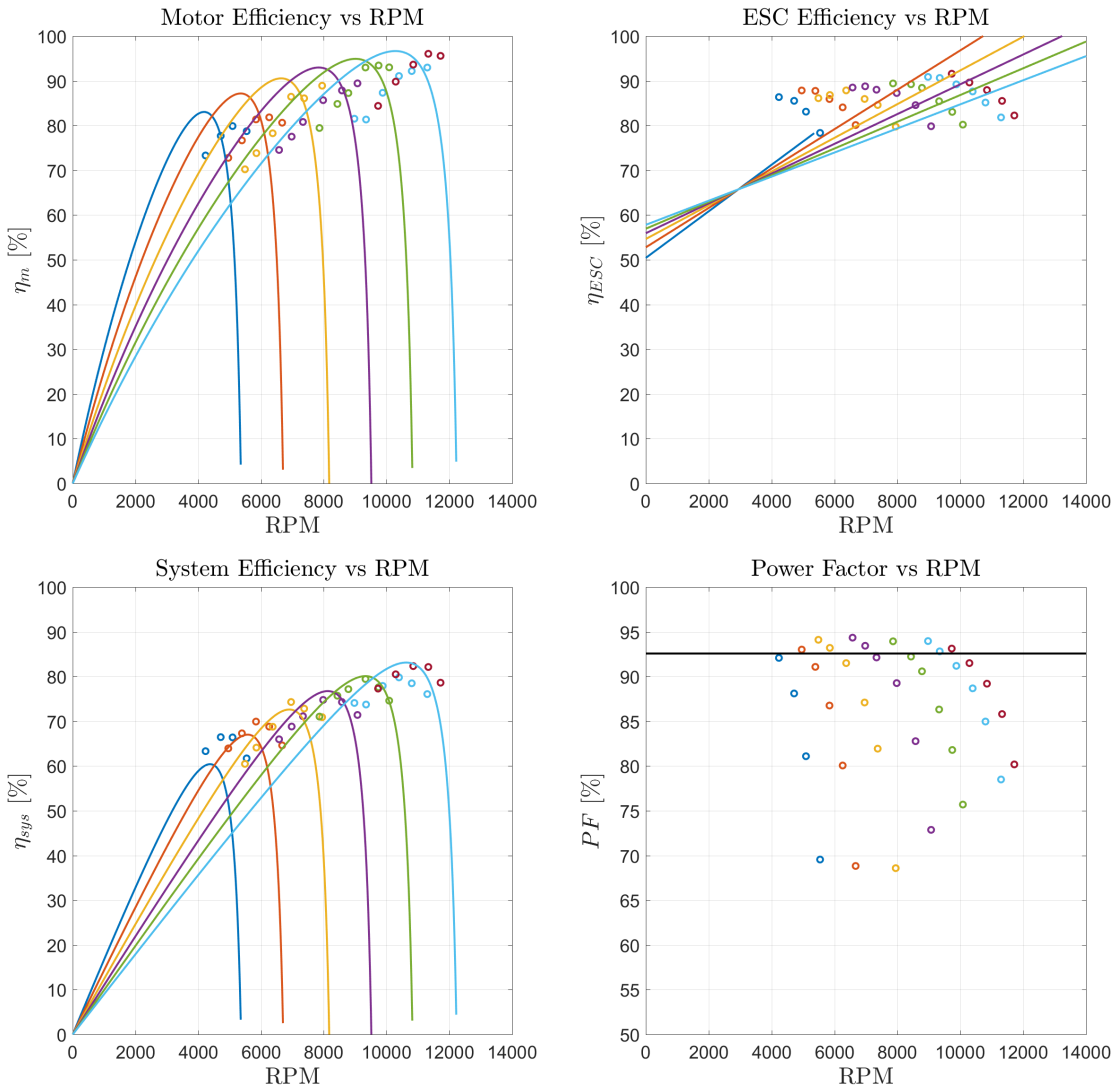

Figure 5.63: Performance plots - DJI 920 KV - DYS BlHeliOpto 40A - 14.8V

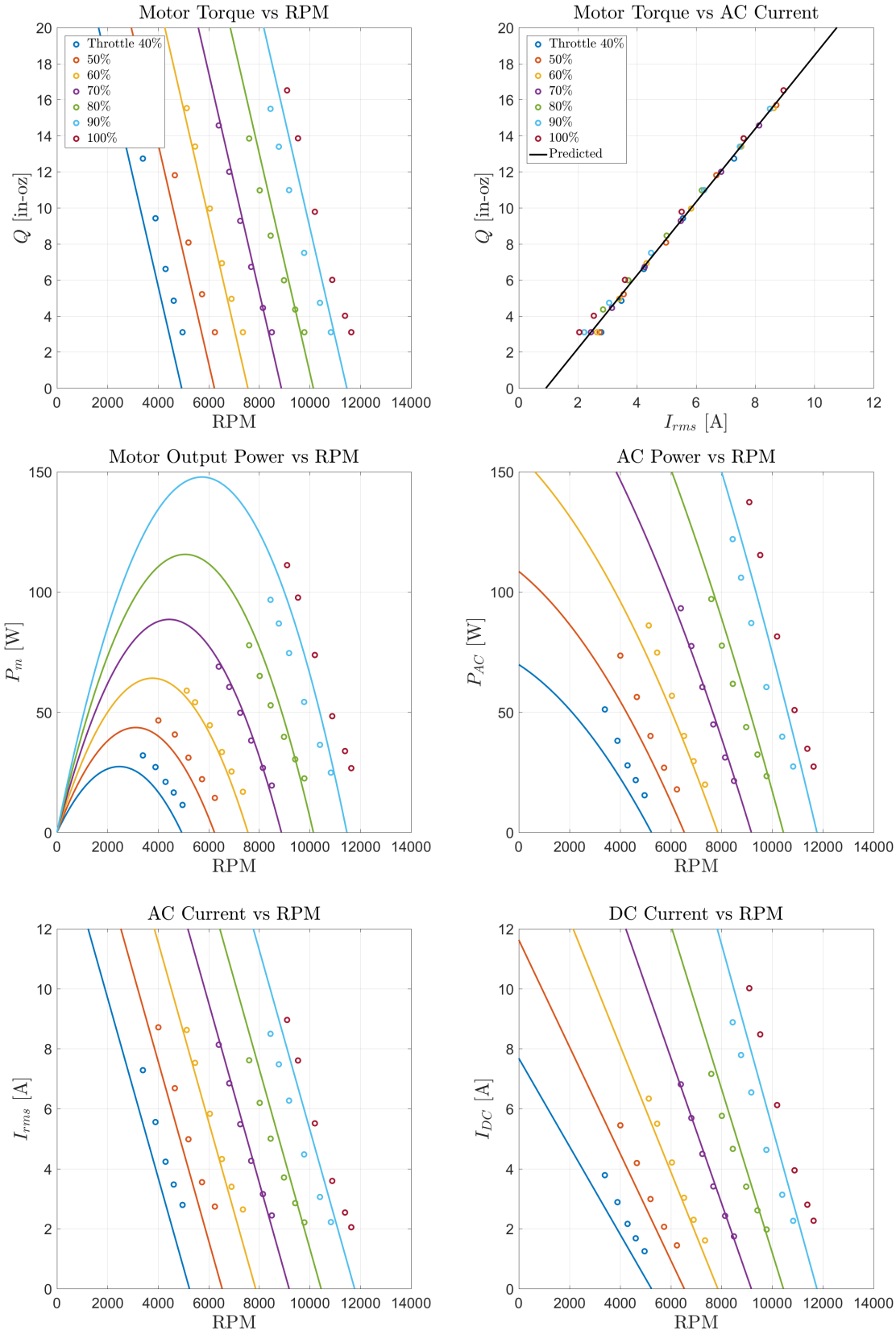

Figure 5.64: Efficiency plots - DJI 920 KV - DYS BlHeliOpto 40A - 14.8V

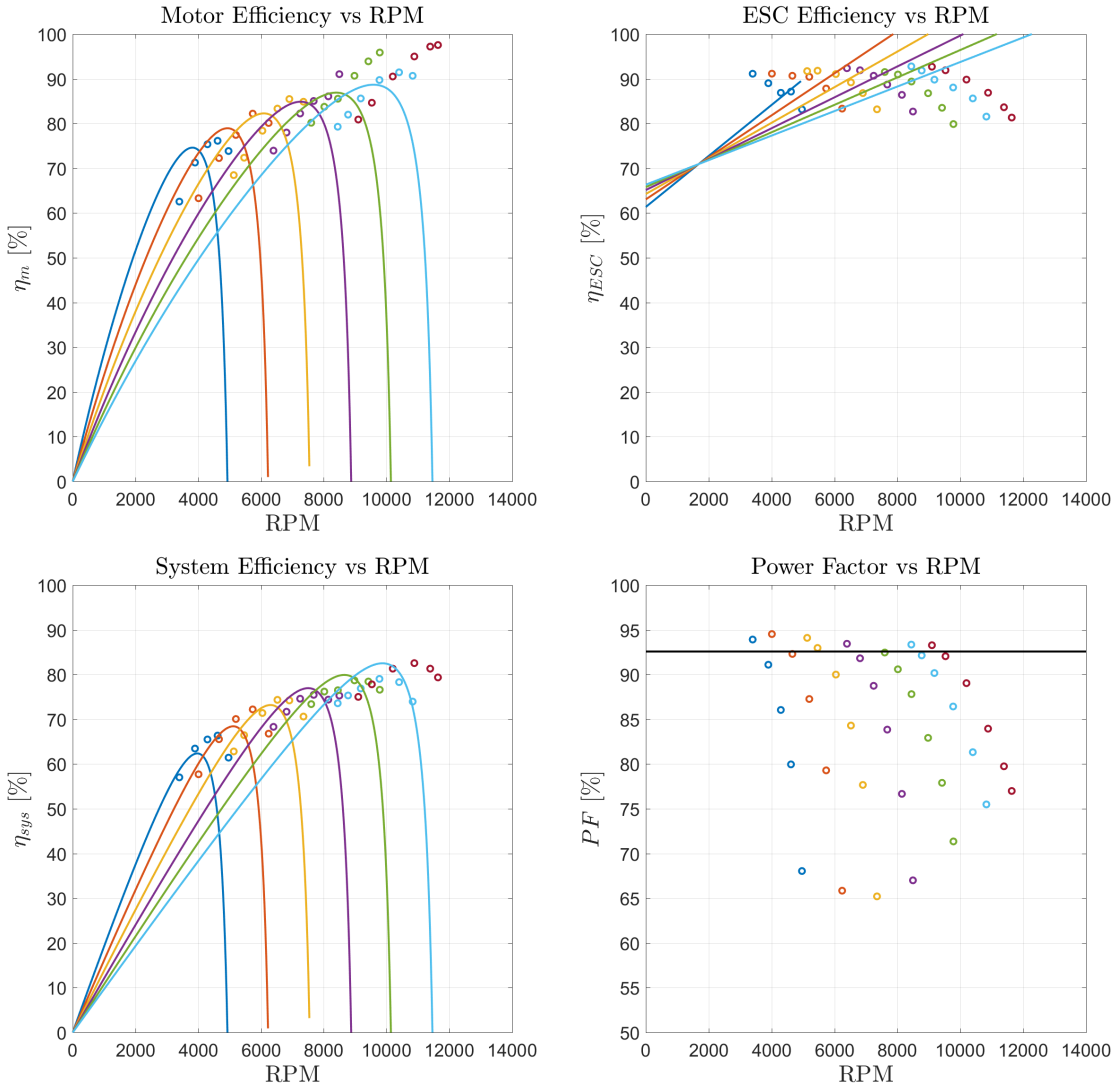

Figure 5.65: Performance plots - EMAX 935 KV - SpiderLite 18A - 14.8V

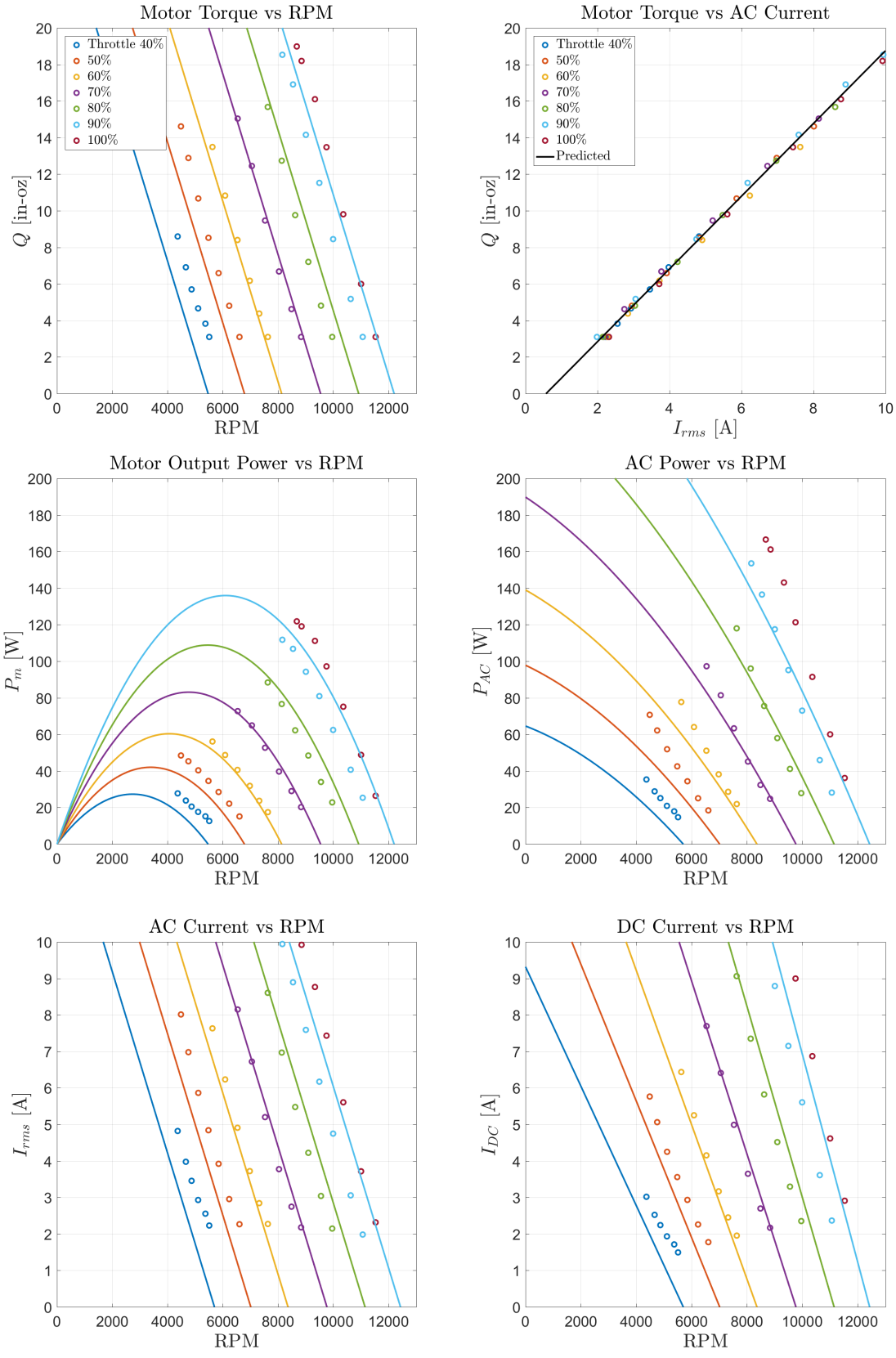

Figure 5.66: Efficiency plots - EMAX 935 KV - SpiderLite 18A - 14.8V

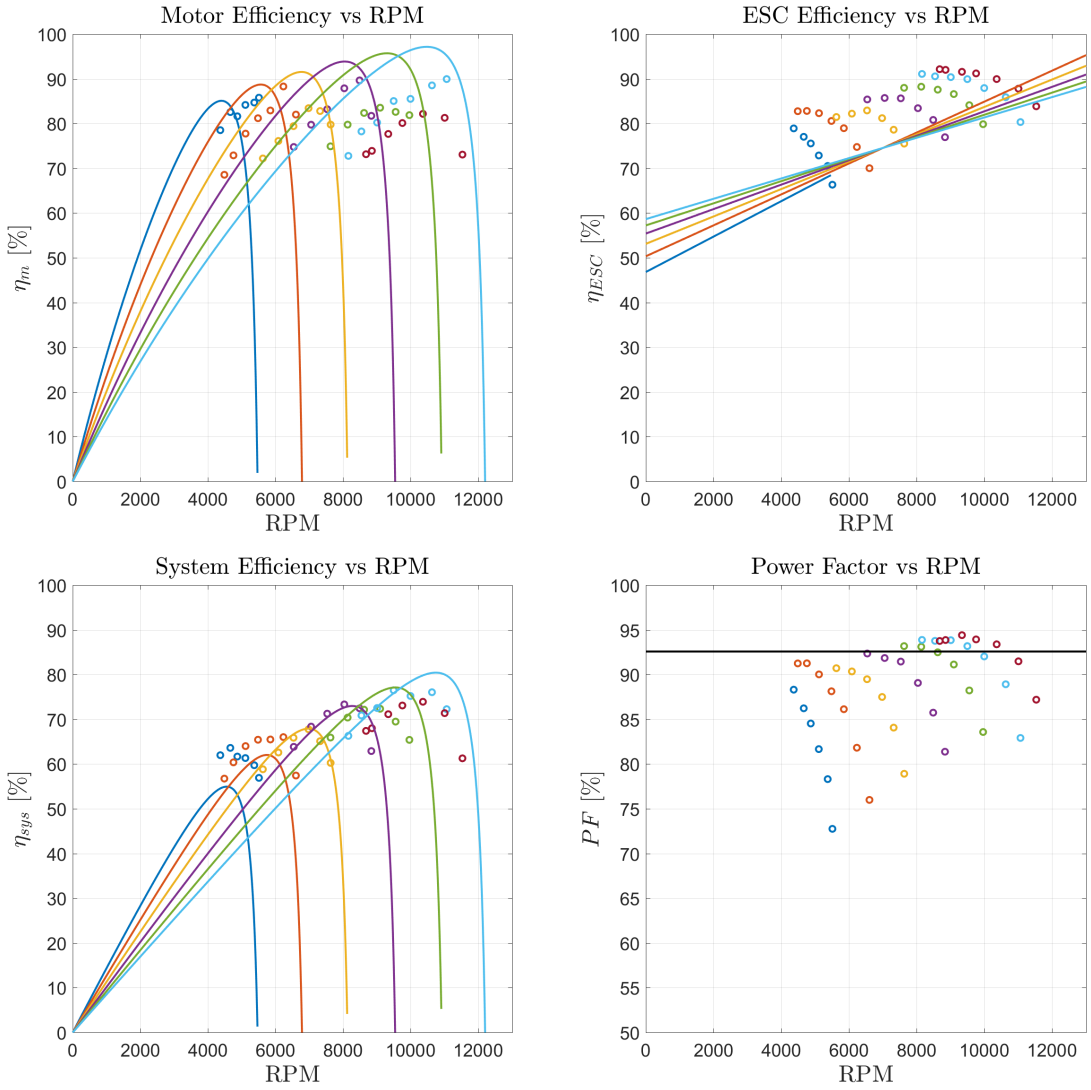

Figure 5.67: Performance plots - EMAX 935 KV - MultiStar 30A - 14.8V

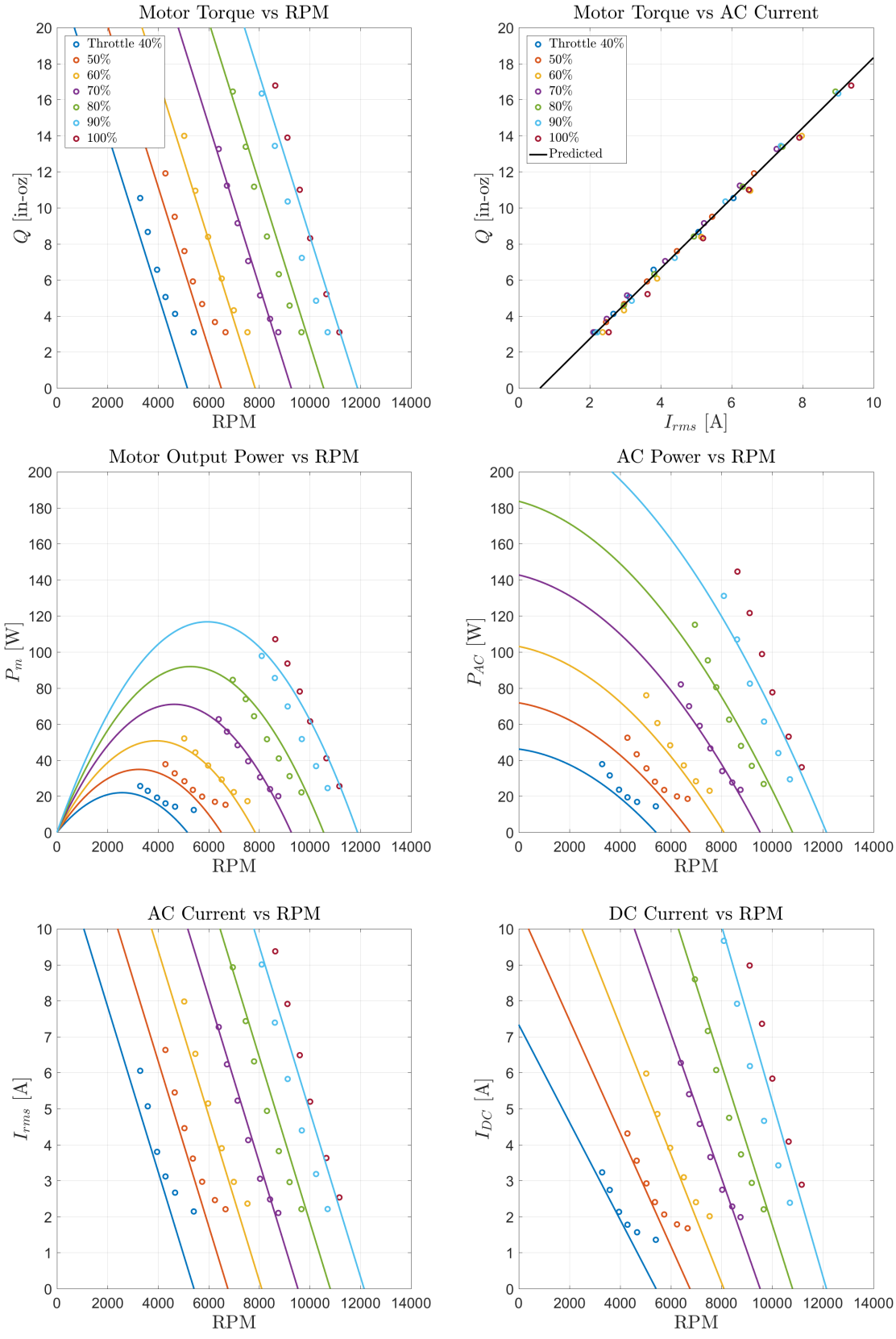

Figure 5.68: Efficiency plots - EMAX 935 KV - MultiStar 30A - 14.8V

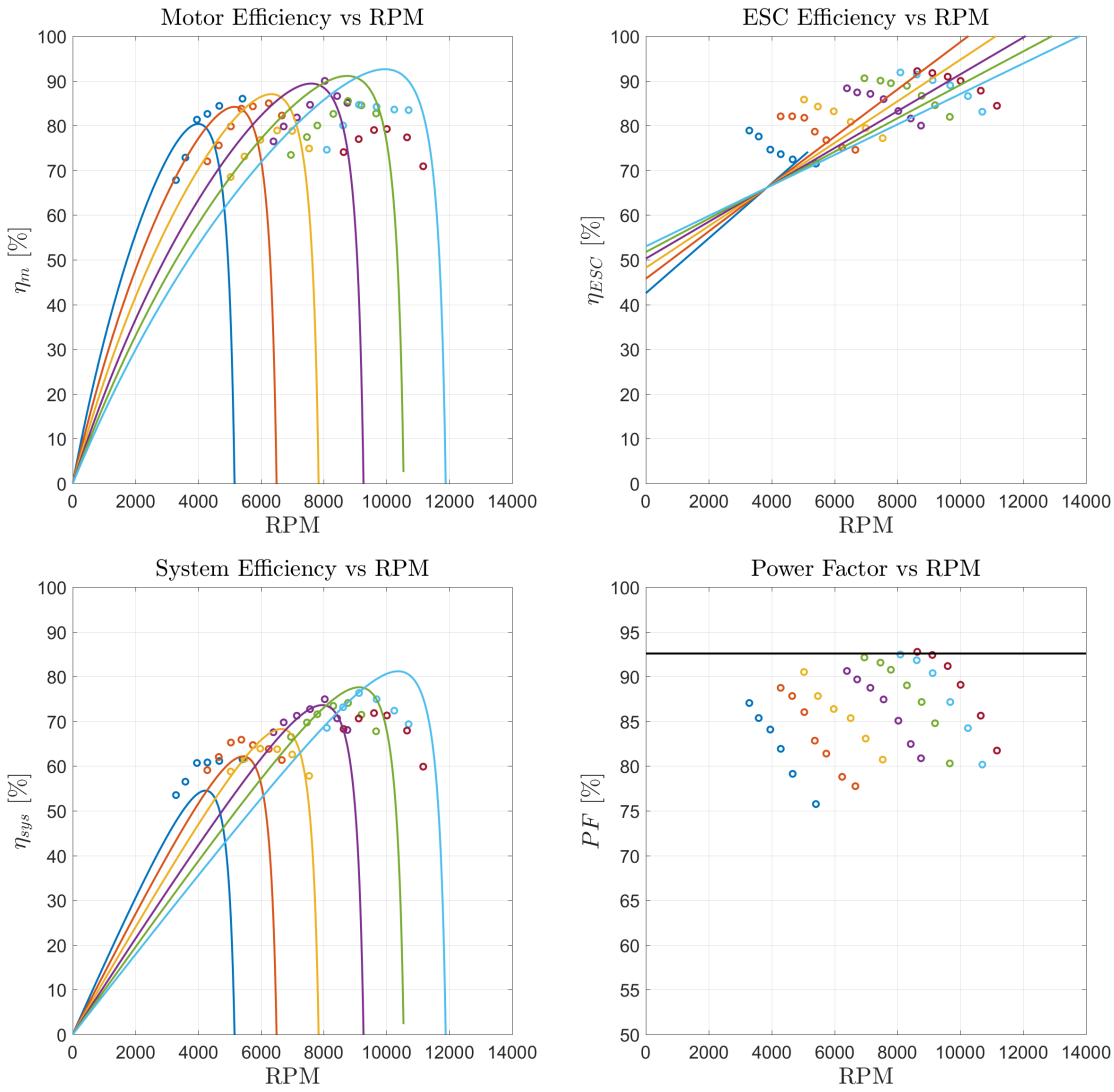

Figure 5.69: Performance plots - EMAX 935 KV - DYS BlHeliOpto 40A - 14.8V

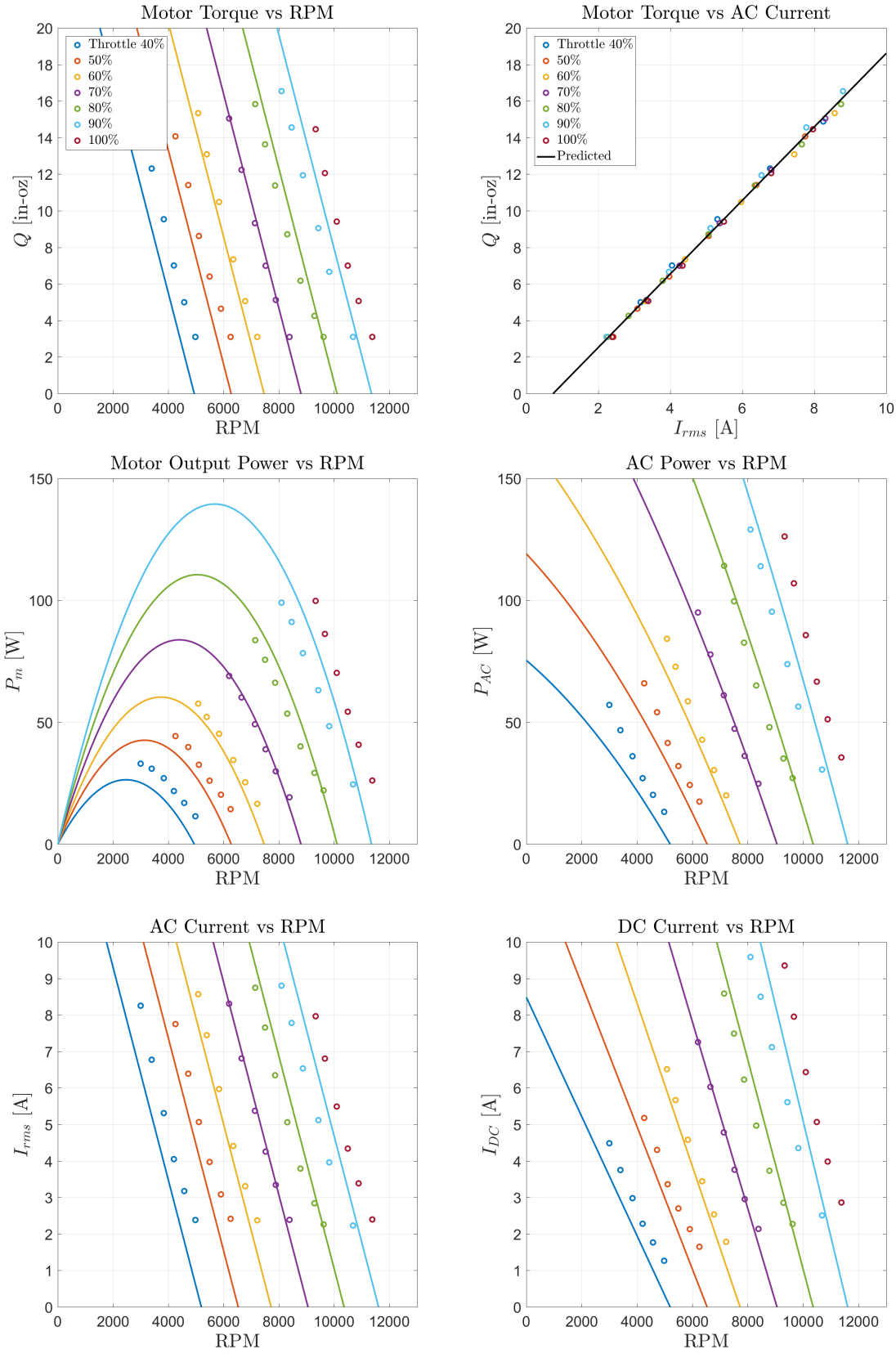

Figure 5.70: Efficiency plots - EMAX 935 KV - DYS BlHeliOpto 40A - 14.8V

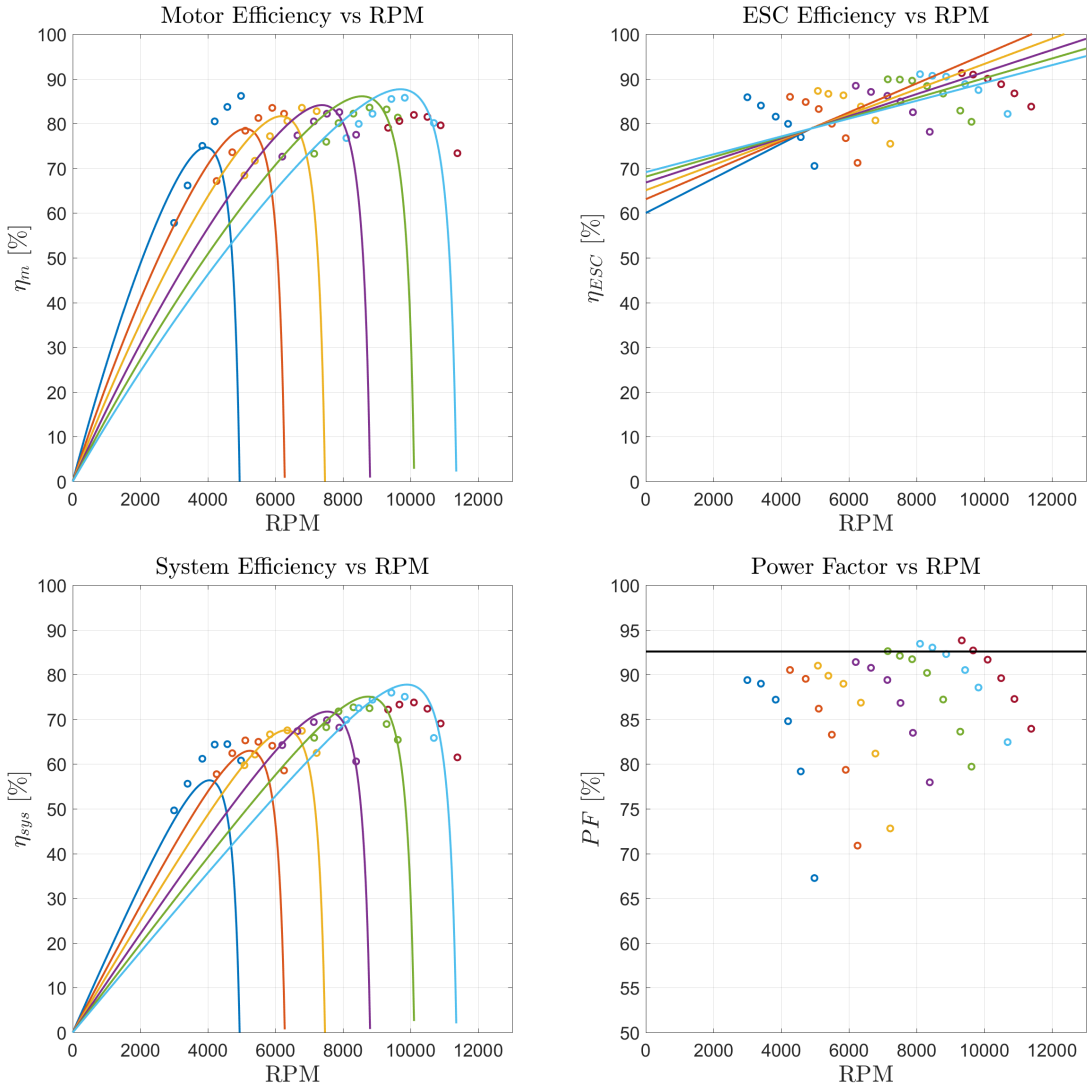

5.4 Determining Motor Parameters from Experimental Data

Once a BLDC motor, ESC, and V_{DC} are tested, the next step is to extract the physical parameters of the model. It is important to have enough points to properly cover the motor's expected operating range, otherwise insufficient data points could result in a poorly fit model (as was with motors tested below 800 KV). This section describes a procedure to minimize the error between experimentally recorded points and model predictions. A summary and description of modeling parameters from Chapter 4 is given in table 5.3.

Table 5.3: ESCs tested using the custom dynamometer.

Constant	Description
K_T [mNm/A]	$Q = K_T I_{rms}$, Motor torque constant
K_E [mVs/rad]	$V_E = K_E \omega$, Motor back EMF constant
I_o [A]	Motor profile rms current
R_m [Ω]	Motor resistance
C_1 [-]	ESC switching slope
C_0 [-]	ESC switching offset
R_{ESC} [Ω]	ESC Resistance

Key importance is placed on matching the Q-rms current, Q-RPM curve, AC power curves, and the DC current draw curves. First K_T, I_o, and R_{ESC} are found, then using these values K_E and R_m are estimated. Once the motor has been described, the ESC transformer coefficients C_0 and C_1 are deduced. This process can be outlined as:

1. Determine K_T and I_o from Q vs I_{rms} plot

2. Estimate R_{ESC} from $V_{LL,rms}$ vs I_{rms} relation

3. Using the estimated motor values, predict K_E and R_m from the Q vs ω plot

4. Evaluate ESC coefficients C_0 and C_1 from I_{DC}/I_{rms} vs T_R

Together, these 6 values predict the performance of the motor and the ESC for all throttle ranges and loads.

Starting with the Q-rms current plot, shown in figure 5.71, the equation relating rms current to output torque is a straight line described by equation 4.35 and is copied below:

$$Q = K_T(I_{rms} - I_o)$$

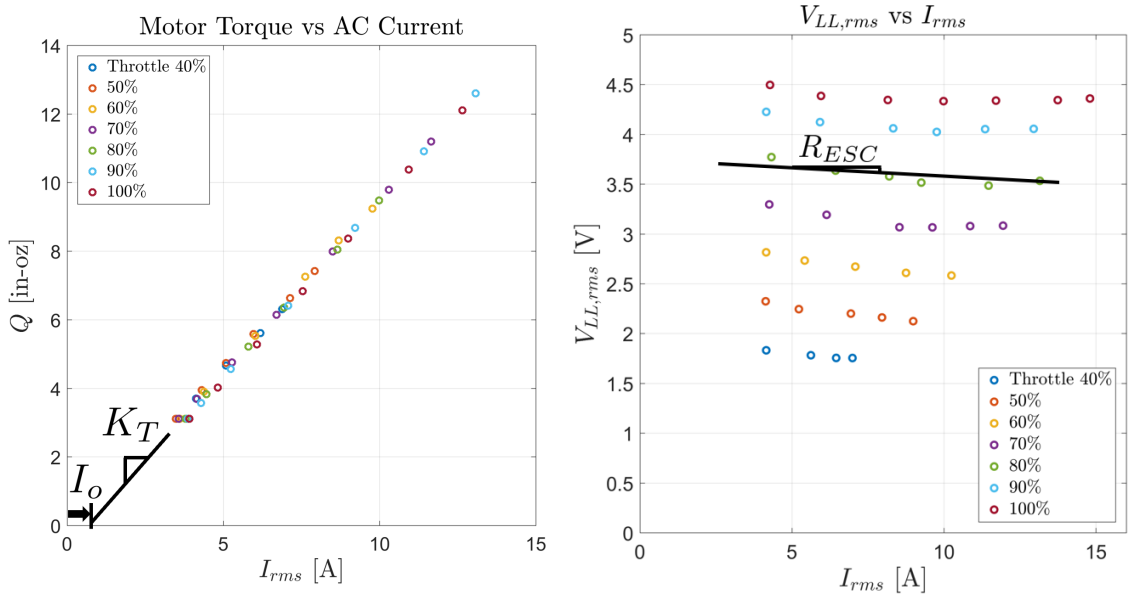

Figure 5.71: Experimentally observed Q-RPM relation.

Figure 5.71 shows that all of the points line on the same line, for all throttles.

To find K_T and I_o a linear relation ($y = mx + b$) is needed with:

$$y = Q \quad x = I_{rms}$$

$$m = K_T \quad b = -K_T I_o$$

For determining phyiscal parameters from experimental data, 2 strategies exist. The first is to determine parameters for each throttle setting and then average the individual estimates together, resulting in a single estimate for all throttle settings. The second method involves formulating a linear least squares problem to minimize the total error for all throttles using a single estimate. Which method is chosen depends on the amount of allowed error.

For K_T and I_o, determining K_T for each throttle setting alone could produce K_T estimates which can change up to 10% between throttle settings. As such, the second method is used, which involves considering each test at a constant throttle containing a vector of information and combining them in a specific manner. Each test at constant throttle produces a vector of experimental obtained points, an example for torque at 40% throttle is:

$$\underline{Q}_{T_R=0.4} = [Q_{1,T_R=0.4} \ \dots \ Q_{k,T_R=0.4}]^T$$

where T_R is the throttle setting, and k is the number of data points collected during that test. Using this notation, y and x are redefined to make vectors containing all sets of data:

$$\underline{y} = \begin{bmatrix} \underline{Q}_{T_R=0.4} \\ \underline{Q}_{T_R=0.5} \\ \vdots \\ \underline{Q}_{T_R=0.8} \\ \underline{Q}_{T_R=0.9} \end{bmatrix} \qquad \underline{x} = \begin{bmatrix} \underline{I}_{rms,T_R=0.4} \\ \underline{I}_{rms,T_R=0.5} \\ \vdots \\ \underline{I}_{rms,T_R=0.8} \\ \underline{I}_{rms,T_R=0.9} \end{bmatrix}$$

Next a linear regression is required to find the values for the slope $\hat{m}$ and the y-intercept $\hat{b}$, which minimizes the error between the experimental values and the estimated regression line. Matlab's $polyfit$ function returned estimates for $\hat{m}$ and $\hat{b}$, allowing K_T and I_o to be estimated.

Before determining the remaining motor parameters, R_{ESC} must be estimated. As current flows across the ESC, a voltage drop of $I_{rms}R_{ESC}$ occurs, meaning less voltage acts on the motor and is given by equation 4.38:

$$V_{LL,rms} = \frac{3}{\sqrt{2}\pi} V_{DC} T_R - I_{rms} R_{ESC}$$

R_{ESC} is found by examining figure 5.71, which shows a linear drop in line-to-line motor voltage with rms current. A linear estimation is applied to each $V_{LL,rms}$ vs I_{rms} relation separately, and then the results were averaged to find a single R_{ESC} to describe the system. This was found to be effective, as R_{ESC} changed less than 5% for each throttle setting. Now that I_o, K_T, and R_{ESC} have been determined, the remaining motor parameters can be extracted.

To determine the motor resistance R_m and back-EMF constant K_E, an ap-

proach similar to finding K_T and I_o is taken. Equation 4.40 relates Q to RPM:

$$Q = \frac{K_T}{R_m + R_{ESC}}[\frac{3}{\sqrt{2}\pi}V_{DC}T_R - I_o(R_m + R_{ESC})] - \frac{K_T K_E}{R_m + R_{ESC}}\omega$$

which depends on throttle. It is more accurate to minimize the error for the entire system at once, rather than for each throttle setting individually and then averaging the results into a single estimate for K_E and R_m. A linear least squares fit is used, which minimizes error between all Q-RPM points and the expected model. However, first equation 4.40 must be written in the following form:

$$\underline{y} = A\underline{x} \tag{5.1}$$

with:

$$\underline{y} = \begin{bmatrix} \underline{Q}_{T_R=0.4} \\ \underline{Q}_{T_R=0.5} \\ \vdots \\ \underline{Q}_{T_R=0.8} \\ \underline{Q}_{T_R=0.9} \end{bmatrix} + K_T I_o \underline{1} \qquad A = K_T \begin{bmatrix} -\underline{\omega}_{T_R=0.4} & \frac{3}{\sqrt{2}\pi}V_{DC}(0.4) \\ -\underline{\omega}_{T_R=0.5} & \frac{3}{\sqrt{2}\pi}V_{DC}(0.5) \\ \vdots & \vdots \\ -\underline{\omega}_{T_R=0.8} & \frac{3}{\sqrt{2}\pi}V_{DC}(0.8) \\ -\underline{\omega}_{T_R=0.9} & \frac{3}{\sqrt{2}\pi}V_{DC}(0.9) \end{bmatrix} \qquad \underline{x} = \begin{bmatrix} \frac{K_E}{R_m+R_{ESC}} \\ \\ \frac{1}{R_m+R_{ESC}} \end{bmatrix}$$

where

$$\underline{1} = [1 \quad 1 \quad \ldots \quad 1 \quad \text{length}(\underline{y})]^T$$

The vector $\underline{1}$ contains only 1s and has as many elements as $\underline{y}$. Once A and $\underline{y}$ are populated with experimental data, a linear least squares regression is applied to

determine a vector $\underline{\hat{x}}$ which has minimal error between the model and experimentally obtained points, found via [43]:

$$\underline{\hat{x}} = (A^T A)^{-1} A^T \underline{y} \tag{5.2}$$

from here, the model parameters for R_m and K_E can be found. At this point, the entire motor (K_T, K_E, I_o, and R_m) and R_{ESC} have been estimated from experimental observations. With the motor modeled, attention turns to the ESC.

ESC transformer relation, equation 4.57, is used to find suitable values for C_0 and C_1 by taking the average ratio of I_{DC}/I_{rms} for each throttle. Matlab's *polyfit* function is used to find a linear fit for C_0 and C_1. Now that the motor and ESC performance parameters have been identified, this model is applied to all of the motors and ESCs studied, with the results listed in tables 5.4 to 5.9.

Table 5.4: Parameters for the DJI 920 KV motor.

		BLDC Motor				ESC		
V_{DC}	ESC	K_T	K_E	I_o	R_m	C_1	C_0	R_{ESC}
[V]	Used [A]	[mNm/A]	[mVs/rad]	[A]	[Ω]	[-]	[-]	[Ω]
7.2	18	13.5796	6.9699	0.2918	0.1408	0.9975	0.2049	0.0725
	30	13.2212	7.1323	0.2721	0.1683	0.9692	0.1774	0.0997
	40	13.5531	7.2492	0.2993	0.1549	1.0078	0.1586	0.0763
11.1	18	12.7273	6.9709	0.3783	0.1557	1.0713	0.1503	0.0802
	30	14.0378	7.2008	0.6722	0.1563	1.0298	0.1084	0.1254
	40	14.1674	7.3004	0.7046	0.1786	1.0540	0.0982	0.0596
14.8	18	14.3306	6.8977	0.7770	0.1686	1.0682	0.1325	0.0983
	40	14.3459	7.3194	0.9183	0.1722	1.0541	0.0661	0.0837

Table 5.5: Parameters for the EMAX 935 KV motor.

		BLDC Motor				ESC		
V_{DC}	ESC	K_T	K_E	I_o	R_m	C_1	C_0	R_{ESC}
[V]	Used [A]	[mNm/A]	[mVs/rad]	[A]	[Ω]	[-]	[-]	[Ω]
	18	14.3088	7.0255	0.3158	0.1522	1.0322	0.2022	0.0777
7.2	30	13.8519	7.1497	0.2838	0.1638	0.9873	0.1596	0.1221
	40	13.9595	7.3758	0.2861	0.1496	1.0178	0.1536	0.0860
	18	13.8310	7.0950	0.4988	0.1692	1.0497	0.2155	0.0642
11.1	30	13.5964	7.2888	0.4528	0.1680	0.9868	0.1989	0.1033
	40	13.9678	7.4391	0.5571	0.1735	1.0522	0.1503	0.0580
	18	14.0402	6.8776	0.5699	0.1956	1.0059	0.2450	0.0943
14.8	30	13.7628	7.0752	0.5981	0.1814	0.9446	0.2102	0.1415
	40	14.1937	7.4209	0.7428	0.1999	1.0561	0.1340	0.0669

Table 5.6: Parameters for the EMAX 1700 KV motor.

		BLDC Motor				ESC		
V_{DC}	ESC	K_T	K_E	I_o	R_m	C_1	C_0	R_{ESC}
[V]	Used [A]	[mNm/A]	[mVs/rad]	[A]	[Ω]	[-]	[-]	[Ω]
	18	7.1635	4.0680	0.4001	0.0839	1.0016	0.2108	0.0578
7.2	30	7.0592	4.1228	0.5337	0.1039	0.9124	0.1763	0.0421
	40	7.1554	4.1339	0.4759	0.0945	0.9619	0.1589	0.0353
	18	7.4288	3.8686	0.8052	0.0831	1.0274	0.1714	0.0565
11.1	30	7.0592	4.0982	0.7585	0.1098	0.9524	0.1658	0.0473
	40	7.2421	4.0784	0.7451	0.1096	0.9822	0.1534	0.0301

Table 5.7: Parameters for the EMAX 1900 KV motor.

		BLDC Motor				ESC		
V_{DC}	ESC	K_T	K_E	I_o	R_m	C_1	C_0	R_{ESC}
[V]	Used [A]	[mNm/A]	[mVs/rad]	[A]	[Ω]	[-]	[-]	[Ω]
7.2	18	6.2241	3.3632	0.2669	0.1222	0.9954	0.2111	0.0428
	30	6.2417	3.6411	0.6699	0.1419	0.9439	0.1605	0.0301
	40	6.2456	3.6113	0.5176	0.1355	0.9588	0.1638	0.0244
11.1	30	6.2710	3.7178	0.6012	0.1357	0.9352	0.1710	0.0433
	40	6.3790	3.6104	0.5685	0.1524	0.9970	0.1471	0.0229

Table 5.8: Parameters for the EMAX 2300 KV motor.

		BLDC Motor				ESC		
V_{DC}	ESC	K_T	K_E	I_o	R_m	C_1	C_0	R_{ESC}
[V]	Used [A]	[mNm/A]	[mVs/rad]	[A]	[Ω]	[-]	[-]	[Ω]
7.2	18	4.9924	2.7274	0.7198	0.0654	0.9638	0.2605	0.0443
	30	4.9681	3.0137	0.7269	0.0743	0.9183	0.1908	0.0366
	40	5.0273	2.9522	0.7179	0.0644	0.9541	0.1868	0.0426

Table 5.9: Parameters for the Samguk 2500 KV motor.

		BLDC Motor				ESC		
V_{DC}	ESC	K_T	K_E	I_o	R_m	C_1	C_0	R_{ESC}
[V]	Used [A]	[mNm/A]	[mVs/rad]	[A]	[Ω]	[-]	[-]	[Ω]
7.2	18	4.6697	2.5155	0.5709	0.0579	0.9707	0.2765	0.0460
	30	4.5483	2.7451	0.9172	0.0688	0.9253	0.1954	0.0387
	40	4.7499	2.7572	1.2073	0.0652	0.9667	0.1840	0.0313

Predicted motor and ESC performance using these parameters are overlaid with experimental results in sections 5.1 to 5.3. The AC motor model predicts mechanical power, AC power, and DC power quite well. However, when estimating

the efficiencies of the motor and ESC, the results are suboptimal. It appears that the motor efficiency is overestimated, whereas the ESC efficiency is underestimated. The product of η_{ESC} and η_m is the system efficiency, which is predicted well by the model.

ESC modeling is a future area of work. It is believed that the type of current sensors used in the high voltage setup causes the apparent 'curving' of the ESC efficiency and power factor plots. Recall these non invasive hall effect sensors contain low pass filtering, which attenuates the higher harmonic content of the signal. A lower current draw would explain the lower AC power, power factor, and ESC efficiency. These results will be further verified in the future with more accurate AC power testing equipment. Next, some common trends in the data are discussed.

5.4.1 Common Trends

Experimental observations reveal 3 trends: a 43% difference in experimental K_E and manufacturer KV values, specific masses of BLDC motors ranging from 0.4 kW/kg to 4.9kW/kg, and experimentally observed values for $K_T/K_E > 1.64$.

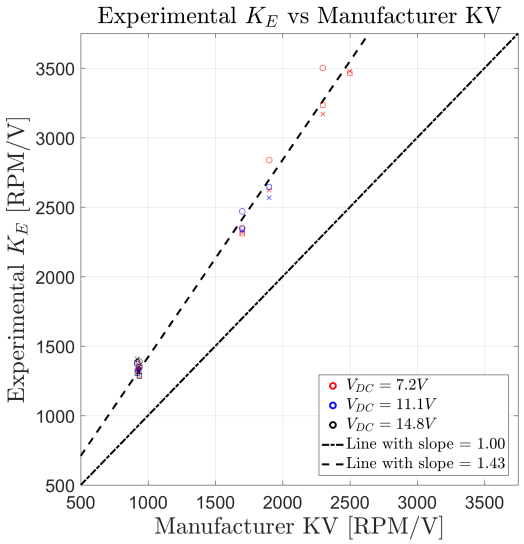

Figure 5.72: Experimentally determined K_E vs manufacturer provided KV for all tests, in the same units. Circles, crosses, and squares indicate the 18 A, 30 A, and 40 A ESCs respectively.

Figure 5.72 shows experimentally obtained values for K_E vs manufacturer provided values for KV, both in terms of RPM/Volt. From the trend, it is clear that experimental K_E values are 43% higher than the manufacturer provided KV value. Section 2.1.2 discussed the differences between K_T, K_E, and KV. Manufacturer provided KV value relates the DC voltage applied to the ESC to the maximum motor no-load speed ω_{NL}:

$$\omega_{NL} = \text{KV } V_{DC}$$

This definition includes the ESC, and thus is not specific to the motor alone. Based on the results from Chapter 4, the motor no load speed is:

$$\omega_{NL} = \frac{\frac{3}{\sqrt{2}\pi} V_{DC} t - (R_m + R_{ESC}) I_o}{K_E} \tag{5.3}$$

It is clear that these definitions of KV and K_E are not related, and that providing KV alone does not describe the motor's performance.

Of key importance with motor models is the ratio of K_T/K_E, with some common examples listed in table 2.1. Most brushed motor models assume that $K_E = K_T$ [12, 13], however, experimental results for the model used in this work show $K_T > K_E$. This discrepancy comes from the fact that all three phases of the brushless motor have been replaced with a single, equivalent circuit. Figure 5.73 shows experimentally obtained K_E values vs K_T values.

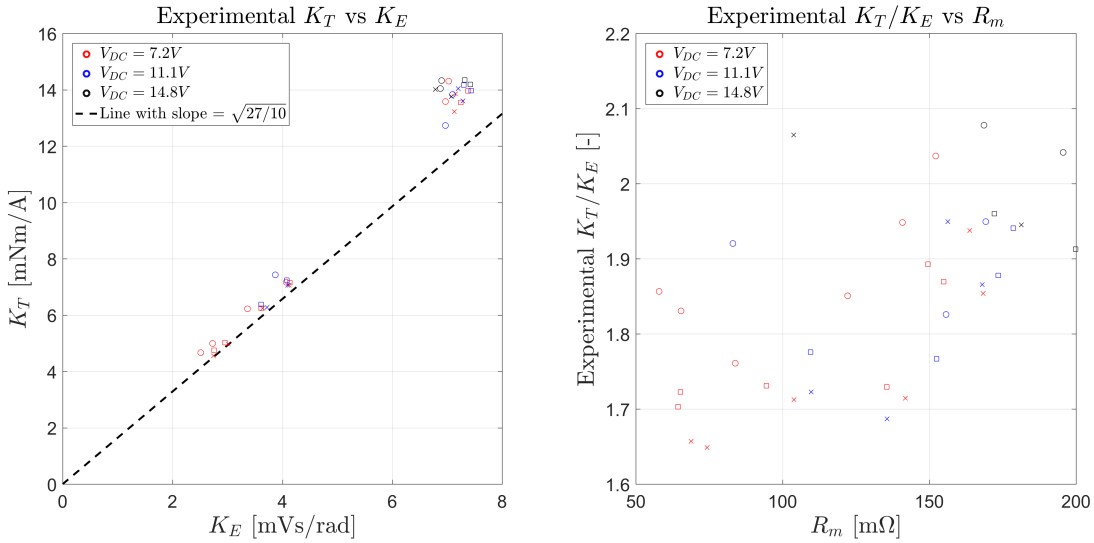

Figure 5.73: K_T vs K_E for all tests. Circles, crosses, and squares indicate the 18 A, 30 A, and 40 A ESCs respectively.

It appears that motors with smaller values of K_T and K_E have a ratio of $K_T/K_E \approx 1.64$. Referencing the motor parameters from tables 5.4 to 5.9 reveals that motors with ratios K_T/K_E closer to 1.64 are physically smaller motors with higher KV ratings. For the model presented in this work, the ideal ratio of K_T/K_E can be found by using an ideal power relation between mechanical and AC power:

$$P_m = P_{AC}$$

$$Q\omega = \sqrt{\frac{27}{10}} V_{LL,rms} I_{rms}$$

In an ideal motor:

$$Q = K_T I_{rms}$$

$$V_{LL,rms} = K_E \omega$$

because $I_o = 0$ and $R_m = 0$. Therefore:

$$(K_T I_{rms})\omega = \sqrt{\frac{27}{10}} (K_E \omega) I_{rms}$$

$$\frac{K_T}{K_E} = \sqrt{\frac{27}{10}} \approx 1.64 \tag{5.4}$$

This explains why some motors appear to approach an ideal ratio of 1.64. However, why do some motors have K_T/K_E ratios close to 1.9? The answer can be found by augmenting the previous K_T/K_E analysis to include some tiny motor resistance

such that $R_m > 0$.

$$V_{LL,rms} = I_{rms}R_m + K_E\omega$$

Additionally, the presence of torque requires $I_{rms} > 0$:

$$R_m > 0 \text{ and } I_{rms} > 0 \implies I_{rms}R_m > 0$$

therefore:

$$I_{rms}R_m + K_E\omega > K_E\omega$$

Returning to the original ideal power equation:

$$P_m = P_{AC}$$

$$Q\omega = \sqrt{\frac{27}{10}}V_{LL,rms}I_{rms}$$

$$(K_T I_{rms})\omega = \sqrt{\frac{27}{10}}(I_{rms}R_m + K_E\omega)I_{rms} > \sqrt{\frac{27}{10}}(K_E\omega)I_{rms}$$

for a nonideal motor:

$$\frac{K_T}{K_E} > \sqrt{\frac{27}{10}}$$

this is supported by plotting K_T/K_E vs R_m in figure 5.73. For motors with larger resistance R_m, the ratio of K_T/K_E is larger than the ideal value of $\sqrt{27/10}$. It is important to note that having a ratio of $K_T/K_E = 1$ does not imply a 100% efficient motor. There is a clear upwards trend: increasing R_m results in a larger ratio of K_T/K_E. Motors with higher R_m are physically larger motors, with higher K_T

and K_E ratings. Power losses associated with the motor places the experimentally recorded value at 1.90, indicating a 15.6% difference from the ideal ratio.

Finally, power to mass ratios for several motors are considered. BLDC motors used for this thesis are commercially available devices, so how do they compare against commercially available brushed motors? To answer this, brushed motors from an online vendor [44] were examined, and their results summarized below:

Table 5.10: Commercially available Brushed Motors at $V_{DC} = 12$ V.

m_m [gr]	Q_s [in-oz]	ω_{NL} [RPM]	P_{max} [W]	P_{max}/m_m [kW/kg]	Max η_m [%]
215	23.0	6100	25.9	0.12	69.4
220	62.5	19300	222.4	1.01	74.2
295	48.0	5600	49.5	0.17	78.7
350	76.1	7000	98.3	0.28	72.0
350	125.7	7000	162.2	0.46	73.0

Brushed motors have specific powers between 0.12-1.01 kW/kg at up to 78.7% efficiency. A small gas engine, the AP Yellowjacket, was analyzed in [9] and has a specific power density of 1.1 kW/kg. For the BLDC motors tested in this thesis, the maximum power point was interpreted from experimentally obtained data points at full throttle.

A key point of this work was to study the ESC effect on BLDC performance. ESC's have a notable impact on augmenting the specific power density of the system. For a quadcopter with 4 ESCs, oversizing the ESC can result in a substansial reduction in mission performance associated with four times the extra mass. To demonstrate this idea, consider the following tables which relate ESC usage to sys-

tem specific mass ratio:

Table 5.11: EMAX 935 KV at 7.2 V.

ESC [A]	P_{max} [W]	P_{max}/m_m [kW/kg]	$P_{max}/(m_m + m_{ESC})$ [kW/kg]
18	46.7	0.93	0.69
30	38.1	0.76	0.48
40	42.3	0.85	0.47

Table 5.12: EMAX 1700 KV at 7.2 V.

ESC [A]	P_{max} [W]	P_{max}/m_m [kW/kg]	$P_{max}/(m_m + m_{ESC})$ [kW/kg]
18	60.0	2.79	2.1
30	61.8	2.5	1.6
40	66.5	2.6	1.5

From the previous tables it is clear that improperly sizing the ESC can result in a 30% reduction in specific system mass. The results of peak mechanical power vs brushless motor mass for each ESC are shown on the next page in figure 5.74. Note that increasing DC voltage increases the peak mechanical output power by equation 2.11.

Figure 5.74: Maximum specific power (P_{max}/m_m) for all BLDC motors tested in this thesis.

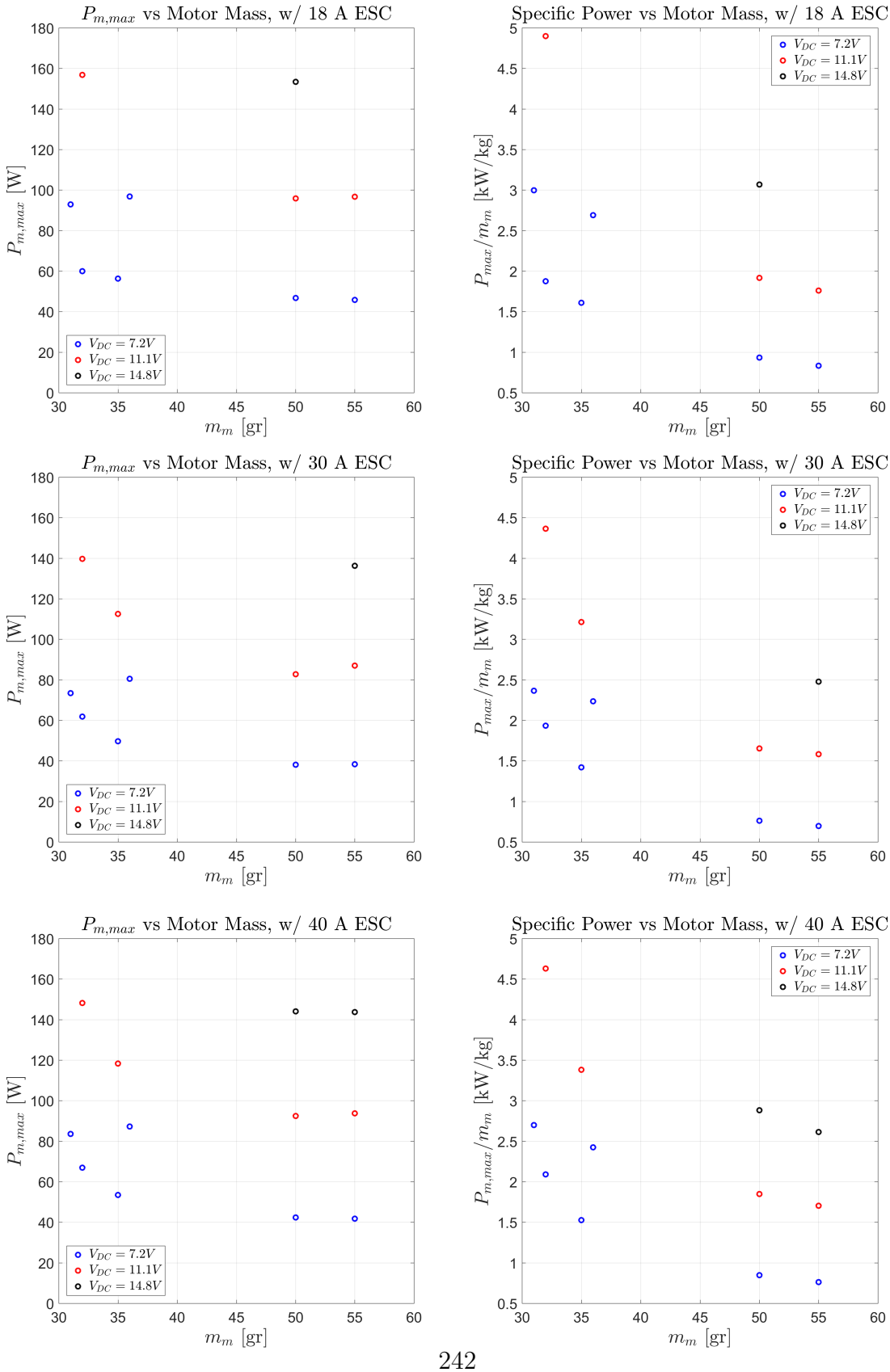

Note how the maximum power changes little for a given motor with a different ESC, however, the effect of increased ESC mass can significantly reduce overall specific power of the propulsion system. Table 5.13 recaps the power to weight ratios of the different motors analyzed thus far:

Table 5.13: Specific powers of different small scale UAV motors.

Type	P_{max}/m_m [kW/kg]
Brushed DC	0.12-1.01
Brushless DC	0.60-4.90
Gas Engine [9]	1.10

Engine selection makes a key impact on aircraft performance. Gas engines do not scale down well to smaller sizes, which is evidenced by the fact that they have mass ratios comparable to brushed motors. On the other hand, gas engines for full size aircraft can be over 10 kW/kg, surpassing even the best BLDC motors. The best airworthy BLDC motors are used on NASA's X-57, and has a continuous specific power of $P_{cont}/m_m = 3$ kW/kg at 95% efficiency [7]. Although a lower kW/kg than the motors tested using the dynamometer, the X-57's electric motors have a noticeable increase in efficiency compared to commercial off the shelf BLDC motors. This reiterates the idea that engineering is a trade off, designing for higher efficiency correlates to a lower specific mass.

Next the idea of motor variation is discussed.

5.5 Motor Variation Tests

Throughout this analysis, it was assumed that the characteristics of each motor is identical to every other motor of the same type. That is, ordering two EMAX 1700 KV motors, one would expect identical performance for both motors under the same operating conditions. However, how true is this assumption? Given the lack of technical information provided by motor manufacturers on their products, is it safe to assume their production methods are reliable? To answer this question, a pack of four identical motors were ordered from a single supplier to determine the amount of variation between the motors. Each motor was evaluated separately with the dynamometer and their performance metrics compared.

Figure 5.75: Four EMAX 1700 KV motors used in the variation tests.

Four EMAX 1700 KV motors were tested with the dynamometer at $V_{DC} = 7.2$ V, and paired with a SpiderLite 18 A ESC, MultiStar 30 A ESC, and DYS BlHeliOpto 40 A ESC. There was no variation testing with different ESCs, as the design space quickly becomes untenable with the number of design variables. Only the motors were swapped, that is motor 1 was tested with the same MultiStar 30

A ESC as motor 2, 3, and 4. The same is true for the other ESCs. If a motor were defective, one would expect there to be a noticeable drop in performance when the motor is compared to the other motors. On the same note, when assigning motor parameters to the data in post processing, it would be clear that a defective motor would have physical parameters that would stand out, when compared to the other motors. Results of the motor variation tests are shown in figures 5.76 to 5.81.

Figure 5.76: Motor variation tests - EMAX 1700 KV - 18 A ESC - 7.2 V

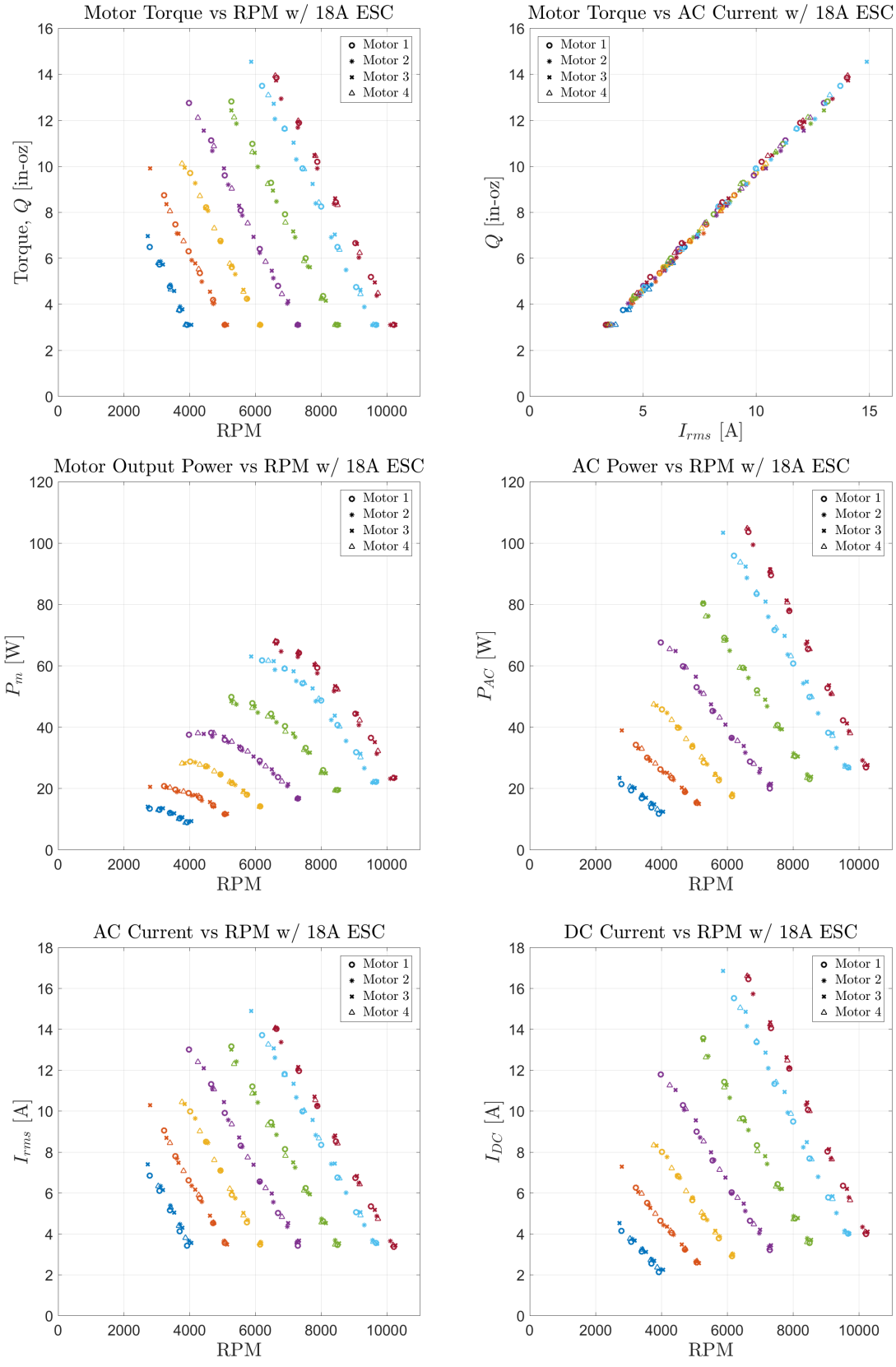

Figure 5.77: Motor variation tests - EMAX 1700 KV - 18 A ESC - 7.2 V

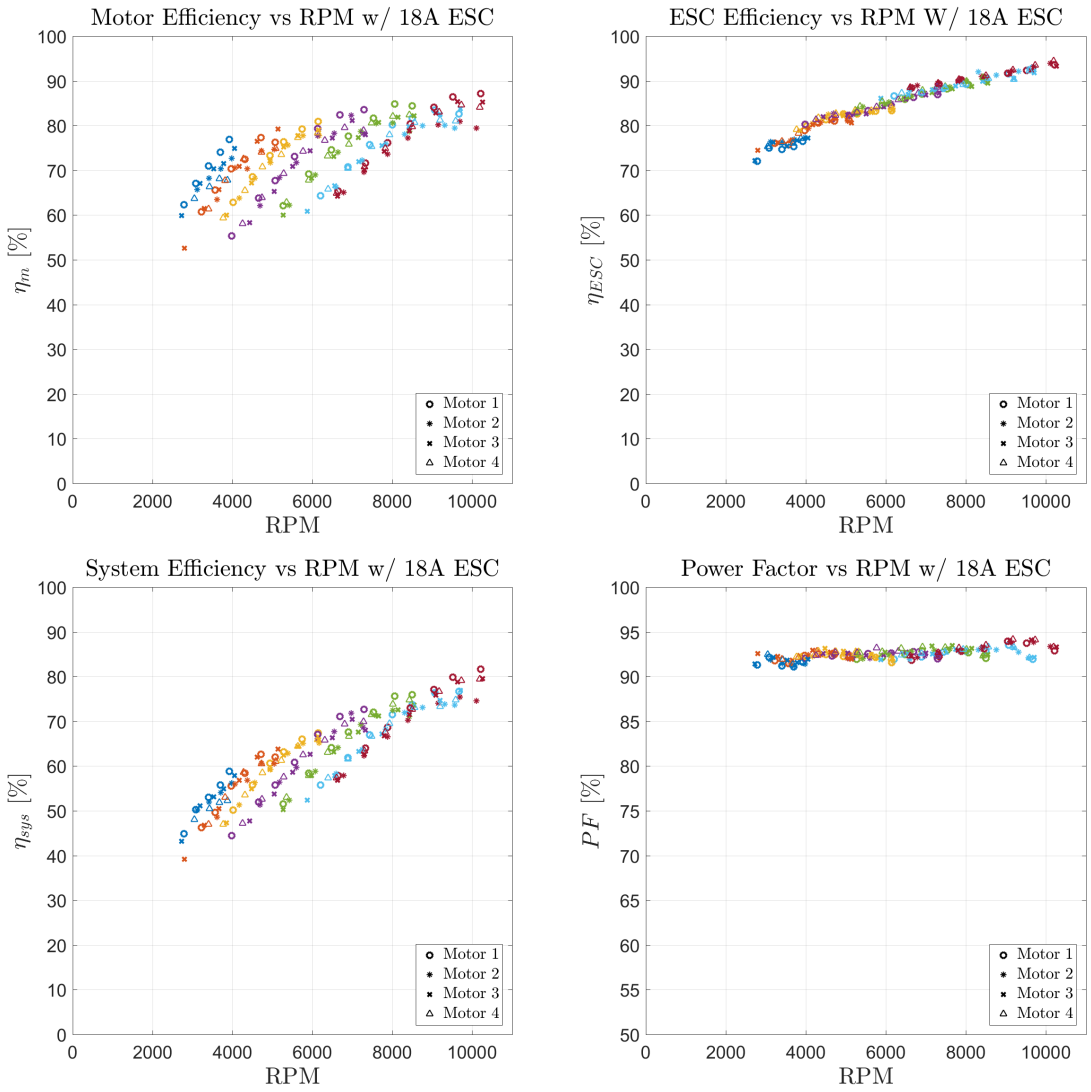

Figure 5.78: Motor variation tests - EMAX 1700 KV - 30 A ESC - 7.2 V

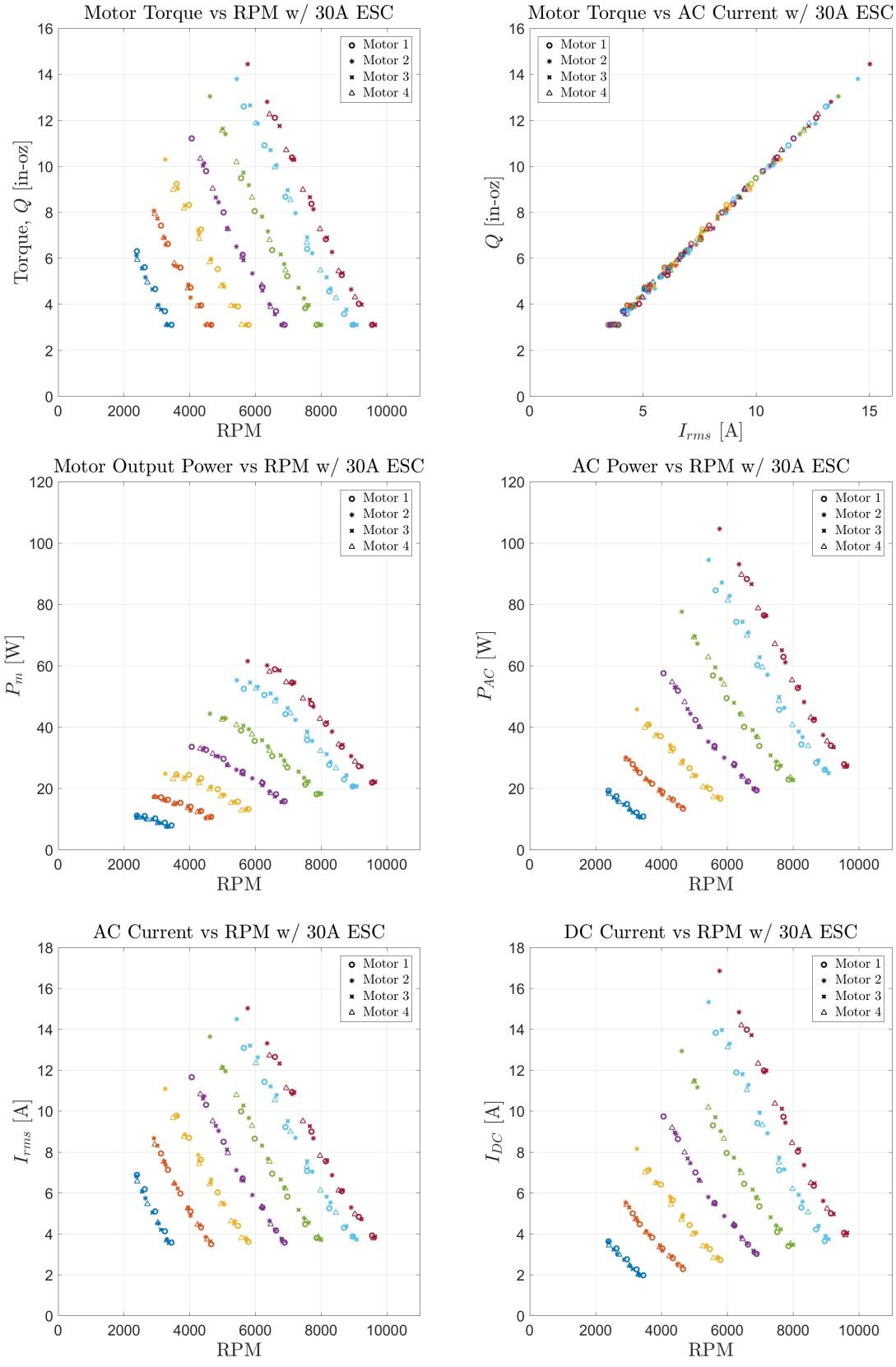

Figure 5.79: Motor variation tests - EMAX 1700 KV - 30 A ESC - 7.2 V

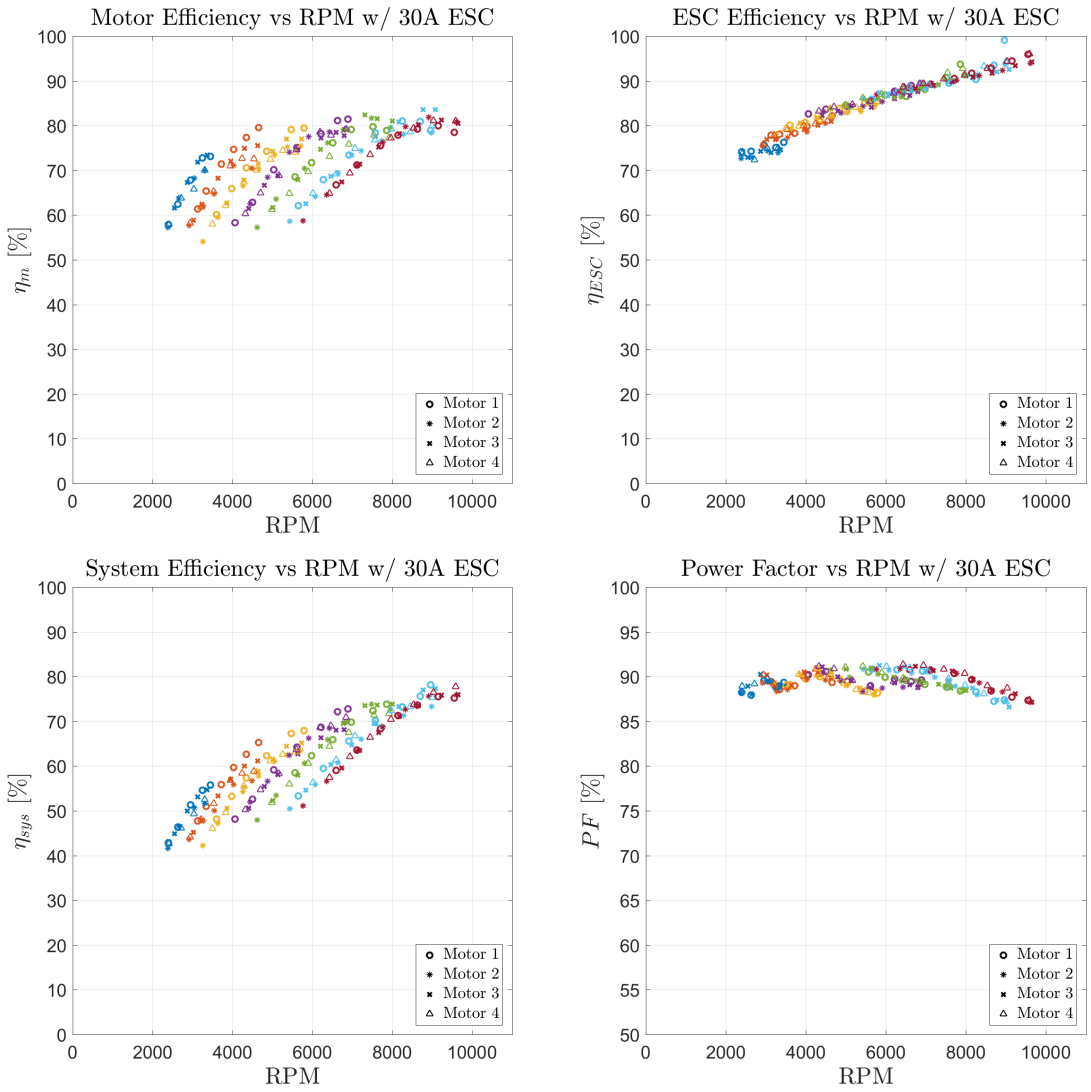

Figure 5.80: Motor variation tests - EMAX 1700 KV - 40 A ESC - 7.2 V

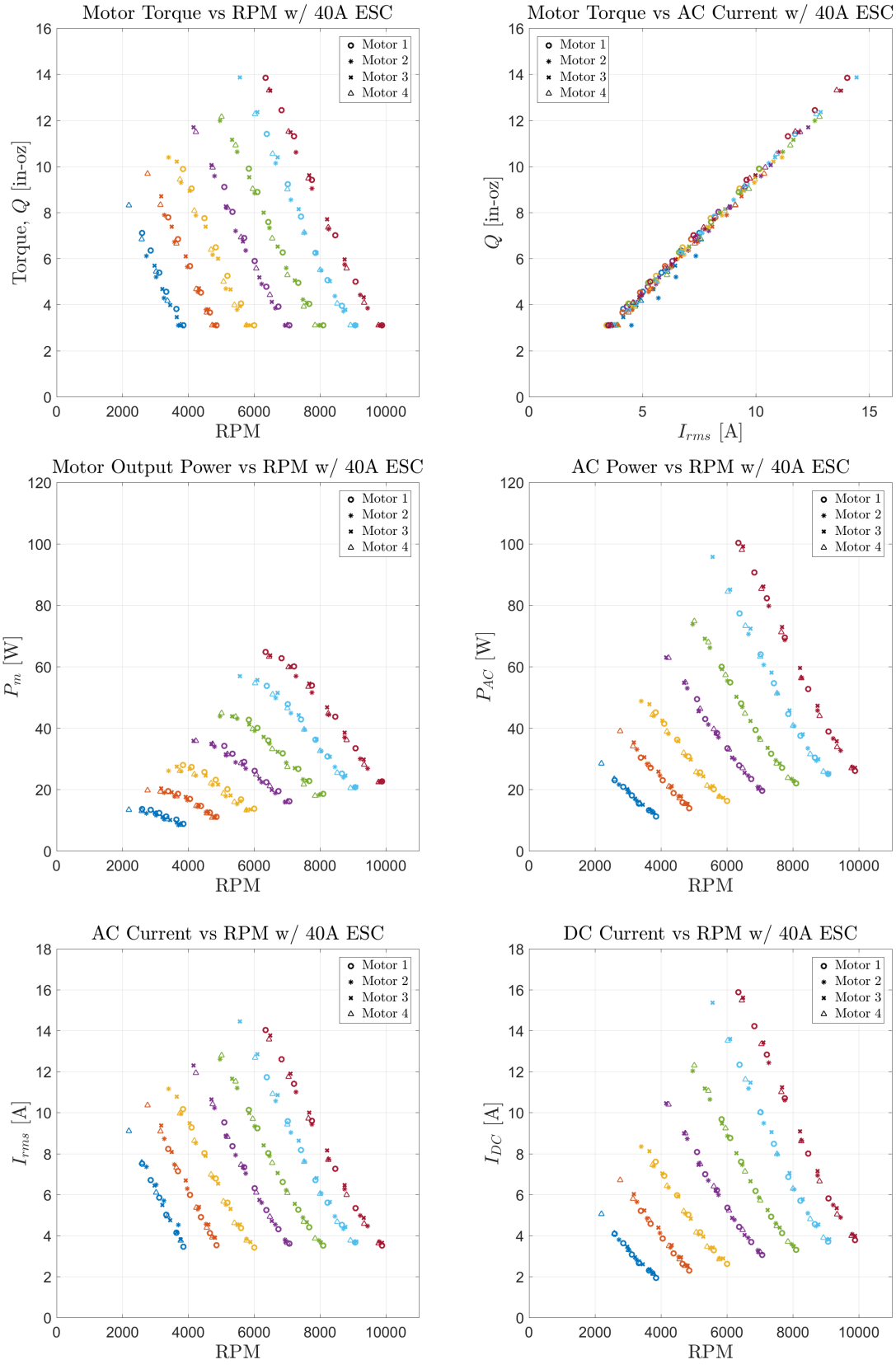

Figure 5.81: Motor variation tests - EMAX 1700 KV - 40 A ESC - 7.2 V

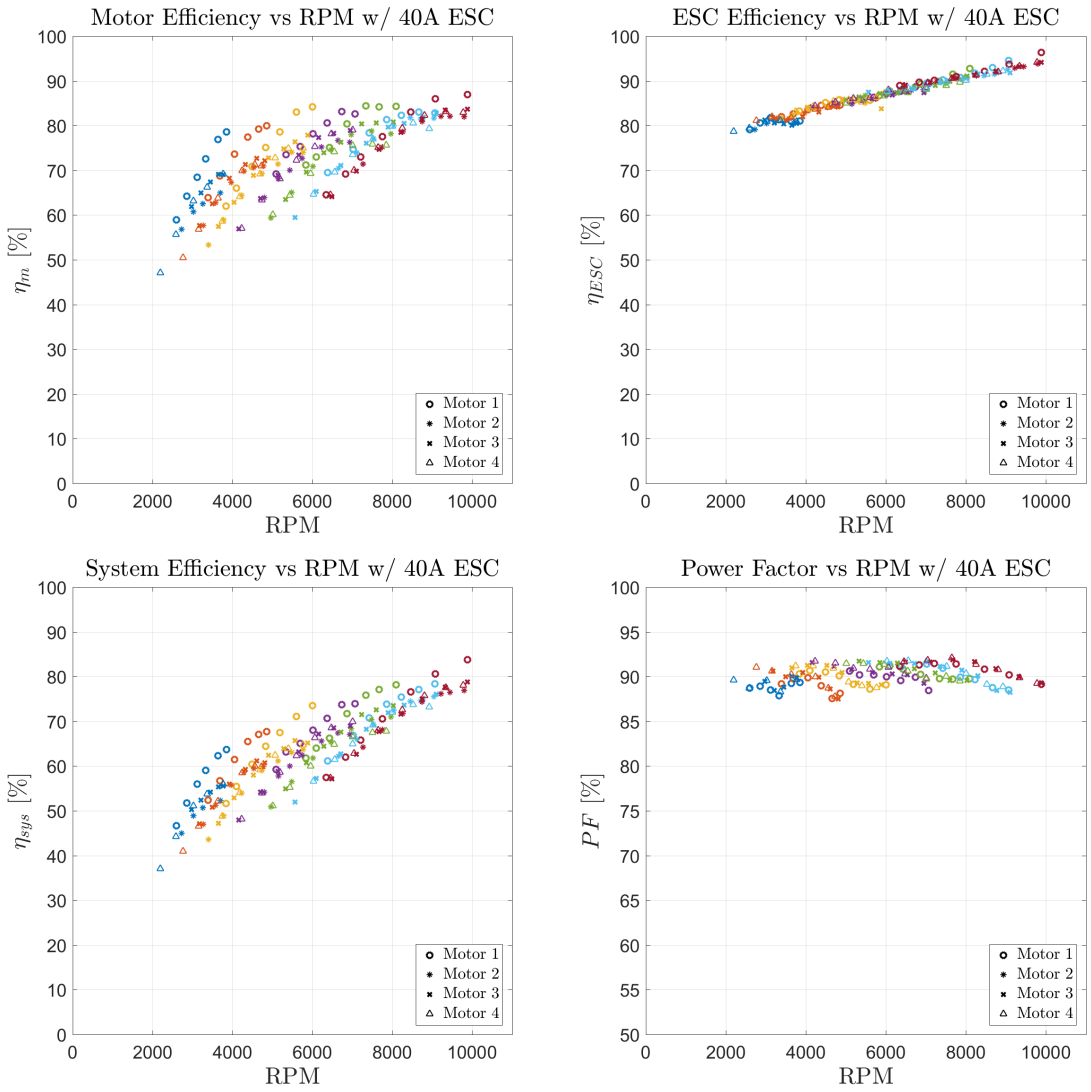

From the perfromance plots, the model parameters for each motor and ESC have been extracted and are shown in tables 5.14 to 5.16.

Table 5.14: Motor variation test results w/ 18 A ESC.

		BLDC Motor				ESC		
Motor [#]	ESC Used [A]	K_T [mNm/A]	K_E [mVs/rad]	I_o [A]	R_m [Ω]	C_1 [-]	C_0 [-]	R_{ESC} [Ω]
1	18	7.1498	3.8690	0.3902	0.0886	1.0002	0.2107	0.0441
2	18	7.1006	3.8852	0.5097	0.0869	0.9979	0.2103	0.0445
3	18	7.0511	3.8475	0.4155	0.0898	1.0121	0.2060	0.0426
4	18	7.2933	3.8598	0.5876	0.0885	1.0111	0.2056	0.0453
Mean		7.1487	3.8654	0.4757	0.0884	1.0053	0.2082	0.0441
Std. Dev. [%]		1.5	0.4	19.0	1.3	0.7	1.3	2.6

Table 5.15: Motor variation test results w/ 30 A ESC.

		BLDC Motor				ESC		
Motor [#]	ESC Used [A]	K_T [mNm/A]	K_E [mVs/rad]	I_o [A]	R_m [Ω]	C_1 [-]	C_0 [-]	R_{ESC} [Ω]
1	30	7.0592	4.1228	0.5337	0.1039	0.9124	0.1763	0.0421
2	30	7.0260	4.1260	0.6364	0.1026	0.9456	0.1635	0.0375
3	30	7.0303	4.0786	0.5530	0.1043	0.9242	0.1789	0.0414
4	30	7.1328	4.1197	0.6856	0.1055	0.9279	0.1733	0.0403
Mean		7.0621	4.1118	0.6022	0.1041	0.9275	0.1730	0.0403
Std. Dev. [%]		0.7	0.5	11.8	1.1	1.5	3.9	5.0

Table 5.16: Motor variation test results w/ 40 A ESC.

		BLDC Motor				ESC		
Motor [#]	ESC Used [A]	K_T [mNm/A]	K_E [mVs/rad]	I_o [A]	R_m [Ω]	C_1 [-]	C_0 [-]	R_{ESC} [Ω]
1	40	7.1554	4.1339	0.4759	0.0945	0.9619	0.1589	0.0353
2	40	7.1989	4.1138	0.8572	0.0986	0.9901	0.1522	0.0309
3	40	7.1390	4.0870	0.6859	0.0999	0.9633	0.1666	0.0314
4	40	7.1723	4.1748	0.7385	0.0994	0.9850	0.1537	0.0318
Mean		7.1664	4.1274	0.6894	0.0981	0.9751	0.1579	0.0324
Std. Dev. [%]		0.36	0.90	23.1	2.5	1.5	4.1	6.2

From tables 5.14 to 5.16, it is clear that the motors show good agreement with one another for K_T, K_E, and R_m, as these parameters contained less than a 5% deviation. It is expected that K_T and K_E should not change between different motors of the same type because they are set by the physical construction of the motor, such as the size of magnets, airgap, and overall electromagnetic design. Motor resistance could change between motors, depending on the length of wire used to connect the ESC to the motor. All tests conducted here used the same length of wire, and thus the grouping of R_m is within 2.5%. However, a significant discrepancy exists for I_o, as this value has a standard deviation of 19.0%, 11.8%, and 23.1% across the different tests. A high I_o means more current I_{rms} is required to generate the same load as a motor with a low I_o and thus a lower motor efficiency η_m.

A high I_o could have several explanations. From handling the motors it was obvious that some EMAX 1700 KV motors were easier to spin than other. If the bearing between the rotor and the stator is not clean, debris could impede the rotation of the motor, accumulating in a higher current required to overcome static friction, hence a higher I_o is needed. Additionally, this hypothesis is supported by the fact that motor 1 consistently has the lowest I_o and the highest motor efficiency. Motor 1 was used extensively on the dynamometer to produce the results shown in table 5.6. During these tests debris stuck in motor 1's bearing could have been dislodged, whereas motors 2-4 were tested directly out of the box. Debris related to shipping the motors (dirt, packaging, etc) remained logged in the bearings, increasing the no-load current.

5.6 Motor and Rotor Pairing

Electric motors and ESCs make up only half of the propulsion system on board an aircraft: the other half is the rotor. With motors and ESCs modeled, this research seeks to improve the design process of electric aircraft by optimally pairing motors and rotors to reduce the total power of an aircraft. To accomplish this goal, a hover test stand was constructed, allowing one to study the performance of a rotor, motor, and ESC simultaneously. Before describing the hover test stand, a brief review of rotors is required.

Rotor thrust T, rotor power P, and rotor torque Q are related to the rotor RPM Ω by [27, 28]:

$$T = C_T \rho A (\Omega R)^2 \tag{5.5}$$

$$Q = C_Q \rho A (\Omega R)^2 R \tag{5.6}$$

$$P = C_P \rho A (\Omega R)^3 \tag{5.7}$$

where C_T, C_Q, and C_P are the thrust, torque, and power coefficients, respectively. Additionally, ρ, R, and A describe the atmospheric density, rotor radius, and rotor disk area. To determine C_T, C_Q, and C_P from airfoil and planform properties is beyond the scope of this thesis, but methods such as blade element momentum theory and free vortex wake methods are used. In the context of this work, the reader must be aware that C_T, C_Q, and C_P change depending on airfoils used, reference flight condition, and planform design. To study a rotor, one can predict

the C_T, C_Q, and C_P from blade design, or one could extract them directly from experimental data.

In the steady state hover condition for a given rotor, C_T, C_Q, and C_P can be determined from experimental results. To do so, one must record the rotor thrust T_R, rotor torque Q_R, and rotor RPM Ω. The rotor thrust and torque both evolve as the square of the rotor RPM, representing a unique distinction for the motor loading condition on the dynamometer. With the use of the magnetic hysteresis brake, the dynamometer was able to vary the load on the motor independent of the rotor speed, creating a linear relationship between torque and RPM for the same throttle. However, as outlined by equation 5.6, the rotor RPM and rotor torque are linked together in a quadratic nature by the rotor design.

To change the rotor thrust, torque, and power, with a given C_T, C_Q, and C_P, one has to change the RPM of the rotor. For aircraft that hover with fixed pitch blades, such as quadcopters, how is this done? The answer is that the user must change the throttle input into the ESC. Increased voltage on the motor causes the mechanical speed to increase. However, increasing speed increases rotor torque, given by equation 5.6. The input to the system is the throttle setting, which increases the rotor speed and RPM. To determine the exact mapping between throttle and rotor performance, a hover test stand was constructed.

5.6.1 Hover Test Stand

The goal of the hover test was to study the interaction between rotors, motors, and ESCs. A hover test stand places a rotor on a motor, and attaches torque and force sensors to the motor in order to record the rotor's performance, shown in figures 5.82. Unique to this setup is the AC power measurement setup, which allows the user to record the AC power exiting the ESC and entering the motor. The full suite of power and test equipment used on the dynamometer are used in the hover test stand.

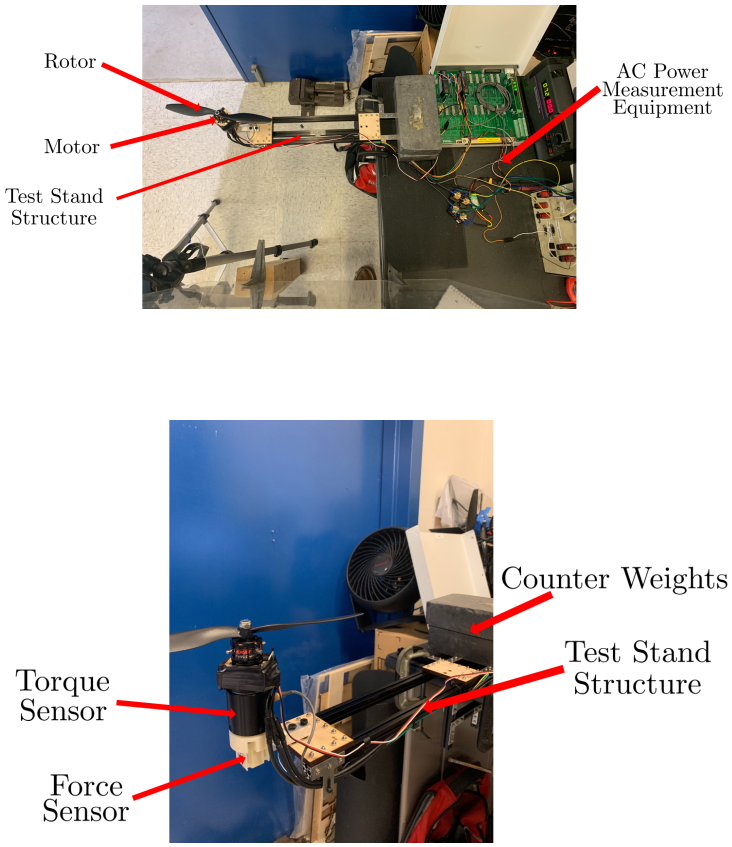

Figure 5.82: Hover test stand.

Spinning a rotor with a motor in conjugation with an ESC creates a set of

experimental data points that are used to verify a combined momentum theory rotor model and BLDC/ESC motor model. An EMAX 935 KV motor and a MultiStar 30 A ESC at $V_{DC} = 7.2$ V configuration was selected as the drive train for the rotor. Two 10 inch diameter commercial off the shelf rotors were used in this test, one with 2 blades (2x1045) and one with 3 blades (3x10). Both rotors are shown in figure 5.83.

Figure 5.83: Rotors used on the hover test stand.

Using these rotors on the hover test stand, the following thrust and torque information was collected:

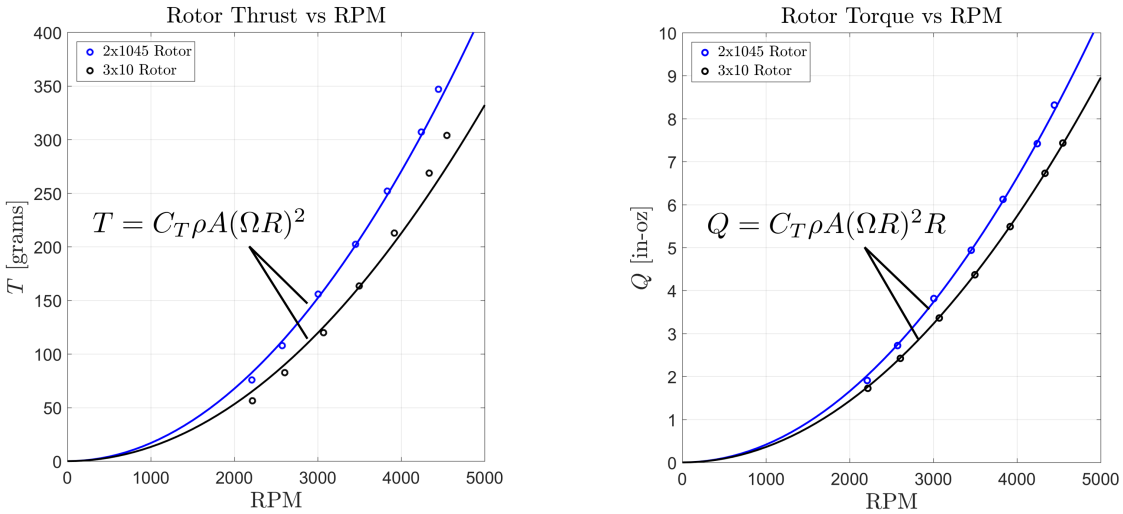

Figure 5.84: Hover test stand results for the 2x1045 and 3x10 rotors. Solid lines indicates momentum theory predictions.

In figure 5.84, the momentum theory estimates for C_T and C_Q are drawn as

solid lines. From the experimentally obtained information shown in figure 5.84, the following table on rotor performance can be created:

Table 5.17: Rotor aerodynamic parameters found from hover test stand.

Rotor	R [in]	N_B	C_T	C_Q	FOM [%]
2x1045	5	2	0.0150	0.0021	62.5
3x10	5	3	0.0118	0.0018	50.4

To better understand the interaction between motors and rotors, the Q-RPM plot of the rotor is overlaid with the Q-RPM plot of the EMAX 935 KV motor in figure 5.85.

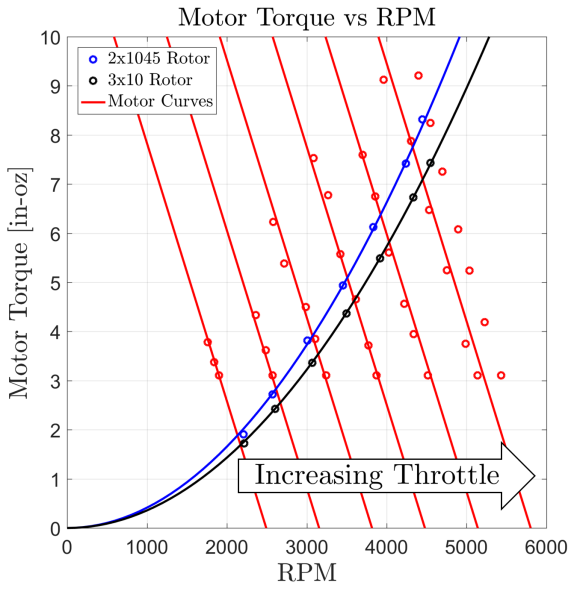

Figure 5.85: Rotor torque requirement overlaid with motor torque-RPM curves.

Consider a nominal point with some Q, RPM, and throttle in figure 5.85. For a motor, moving right on the Q-RPM plot requires an increase in motor voltage, which is achieved with a higher throttle setting. Normally the load on the motor is constant, meaning increasing voltage only increases the RPM of the motor and

thus new points added are on a horizontal line. However, with a rotor, increasing RPM increases torque, meaning that as throttle increases the evolution of points is now horizontal and upwards. Equation 5.6 describes this evolution, and thus can be modeled.

The equivalent BLDC motor equations from Chapter 4 can be rewritten to model the changing rotor load. As with the dynamometer, the operator's only input into the motor and ESC is the throttle T_R, and the power required is set by the motor parameters and the load. Similarly, we seek a relationship between input throttle, the rotor's rotational speed, and the required power. It is known that changing the throttle increases the rotational speed of the motor, but how does this pair with the increasing torque requirement? Recall the expressions for motor and rotor torque:

$$Q_{rotor} = C_Q \rho A (\Omega R)^2 R$$

$$Q_{motor} = K_T (I_{rms} - I_o)$$

In a steady state condition with a direct drive configuration, both the rotor's loads and speeds are equal to the motor's:

$$Q_{motor} = Q_{rotor} \qquad \omega = \Omega$$

Therefore an expression relating the rotor speed Ω to the rms current I_{rms} can be found:

$$I_{rms} = \frac{C_Q \rho A R^3}{K_T} \Omega^2 + I_o = K_{Q/T} \Omega^2 + I_o \tag{5.8}$$

$$K_{Q/T} \triangleq \frac{C_Q \rho A R^3}{K_T}$$

where $K_{Q/T}$ is a constant relating rotor to motor torque. Now that a mapping between rotor speed and motor current exists, equation 5.8 can be combined with the equivalent AC motor equations to determine the relationship between throttle and rotor speed Ω:

$$\frac{3}{\sqrt{2}\pi} V_{DC} T_R = (R_{ESC} + R_m) I_{rms} + K_E \Omega$$

$$\frac{3}{\sqrt{2}\pi} V_{DC} T_R = (R_{ESC} + R_m)(K_{Q/T}\Omega^2 + I_o) + K_E \Omega$$

$$\Omega = \frac{-K_E + \sqrt{K_E^2 + 4K_{Q/T}(R_{ESC} + R_m)(\frac{3}{\sqrt{2}\pi} V_{DC} T_R - I_o(R_{ESC} + R_m))}}{2K_{Q/T}(R_{ESC} + R_m)} \tag{5.9}$$

Combining a momentum theory rotor model with the AC motor model reveals the effect of throttle to rotor performance: increasing throttle T_R causes a square root increase in rotor speed Ω. With an understanding on how RPM vs throttle evolves, predictions for the rotor thrust, torque, and power can be made with equations 5.5 to 5.6. With the throttle, voltage, and load defined, the remainder of the AC motor and ESC equations can be used to determine the motor and ESC's performance.

As a result of dynamometer characterization, model parameters for the ESC and BLDC motor can be simply read off table 5.5, and using equations 5.9 the load on the motor is determined. Now that the rotor, motor, ESC parameters are determined, the predicted results can be compared to the experimentally obtained data, which is shown in figure 5.86.

Figure 5.86: Predicted vs experimental results for the hover test stand.

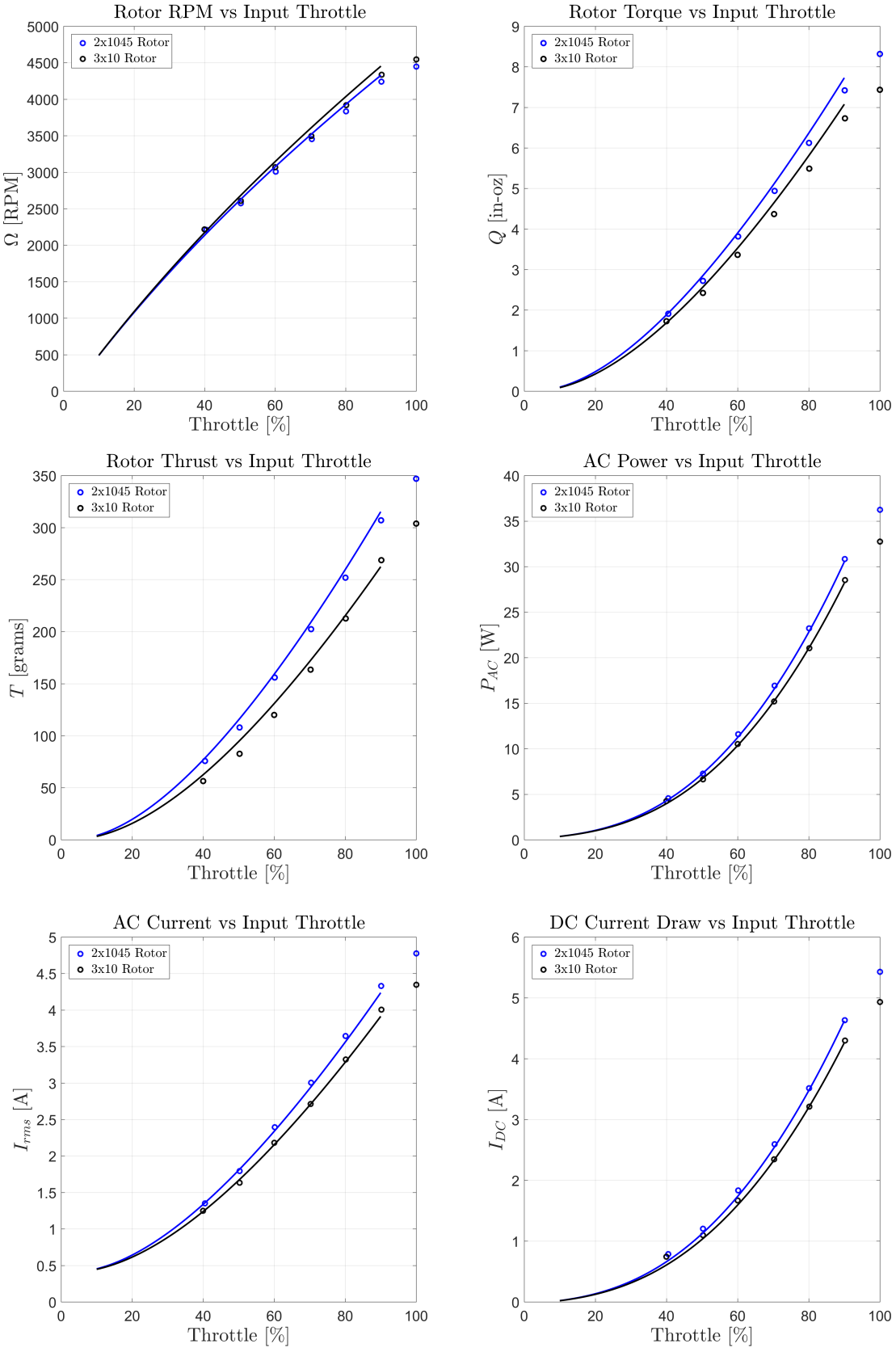

Predicted results match well with experiments, indicating that this motor and rotor pairing is valid for a given C_T, C_Q, and C_P. Additionally, a separate RPM and torque sensor are used on the hover test stand, indicating repeatability as the both the dynamometer and the hover test stand results show good agreement with one another. Using the hover test stand, rotor performance metrics were extracted directly from the test data. However, in the future it would be better to predict both the rotor performance and motor performance during the design phase.

The C_T, C_Q, and C_P obtained via the test stand in hover do not represent the rotor during forward flight or climb, meaning that a more precise aerodynamic theory is required to describe the rotor requirements in these flight conditions. A small 1,000 gram electric helicopter is analyzed in the next section, to better understand how the rotor's power, RPM, and torque requirements relate to the motor and ESC in forward flight. This demonstrates the value of combining a forward flight aerodynamic model with the BLDC motor and ESC equations.

5.6.2 Example Helicopter Propulsive Trim

BLDC motor and ESC selection has a significant impact on electric aircraft performance. To better understand this selection process, the analysis techniques described in this thesis are applied to a small commercial off the shelf electric helicopter. Design tradeoffs between different motors, ESCs, and voltages are explored, with this section's trimming an electric helicopter and estimating its time of flight using the motor and ESC equations developed in Chapter 4.

Suppose the mission is to determine the propulsion configuration for an electric helicopter, shown in figure 5.87, with the longest time of flight and payload. What motor, ESC, and V_{DC} configuration should be chosen? A higher V_{DC} implies a lower I_{DC} and thus a longer time of flight. However, a heavier battery reduces the amount of payload. Additionally, how does ESC selection change the overall helicopter's performance? Is it worth the increase in mass to have a lower voltage drop R_{ESC} associated with the 40 A ESC, or will a lower rated ESC prove sufficient? These questions are critical to a designer, and shall be addressed here. Primary objectives of this exercise are:

1. Trim a 1,000 gram electric helicopter to determine the required amount of rotor power.

2. Maximize the time of flight and payload.

3. Determine trade offs between motors, ESCs, and voltages combinations to the same trimmed helicopter.

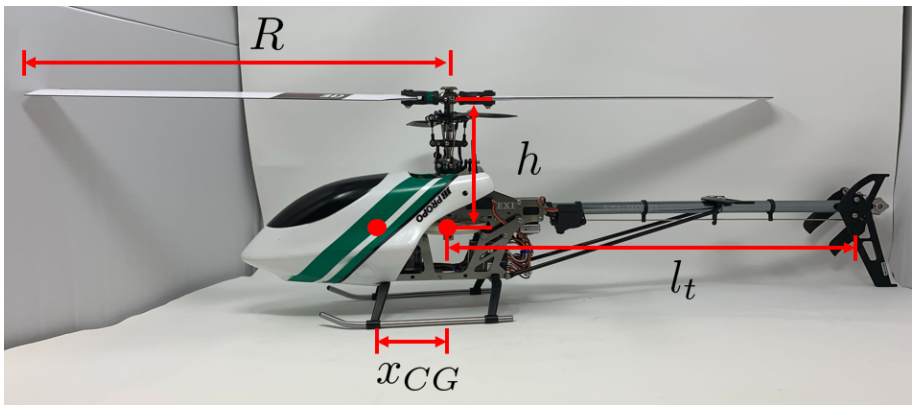

Figure 5.87: Helicopter used for trim and motor/ESC evaluation.

The helicopter selected for these example calculations has a single hingeless rotor and is detailed below in table 5.18, and shown in figure 5.87.

Table 5.18: Parameters for the helicopter used in the trim analysis.

Parameter	Value
GTO Mass, M	1000 gr
Radius, R	355.6 mm
Chord, c	32.6 mm
Number of Blades, N_B	2
Solidity, σ	5.84 %
Tip Speed, v_{tip}	65 m/s
Rotor RPM, Ω	1750 RPM

Parameter	Value
Lift Slope, $C_{l\alpha}$	5.73 rad^{-1}
Drag Coefficient, C_{do}	0.01
Flap Frequency, ν_β	1.10 rev^{-1}
Lock Number, γ	5.4
Flap Hinge Location, e/R	14.3 %
Induced Power Factor, κ	1.10
Blade Loading, C_T/σ	0.081

Parameter	Value
Hub Location above Hub, h	127 mm
Tail location, l_t	406 mm
CG Location from Hub, x_{CG}, y_{CG}	50.8 mm, 0 mm
Gear ratio, GR	6
Flat Plate Area Ratio, f/A	0.02
Battery Capacity, C	3000 mAH
Battery Discharge Coefficient, d	0.75
Figure of Merit, FOM	54.3%

Gross take-off (GTO) mass M of the helicopter is kept constant at 1,000 grams for all configurations, so that different designs can be compared with the same trim analysis, meaning that the amount of payload of the helicopter is varied. The helicopter's empty mass m_e (i.e. no payload, no battery, no motor, and no ESC) is 580 grams. Two batteries were selected from vendors, a 3000 mAh 20C 2S and a 3000 mAh 20C 3S battery, with masses of $m_{bat,2S} = 161$ grams and $m_{bat,3S} = 269$ grams. Motor masses m_m and ESC masses m_{ESC} are provided in tables 5.1 and 5.2.

For a given configuration, the amount of payload is:

$$m_{pl} = M - m_e - m_m - m_{ESC} - m_{bat} \tag{5.10}$$

which changes based on battery voltage, motor, and ESC. However, the total HC mass always sums up to 1000 grams, in order to only create one trim response for the helicopter to keep the comparison even. Once the amount of power for a given flight speed is determined, the time of flight can be estimated from the required power draw.

The DC power supply for this aircraft is a liquid polymer (LiPo) battery. For most batteries, it is common to not discharge them to 100%, as this could cause serious damage to the chemical makeup of the battery [45]. To prevent this, a discharge coefficient is used, which limits the effective battery capacity to:

$$C_{eff} = dC = 2250\ mAH \tag{5.11}$$

where d is the discharge coefficient. For a given DC current draw I_{DC}, the amount of time TOF to discharge the effective battery capacity is:

$$TOF = \frac{C_{eff}}{I_{DC}} = \frac{dC}{I_{DC}} \tag{5.12}$$

which can be used to estimate Time of Hover (TOH) and Time of Forward Flight (TOF). However, first the required DC current draw must be determined, which requires the HC to be trimmed.

Trimming an aircraft requires all 6 degrees of freedom are in equilibrium [27, 28]. That is, no net force is acting on the helicopter in any direction, and is accomplished by iterating between control inputs and aircraft states until an equilibrium is achieved. A discussion on the exact method and equations used to trim a helicopter are beyond the scope of this work, but the results are shown in figure 5.88. Once the aircraft has been trimmed, the required rotor power can be found using gear ratio relations.

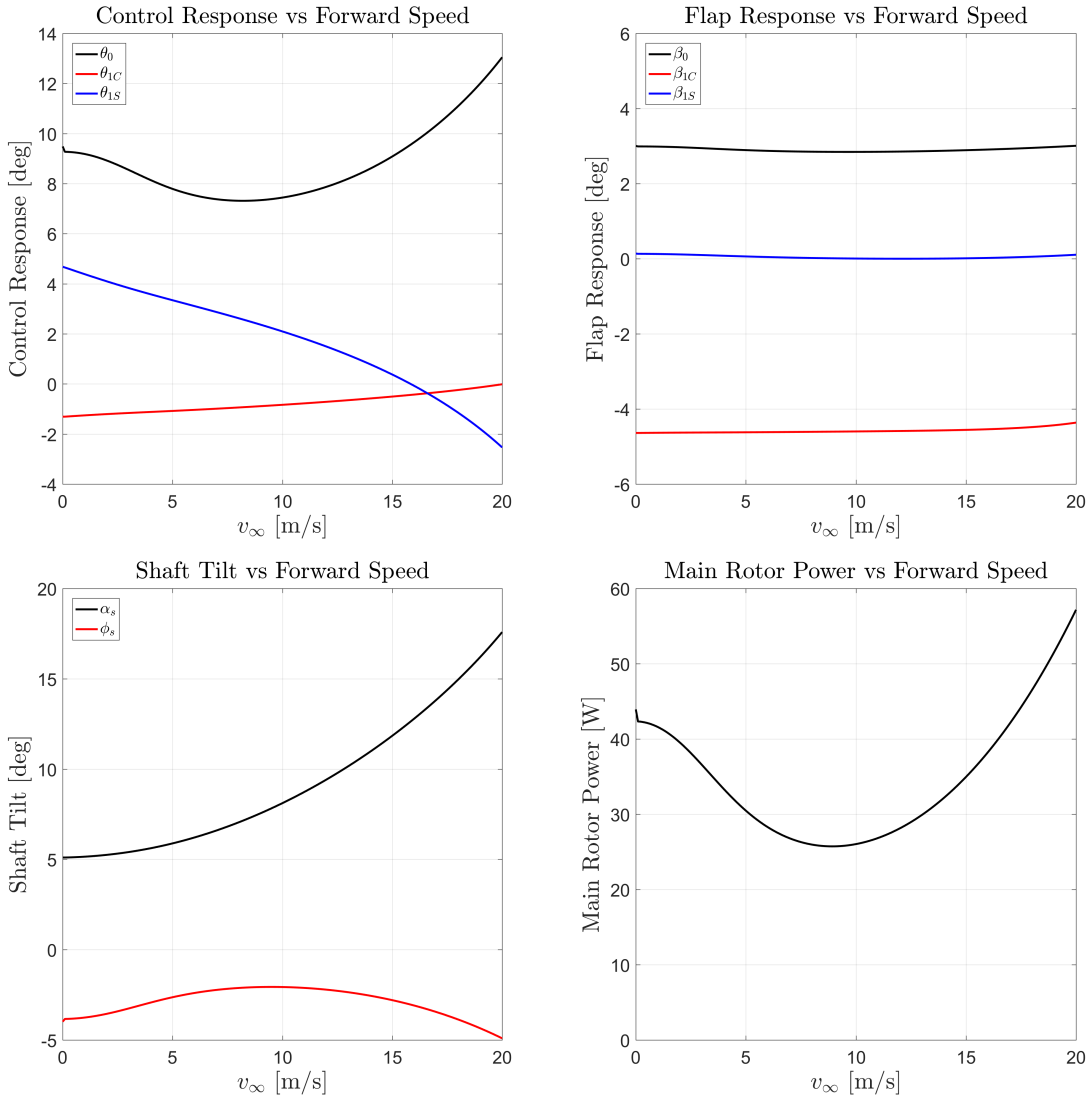

Figure 5.88: Helicopter trim response in forward flight.

Figure 5.88 shows the helicopter's power requirement in forward flight, but how do these relate to the motor and ESC's requirements? As with the hover test stand, the input throttle to the ESC determines the motor's response. Again, a relation between rotor loads and input throttle must be described mathematically, and is found via the gearing of the helicopter. From the rotor response, the required motor torque is [33]:

$$Q_{motor} = \frac{1}{GR}\frac{P_R}{\Omega} = \frac{1}{GR}Q_{rotor} \tag{5.13}$$

and the motor RPM is:

$$\omega = GR\,\Omega \tag{5.14}$$

It is important to note that the rotor torque changes with forward flight, but the rotor RPM does not. With the motor's load and speed determined, the remaining variable is the ESC throttle T_R and is found by manipulating equations 4.35 and 4.40:

$$I_{rms} = \frac{Q}{K_T} + I_o$$

$$T_R = \frac{I_{rms}(R_m + R_{ESC}) + K_E\omega}{\frac{3}{\sqrt{2}\pi}V_{DC}} \tag{5.15}$$

With the throttle evaluated, the ESC transformer relations can be used to find the steady state DC current draw out of the battery via equation 4.58:

$$I_{DC} = (C_1 T_R + C_0) I_{rms}$$

There are two points of interest for this analysis: hover and the speed of minimum

rotor power. Speed for minimum power, also known as cruise speed v_{cruise}, is the forward speed where the rotor requires the least power to operate, and corresponds to the longest endurance, or TOF, for the helicopter. Combining equations 5.13 to 5.15 and equation 4.35, one can arrive at the following plots for required input throttle and DC current draw, shown in figure 5.89.

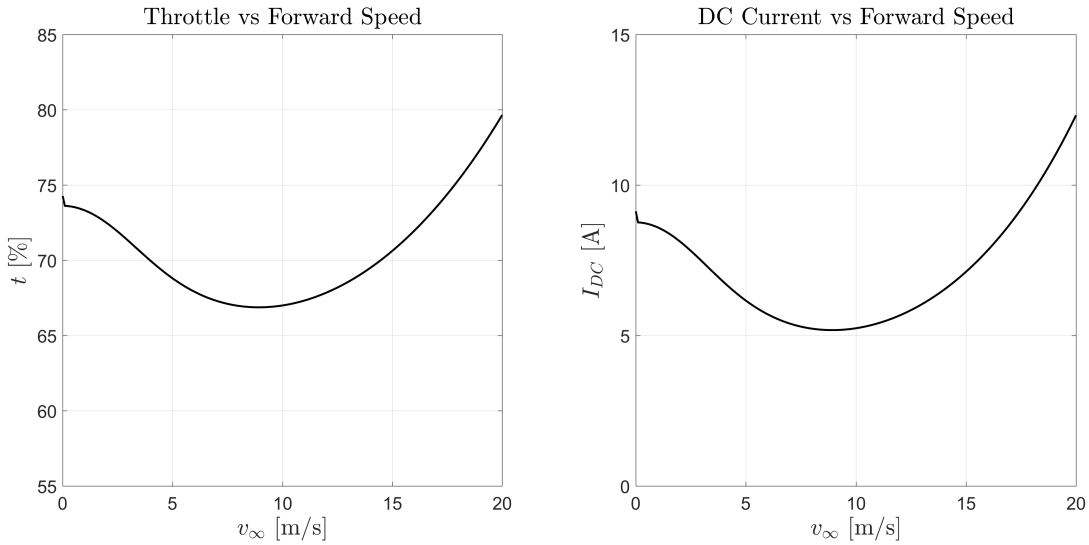

Figure 5.89: Samguk 2500KV motor and SpiderLite 18A ESC response in forward flight.

Based on the rotor torque and RPM requirements, three motors were selected: the EMAX 1700KV at $V_{DC} = 11.1$ V, the EMAX 2300 KV at $V_{DC} = 7.4$ V, and the Samguk 2500 KV at $V_{DC} = 7.4$ V. All motors were considered, however, most configurations either required hover throttles above 100%, which is nonphysical, or required the GTO mass of the helicopter to surpass 1000 grams. All three ESCs were considered for this test, in order to explore the tradeoffs between ESC selection. Recall that the objective is to determine a configuration that maximizes the helicopter's payload capacity and time of flight. Therefore, to grade each motor,

voltage, and ESC combination, the following score is used:

$$S = (TOF\ [min]) \times (m_{pl}\ [gr]) \tag{5.16}$$

which is the product of the time of flight with the payload. The score favors a long time of flight and a greater payload, heavier motors have less payload but a longer time of flight, which makes the relationship interesting. Additionally, having a score defined this way allows for comparing hover and forward flight performance. The results for this design and trim analysis are shown in tables 5.19 and 5.20.

Table 5.19: Results for the example helicopter in hover.

Propulsion System	ESC Used [A]	m_{pl} [gr]	TOH [min]	I_{DC} [A]	T_R [%]	S_H [gr-min]
EMAX	18	108	24.99	5.40	68.17	2699
1700 KV	30	96	24.25	5.57	73.47	2328
at $V_{DC} = 11.1$ V	40	92	25.17	5.36	71.40	2315
EMAX	18	217	15.10	8.94	79.08	3277
2300 KV	30	205	15.71	8.59	85.69	3221
at $V_{DC} = 7.4$ V	40	201	15.82	8.54	83.43	3180
Samguk	18	212	14.80	9.12	74.26	3138
2500 KV	30	200	14.66	9.21	81.12	2932
at $V_{DC} = 7.4$ V	40	196	14.75	9.15	79.16	2891

Table 5.20: Results for the example helicopter in forward flight.

Propulsion System	ESC Used [A]	m_{pl} [gr]	TOF [min]	v_{cruise} [m/s]	Range [km]	I_{DC} [A]	T_R [%]	S_F [gr-min]
EMAX	18	108	41.09	8.90	21.94	3.29	64.01	4438
1700 KV	30	96	40.40	8.90	21.57	3.34	68.55	3878
at $V_{DC} = 11.1$ V	40	92	41.69	8.90	22.26	3.24	67.13	3835
EMAX	18	217	26.16	8.90	13.97	5.16	71.78	5678
2300 KV	30	205	27.24	8.90	14.55	4.96	78.27	5584
at $V_{DC} = 7.4$ V	40	201	27.39	8.90	14.63	4.93	76.36	5505
Samguk	18	212	26.07	8.90	13.92	5.18	66.87	5527
2500 KV	30	200	25.42	8.90	13.58	5.31	73.35	5084
at $V_{DC} = 7.4$ V	40	196	24.85	8.90	13.27	5.43	72.41	4871

Interestingly, the combination with the highest score for both hover and forward flight is the EMAX 2300 KV motor with an 18 A ESC with $V_{DC} = 7.2$ V. Although the 40 A ESC typically requires less DC current to be drawn from the battery, this is not enough of a performance gain to offset the loss in payload associated with a heavier ESC mass. The 18 A and 40 A ESC have masses of 11 and 27 grams respectively, meaning that the 40 A ESC would need to reduce DC current draw by at least 60% to stay competitive, and yet that does not occur.

Running at V_{DC} of only 7.4 V reveals another interesting conclusion: that higher voltage does not always translate into better performance. Battery capacity remains constant, meaning the addition of an extra cell to a 2S battery to create a 3S battery brings along a mass penalty. Benefits for the 3S design are found when examining the TOF and range, as the 3S design has a 57% increase in range and TOF when compared to the EMAX 2300 KV design at 2S. Additionally, the

3S design is both hovering and cruising at a lower throttle, meaning more control margin is available for climbing and maneuvering.

It is worth noting that the selection of the proper configuration is up to the designer and is set by the mission requirements. For example, if the payload mass had been set to 100 grams, the 3S design would be selected. However, by changing the rules of evaluation, one can make different arguments as to the best design. For the first time, this work allows for designers to compute time of flight estimates for electric aircraft, determine pairing relationship between ESC and BLDC motor, and to evaluate tradeoffs in DC voltage selection.

Chapter 6: Conclusions

6.1 Summary of Research

This work consisted of three major phases: development of a dynamometer including DC, AC, and mechanical power analyzers, experimental testing of BLDC motors and ESCs at different voltages, and determining an analytical model which relates phyiscal motor parameters to experimental data. A custom dynamometer was developed at the University of Maryland to characterize the performance of BLDC motors and ESCs. By recording the DC, AC, and mechanical power through the system, efficiency metrics can be obtained for the ESC, BLDC motor, and overall system. 6 motors, with KV ratings between 920 KV to 2500 KV, were paired with 3 ESCs at DC voltages between 7.2 V to 14.8 V. This work represents the largest and most comprehensive investigation of BLDC motors and ESCs to date. Key features of the dynamometer are use of a 2 DAQ setup to record the AC power entering the BLDC motor using the 2-wattmeter method.

A total of 34 combinations of ESCs, BLDC motors, and V_{DC} were tested on the custom dynamometer. From the results of these experiments, an analytical model was developed to predict motor performance with different ESCs and BLDC motors. Significant work to model the ESC, which is typically neglected in research,

shows that 2 primary power losses occur: a switching loss and a conduction loss. Improved understanding of motor and ESC characterization is essential to enhance electric aircraft designs in the future.

6.2 Conclusions

Several conclusions related to motor and ESC performance can be drawn from this work.

1. A first principles analytical model was developed to understand the type of power losses that occur within an ESC and BLDC motor system. A brushed DC motor model was modified to include AC voltage and current quantities, which better describe the inputs to the motor. This model was fit to the experimental data and shows good agreement for Q, I_{rms}, $V_{LL,rms}$, P_{AC}, and I_{DC}.

2. Simplifying the 3 phase AC circuit into a single phase equivalent circuit was shown to be an effective modeling tool. Physical parameters related to the motor's performance can be fit to this model, allowing for motors and ESCs to be used in a rigorous design manner. Four parameters are required to describe the BLDC motor: K_T, K_E, I_o, and R_m. Unique to this thesis is the description of the three ESC parameters: C_0, C_1, and R_{ESC}.

3. BLDC motors tested contain specific peak power ratios of 0.94 to 4.90 kW/kg. It was shown that each ESC does not significantly increase or decrease the

maximum power output of the motor, thereby further reiterating the need to not use a higher rated ESC if possible.

4. Manufacturer specified KV rating is of no practical engineering use. Comparing manufacturer specified KV values to the experimentally obtained K_E values show a 40% discrepancy. Furthering this argument is the fact that most motor models use $K_T = K_E$, however, the model presented in this thesis uses an ideal ratio of K_T/K_E is $\sqrt{27/10} \approx 1.64$. Power losses associated with the motor places the experimentally recorded value at 1.90, indicating a 15.6% difference from the ideal ratio. This places the manufacturer given KV rating well outside the bounds of reliable use.

5. ESC operation is a function of the user throttle. It was found that both output rms voltage and rms current are functions of the user throttle. This allowed for the development of an analytical ESC transformer model, which relates DC power to AC power using the input throttle and motor rms current. Saturation occurs in ESCs between 90% to 100% throttle, meaning that the motor never experiences the full $0.675V_{DC}$ rms voltage, reducing the maximum ω_{NL} of the motor by 5%.

6. ESC's have higher efficiencies at full throttle, as the switching losses are minimized. Switching losses stem from the rapid turning on and off of the MOSFET to augment the output rms voltage and rms current. At 100% throttle, the MOSFETs are placed in an always conducting mode, indicating that only switches related to commutating the motor occur. Additionally, switching

losses increase with increasing DC voltages.

7. Maximum efficiency points for brushless DC motors occur at high RPM and low torque. ESC efficiency generally decreases linearly with rms current, making the overall maximum efficiency for the system occur when the motor is operating at maximum efficiency. Selection of ESC changes the motor rms voltage, with higher rated ESCs having a lower R_{ESC}, associated with more expensive MOSFETs.

8. As evidenced by the hover test stand, predicting rotors, motors and ESCs performance was achieved, allowing brushless motors to enter the design space of electric aircraft in a more rigorous manner. For a fixed pitch direct drive configuration, increasing motor throttle represents a $Q \propto \sqrt{T_R}$ increase in rotor speed. Motor and ESC selection has a profound impact on electric aircraft performance, as oversizing or undersizing the propulsion system could reduce mission capabilities.

6.3 Future Work

With the growing demand for high performance electric aircraft, there are many directions for this research to expand into, with some key areas listed.

1. **Larger Dynamometers:** The dynamometer outlined in this paper can serve as a template to modify over the coming years. The active component in studying the performance of motors is the brake, shown in figure 3.1, and

is responsible for augmenting the load on the motor in a controlled fashion. Studying larger motors is simple, as only the brake needs to be enhanced to a larger maximum torque and speed. Magtrol, the company that sells the brake used in this thesis, produces brakes rated for as large as 3500 in-oz of torque, 350 times the rating of the brake used in this work.

2. **Smaller Dynamometers:** When it comes to dynamometers, it also pays to think smaller. As discussed in the beginning of chapter 4, brakes have an inherent cogging torque, meaning that studying the performance of the motors near ω_{NL} is not possible, where the maximum motor efficiency occurs. By downsizing the brake used, the static 3.1 in-oz load would be eliminated, allowing for a more complete range of operating points to be covered. Additionally, with a lower cogging torque, gearing the motors becomes an option. Recall that higher KV motors were not tested at the higher voltage levels because of the brake's 20,000 RPM limit. However, if the motor could be geared such that the RPM of the brake stays below the limit, then all motors could be tested at higher voltages. Finally, many potential ESC and BLDC motor tests had to be turned away as a result of the cogging torque. By eliminating the cogging torque with a smaller brake, more ESCs could be tested, expanding the design space considerably.

3. **Improved AC Power Measurements:** For any future dynamometers there is a clear need for accurate AC power measurement techniques. Refinements in AC power techniques should include shunt resistor based current measure-

ments at higher voltages. Other areas for improvement are DAQs with faster read rates, as this will be critical to studying motors with higher numbers of pole pair ($N_p > 10$).

4. **Refined BLDC Motor and ESC Modeling:** Improvements in the model to study ESCs and predict ESC performance at higher voltages is necessary. Future enhanced AC power measurements techniques will reduce experimental error, identifying clear trends for ESC efficiencies. From the low voltage AC power setup, it was clear that ESC efficiency vs RPM is a straight line, however, this result needs to be confirmed at higher voltages using accurate AC power measurement techniques. Additionally, an improved understanding of MOSFET characteristics, which lie at the heart of any inverter, is critical to predicting ESC power losses.

5. **Closed Loop Control:** Equations from chapter 4 on BLDC motor and ESC performance describe the steady state condition, but future work is to extend this framework to include time varying dynamics. A state space based model could be developed to describe the motor's performance with time varying throttle, current, and loading. A closed loop controller could be developed around this framework which would be critical for improved performance on quadcopters and other electric aircrafts. Controller goals could include RPM tracking and optimal gain selection that minimizes DC current spikes.

6. **Testing of AC Induction Motors:** AC Induction Motors are favored candidates for high performance manned electrical aircraft for due to their increased

power rating, reliability, and mature electromagnetic designs. A focus of this work would be characterizing and modeling AC induction motors. Tradeoffs between the scale, size, weight, and performance of AC induction motors and BLDC motors can be explored for rigorous design use. AC induction drive power loss and efficiency performance should also be compared to ESC performance.

7. **Heuristic Modeling:** From the catalogs of experimental data and modeling parameters, heuristic functions can be created to assist in aircraft sizing requirements. Heuristics should relate motor torque, efficiency, and peak power to the number of poles, motor mass, motor volume, and motor price. ESC heuristics should relate MOSFET switching variables and ESC resistance to the rated DC current draw, ESC mass, ESC cost, and ESC brand. For both sets of BLDC motor and ESC heuristic equations, a large emphasis should be placed on the cost per unit of each item, for a given amount of torque, power, etc. Distributed electric propulsion electric aircraft require four or more sets of ESCs and BLDC motors. Factoring monetary cost into the analysis will be critical for mass producing a given design.

8. **Optimal Motor and Rotor Pairing:** With an enhanced understanding of motor and ESC requirements, fitting specific motors and ESCs with specific rotors can be achieved. Rotor design dictates that a certain rotor RPM and torque are required to satisfy propulsion, thrust, and control requirements. Once this has been achieved, the rotor requires can be paired with the BLDC

motor and ESC catalog from Chapter 5 to determine the configuration that minimizes the total power draw of the system. Iteration between the rotor design and BLDC motor/ESC selection can further reduce system power, enhancing time of flights for electric aircrafts.

Bibliography

[1] *2019 World Civil Unmanned Aerial Systems Market Profile & Forecast*. Teal Group Corporation, 2019.

[2] M Moore. Uber elevate: evtol urban mobility. *Rotorcraft Business & Technology Summit*, 2017.

[3] KI Swartz. Charging forward: New evtol concepts advance. *Vertiflite*, 4:24–29, 2017.

[4] George Bye. Fly the electric skies. *IEEE Spectrum*, 54(9):26–31, 2017.

[5] Richard Whittle. Air mobility bonanza beckons electric vtol developers. *Vertiflite*, 2017.

[6] Vertical Flight Society. evtol aircraft directoryhome — evtol aircraft directory. `https://evtol.news/aircraft/`, 2017.

[7] Nicholas K Borer, Michael D Patterson, Jeffrey K Viken, Mark D Moore, JoeBen Bevirt, Alex M Stoll, and Andrew R Gibson. Design and performance of the nasa sceptor distributed electric propulsion flight demonstrator. In *16th AIAA Aviation Technology, Integration, and Operations Conference*, page 3920, 2016.

[8] NASA. X-57 'maxwell': Nasa electric research plane gets x number, new name, 2016. https://phys.org/pdf385448350.pdf.

[9] Shyam Kumar Menon. *Performance measurement and scaling in small internal combustion engines*. University of Maryland, College Park, 2006.

[10] Andy Yoon, Xuan Yi, Jon Martin, Yuanshan Chen, and Kiruba Haran. A high-speed, high-frequency, air-core pm machine for aircraft application. In *2016 IEEE Power and Energy Conference at Illinois (PECI)*, pages 1–4. IEEE, 2016.

[11] Xuan Yi and Kiruba S Haran. Thermal integration of a high-frequency high-specific-power motor within electrically variable engine. In *AIAA Propulsion and Energy 2019 Forum*, page 4405, 2019.

[12] Takashi Kenjō and Shigenobu Nagamori. *Permanent-magnet and brushless DC motors*, volume 18. Oxford University Press, USA, 1985.

[13] James R Hendershot and Timothy John Eastham Miller. *Design of brushless permanent-magnet machines*. Motor Design Books, 2010.

[14] Murat Bronz, Jean-Marc Moschetta, and Gautier Hattenberger. Multi-point optimisation of a propulsion set as applied to a multi-tasking mav. 2012.

[15] Duane C Hanselman. *Brushless permanent magnet motor design*. The Writers' Collective, 2003.

[16] Kay Hameyer and Ronnie JM Belmans. Permanent magnet excited brushed dc motors. *IEEE Transactions on industrial electronics*, 43(2):247–255, 1996.

[17] Stefan Baldursson. Bldc motor modelling and control-a matlab®/simulink® implementation. Master's thesis, 2005.

[18] Farhan Ahmad, Mukul Pandey, and Mohammad Zaid. Sensorless control of brushless dc motor by zero-crossing detection pulse generation with adaptive power factor control technique. In *2018 IEEE International Conference on Environment and Electrical Engineering and 2018 IEEE Industrial and Commercial Power Systems Europe (EEEIC/I&CPS Europe)*, pages 1–6. IEEE, 2018.

[19] José Carlos Gamazo-Real, Ernesto Vázquez-Sánchez, and Jaime Gómez-Gil. Position and speed control of brushless dc motors using sensorless techniques and application trends. *sensors*, 10(7):6901–6947, 2010.

[20] Jianwen Shao, Dennis Nolan, and Thomas Hopkins. A novel direct back emf detection for sensorless brushless dc (bldc) motor drives. In *APEC. Seventeenth Annual IEEE Applied Power Electronics Conference and Exposition (Cat. No. 02CH37335)*, volume 1, pages 33–37. IEEE, 2002.

[21] Ned Mohan and Tore M Undeland. *Power electronics: converters, applications, and design*. John wiley & sons, 2007.

[22] J David Irwin. *Basic engineering circuit analysis*. Macmillan Pub. Co., 1987.

[23] Magtrol. Hysteresis devices for tension and torque control, 2019. https://www.magtrol.com/wp-content/uploads/brakes-clutches.pdf.

[24] Magtrol. Hb/hc user's manual, 2019. https://www.magtrol.com/wp-content/uploads/hbmanual.pdf.

[25] Magtrol. Hb-10-2 nominal performance characteristic curve torque vs. current, 2019. https://www.magtrol.com/wp-content/uploads/hb-10-2curve.pdf.

[26] J David Irwin and R Mark Nelms. *Basic engineering circuit analysis*. John Wiley & Sons, 2007.

[27] Gordon J Leishman. *Principles of helicopter aerodynamics with CD extra*. Cambridge university press, 2006.

[28] Raymond W Prouty. *Helicopter performance, stability, and control*. 1995.

[29] Darren Lance Gabriel, Johan Meyer, and Francois Du Plessis. Brushless dc motor characterisation and selection for a fixed wing uav. In *IEEE Africon'11*, pages 1–6. IEEE, 2011.

[30] Clayton R Green and Robert A McDonald. Modeling and test of the efficiency of electronic speed controllers for brushless dc motors. In *15th AIAA Aviation Technology, Integration, and Operations Conference*, page 3191, 2015.

[31] KA Bakshi AV Bakshi UA Bakshi. *Electrical Measurements & Measuring Instruments*. Technical Publications, 2007.

[32] Mulukutla S Sarma. *Introduction to electrical engineering*. Oxford University Press New York, 2001.

[33] B. Mills and A. Datta. Analysis of a permanent magnet synchronous motor coupled to a flexible rotor for electric vtol. In *AHS International 74th Annual Forum*, pages 1–14, May 14th-17th, 2017.

[34] Anand Saxena. *Primary control of a Mach scale swashplateless rotor using brushless DC motor actuated trailing edge flaps*. PhD thesis, University of Maryland, College Park, 2015.

[35] G Renukadevi and K Rajambal. Generalized dq model of n-phase induction motor drive. *International Journal of Electrical, Computer, Energetic, Electronic and Communication Engineering*, 6(9):1066–1075, 2012.

[36] Y Yao, DC Lu, and D Verstraete. Power loss modelling of mosfet inverter for low-power permanent magnet synchronous motor drive. In *2013 1st International Future Energy Electronics Conference (IFEEC)*, pages 849–854. IEEE, 2013.

[37] Yali Xiong, Shan Sun, Hongwei Jia, Patrick Shea, and Z John Shen. New physical insights on power mosfet switching losses. *IEEE Transactions on Power Electronics*, 24(2):525–531, 2009.

[38] F Fürst. design of a 48 v three-phase inverter for automotive applications. *Master's thesis in Electric Power Engineering. Gothenburg, Sweden: Chalmers University of Technology: Department of Energy and Environment*, 2015.

[39] Andrew Gong and Dries Verstraete. Experimental testing of electronic speed controllers for uavs. In *53rd AIAA/SAE/ASEE Joint Propulsion Conference*, page 4955, 2017.

[40] Ettore Scabeni Glitz and Martin Ordonez. Mosfet power loss estimation in llc resonant converters: Time interval analysis. *IEEE Transactions on Power Electronics*, 2019.

[41] Robert W Erickson and Dragan Maksimovic. *Fundamentals of power electronics*. Springer Science & Business Media, 2007.

[42] Aaron M Harrington and Christopher Kroninger. Characterization of small dc brushed and brushless motors. *Army Research Lab Vehicle Technology Directorate, Aberdeen Proving Ground, MD, Report No. ARL-TR-6389.*, 2013.

[43] Stephen Boyd and Lieven Vandenberghe. *Introduction to applied linear algebra: vectors, matrices, and least squares*. Cambridge university press, 2018.

[44] RobotShop. Brushed dc motors, 2019. https://www.robotshop.com/en/dc-motors.html.

[45] Thomas B Reddy. *Linden's handbook of batteries*, volume 4. McGraw-hill New York, 2011.